The Dissertation Committee for Babak Poursartip
certifies that this is the approved version of the following dissertation:

Topographic amplification of seismic motion

Committee:

Loukas F. Kallivokas, Supervisor

Dominic Assimaki

Leszek F. Demkowicz

Lance Manuel

Kenneth H. Stokoe II

John L. Tassoulas

Topographic amplification of seismic motion

by

Babak Poursartip, B.Sc.; M.Sc.

DISSERTATION

Presented to the Faculty of the Graduate School of

The University of Texas at Austin

in Partial Fulfillment

of the Requirements

for the Degree of

DOCTOR OF PHILOSOPHY

THE UNIVERSITY OF TEXAS AT AUSTIN

May 2017

Dedicated to my beloved family.

Without your love, support, and encouragement, none of this would have been possible.

Acknowledgments

I would like to offer my sincere thanks to Professor Loukas F. Kallivokas for his ideas on this research, for his patience and motivation, and for the support of my Ph.D. study. This project would not have been possible without his invaluable help and supervision.

I am deeply indebted to Professors John L. Tassoulas and Leszek F. Demkowicz for their inspiring courses and serving as my committee members. Special gratitude is also extended to Professors Dominic Assimaki, Lance Manuel, and Kenneth H. Stokoe II for serving on my dissertation committee and for their helpful suggestions. Many thanks are also due to Professor Vahid Lotfi, my Master's advisor, for shaping my academic life. For that I will be ever grateful to him.

My sincere thanks also goes to Mrs. Pam Dahl, the General Engineering Coordinator, who gave me the chance to serve as the instructor of the Differential Equations course; Teresa Howard, Research Scientist Associate at the Center for Space Research, for helping me with extracting topographic data; Gregory Dorsey Abram, Research Scientist at Texas Advanced Computing Center, for helping me with the large-scale visualization; and Dr. Francisco J. Sánchez-Sesma, Professor at Instituto de Ingeniería, Mexico, for his invaluable comments on my research. I would like to thank my colleagues and officemates who gave me the joy of working in such a friendly and creative environment: Joeny Bui, Hossein Fadaei, Heedong Goh,

Chanseok Jeong, Pranav Karve, Seungbum Koo, Sezgin Kucukcoban, Hamidreza Mashayekh, Jae Sang Moon, Hieu Huy Nguyen, Cuong Nguyen, Ali Morovat, Pasca Patta, and Eric L. Sammarco. They have inspired me, challenged me, and contributed greatly to my knowledge.

Appreciation also goes out to Dr. Arash Fathi for years of friendship and cooperation in academia. I am also grateful to my friends I met in Austin for their support and understanding: Shiva & Babak, Mahsa & Vahid, Shiva, Maryam & Ehsan, Neda & Hossein, Ata, Azaret, Lan, Serena, Moggan & Arash. I have greatly appreciated those who supported me in any respect during the completion of this dissertation.

I cannot find words to express my heartfelt gratitude to my immediate family, who supported and encouraged me in the study. They have been an important and indispensable source of love and spiritual strength.

Support for the author's research has been provided by the National Science Foundation under grant awards CMMI-1030728. This support is gratefully acknowledged.

Topographic amplification of seismic motion

Babak Poursartip, Ph.D.
The University of Texas at Austin, 2017

Supervisor: Loukas F. Kallivokas

Seismic hazard assessment relies increasingly on the numerical simulation of ground motion, since recent advances in numerical methods and computer architectures have made it ever more practical to obtain the surface response to idealized or realistic seismic events. The key motivation stems from the need to assess the performance of sensitive components of the civil infrastructure (nuclear power plants, bridges, lifelines, etc.), when subjected to realistic scenarios of seismic events. To date, most simulation tools rely on a flat-earth assumption, which ignores topography and its effects on seismic motion amplification. In an attempt to narrow the gap between modeling and physical reality, in this dissertation we study systematically the effects topographic features have on the surface motion when compared against motion obtained using a flat-surface assumption.

To this end, we discuss first an integrated approach that deploys best-practice tools for simulating seismic events in arbitrarily heterogeneous formations, while also accounting for topography. Specifically, we describe an explicit forward wave solver based on a hybrid formulation that couples a single-field formulation for the computational domain with an unsplit mixed-field formulation for Perfectly-Matched-Layers

(PMLs or M-PMLs) used to limit the computational domain. We use spectral elements for spatial discretization, and an efficient Runge-Kutta explicit solver for time integration. Due to the material heterogeneity and the contrasting discretization needs it imposes, we also use an adaptive Runge-Kutta-Fehlberg time-marching scheme to optimally adjust the time step so that the local truncation error rests below a predefined tolerance. To account for the seismic load, we use the Domain-Reduction-Method to introduce the incoming seismic motion in the computational domain whenever the introduction of the actual seismic source would make the computational domain unnecessarily large. Lastly, we couple the DRM with the PMLs to complete the seismic motion simulation engine.

Using the developed toolchain, we then report results of parametric studies involving idealized topographic features, which show motion amplification that depends, as expected, on the relation between the topographic features' characteristics and the dominant wavelength. More interestingly, we also report motion de-amplification patterns. Given the prevalence of lower dimensionality models for seismic risk assessment, we also report on the effects model dimensionality has in the presence of heterogeneity and topography.

The results reported herein, support the thesis that, for purposes of seismic risk assessment, topography and heterogeneity are best treated when fully accounted for in three-dimensional models. Even this is only a first and necessary step towards higher fidelity modeling of seismic motion effects.

Table of Contents

List of Tables

List of Figures

List of Algorithms

Chapter 1

Introduction[1]

1.1 Motivation

Understanding and quantifying the seismic response in regions with surface irregularities, such as hills, valleys, and alluvial basins, have been the focus of seismologists and earthquake engineers for decades. The interest remains strong since discrepancies still exist between the recorded surface motion from strong earthquakes and numerical simulations. There are many reasons for the discrepancies, but chief among them are uncertainties about the subsurface properties (velocity model, fault location/geometry, etc.) used in seismic motion simulations, uncertainties in quantifying the seismic source mechanisms, and the lack of adequate representation of topographic features. Empirical evidence following strong earthquakes suggests that topographic features may induce amplification, and even de-amplification, in the proximity of a topographic feature. For example, Figure 1.1 depicts damage following the 2010 Haiti earthquake, where buildings closer to the hill's crest suffered more damage than those along the hillside.

[1]Portion of this chapter has been published in: B. Poursartip, A. Fathi, L.F. Kallivokas, "Seismic wave amplification by topographic features: A parametric study," *Soil Dynamics and Earthquake Engineering*, 92, 503-527, 2017. The dissertation author had significant contribution to the article.

Figure 1.1: Destruction pattern on a hill following the 2010 Haiti earthquake

Despite the ever increasing adoption of wave motion simulations for assessing seismic hazard, most numerical assessment/simulations are still based on oversimplifying assumptions, including flat-surface models, horizontally layered models, and vertically propagating plane waves (Figure 1.2(a)). Such assumptions allow for one-dimensional models, which tend to underestimate motion amplification and fail to adequately capture the motion complexity associated with the physical setting (Figure 1.2(b)). On the other hand, continued advances in the computational sciences and engineering allow for simulations that bring us closer to the physical reality without imposing onerous requirement on the computational resources. Three-dimensional modeling of seismic motion is, in our view, the preferred pass for assessing seismic risk.

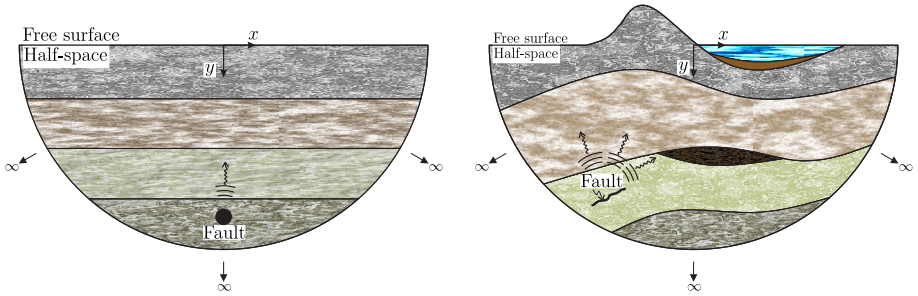

Figure 1.2: Ground idealization: simplified seismic model versus physical reality

1.2 Topographic effects –A review

The literature on the effect of surface geometry on wave motion falls into three general categories: (i) observations from earthquakes and field experiments; (ii) studies based on analytical and semi-analytical solutions for simple topographic geometries, such as a triangular wedge or a semi-circular valley; and (iii) parametric studies based on numerical simulations.

1.2.1 Topographic effects –Field observations

Several observations on the effects of topography on seismic wave amplification have been reported. They include, for example, observations in the aftermath of the 1971 San Fernando Valley earthquake [39], of the 1987 Whittier Narrows earthquake [157], and of the 2002 Molise earthquake in Italy [199]. Çelebi (1987) [56] investigated the topological amplification of the 1985 Chile earthquake and reported on the damage pattern to structures situated on ridges and soft soil sites. He concluded that the unusual patterns of structural damage resulted from the frequency-dependent amplification due to f surface irregularities. Later, in 1991, Çelebi [57] collected and

summarized the results of case studies on three earthquakes, and provided evidence of topographic amplification for a particular range of frequencies. Hartzell et al. (1994) [119] studied the cause of the structural damage and ground cracking observed at the Robinwood Ridge during the 1989 Loma Prieta earthquake and argued that the presence of ridges intensifies the motion amplification. In another study by Bouchon and Barker (1996) [43] using the records collected at the Tarzana station during the 1994 Northridge earthquake, a five-fold topographic amplification has been reported. Geli et al. (1988) [105] pointed out that numerical simulations underestimate the topographic amplifications, blaming simplified models for the discrepancies.

Assimaki studied the 1999 Athens earthquake in Greece [14, 16] and showed that the observed amplification of seismic motion in the vicinity of a cliff crest could only be predicted by simultaneously accounting for the topographic geometry, stratigraphy, and nonlinearity. The analysis of the Tarzana Hill recordings from the 1987 Whittier Narrows and the 1994 Northridge earthquakes by Graizer (2009) [109] showed that the observed amplification was due to the combined effects of topography and layering that resulted in trapping energy within a low-velocity layer near the surface. Similar observations were also reported in Sánchez-Sesma (1987) [251], Aki (1993) [3], Massa et al. (2010) [200], and Buech et al. (2010) [47].

Field experiments could also provide insight into the effect topography plays in seismic amplification, but due to cost considerations there have only been a few reported attempts. Buech et al. (2010) [47] installed a seismic array along the crest of a hill in New Zealand to record earthquake data. They reported high amplification along the crest, as large as eleven times of the motion on the flat surface. Massa et

al. (2010) [200] performed a similar experiment using data from a seismic network installed on a ridge in central Italy. They reported amplification as large as 4.5 at specific frequencies. More recently, Wood and Cox (2015) [294] exploited ground shaking generated in a coal mine in central Utah and reported significant amplitude changes due to topography. Stolte et al. (2017) [277] conducted an experiment on a ridge near Los Alamos, New Mexico to study topographic amplification of seismic waves.

1.2.2 Topographic review –Analytical and semi-analytical solutions

Whereas exact solutions of wave motion in a homogeneous, flat-surface, half-space are readily available, closed-form solutions for a half-space exhibiting a surface irregularity, even one described by a canonical shape, are scantier. Among such exact solutions, the greatest attention has been paid to the scattering of SH waves, owing to the scalar form of the associated wave equation. One of the earliest studies is due to Sills (1978) [269], where a method was developed to solve the scattering of SH-waves by an arbitrary topography in a homogeneous, semi-infinite half-space using an integral equation. Sills applied the method to a semi-circular hill, to a Gaussian hill, and to a combination of a hill and a valley for various wave motion characteristics. Trifunac (1973) [285] presented a closed-form solution for the diffraction of SH waves by a semi-cylindrical canyon and reported strong amplification near the feature. Sánchez-Sesma et al. (1982) [256] developed a boundary integral method for the scattering of SH waves by any irregular feature. In 1985, Sánchez-Sesma [260] described another method particularly suited for infinite wedge-shaped hills and val-

leys. Smerzini et al. (2009) [270] presented a theoretical approach to study the effects a circular underground cavity has on surface motion. Additional references can be found in Sánchez-Sesma et al. (2005) [261], and Qui et al. (2005) [85].

Exact solutions for the vector equation, accounting for P and SV waves in the presence of a surface feature are even scantier than the SH case. One exception is the analytical solution proposed by Sánchez-Sesma (1990) for an infinite wedge [252]. Snieder (1986) [272] also developed an explicit formula to analyze three-dimensional surface-wave scattering by hills in a continuous elastic medium. Paolucci (2002) [224] has also provided a simple approximate expression for the fundamental frequency of triangular hills. Flat-surface solutions are more common, starting from the work of Lamb (1904) [181] for the wave propagation in a semi-infinite, isotropic, elastic half-space due to an arbitrary force at a point. Garvin (1956) [101] also derived the analytical solution to a line source in a homogeneous elastic half-space. Hisada (1994,1995) [128, 129] employed Green's function to obtain the solution to a point source load within a layered half-space.

1.2.3 Topographic effects –Numerical studies

A few parametric studies conducted so far shed light on the problem of seismic amplification. Bard (1982) [25] used the Aki-Larner technique to perform a parametric study to investigate topographic effects through their dependencies on incident wave type, frequency, and incident angle. Ashford and Sitar (1997) [12], and Ashford et al. (1997) [13] performed a frequency-domain parametric study on the effect of single-slope topography on the propagation of shear waves. Assimaki et al. (2005)

[14] affirmed the significance of topography by performing a time-domain parametric study on a single slope geometry. They concluded that the frequency content of the excitation, stratigraphy, and the geometry of the cliff are all important in the amplification of incoming seismic waves. Bouckovalas and Papadimitriou (2005) [45] investigated the amplification effects a step-like slope topography has on a vertically propagating SV-wave.

1.2.4 Discrepancies between observations and simulations

A few studies suggest that numerical solutions tend to underestimate the seismic wave amplifications. Geli et al. (1988) [105] reviewed several experimental observations and compared them with numerical results and concluded that the numerical simulations underestimate the topographic amplifications in the majority of cases, mainly because of the oversimplified assumptions considered in the computational models. Bard (1999) [24], based on field data claimed that, while there is a qualitative agreement between theory and observations, a clear discrepancy exists, with larger amplifications seen in the field data. Semblat et al. (2005) [264] focused on the influence of the complexity of the soil layering on site effects. They claimed that the geometry of the basin has a strong impact on the amplification of seismic waves and on time duration lengthening.

1.3 Research objectives

Although much work has been done to date, the influence of surface topography is still ignored in seismic code provisions, since the codification of the links between

amplification and topographic characteristics remains a challenge. The main goal of this dissertation is to contribute to a better understanding of the effects of surface topography on site response. Toward this goal, we first describe a methodology for solving wave equations in two- and three-dimensional elastic, semi-infinite, heterogeneous media with irregular surface, both in the time- and frequency-domains.

Once the computational tool, which fully accounts for the effects of topography and heterogeneity, has been established and verified, in a second step, we study the topography effects by identifying, via a systematic parametric investigation, conditions that influence the intensity of topographic amplification. To this end, we consider parameters such as feature geometry, incident wave type, angle of incidence, Poisson's ratio, and incident wave frequency. In this study, we focus on P and SV waves, and omit SH waves because their effects have already been adequately addressed in the literature.

1.4 Review of applicable methods

We review next numerical models pertinent to the study of seismic amplification due to surface irregularities in sedimentary valleys. The literature is vast and can be categorized, according to the objectives of this study, into four areas:

1. *Wave simulation methods:* numerical techniques capable of modeling wave motion.
2. *Seismic source modeling:* methods to account for seismic input.
3. *Domain truncation:* methods for limiting the extent of the computational do-

main, while mimicking the behavior of an otherwise semi-infinite physical domain.

4. *Large-scale seismic motion simulations:* review of notable developments involving actual geologic formations subjected to realistic seismic scenarios.

1.4.1 Wave simulation methods

In the absence of exact solutions, numerical tools have long been used for simulating wave motion in complex domains. In this section, we briefly address various numerical techniques that have been used in large-scale seismic wave simulations.

1.4.1.1 Finite difference method

The finite Difference Method (FDM) is the primary numerical method used in seismology due to its simplicity. However, modeling complex surface features or heterogeneous domains is not trivial with FDM due to the need for a structured grid.

Early seismic studies using FDM were mostly focused on two-dimensional models: Alterman and Karal (1968) [5] formulated the wave propagation problem in layered elastic media; Boore (1972) [39] used FDM to study the effects idealized mountain geometries have on the amplification and de-amplification of SH-waves; Vidale and Helmberger (1988) [287] simulated the propagation of low-frequency (0.1 Hz to 0.5 Hz) SH and P-SV waves due to the 1971 San Fernando earthquake using a two-dimensional model; Levander (1988) [183] exploited a staggered-grid finite difference formulation to reduce the harmful effects of grid dispersion and investigated the wave propagation in mixed acoustic-elastic media. Similar studies include: Kelly et

al. (1976) [158], Pitarka et al. (1994) [235], Scrivner et al. (1994) [263] and irregular grid FD by Opršal and Zahradník (1999) [221].

The simulation of the Loma Prieta earthquake in the Santa Clara Valley by Frankel and Vidale (1992) [97] is one of the earliest three-dimensional finite difference studies. In another work, Frankel (1993) [95] showed the significant difference between the synthetic seismograms obtained from the three-dimensional simulation of a hypothetical earthquake in the San Bernardino basin, compared with those derived from a two-dimensional model. Furthermore, he simulated the San Andreas fault to demonstrate that the rupture directivity affects the pattern of maximum ground motions on the surface of the basin. Similarly, Yomogida and Etgen (1993) [295] developed a three-dimensional staggered-grid technique with a higher-order scheme to minimize the numerical dispersion, and simulated the 1987 Whittier-Narrows earthquake in the Los Angeles basin using a point source model; McLaughlin and Day (1994) [203] analyzed numerically the 1994 Northridge earthquake; Graves [110, 111, 112] also applied a staggered-grid finite difference technique endowed with a memory optimization procedure to study the amplification of seismic waves; Graves (1993) [110] simulated the San Francisco Marina District basin and observed significant amplification and a longer shaking duration relative to the response recorded at the nearby rock; Graves [112] reviewed the effects of source parameters such as seismic moment, slip rise time, and slip distribution on the seismic response.

Pitarka (1999) [233], and Opršal and Zahradnik (1999,2002) [221, 222] combined the staggered-grid with a non-uniform grid to improve the efficiency of their finite difference method when applied to large-scale domains. Aoi and Fujiwara

(1999) [9] used discontinuous grids to reduce the computational cost of heterogeneous three-dimensional domain simulations. Similar studies include Olsen et al. (1995) [220], Moczo et al. (1999,2001) [211, 210], Zingg et al. (2000) [301], Sørensen et al. (2006) [274].

Pitarka et al. (1998) [234] is one of the earliest attempts to simulate the three-dimensional near-fault ground-motion amplification at long periods (greater than $1.25s$), using a kinematic earthquake rupture model. They simulated the 1995 Kobe earthquake to conclude that the basin-edge effect influences the ground motion amplification pattern. In another work, Frankel and Stephenson (2000) [96] developed a three-dimensional finite difference code and validated the results with the available synthetics for the Seattle fault zone. Their results show a remarkable amplification of surface waves due to basin edge effects and due to the shallow basin deposits.

1.4.1.2 Boundary element and boundary integral methods

The boundary element method (BEM) has been used in the context of seismic wave motion studies: it has the advantage of dimensionality reduction and of accounting exactly for the radiation condition., but is limited to linear homogeneous domains for which the Green's function is available. Two major BEM approaches exist, direct (DBEM) and indirect (IBEM), where, according to Sánchez-Sesma and Campillo (1991) [254] and Zeng and Bielak (1994) [298], they are mathematically equivalent.

Examples of the DBEM include the works by Wong and Jennings (1975) [293], Fishman and Ahmad (1997) [94], Reinoso et al. (1997) [245], Álvarez-Rubio et al.

(2004) [7], Kamalian et al. [143, 273], Nguyen and Gatmiri (2007) [213], Bouchon and Braker (1996) [43], Campillo (1987) [51], and, Campillo and Bouchon (1985) [52].

Indirect boundary element (IBEM) is frequently used in this field, see for example [259, 260, 256]. Sánchez-Sesma and Luzón (1995) [257] analyzed the response of Rayleigh, P- and S- waves in three-dimensional alluvial valleys. The seismic response in the Volvi sedimentary basin in the northern Greece is studied in [6, 7, 135] using IBEM. Sánchez-Sesma (1999) [286] simulated wave propagation in irregularly layered, elastic, two-dimensional media with internal line sources. Zepeda et al. (2003) [106] and Luzón et al. (2003) [188] applied IBEM to model heterogeneous sedimentary basins under SH-waves. Similar studies include the work by Sánchez-Sesma and Campillo (1993) [255], Sánchez-Sesma et al. (2001) [258], Luzón et al. (2003) [188], Gil-Zepeda et al. (2003) [106], Sánchez-Sesma 2010 [253], and Rodríguez-Castellanos et al. (2011) [248].

Sánchez-Sesma and Luzón (1995) [257] and Bouchon (1979) [40] substituted the complex Green's function solution with the discrete wavenumber method, introduced by Bouchon and Aki (1977) [42] and Kawase (1988) [156] for two-dimensional models. Later, Kim and Papageorgiou (1993) [160] extended this method to three-dimensional models.

1.4.1.3 Finite element method

The finite element method (FEM) offers more flexibility in simulating geometrically complex domains, thus providing a convenient tool for seismic simulations, especially

for large basins characterized by heterogeneity and strong topographic features.

The work by Lysmer and Drake (1971, 1972) [189, 190] is among the earliest applications of finite elements in wave simulations. They studied Love and Rayleigh waves in a non-horizontally layered half-plane that resembles an alluvial valley. Archuleta and Frazier (1978) [11] presented a method for simulating a finite fault in a three-dimensional semi-infinite medium. Toshinawa and Ohmachi (1992) [284] modeled Love waves in the Kanto Plain sedimentary basin in Japan and observed a greater amplification and time duration in comparison with two-dimensional results. Bielak et al. (1999) [38] obtained the ground motion for a vertically propagating SH-wave in a small valley in Kirovakan during the 1988 Armenia earthquake. They generated synthetic accelerograms on the surface of the valley for various sites and compared the results with the free-field motion to get the amplification factor.

Hisada et al. (1998) [130] used an unstructured mesh in the Osaka basin model to investigate the long-period strong motion during the Kobe earthquake. Assimaki et al. (2005) [15] investigated the local site effects during the 1999 Athens earthquake using an unstructured finite element model.

1.4.1.4 Hybrid methods

In order to take advantage of more than one technique, one can combine various computational methods to form a hybrid one. For example one can couple the simplicity of the finite difference method with the ease of implementing the traction-free condition on an irregular surface of the finite element method. Ohtsuki and Harumi (1983) [214] and Outsuki et al. (1984) [215] combined finite elements with a

particle method to simulate SV-wave propagation in an elastic medium with irregular surfaces. Similarly, Moczo et al. (1997) [209] combined finite elements for modeling topographic features, with FDM for the rest of the domain, and studied the P-SV wave propagation in a viscoelastic heterogeneous medium with irregular topography.

1.4.1.5 Spectral element method

The spectral element method (SEM) enjoys the accuracy of the pseudo-spectral method (PSM) with the flexibility of the finite element method. The spectral element method was originally introduced by Orszag (1980) [223] and Patera (1984) [228] in fluid dynamics, and was applied in elastodynamics problems by Gazdag (1981) [103] and Kosloff and Baysal (1982) [177].

Spectral elements are superior to finite elements in the sense that the mass matrix can be diagonalized, which, in turn, allows for easy parallelization if an explicit solver is utilized. In the context of elastic wave propagation spectral elements have been used is used by Faccioli et al. (1997) [84], Komatitsch and Tromp (1999) [166], Komatitsch and Vilotte (1998) [171].

Komatitsch and Vilotte (1998) [171] introduced spectral elements in seismology. They verified their two- and three-dimensional formulations using Lamb's problem (1904) [181] and Garvin's problem (1956) [101]. In 1999, Komatitsch et al. [172] compared the spectral elements results due to the propagation of Rayleigh incident waves in a domain with a semi-circular canyon with the discrete wavenumber/boundary elements results for the same problem obtained by Kawase (1988) [156]. Komatitsch et al. (2001) [165] presented an unstructured spectral element

method for two-dimensional wave simulation using triangular and quadrilateral elements. Komatitsch and Tromp (1999) [166] adopted the spectral element method to simulate seismic waves due to a moment tensor source in a three-dimensional layer-cake model and verified the results with Bouchon (1981) [41]. Additionally, in the same work, they verified the propagation of P-waves in a homogeneous hemispherical carter with Sánchez-Sesma (1983) [259]. Furumura and Koketsu (2000) [98] used a parallel pseudo-spectral technique to simulate the 1995 Kobe earthquake. Seriani (1997,1998) [265, 266] proposed a high performance iterative solution for spectral element method to model seismic waves. For a detailed review on the application of spectral elements in seismology, see also Peter et al. (2011) [231].

The ability to use unstructured meshes, made of, e.g. triangles or tetrahedra, for discretizing topographic features and fault geometries is essential. Using spectral elements for an unstructured mesh is difficult: the difficulty stems from the fact that Gauss-Lobatto quadrature points are only known for tensor-product elements, such as quadrilaterals or hexahedra, but not for non-tensor-product elements such as triangles or tetrahedra. Dubiner (1991) [77] used Jacobi polynomials to obtain a tensor-product-like spectral method for triangles by mapping the triangle to a rectangle using a non-rotational collapsed coordinate system in combination with a warped tensor product. Sherwin and Karniadakis [267, 268, 290] modified Dubiner's idea to construct an unstructured spectral element basis which can be applied to triangular and tetrahedral elements. Taylor et al. (2000) [280, 281] tackled the problem by designing an algorithm to compute the Fekete points (set of points for polynomial interpolation) for a triangle. Komatitsch et al. (2001) [165] also developed

Fekete points for triangles such that they match the quadrature points in quadrilateral elements and allow for a conforming mesh in a domain discretized using both quadrilateral and triangular elements. Hesthaven and Teng (2000) [124] developed a stable, high-order solution for partial differential equations on complex domains. Cohen et al. (2001) [66] and Cohen (2002) [64] also computed quadrature points for various two- and three-dimensional unstructured elements of various order. Mercerat, Vilotte, and Sánchez-Sesma (2006) [205] presented the Triangular Spectral Element Method (TSEM) by resorting to a multi-variable Lagrange interpolation, however, the method results in a consistent mass matrix that adds complexity to the time marching algorithm (see Pasquetti and Rappetti (2004,2006,2010) [225, 226, 227] on the convergence of various TSEM approaches.

Using non-conforming meshes is an alternative method for discretizing complex domains. Casadei et al. (2002) [54] proposed a hybrid finite element/spectral element method for seismic simulations in complex domains. Chaljub et al. (2003) [58] used Gauss-Lobatto-Legendre quadrature with a non-conforming mesh to approximate the elastic wave propagation in an isotropic solid-fluid sphere. Rodríguez-Rozas and Diaz (2016) [249] used a non-conforming mesh to improve the efficiency of the numerical solution of time-dependent acoustic-elastic coupled problems, via an independent discretization of domains with various material properties.

1.4.1.6 Discontinuous Galerkin method

The primary advantage of discontinuous Galerkin method (DG) in solving differential equations is that DG does not require the continuity of variables along the element's

edges, allowing for a simple matrix assembly process, flexible mesh refinement and adaptivity, easy discretization of complex domain, highly scalable parallel algorithms, plus non-uniform high-order local approximations, all at the cost of higher number of total unknowns in comparison to the finite element method. Käser and Dumbser (2006) [154] implemented the DG method for wave simulation in a two-dimensional domain, discretized with an arbitrary high-order accuracy in space and time using triangular elements. Wilcox et al. (2010) [291] used DG for coupled elastic-acoustic media. See also Grote et al. (2006) [113] and Hu et al. (1999) [132] for similar DG applications in seismology.

We remark that Adaptive Mesh Refinement (AMR) , regardless of the numerical technique, can potentially be applied in the solution of any differential equation in favor of accuracy and cost reduction. In this way, at each time-step (or every few), the required level of accuracy will be assessed in the domain, and grids will be adaptively refined to satisfy the required accuracy. This method, however, has been rarely used in seismology (see Burstedde et al. (2009) [50] for notable exception).

1.4.2 Seismic source modeling

Introducing the seismic load in the numerical model is one of the key challenges in seismic wave motion simulations. The source of difficulty is twofold: (i) the fault rupture mechanism is not fully understood; (ii) there has yet to be a widely accepted and adopted kinematic seismic source model. Overall, two main approaches can be considered in seismic source simulations:

1. The seismic source is included within the computational domain (Figure 1.3(a)).

This model affords a realistic approach for seismic motion simulation. However, the approach requires a large computational domain since the source is oftentimes located far away from the domain of interest.

At least, two types of source models are possible: (a) point source, which can be used in simulating weak earthquakes (e.g., aftershocks) or faults with negligible size effects compared to the dimension of the seismic zone; and (b) extended source model used to simulate strong earthquake events (e.g., main shocks) or faults whose size is relatively large in comparison to the size of the seismic zone.

2. The seismic source lies outside the computational domain (Figure 1.3(b)). In this case, the seismic load is introduced in the model in the form of effective forces applied either on the truncated boundary of the computational domain or on some other artificial boundary within the computational domain. Simulations of this kind, since are usually of a small size, are useful for investigating the local effects of earthquakes.

1.4.2.1 Point seismic source model

Nakano (1923) [212] tried to simulate earthquake loads for the first time using a point source in the form of an explosion, but, the results were not promising. The most common point source models are realized via a double-couple [95, 111, 112, 166, 222, 263]; the details will be described in Section 2.2.1.

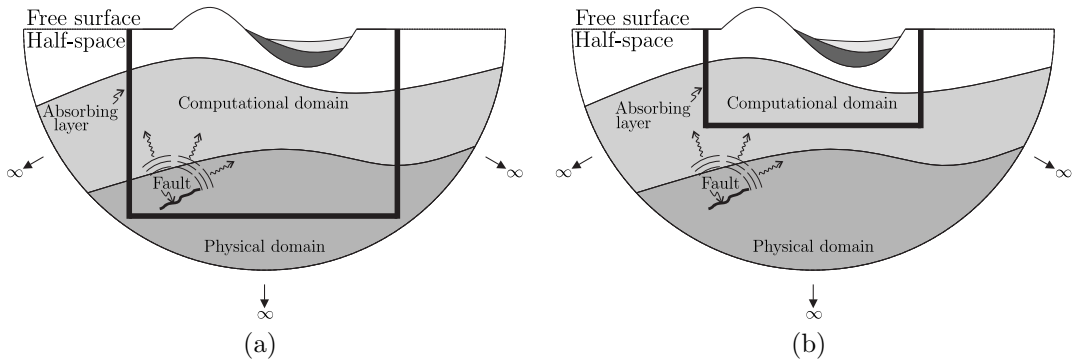

Figure 1.3: Schematic approaches toward seismic wave simulation: (a) applying seismic loads to the computational domain excluding the source, (b) seismic source simulation in the computational domain

1.4.2.2 Extended seismic source model

Theoretical studies on simulating the seismic fault as an extended source are scant owing to the complex nature of the fault, and, oftentimes encompass simplified assumptions, such as planar fault geometry, constant rupture velocity, uniform slip, etc. Archuleta and Frazier (1978) [11] discussed a propagating stress relaxation formulation, which takes into account the geometry and the properties of the fault, for a finite fault plane in a three-dimensional half-space. Frankel (1993) [95] and Olsen et al. (1995) [217] succeeded in simulating a planar vertical right-lateral strike-slip fault with constant rupture velocity (80% of the shear velocity) as a series of point loads in the direction of the fault surface. Each point imposes the loads using a double-couple, with a Gaussian distribution as the slip function.

The dynamic rupture model is a more accurate method to simulate a fault: Galvez et al. (2014) [100] implemented a dynamic rupture model into a parallel

spectral element code and validated the results. Pelties et al. (2012) [229] and (2014) [230] and Puente et al. (2009) [73] introduced a high-order derivative discontinuous Galerkin (ADER-DG) method for dynamic rupture models (see [99, 133, 145, 204]).

A few studies used a simple extended fault model to investigate the effects of source properties on seismic motion. Day et al. (2008) [72] studied the effects of source geometry and magnitude on response spectral amplification within the Los Angeles basin. Mai and Beroza (2000) [194], and Prieto et al. (2004) [241] studied whether the surface seismic motion is directly proportional to the fault parameters –such as fault length, fault width, average slip, and the seismic moment– for a few earthquake scenarios. Mai and Beroza (2002) [195], and Guatteri et al. (2003) [114] used a random field to simulate slip distribution in order to propose a stochastic source model. Bouchon et al. (2010) [44] studied the characteristics of supershear earthquakes, where the rupture velocity along the fault surface exceeds the seismic shear wave velocity.

Geological field studies reveal that fault planes are non-planar and include strong irregularities. Thus, the perfectly planar assumption for faults, which is an acceptable assumption in seismology, may not be accurate. Cruz-Atienza and Virieux (2004) [71] used a staggered-grid finite difference method to simulate a two-dimensional model of an arbitrary non-planar fault in a heterogeneous medium. Käser and Gallovič (2008) [155] used a discontinuous Galerkin method to investigate the influence of various rupture models on synthetic velocity seismograms. Harris and Day (1999) [118] also used multiplanar faults in their simulations and reported the effects of geometric discontinuities on the generation of strong seismic

wave propagation.

1.4.2.3 Effective forces of seismic loads

The early studies on prescribing seismic excitations are mostly focused on effective generalized forces for soil-structure interaction analyses. For instance, Thau (1967) [283] and Luco et al. (1975) [187] proposed generalized forces in terms of the motion a rigid, massless, foundation would experience under a prescribed incoming wave in a linear viscoelastic medium. Similarly, Gutierrez and Chopra (1978) [115] expanded the results for structures on flexible foundations. In both studies, effective seismic forces are prescribed on the interface between the structure (including the foundation) and the surrounding soil

Herrera and Bielak (1977) [123] approached the dynamic soil-structure problem by proposing a novel framework. Having the solution to the seismic motion in an elastic half-space in the absence of structures, i.e., the free-field solution, they confirmed that the excitation can be transmitted through the computational domain via an auxiliary boundary layer that separates the homogeneous linear half-space from a smaller domain of interest that contains the structure. This technique allows for the simulation of the nonlinear behavior of structures and the surrounding soil. In an attempt to develop a numerical approach for wave motion simulation, Bielak and Christiano [33] adjusted the same idea by discretizing the strong form in the Galerkin sense and suggested two equivalent techniques. The first technique is a direct method, where the response of the structure and of the soil medium are computed simultaneously, while the second technique treats the structure and the soil

separately. The main focus of these studies was the nonlinear behavior of structures due to seismic excitation Cremonini et al. (1988) [70] implemented the method for a linear, two-dimensional domain.

In 1994, Loukakis and Bielak [186] shifted the focus of previous studies from the soil-structure interaction problem to simulate two-dimensional sedimentary valleys in a half-space due to a SV incident wave, regardless of the presence of structures. Applying the original idea from [123], their formulation only relies on the free-field motion, as opposed to Bielak and Christiano (1984) [33], where the free-field tractions are needed as well. Bielak et al. (1995) [36] tackled the problem of SH-wave propagation in elastic heterogeneous valleys of arbitrary shapes. They enriched the core idea of [123] with a second-order absorbing boundary condition derived in Barry et al. (1988) [26].

Later, Bielak et al. [37] compiled the previous findings in a two-step method called *Domain Reduction Method* (DRM) to replace the seismic source by effective forces. The details of this method are discussed in Section 2.2.3. Yoshimura et al. (2003) [296] applied the DRM to several test cases and verified the DRM formulation by comparing the results with a Green's function method. They also showed the application of the DRM in large-scale simulations containing fault and geological irregularities. Zahradník and Moczo (1996) [297], and Moczo et el. (1996) [209] used a similar two-step time-domain method for computing seismic motion in a heterogeneous viscoelastic domain. In the first step, they used a discrete-wavenumber method to compute the total displacement field in a two-dimensional half-space without geological features, and recorded the wave-field along two lines close to the features. In

the second step, the seismic loads were applied to a smaller computational domain, containing the geological features, obtained by truncating the physical domain with absorbing boundaries prescribed on the truncation surfaces. Kontoe et al. (2008) [173] also extended the DRM method for coupled consolidation problems.

1.4.3 Domain truncation

The numerical simulation of wave motion in an unbounded domain requires negotiation of the infinite or semi-infinite extent of the domain: when domain discretization methods are used, the physical domain must be truncated and appropriate conditions must be introduced at the truncation surface. Ideally, the truncation surface must allow for the safe passage of outgoing waves with no reflections from the truncation surface. Placement of absorbing boundaries has extensive applications in problems dealing with wave propagation, among them are site characterization using full-waveform inversion [87, 88, 142], enhanced oil recovery techniques using energy focusing [148, 149, 150, 151], and earthquake engineering [237, 238, 239, 240] . The literature on appropriate truncation conditions for elastodynamics is rich and the topic remains open.

Absorbing boundary conditions can be classified into local and non-local. Non-local boundary conditions are considered to be exact, albeit, computationally expensive. The spatial non-locality comes from the fact that the motion at any point along the truncation surface is coupled with the motion at every other point along the same surface. The temporal non-locality manifests itself in convolution integrals. Domain truncation strategies based on the boundary element methods

(BEM) and Dirichlet-to-Neumann (DtN) maps [138] are among non-local treatments. Local boundary conditions, by contrast, relax the spatial and temporal non-localities, are economical, but usually less accurate than non-local treatments. One of the earliest local techniques is the one proposed by Lysmer and Kuhlemeyer (1969) [191], where dashpots were used on the truncation surface for absorbing outgoing waves.

Two categories of local boundary conditions for time-domain simulations are Non-Reflecting Boundary Conditions (NRBC) and Perfectly-Matched-Layers (PML). Early developments in local methods include the works by Engquist and Majda (1977) [63] and Lindman (1975) [184] for the scalar wave equation, which were later extended to elastodynamics by Clayton and Engquist (1977) [79], and Randall (1989) [244]. Kallivokas et al. (1991) [141] and Collino (1993) [67] were among the first to offer practical high-order NRBC for the scalar wave equation; extensions to elastodynamics appeared later by Joly and Tsogka (2008,2010) [138, 139]. Similar conditions can also be found in Higdon [126] for the scalar wave equation and [125, 127] for elastic waves. Other works include Givoli and Neta (2003) [107], Hagstrom and Warburton (2004) [116], Rabinovich et al. (2011) [243], and Baffet et al. (2012) [17].

The Perfectly-Matched-Layers method is a buffer zone that surrounds the computational domain along the truncation surfaces within which the outgoing waves are forced to decay. In this sense, the PML is an absorbing boundary. The PMLs appear to be among the best choices for domain truncation owing especially to their ability to handle heterogeneity. The PML was developed first by Bérenger in 1994 for the simulation of electromagnetic waves in infinite domains [32]. Bérenger's idea of the PML was later interpreted as a mapping of the physical coordinates onto the

complex space, referred to as complex coordinate stretching [60, 62, 282]. This reinterpretation allowed a systematic development and adoption of the PML in other wave-driven problems, including elastodynamics [61, 68], the linearized Euler equations [131], the Helmholtz equation [117], and poroelastodynamic [299]. A unified framework for obtaining the stretched weak form from a standard weak form is discussed in [201] for several differential operators.

Two major classes of PML formulations, depending on how field variables are treated, are split-field and unsplit-field. In the split-field formulation, each field variable is split into components perpendicular and parallel to the interface boundary, resulting in a modification in the underlying differential equations and in an increase in the number of unknowns. In the unsplit-field formulation, however, the general structure of the underlying differential equations is preserved, at the expense of increased complexity.

Gedney (1996) [104] proposed an unsplit formulation for electromagnetic waves. Abarbanel and Gottlieb (1997) [1] showed that Bérenger's split-form is only weakly well-posed, and therefore is prone to instability. Bécache (2003) [29] investigated the stability of elastodynamics split-field PML formulations for anisotropic and orthotropic materials. Appelö and Kreiss [10] also proposed a new formulation that does not directly rely on complex coordinate stretching and discussed the stability of the PML for anisotropic materials. In [250], Sagiyama et al. attributed the instabilities in isotropic cases to advection-like terms in the PML formulation, and suggested using numerical diffusion to circumvent them. Liu [185] developed a PML formulation for cylindrical and spherical coordinate systems. A few studies suggested

mixed velocity-stress PML models; among them are: Chew and Liu (1996) [61], were the first to extend the PML from electromagnetics to elastodynamics; Hastings et al. (1996) [120] proposed a velocity-stress treatment using displacement potentials; Collino and Tsogka (2001) [68] studied a velocity-stress formulation with applications to anisotropic heterogeneous media; Bécache al. [30] proposed a velocity-stress formulation using mixed finite elements and the fictitious domain method to account for topography; Festa and Vilotte [92] suggested a mixed velocity-stress formulation with a staggered time-stepping scheme. Komatitsch and Tromp [169] proposed a displacement-only formulation in which stress components are eliminated at the expense of splitting the displacement field into four components. Cohen and Fauqueux [65] reported a mixed spectral element formulation based on a novel decomposition of the elastodynamics equations into a first-order system. Festa and Nielsen [91] studied the performance of PML for surface waves, and later, in [90], Festa et al. suggested using complex-frequency-shifted (CFS) stretching functions to avoid instabilities that may occur in such problems.

There is a remarkable literature devoted to unsplit-field treatments in elastodynamics. Duru and Kreiss [78] proposed a well-posed discretely-stable unsplit formulation. Basu and Chopra (2004) [28] presented a displacement-only procedure that relies on stress-histories and later, Basu (2009) [27] extended this work to three-dimensional problems, using mass-lumping and explicit time-stepping. Martin et al. [196, 197] developed a computationally efficient procedure that couples a velocity-stress Convolutional PML (CPML) with a displacement-only formulation in the interior domain for two-dimensional problems. Kucukcoban and Kallivokas

[178] developed a displacement-stress formulation for axisymmetric problems, and also for problems in a cartesian coordinate system [179], using a mixed-field formulation. In [180], Kucukcoban and Kallivokas discussed a symmetric displacement-stress formulation using a mixed-field formulation for the PML, coupled with standard displacement-only formulation for the interior domain. See also [76, 164, 289], where the authors explored alternative PML formulations.

Various coordinate stretching functions are considered in PML formulations. The classical stretching function, allegedly, allows spurious growth when waves impinge on the PML at grazing incidence, which has been attributed to the zero-frequency singularity of the stretching function. Drossaert and Giannopoulos (2007) [76], utilized a Complex-Frequency-Shifted (CFS) stretching function, to remove this singularity. Although the CFS-PML provides better stability, it loses its absorptive competence at low frequencies [69]. The CFS-PML entails special convolutional operators, which can be efficiently implemented, leading to the convolution PML (CPML) [247]. Meza-Fajardo and Papageorgiou [206, 208] proposed a multi-axial stretching approach and demonstrated its successful performance for waves traveling through the PML at grazing incidence as well as for problems involving anisotropy. It was reported that their formulation is not perfectly matched [74, 75]; however, later on, Meza-Fajardo and Papageorgiou showed that the multi-axial perfectly-matched-layer (M-PML) is indeed perfectly matched in Bérenger's sense, and it provides domain truncations that are at least as accurate as the classical PML when stable [207]. In a more recent study, Ping et al. [232] have shown that the M-PML may perform less accurately than the classical PML when stable. Similar observations were also

reported in [89].

1.4.4 Large-scale seismic motion simulations

Here, we review studies aimed at simulating seismic wave motion in real geologic formations, thus requiring large-scale computation. Note that most published results are focused on California basins because past earthquake records are extensively available in this highly populated seismic zone, while the geological structure is also well characterized. For example, Magistrale et al. (1998,2000) [193, 192] presented a detailed three-dimensional seismic velocity model of the major southern California basins, including Los Angeles basin, Ventura basin, San Gabriel Valley, San Fernando Valley, Chino basin, San Bernardino Valley, and the Salton Trough, developed by the Southern California Earthquake Center and designed to serve as a reference model for multidisciplinary research activities in the area.

We remark that the maximum allowable wave frequency in the domain is limited by the available computational resources. As the frequency increases (i.e., shorter wavelength) to capture the wave accurately, we need a finer discretization, typically resulting in a larger system. Note also that in heterogeneous domains, the case of variable element size in layers with different wave velocities, allow a reduction in the computational cost. The majority of the studies are so far restricted to up to 1 Hz, and in some rare cases up to 4 Hz.

Frankel and Vidale (1992) [97] used finite differences to regenerate the effects of the 1989 Loma Prieta aftershock in Santa Clara valley, California in a model of size $30 \times 22 \times 6\,\mathrm{km}^3$. They assumed a flat surface model with 100m grid size leading

to a total of 3.96 million nodes with 6 points points per shear wave wavelength that was supposed to be adequate for frequencies up to 1 Hz. Frankel (1993) [95] simulated two hypothetical seismic events using an extended rupture model in the San Bernardino valley to conclude that the rupture directivity and asperity locations play a significant role. Wald and Graves (1998) [288] used a finite difference technique to conduct a three-dimensional simulation in the Los Angeles basin, considering no attenuation mechanism nor topography, which using the strong motion data recorded from the 1992 Landers earthquake. They reported a significant difference between the numerical simulations and the recorded motion. Hisada et al. (1998) [130] studied the motion amplification in the Osaka basin under the 1995 Kobe earthquake using a wavelength adaptive model with unstructured hexahedral elements.

Chaljub et al. (2003) [58] presented a parallel spectral element method for non-conforming grids that accounts for fluid-solid interaction and performed a few benchmark tests to illustrate the accuracy of the method. In a notable study in 2010, Chaljub et al. [59] compared the results of numerical simulations of the Grenoble valley in France conducted by four teams using various techniques: a fourth-order velocity-stress finite difference scheme on an arbitrary discontinuous grid, two mildly different spectral element methods, and a velocity-stress arbitrary high-order derivative discontinuous Galerkin method. The seismic source was a finite kinematic fault in a domain, where surface topography and attenuation in terms of quality factor were considered.

Olsen et al. (1995) [217] used a staggered-grid finite difference method to analyze a synthetic earthquake of magnitude 7.75 up to a maximum frequency of

0.4 Hz in a large portion of Los Angeles basin ($230.0 \times 140.4 \times 46.0\,\mathrm{km}^3$) including the San Andreas fault, approximated as a plane rupture. Surface topography is not included in the simulation and Clayton and Engquist's absorbing condition (1977) [63] was used on the truncation boundaries. Olsen et al. (1995) [220] investigated the seismic amplification pattern in a large portion of the Salt Lake Valley, Utah ($48 \times 25 \times 1.3\,\mathrm{km}^3$) for a broader range of frequencies from 0.2 to 1.2 Hz under vertical and horizontal plane P incident wave. Olsen et al. (1996) [216] applied three various seismic events to a larger domain of size $155 \times 134 \times 34\,\mathrm{km}^3$ in the Los Angeles basin. Olsen et al. [218, 219], in a project called *TeraShake* studied the Los Angeles basin using structured grids.

One prominent large-scale finite element seismic simulation is the work of Bao et al. (1998) [22], where the seismic motion in the San Fernando valley of dimension $54 \times 33 \times 15\,\mathrm{km}^3$ had been simulated. The discretization allows for a maximum frequency of 1.6 Hz using linear tetrahedral elements. Dashpots were used as the absorbing boundary condition on the truncation surfaces. Geological effects have been excluded from the simulation and Rayleigh viscous damping was considered for material damping. They modeled an aftershock of the 1994 Northridge earthquake through the Domain Reduction Method [33, 70], as explained in Sections 1.4.2.3 and 2.2.3.1, instead of directly including the source within the computational domain. Similar simulations were conducted in Kim et al. (2003) [159] and Bielak et al. (2005) [34] using hexahedral unstructured elements for a maximum frequency of 1 Hz. They substituted the absorbing boundary condition by Stacey's formulation [275] and focused more on the efficiency of their parallel algorithm. In 2014, Restrepo

and Bielak [246] devised a technique to incorporate arbitrary topography in a domain discretized using a structured mesh.

A team of scientists in 2008 compared the results of five independent three-dimensional codes, four of which are finite difference codes and one is a finite element code, based on Bao et al. (1998) [22], to study the effects of sixty earthquake scenarios in the southern California region [72]. The finite difference codes are identical in terms of the theory and are designed for uniform, structured, cubic grids, with staggered velocity, fourth-order accurate in space and second-order in time. However, the codes are different in terms of absorbing boundary conditions and attenuations. Due to the uniform mesh discretization, the free-surface was assumed to be flat and topography effects were neglected. In conclusion, they parameterized the effects of source using spectral acceleration.

Similarly, Bielak et al. (2010) [35] examined the results of simulating the ShakeOut earthquake scenario, a hypothetical seismic event along the San Andreas fault developed by the U.S. Geological Survey (see Jones et al. (2008) [140]), using three separate modeling techniques, two finite difference codes and one finite element code. In the finite element models, the Lysmer and Kuhlemeyer absorbing condition and Rayleigh damping were used in an unstructured grid. In the finite difference models, the structured grids were used with Clayton and Engquist (1977) [63] or perfectly-matched-layers (Meza-Fajardo and Papageorgiou (2008) [206]) as the absorbing boundaries, and a Q factor attenuation model. The domain size, owing to the computer limitations is smaller in the finite difference models. They concluded that all three models generate, more or less, similar results with small discrepancies.

Taborda and Bielak (2013) [279] used a finite elements model to simulate the 2008 Chino Hills earthquake in California for frequencies up to 4 Hz. They reported an acceptable agreement between the synthetics obtained from the numerical simulations for low frequencies with the recorded seismograms.

Komatitsch and Tromp (2002,2005) [167, 168, 170] demonstrated a spectral element methodology using a conforming domain discretization with hexahedral elements to simulate the entire Earth. They considered shear quality factor attenuation, surface topography, and fluid-soil coupling. Similar experiments were conducted by Carrington et al. (2008) [53]. Komatitsch et al. (2004) [163] implemented the spectral element method to simulate two earthquake events, Hollywood earthquake 2001 and Yorba Linda earthquake 2002, in an improved sedimentary model of Los Angeles basin that covers a larger part of the area with higher accuracy. They considered various wave velocity, density, topography and bathymetry, and attenuation, and reported a close agreement between data and synthetic seismograms. Lee et al. (2009) [182] studied the effects of surface topography on ground motion in Yangmingshan National Park in northern Taiwan for frequencies up to 10 Hz. They reported that the mountain peaks increase and the valleys decrease the PGA in comparison with the flat surface.

Komatitsch et al. (2010) [162] developed a high-order finite-element parallel code using Graphics Processing Units (GPUs), instead of CPUs, aiming at improving the scalability of the parallel seismic simulations. They reported a remarkable speedup, although the speedup is valid only for single-precision algorithms. Mazzieri et al. (2013) [202] presented a high performance code called SPEED (SPectral

Element in Elastodynamics with Discontinuous Galerkin) for three-dimensional simulation of wave propagation in viscoelastic heterogeneous domains. They modeled the 2011 earthquake in the Central Business District of Christchurch, New Zealand.

1.5 Methodology overview

The primary aim of this research is to assess the effect topography has on the seismic motion via parametric studies. To this end, we deploy best-practice methods for simulating seismic motion in arbitrarily heterogeneous two- and three-dimensional formations, by integrating existing methods, improving upon others, or by extending past developments. Specifically:

- On elastic wave simulation in heterogeneous domains:

  We describe an explicit forward wave solver based on a hybrid formulation that couples a single-field formulation for the computational domain with an unsplit mixed-field formulation for Perfectly-Matched-Layers (PMLs or M-PMLs), used to limit the computational domain.

- On seismic input:

  We adopt two strategies: (i) the direct simulation of a seismic source within the computational domain in the form of a double-couple and (ii) indirect accounting of the seismic source through the Domain Reduction Method (DRM). Specifically, we describe the coupling of the DRM with the PMLs to allow for seismic input when the source is not within the computational domain.

- On the algorithmic performance:

To improve on the algorithmic performance, and allow for large-scale simulations, adopt spectral elements, reduce the wave propagation problem to first-order, we adopt an explicit solver, and deploy an adaptive time integrator to optimize the time-step.

1.6 Dissertation outline

This dissertation is organized as follows:

In Chapter 2, we discuss the mathematical formulation pertaining to seismic wave motion simulation in two- and three-dimensional arbitrarily heterogeneous domains. In particular, Section 2.1 describes the development of the Perfectly-Matched-Layers (PML). Next, in Section 2.2, we discuss the seismic source simulation techniques. Finally, in Section 2.3 we discuss different time-integration algorithms used in this study.

In Chapter 3 we report the results of various verification examples. In particular, we compare our numerical results against analytical solutions and results from published numerical simulations.

Chapter 4 we present the results of an extensive frequency-domain parametric study on the effects of two-dimensional idealized geometries (hills and valleys) on the amplification/de-amplification of seismic waves.

In Chapter 5 we report on topographic amplifications via time-domain simulations. In particular, we discuss the effects dimensionality has on the amplification of seismic waves, by comparing between one-, two-, and three-dimensional models.

In Chapter 6 we summarize the remarks and findings, and suggest future directions to this work.

Details of the theoretical development and the PML matrices are included in Appendix A. In Appendix B, we provide the details of the time-integrator and of the corresponding algorithms. Next, Appendix C briefly explains various components of the developed numerical toolchain. Lastly, in Appendix D we comment on the efficiency of the time adaptive algorithm.

Chapter 2

Mathematical and numerical modeling[1]

In this chapter, we present the mathematical framework of a forward wave solver approach based on a hybrid formulation that includes Perfectly-Matched-Layers (PMLs) for limiting the computational domain; unstructured spectral elements for spatial discretization; seismic source modeling using a double-couple technique; seismic source modeling using the Domain-Reduction-Method (DRM) that permits placement of seismic sources within the computational domain; the coupling of the DRM with PMLs; the time-integration schemes to march in time; and parallelizing tools that allow for a scalable and cost-effective numerical simulation of wave propagation.

2.1 Wave modeling in unbounded domains

Wave motion simulation in unbounded, heterogeneous domains requires negotiation of the semi-infinite extent of the physical domain, which entails the introduction of artificial (non-physical) boundaries surrounding the finite computational domain on the truncation surface, as illustrated in Figure 2.1. These boundaries need special

[1]Portion of this chapter has been published in: A. Fathi, B. Poursartip, L.F. Kallivokas, "Time-domain hybrid formulations for wave simulations in three-dimensional PML-truncated heterogeneous media," *International Journal for Numerical Methods in Engineering*, 101, 165-198, 2015. The dissertation author had significant contribution to the article.

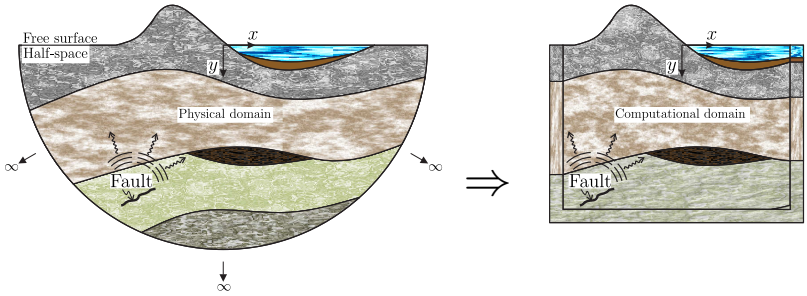

Figure 2.1: Negotiating the extent of physical domain

treatment in order for the finite domain of interest to mimic the physical behavior of the non-truncated domain, while minimizing spurious reflections that could pollute the solution within the computational domain. Among several methods proposed to treat the truncation boundaries, Perfectly-Matched-Layers (PMLs) appear to be one of the best choices owing, especially, to their ability to handle heterogeneity for all angles of incidence and frequencies. In this section, we review the main elements for an unsplit-field, mixed displacement-stress, PML formulation, for two- and three-dimensional elastodynamics.

2.1.1 Perfectly-Matched-Layer (PML) absorbing boundary condition

The key idea of the PML is to attach a high-attenuation zone to the truncation surface of the regular domain, as shown in Figure 2.2, within which outgoing waves are forced to decay. The material properties of the buffer zone should be defined such that (i) continuity at the interface of the regular domain and the buffer zone be maintained in order to ensure that the interface is invisible to outgoing waves; and (ii) the outgoing waves attenuate quickly within the PML zone before they reflect

back to the regular domain due to the reflection at the fixed boundaries on the terminating surface of the PML buffer zone.

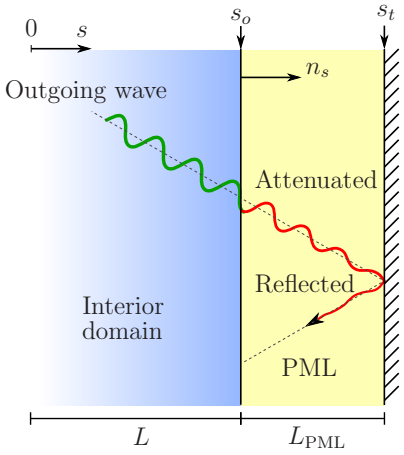

Figure 2.2: A PML truncation boundary in the direction of coordinate s

The PML zone, mathematically, can be obtained by mapping the spatial coordinates onto the complex space, using stretching functions. To this end, let s denote the physical coordinate variable along the direction normal to the interface of the interior domain as shown in Figure 2.2, where the interior domain extends between 0 and s_0, i.e., $0 < s_0$. The PML extends between s_0 and s_t, where $s_t - s_0 = L_{\text{PML}}$. Next, the coordinate s is mapped onto $\tilde{s}$ within the PML region according to:

$$s \mapsto \tilde{s} = s_o + \int_{s_o}^{s} \lambda_s(s' - s_o, \omega) ds', \tag{2.1}$$

where ω denotes circular frequency, and λ_s represents the stretching function. Among various forms of stretching functions, here we adopt the most-widely used form of a stretching function due to its straightforward implementation and improved perfor-

mance with low-frequency propagating waves:

$$\lambda_s(s,\omega) = \alpha_s(s) + \frac{1}{i\omega}\beta_s(s), \tag{2.2}$$

where α_s is the scaling function that stretches the coordinate variable s, effectively resulting in an artificial geometric damping; while β_s is the attenuation function. For the interface to be invisible to the waves entering the PML (perfect matching), $\alpha_s|_{s=s_0} = 1$, and $\beta_s|_{s=s_0} = 0$. Moreover, α_s and β_s must be positive, non-decreasing functions of s.

Let us examine the one-dimensional wave motion in the stretched coordinate system. Introducing the stretched coordinate in the propagating waves, in the form $\exp(-iks)$, and in the evanescent waves, in the form of $\exp(-ks)$, we obtain:

$$\begin{aligned}
&\textit{propagating}: \quad \exp(-ik\tilde{s}) = \exp\left(-ik\int_0^s \alpha_s(s')ds'\right)\exp\left(-\frac{k}{\omega}\int_0^s \beta_s(s')ds'\right).\\
&\textit{evanescent}: \quad \exp(-k\tilde{s}) = \exp\left(-k\int_0^s \alpha_s(s')ds'\right)\exp\left(i\frac{k}{\omega}\int_0^s \beta_s(s')ds'\right).
\end{aligned}$$

Provided that $\alpha_s(s) > 1$ and $\beta_s(s) > 0$, the imaginary part of the stretching function, β_s, enforces the amplitude decay of the propagating waves whereas for the evanescent wave, the real part, α_s, is responsible for the exponential decay.

Among several recommended stretching functions, we consider a polynomial function, which allows for a smoothly-varying profile in the PML zone, as in:

$$\alpha_s(s) = 1 + \alpha_o\left[\frac{(s-s_o)n_s}{L_{\mathrm{PML}}}\right]^m, \qquad s_o \le s \le s_t, \tag{2.3a}$$

$$\beta_s(s) = \beta_o\left[\frac{(s-s_o)n_s}{L_{\mathrm{PML}}}\right]^m, \qquad s_o \le s \le s_t, \tag{2.3b}$$

where α_0 and β_0 are user-tunable parameters that control the amplitude decay, and m denotes the polynomial degree. Note that $\alpha_0 = 1$ and $\beta_s = 0$ on the PML interface ($s = s_0$).

The wave attenuation varies smoothly within the PML zone, with m controlling the shape of the attenuation profile so that a sharper transition could be imposed either closer to the PML-regular domain interface, or closer to the fixed PML boundary. The wavelength of the outgoing waves decreases as the waves travel in the PML zone, which, then, requires a finer discretization closer to the fixed PML boundary. In this work, we favor a uniform mesh within the PML zone, and adopt quadratic profiles ($m = 2$).

Having establishing the stretched coordinate, we apply next the fundamental theorem of calculus to (2.1), to arrive at:

$$\frac{d\tilde{s}}{ds} = \frac{d}{ds}\int_{s_o}^{s} \lambda_s(s', \omega)\ ds' = \lambda_s(s, \omega). \tag{2.4}$$

The physical coordinate system, hence, is related to the stretched coordinate through:

$$\frac{d(\cdot)}{d\tilde{s}} = \frac{1}{\lambda_s(s, \omega)}\frac{d(\cdot)}{ds}. \tag{2.5}$$

The governing wave equation for a linear, elastic material, in the absence of body forces, can be written as the following system in the time-domain:

$$\mathbf{div}\,\mathcal{S}^T = \rho\ddot{\mathbf{u}}, \tag{2.6a}$$

$$\mathcal{S} = \mu\left[\nabla\mathbf{u} + (\nabla\mathbf{u})^T\right] + \lambda(\mathrm{div}\,\mathbf{u})\mathcal{I}, \tag{2.6b}$$

where (2.6a) represents conservation of linear momentum, and (2.6b) is the combined constitutive and kinematic equations; $\mathcal{S}$ denotes the Cauchy stress tensor, $\mathbf{u}$ is the

displacement vector, ρ denotes mass density, λ and μ are the two Lamé parameters, $\mathcal{I}$ is the second-order identity tensor, and a dot ($\dot{}$) denotes differentiation with respect to time of the subtended variable.

To apply the coordinate stretching, we first transform the elastic wave equations (2.5) in the frequency-domain via Fourier-transforms, to obtain:

$$\mathbf{div}\,\hat{\mathcal{S}}^T + \hat{\mathbf{b}} = (i\omega)^2\rho\hat{\mathbf{u}}, \tag{2.7a}$$

$$\hat{\mathcal{S}} = \mu\left[\nabla\hat{\mathbf{u}} + (\nabla\hat{\mathbf{u}})^T\right] + \lambda(\operatorname{div}\hat{\mathbf{u}})\mathcal{I}, \tag{2.7b}$$

where a caret ($\hat{}$) denotes the Fourier transform of the subtended variable, and spatial and frequency dependency of the variables are suppressed for brevity. In the following sections, we derive the corresponding two- and three-dimensional PML formulations.

2.1.2 The PML in 2D-truncated domains[2]

Let us complex-stretch the x and y physical coordinates in (2.7a) into $\tilde{x}$ and $\tilde{y}$, respectively:

$$\frac{\partial\hat{\mathcal{S}}_{xx}}{\partial\tilde{x}} + \frac{\partial\hat{\mathcal{S}}_{yx}}{\partial\tilde{y}} = (i\omega)^2\rho\hat{u}_x, \tag{2.8a}$$

$$\frac{\partial\hat{\mathcal{S}}_{xy}}{\partial\tilde{x}} + \frac{\partial\hat{\mathcal{S}}_{yy}}{\partial\tilde{y}} = (i\omega)^2\rho\hat{u}_y, \tag{2.8b}$$

where $\mathcal{S}_{ij}$ and u_i denote stress tensor components and displacement vector components, respectively. Applying the derivative rule (2.5) to (2.8), we can express (2.8)

[2]The development in this section was first presented in Kucukcoban and Kallivokas (2011) [179]

in the unstretched coordinate system as:

$$\frac{1}{\lambda_x}\frac{\partial \hat{\mathcal{S}}_{xx}}{\partial x} + \frac{1}{\lambda_y}\frac{\partial \hat{\mathcal{S}}_{yx}}{\partial y} = (i\omega)^2 \rho \hat{u}_x, \tag{2.9a}$$

$$\frac{1}{\lambda_x}\frac{\partial \hat{\mathcal{S}}_{xy}}{\partial x} + \frac{1}{\lambda_y}\frac{\partial \hat{\mathcal{S}}_{yy}}{\partial y} = (i\omega)^2 \rho \hat{u}_y. \tag{2.9b}$$

Multiplying (2.9) by $\lambda_x \lambda_y$ results in:

$$\mathbf{div}\left(\hat{\mathcal{S}}^T \Lambda\right) = (i\omega)^2 \rho \ \lambda_x \lambda_y \ \hat{\mathbf{u}}, \tag{2.10}$$

where the stretching tensor Λ is defined as:

$$\Lambda = \begin{bmatrix} \lambda_y & 0 \\ 0 & \lambda_x, \end{bmatrix} = \begin{bmatrix} \alpha_y & 0 \\ 0 & \alpha_x \end{bmatrix} + \frac{1}{i\omega}\begin{bmatrix} \beta_y & 0 \\ 0 & \beta_x \end{bmatrix} = \Lambda_e + \frac{1}{i\omega}\Lambda_p. \tag{2.11}$$

Note that Λ_e reduces to the identity tensor within the regular domain, while Λ_p vanishes identically. Substituting (2.2) and (2.11) in (2.10), results in:

$$\mathbf{div}\left(\hat{\mathcal{S}}^T \Lambda_e + \frac{1}{i\omega}\hat{\mathcal{S}}^T \Lambda_p\right) = \rho\left[(i\omega)^2 a\hat{\mathbf{u}} + i\omega b\hat{\mathbf{u}} + c\hat{\mathbf{u}}\right], \tag{2.12}$$

where

$$a = \alpha_x \ \alpha_y,$$

$$b = \alpha_x \ \beta_y + \alpha_y \ \beta_x,$$

$$c = \beta_x \ \beta_y.$$

Multiplying (2.12) by $i\omega$, we obtain:

$$\mathbf{div}\left(i\omega\hat{\mathcal{S}}^T \Lambda_e + \hat{\mathcal{S}}^T \Lambda_p\right) = \rho\left[(i\omega)^3 a\hat{\mathbf{u}} + (i\omega)^2 b\hat{\mathbf{u}} + i\omega c\hat{\mathbf{u}}\right], \tag{2.13}$$

Next, we stretch the coordinates in the combined constitutive and kinematic equations (2.7b); there results:

$$\hat{\mathcal{S}} \;=\; \mu\left\{(\nabla\hat{\mathbf{u}})\begin{bmatrix}\frac{1}{\lambda_x} & 0\\ 0 & \frac{1}{\lambda_y}\end{bmatrix} + \begin{bmatrix}\frac{1}{\lambda_x} & 0\\ 0 & \frac{1}{\lambda_y}\end{bmatrix}(\nabla\hat{\mathbf{u}})^T\right\} \;+\; \lambda\Big(\frac{1}{\lambda_x}\frac{\partial\hat{u}_x}{\partial x} \;+\; \frac{1}{\lambda_y}\frac{\partial\hat{u}_y}{\partial y}\Big)\mathcal{I}. \quad (2.14)$$

Multiplying (2.14) by $\lambda_x\lambda_y$, results in:

$$\lambda_x\lambda_y\hat{\mathcal{S}} = \mu\left[\nabla\hat{\mathbf{u}}\;\Lambda + \Lambda\,(\nabla\hat{\mathbf{u}})^T\right] + \lambda\,\mathrm{div}(\Lambda\hat{\mathbf{u}})\mathcal{I}. \quad (2.15)$$

Multiplying (2.15) by $(i\omega)^2$ and using (2.2) and (2.11), we obtain:

$$(i\omega)a\hat{\mathcal{S}} + b\hat{\mathcal{S}} + \frac{1}{i\omega}c\hat{\mathcal{S}} = (i\omega)\mu\left[(\nabla\hat{\mathbf{u}})\Lambda_e + \Lambda_e(\nabla\hat{\mathbf{u}})^T\right] + \mu\left[(\nabla\hat{\mathbf{u}})\Lambda_p + \Lambda_p(\nabla\hat{\mathbf{u}})^T\right]$$
$$+ (i\omega)\lambda\,\mathrm{div}(\Lambda_e\hat{\mathbf{u}})\mathcal{I} + \lambda\,\mathrm{div}(\Lambda_p\hat{\mathbf{u}})\mathcal{I}. \quad (2.16)$$

Equations (2.13) and (2.16) constitute the corresponding frequency-domain governing equations in the stretched coordinate system. Then, to obtain the corresponding time-domain equations, we apply the inverse Fourier transform, to obtain:

$$\mathbf{div}\left[\mathcal{S}^T\Lambda_e + \left(\int_0^t \mathcal{S}^T d\tau\right)\Lambda_p\right] = \rho\left(a\ddot{\mathbf{u}} + b\dot{\mathbf{u}} + c\mathbf{u}\right), \quad (2.17a)$$

$$a\dot{\mathcal{S}} + b\mathcal{S} + c\left(\int_0^t \mathcal{S}d\tau\right) = \mu\left[(\nabla\dot{\mathbf{u}})\Lambda_e + \Lambda_e(\nabla\dot{\mathbf{u}})^T + (\nabla\mathbf{u})\Lambda_p + \Lambda_p(\nabla\mathbf{u})^T\right]$$
$$+ \lambda\left[\mathrm{div}(\Lambda_e\dot{\mathbf{u}}) + \mathrm{div}(\Lambda_p\mathbf{u})\right]\mathcal{I}. \quad (2.17b)$$

Finally, we introduce the auxiliary variable $\mathbf{S}(\mathbf{x},t)$, which can also be interpreted as the stress history variable:

$$\mathbf{S}(\mathbf{x},t) = \int_0^t \mathcal{S}(\mathbf{x},\tau)d\tau. \quad (2.18a)$$

Clearly,

$$\dot{\mathbf{S}}(\mathbf{x},t) = \mathcal{S}(\mathbf{x},t), \qquad \ddot{\mathbf{S}}(\mathbf{x},t) = \dot{\mathcal{S}}(\mathbf{x},t). \tag{2.18b}$$

Substituting (2.18) in (2.17), we obtain:

$$\mathbf{div}\left(\dot{\mathbf{S}}^T\Lambda_e + \mathbf{S}^T\Lambda_p\right) = \rho\left(a\ddot{\mathbf{u}} + b\dot{\mathbf{u}} + c\mathbf{u}\right), \tag{2.19a}$$

$$\begin{aligned} &a\ddot{\mathbf{S}} + b\dot{\mathbf{S}} + c\mathbf{S} = \\ &\mu\left[(\nabla\dot{\mathbf{u}})\Lambda_e + \Lambda_e(\nabla\dot{\mathbf{u}})^T + (\nabla\mathbf{u})\Lambda_p + \Lambda_p(\nabla\mathbf{u})^T\right] + \\ &\lambda\left[\mathrm{div}(\Lambda_e\dot{\mathbf{u}}) + \mathrm{div}(\Lambda_p\mathbf{u})\right]\mathcal{I}. \end{aligned} \tag{2.19b}$$

Equations (2.19) are the corresponding time-domain PML balance of linear momentum, and the combined constitutive and kinematic equations, respectively. The next step would be the spatial discretization using a Galerkin method to arrive at a second-order, continuous-in-time, system of ordinary differential equations.

It is possible to use (2.19) for the interior domain and the PML zone, which, in turn, amounts to considering stress and displacement components as unknowns in both the interior domain and the PML buffer zone. In order to reduce the computational cost, instead, we resort to a hybrid approach, originally developed in [180], where the interior domain is treated with a standard displacement-only formulation, coupled with the PML equations in the buffer zone.

Accordingly, find $\mathbf{u}(\mathbf{x},t)$ in $\Omega^{\mathrm{RD}} \cup \Omega^{\mathrm{PML}}$, and $\mathbf{S}(\mathbf{x},t)$ in Ω^{PML} (see Figure 2.3 for domain and boundary designations), where $\mathbf{u}$ and $\mathbf{S}$ reside in appropriate function

spaces and:

$$\mathbf{div}\left\{\mu\left[\nabla\mathbf{u}+(\nabla\mathbf{u})^T\right]+\lambda(\operatorname{div}\mathbf{u})\mathcal{I}\right\}=\rho\ddot{\mathbf{u}} \qquad \text{in } \Omega^{\mathrm{RD}}\times\mathsf{J}, \tag{2.20a}$$

$$\mathbf{div}\left(\dot{\mathbf{S}}^T\Lambda_e+\mathbf{S}^T\Lambda_p\right)=\rho\left(a\ddot{\mathbf{u}}+b\dot{\mathbf{u}}+c\mathbf{u}\right) \qquad \text{in } \Omega^{\mathrm{PML}}\times\mathsf{J}, \tag{2.20b}$$

$$\begin{aligned} a\ddot{\mathbf{S}}+b\dot{\mathbf{S}}+c\mathbf{S}&=\mu\left[(\nabla\dot{\mathbf{u}})\Lambda_e+\Lambda_e(\nabla\dot{\mathbf{u}})^T+(\nabla\mathbf{u})\Lambda_p+\Lambda_p(\nabla\mathbf{u})^T\right]\\ &\quad+\lambda\left[\operatorname{div}(\Lambda_e\dot{\mathbf{u}})+\operatorname{div}(\Lambda_p\mathbf{u})\right]\mathcal{I} \qquad \text{in } \Omega^{\mathrm{PML}}\times\mathsf{J}. \end{aligned} \tag{2.20c}$$

The system is initially at rest, and subject to the following boundary and interface conditions:

$$\left\{\mu\left[\nabla\mathbf{u}+(\nabla\mathbf{u})^T\right]+\lambda(\operatorname{div}\mathbf{u})\mathcal{I}\right\}\mathbf{n}^+=\boldsymbol{g}_n \qquad \text{on } \Gamma_N^{\mathrm{RD}}\times\mathsf{J}, \tag{2.21a}$$

$$(\dot{\mathbf{S}}^T\Lambda_e+\mathbf{S}^T\Lambda_p)\mathbf{n}^-=\mathbf{0} \qquad \text{on } \Gamma_N^{\mathrm{PML}}\times\mathsf{J}, \tag{2.21b}$$

$$\mathbf{u}=\mathbf{0} \qquad \text{on } \Gamma_D^{\mathrm{PML}}\times\mathsf{J}, \tag{2.21c}$$

$$\mathbf{u}^+=\mathbf{u}^- \qquad \text{on } \Gamma^{\mathrm{I}}\times\mathsf{J}, \tag{2.21d}$$

$$\left\{\mu\left[\nabla\mathbf{u}+(\nabla\mathbf{u})^T\right]+\lambda(\operatorname{div}\mathbf{u})\mathcal{I}\right\}\mathbf{n}^++(\dot{\mathbf{S}}^T\Lambda_e+\mathbf{S}^T\Lambda_p)\mathbf{n}^-=0 \quad \text{on } \Gamma^{\mathrm{I}}\times\mathsf{J}, \tag{2.21e}$$

where, again, Ω^{RD} denotes the interior (regular) domain, Ω^{PML} represents the region occupied by the PML buffer zone, Γ^{I} is the interface boundary between the interior and PML domains, Γ_N^{RD} and Γ_N^{PML} denote the free (top surface) boundary of the interior domain and PML, respectively, and $\mathsf{J}=(0,T]$ is the time interval of interest.

Equation (2.21e) enforces the balance of tractions at the interface between the interior domain and the PML. Moreover, (2.21d) implies the continuity of displacements at the interface; (2.21a) specifies tractions ($\boldsymbol{g}_n$) on the top surface of

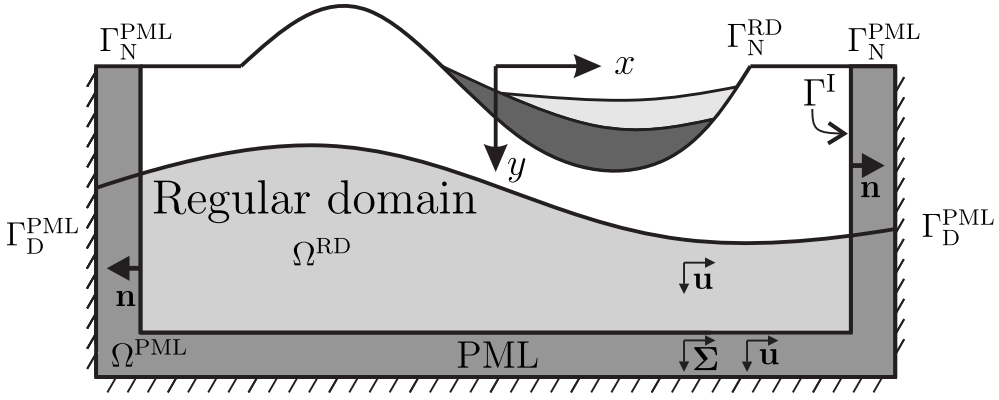

Figure 2.3: PML-truncated semi-infinite domain

the interior domain, and (2.21b) implies traction-free boundary condition on the top PML surface. We consider fixed boundaries for the PML on the sides and at the bottom, as indicated by (2.21c).

Next, we seek a weak form, corresponding to the strong form of (2.20) and (2.21), in the Galerkin sense. Specifically, we take the inner (vector) products of (2.20a) and (2.20b) with (vector) test function $\mathbf{w}(\mathbf{x})$, and integrate by parts over their corresponding domains. Incorporating (2.21d)-(2.21e) eliminates the interface boundary terms and results in (2.22a). Next, we take the inner product of (2.20c) with (tensor) test function $\mathbf{T}(\mathbf{x})$; there results (2.22b). Accordingly, find $\mathbf{u} \in \mathbf{H}^1(\Omega)\times$

J, and $\mathbf{S} \in \mathcal{L}^2(\Omega) \times \mathsf{J}$, such that:

$$\int_{\Omega^{\mathrm{RD}}} \nabla \mathbf{w} : \left\{ \mu \left[\nabla \mathbf{u} + (\nabla \mathbf{u})^T \right] + \lambda (\operatorname{div} \mathbf{u}) \mathcal{I} \right\} \, \mathrm{d}\Omega + \int_{\Omega^{\mathrm{PML}}} (\dot{\mathbf{S}}^T \Lambda_e + \mathbf{S}^T \Lambda_p) \mathrm{d}\Omega$$
$$+ \int_{\Omega^{\mathrm{RD}}} \mathbf{w} \cdot \rho \ddot{\mathbf{u}} \, \mathrm{d}\Omega + \int_{\Omega^{\mathrm{PML}}} \mathbf{w} \cdot \rho \left(a \ddot{\mathbf{u}} + b \dot{\mathbf{u}} + c \mathbf{u} \right) \mathrm{d}\Omega = \int_{\Gamma_N^{\mathrm{RD}}} \mathbf{w} \cdot \boldsymbol{g}_n \, \mathrm{d}\Gamma + \int_{\Omega^{\mathrm{RD}}} \mathbf{w} \cdot \mathbf{b} \, \mathrm{d}\Omega, \tag{2.22a}$$

$$\int_{\Omega^{\mathrm{PML}}} \mathbf{T} : \left(a \ddot{\mathbf{S}} + b \dot{\mathbf{S}} + c \mathbf{S} \right) \mathrm{d}\Omega = \int_{\Omega^{\mathrm{PML}}} \mathbf{T} : \mu \left[(\nabla \dot{\mathbf{u}}) \Lambda_e + \Lambda_e (\nabla \dot{\mathbf{u}})^T + (\nabla \mathbf{u}) \Lambda_p + \Lambda_p (\nabla \mathbf{u})^T \right]$$
$$+ \mathbf{T} : \lambda \left[\operatorname{div}(\Lambda_e \dot{\mathbf{u}}) + \operatorname{div}(\Lambda_p \mathbf{u}) \right] \mathcal{I} \mathrm{d}\Omega, \tag{2.22b}$$

for every $\mathbf{w} \in \mathbf{H}^1(\Omega)$ and $\mathbf{T} \in \mathcal{L}^2(\Omega)$, where $\boldsymbol{g}_n \in \mathbf{L}^2(\Omega) \times \mathsf{J}$, and $\mathbf{b} \in \mathbf{L}^2(\Omega) \times \mathsf{J}$. Function spaces for scalar- (v), vector- ($\mathbf{v}$), and tensor-valued ($\mathcal{A}$) functions are defined as:

$$L^2(\Omega) = \left\{ v : \int_\Omega |v|^2 d\mathbf{x} < \infty \right\}, \tag{2.23a}$$
$$\mathbf{L}^2(\Omega) = \left\{ \mathbf{v} : \mathbf{v} \in (L^2(\Omega))^2 \right\}, \tag{2.23b}$$
$$\mathcal{L}^2(\Omega) = \left\{ \mathcal{A} : \mathcal{A} \in (L^2(\Omega))^{2\times 2} \right\}, \tag{2.23c}$$
$$H^1(\Omega) = \left\{ v : \int_\Omega \left(|v|^2 + |\nabla v|^2 \right) d\mathbf{x} < \infty, \; v|_{\Gamma_D^{\mathrm{PML}}} = 0 \right\}, \tag{2.23d}$$
$$\mathbf{H}^1(\Omega) = \left\{ \mathbf{v} : \mathbf{v} \in (H^1(\Omega))^2 \right\}. \tag{2.23e}$$

In order to resolve (2.22) numerically, we use standard finite-dimensional subspaces. Specifically, we introduce finite-dimensional subspaces $\boldsymbol{\Xi}_h \subset \mathbf{H}^1(\Omega)$ and $\boldsymbol{\Upsilon}_h \subset \mathcal{L}^2(\Omega)$, with basis functions $\boldsymbol{\Phi}$ and $\boldsymbol{\Psi}$, respectively. We then approximate $\mathbf{u}(\mathbf{x}, t)$ with $\mathbf{u}_h(\mathbf{x}, t) \in \boldsymbol{\Xi}_h \times \mathsf{J}$, and $\mathbf{S}(\mathbf{x}, t)$ with $\mathbf{S}_h(\mathbf{x}, t) \in \boldsymbol{\Upsilon}_h \times \mathsf{J}$, as detailed below:

$$\mathbf{u}_h(\mathbf{x},t) = \begin{bmatrix} \mathbf{\Phi}^T(\mathbf{x})\mathbf{u}_x(t) \\ \mathbf{\Phi}^T(\mathbf{x})\mathbf{u}_y(t) \end{bmatrix}, \tag{2.24a}$$

$$\mathbf{S}_h(\mathbf{x},t) = \begin{bmatrix} \mathbf{\Psi}^T(\mathbf{x})\mathbf{S}_{xx}(t) & \mathbf{\Psi}^T(\mathbf{x})\mathbf{S}_{xy}(t) \\ \mathbf{\Psi}^T(\mathbf{x})\mathbf{S}_{yx}(t) & \mathbf{\Psi}^T(\mathbf{x})\mathbf{S}_{yy}(t) \end{bmatrix}. \tag{2.24b}$$

In a similar fashion, we approximate the test functions, $\mathbf{w}(\mathbf{x})$ with $\mathbf{w}_h(\mathbf{x}) \in \mathbf{\Xi}_h$, and $\mathbf{T}(\mathbf{x})$ with $\mathbf{T}_h(\mathbf{x}) \in \mathbf{\Upsilon}_h$; therefore:

$$\mathbf{w}_h(\mathbf{x}) = \begin{bmatrix} \mathbf{w}_x^T\mathbf{\Phi}(\mathbf{x}) \\ \mathbf{w}_y^T\mathbf{\Phi}(\mathbf{x}) \end{bmatrix}, \tag{2.25a}$$

$$\mathbf{T}_h(\mathbf{x}) = \begin{bmatrix} \mathbf{T}_{xx}^T\mathbf{\Psi}(\mathbf{x}) & \mathbf{T}_{xy}^T\mathbf{\Psi}(\mathbf{x}) \\ \mathbf{T}_{yx}^T\mathbf{\Psi}(\mathbf{x}) & \mathbf{T}_{yy}^T\mathbf{\Psi}(\mathbf{x}) \end{bmatrix}. \tag{2.25b}$$

Incorporating (2.24) and (2.25) into (2.22), results in the following semi-discrete form:

$$\mathbf{M}\ddot{\mathbf{d}} + \mathbf{C}\dot{\mathbf{d}} + \mathbf{K}\mathbf{d} = \mathbf{f}, \tag{2.26}$$

where spatial and temporal dependencies are suppressed for brevity, and system matrices, $\mathbf{M}$, $\mathbf{C}$, $\mathbf{K}$, and vectors $\mathbf{d}$ and $\mathbf{f}$, are defined as:

$$\mathbf{M} = \begin{bmatrix} \bar{\mathbf{M}}_{\mathrm{RD}} + \bar{\mathbf{M}}_a & \mathbf{0} \\ \mathbf{0} & \mathbf{N}_a \end{bmatrix}, \qquad \mathbf{C} = \begin{bmatrix} \bar{\mathbf{M}}_b & \bar{\mathbf{A}}_{eu} \\ -\bar{\mathbf{A}}_{el}^{\mathrm{T}} & \mathbf{N}_b \end{bmatrix}, \tag{2.27a}$$

$$\mathbf{K} = \begin{bmatrix} \bar{\mathbf{K}}_{\mathrm{RD}} + \bar{\mathbf{M}}_c & \bar{\mathbf{A}}_{pu} \\ -\bar{\mathbf{A}}_{pl}^{\mathrm{T}} & \mathbf{N}_c \end{bmatrix}, \qquad \mathbf{d} = \begin{bmatrix} \mathbf{U} \\ \mathbf{\Sigma} \end{bmatrix}, \qquad \mathbf{f} = \begin{bmatrix} \bar{\mathbf{f}}_{\mathrm{RD}} \\ \mathbf{0} \end{bmatrix}, \tag{2.27b}$$

where subscript RD refers to the interior (regular) domain, and $\mathbf{M}_{\mathrm{RD}}$, $\mathbf{K}_{\mathrm{RD}}$, and $\mathbf{f}_{\mathrm{RD}}$, correspond to the standard mass matrix, stiffness matrix, and vector of nodal forces in the interior domain, respectively, and a bar indicates their extension to encompass all the displacement degrees-of-freedom; $\mathbf{U}$ and $\mathbf{\Sigma}$ comprise the vector of nodal displacements and stresses. Moreover, $\mathbf{U}$ is partitioned such that its first entries

belong solely to the interior domain, followed by those on the interface boundary between the interior domain and the PML buffer, and finally those that are located only within the PML. The rest of the submatrices in (2.27) correspond to the PML buffer zone (see Figure 2.4 for a schematic partitioning, and Appendix A.1.1 for submatrix definitions; the dotted line in Figure 2.4 separates displacement from stress degrees-of-freedom).

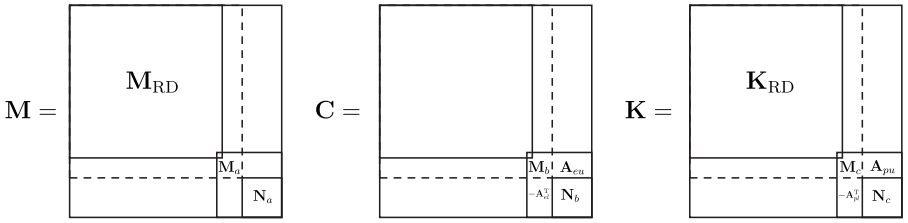

Figure 2.4: Partitioning of submatrices in (2.27)

We remark that the upper-left corner blocks of $\mathbf{M}$ and $\mathbf{K}$ correspond to the mass and stiffness matrices of a standard displacement-only formulation, as depicted in Figure 2.4. This implies that in order to accommodate PML capability into existing codes, one needs to account for the submatrices on the lower-right blocks of $\mathbf{M}$, $\mathbf{C}$, and $\mathbf{K}$. Notice that the semi-discrete form (2.26) is not symmetric. In fact, a block-diagonal structure for $\mathbf{M}$ comes at the price of losing symmetry. Alternatively, one may preserve symmetry of the matrices in the semi-discrete form at the expense of losing the block-diagonal form of $\mathbf{M}$, and thus the ability for explicit time-integration.

2.1.3 The PML in 3D-truncated domains[3]

The development of the 3D PML follows similar steps with those taken for the 2D case. However, the presence of a third equilibrium equation, or said differently, the third spatial derivation, raises the temporal complexity.

Let us complex-stretch the x, y and z physical coordinates into $\tilde{x}$, $\tilde{y}$, and $\tilde{z}$, respectively, in (2.7a):

$$\frac{\partial \hat{\mathcal{S}}_{xx}}{\partial \tilde{x}} + \frac{\partial \hat{\mathcal{S}}_{yx}}{\partial \tilde{y}} + \frac{\partial \hat{\mathcal{S}}_{zx}}{\partial \tilde{z}} = (i\omega)^2 \rho \ \hat{u}_x, \tag{2.28a}$$

$$\frac{\partial \hat{\mathcal{S}}_{xy}}{\partial \tilde{x}} + \frac{\partial \hat{\mathcal{S}}_{yy}}{\partial \tilde{y}} + \frac{\partial \hat{\mathcal{S}}_{zy}}{\partial \tilde{z}} = (i\omega)^2 \rho \ \hat{u}_y, \tag{2.28b}$$

$$\frac{\partial \hat{\mathcal{S}}_{xz}}{\partial \tilde{x}} + \frac{\partial \hat{\mathcal{S}}_{yz}}{\partial \tilde{y}} + \frac{\partial \hat{\mathcal{S}}_{zz}}{\partial \tilde{z}} = (i\omega)^2 \rho \ \hat{u}_z, \tag{2.28c}$$

Applying the derivative rule (2.5) to (2.28), we can express (2.28) in the unstretched coordinate system as follows:

$$\frac{1}{\lambda_x}\frac{\partial \hat{\mathcal{S}}_{xx}}{\partial x} + \frac{1}{\lambda_y}\frac{\partial \hat{\mathcal{S}}_{yx}}{\partial y} + \frac{1}{\lambda_z}\frac{\partial \hat{\mathcal{S}}_{zx}}{\partial z} = (i\omega)^2 \rho \ \hat{u}_x, \tag{2.29a}$$

$$\frac{1}{\lambda_x}\frac{\partial \hat{\mathcal{S}}_{xy}}{\partial x} + \frac{1}{\lambda_y}\frac{\partial \hat{\mathcal{S}}_{yy}}{\partial y} + \frac{1}{\lambda_z}\frac{\partial \hat{\mathcal{S}}_{zy}}{\partial z} = (i\omega)^2 \rho \ \hat{u}_y, \tag{2.29b}$$

$$\frac{1}{\lambda_x}\frac{\partial \hat{\mathcal{S}}_{xz}}{\partial x} + \frac{1}{\lambda_y}\frac{\partial \hat{\mathcal{S}}_{yz}}{\partial y} + \frac{1}{\lambda_z}\frac{\partial \hat{\mathcal{S}}_{zz}}{\partial z} = (i\omega)^2 \rho \ \hat{u}_z. \tag{2.29c}$$

Multiplying (2.29) by $\lambda_x \lambda_y \lambda_z$ results in:

$$\mathbf{div}\left(\hat{\mathcal{S}}^T \Lambda\right) = (i\omega)^2 \rho \ \lambda_x \lambda_y \lambda_z \ \hat{\mathbf{u}}, \tag{2.30}$$

[3]The development in this section was first published in Fathi et al. (2015) [89]

where the stretching tensor Λ is defined as:

$$\Lambda = \begin{bmatrix} \lambda_y\lambda_z & 0 & 0 \\ 0 & \lambda_x\lambda_z & 0 \\ 0 & 0 & \lambda_x\lambda_y \end{bmatrix} = \begin{bmatrix} \alpha_y\alpha_z & 0 & 0 \\ 0 & \alpha_x\alpha_z & 0 \\ 0 & 0 & \alpha_x\alpha_y \end{bmatrix} + \frac{1}{(i\omega)} \begin{bmatrix} \alpha_y\beta_z + \alpha_z\beta_y & 0 & 0 \\ 0 & \alpha_x\beta_z + \alpha_z\beta_x & 0 \\ 0 & 0 & \alpha_x\beta_y + \alpha_y\beta_x \end{bmatrix} + \frac{1}{(i\omega)^2} \begin{bmatrix} \beta_y\beta_z & 0 & 0 \\ 0 & \beta_x\beta_z & 0 \\ 0 & 0 & \beta_x\beta_y \end{bmatrix} = \Lambda_e + \frac{1}{i\omega}\Lambda_p + \frac{1}{(i\omega)^2}\Lambda_w. \quad (2.31)$$

Note that Λ_e reduces to the identity tensor within the regular domain, while Λ_p and Λ_w vanish identically. Substituting (2.2) and (2.31) in (2.30), results in:

$$\mathbf{div}\left(\hat{\mathcal{S}}^T\Lambda_e + \frac{1}{i\omega}\hat{\mathcal{S}}^T\Lambda_p + \frac{1}{(i\omega)^2}\hat{\mathcal{S}}^T\Lambda_w\right) = \rho\left[(i\omega)^2 a\hat{\mathbf{u}} + i\omega b\hat{\mathbf{u}} + c\hat{\mathbf{u}} + \frac{d}{i\omega}\hat{\mathbf{u}}\right], \quad (2.32)$$

where

$$\begin{aligned} a &= \alpha_x\ \alpha_y\ \alpha_z, \\ b &= \alpha_x\ \alpha_y\ \beta_z + \alpha_x\ \alpha_z\ \beta_y + \alpha_y\ \alpha_z\ \beta_x, \\ c &= \alpha_x\ \beta_y\ \beta_z + \alpha_y\ \beta_z\ \beta_x + \alpha_z\ \beta_y\ \beta_x, \\ d &= \beta_x\ \beta_y\ \beta_z. \end{aligned} \quad (2.33)$$

Multiplying (2.32) by $i\omega$, we obtain:

$$\mathbf{div}\left(i\omega\hat{\mathcal{S}}^T\Lambda_e + \hat{\mathcal{S}}^T\Lambda_p + \frac{1}{i\omega}\hat{\mathcal{S}}^T\Lambda_w\right) = \rho\left[(i\omega)^3 a\hat{\mathbf{u}} + (i\omega)^2 b\hat{\mathbf{u}} + i\omega c\hat{\mathbf{u}} + d\hat{\mathbf{u}}\right]. \quad (2.34)$$

Next, we stretch the coordinates in the combined constitutive and kinematic equations (2.7b); there results:

$$\hat{\mathcal{S}} = \mu\left\{(\nabla\hat{\mathbf{u}})\begin{bmatrix} \frac{1}{\lambda_x} & 0 & 0 \\ 0 & \frac{1}{\lambda_y} & 0 \\ 0 & 0 & \frac{1}{\lambda_z} \end{bmatrix} + \begin{bmatrix} \frac{1}{\lambda_x} & 0 & 0 \\ 0 & \frac{1}{\lambda_y} & 0 \\ 0 & 0 & \frac{1}{\lambda_z} \end{bmatrix}(\nabla\hat{\mathbf{u}})^T\right\} + \lambda\Big(\frac{1}{\lambda_x}\frac{\partial\hat{u}_x}{\partial x} + \frac{1}{\lambda_y}\frac{\partial\hat{u}_y}{\partial y} + \frac{1}{\lambda_z}\frac{\partial\hat{u}_z}{\partial z}\Big)\mathcal{I}. \quad (2.35)$$

Multiplying (2.35) by $\lambda_x\lambda_y\lambda_z$ results in:

$$\lambda_x\lambda_y\lambda_z\hat{\mathcal{S}} = \mu\left[\nabla\hat{\mathbf{u}}\ \Lambda + \Lambda\left(\nabla\hat{\mathbf{u}}\right)^T\right] + \lambda\,\mathrm{div}(\Lambda\hat{\mathbf{u}})\mathcal{I}, \tag{2.36}$$

Multiplying (2.36) by $(i\omega)^2$ and using (2.2) and (2.31), we obtain:

$$\begin{aligned}(i\omega)^2 a\hat{\mathcal{S}} + i\omega b\hat{\mathcal{S}} + c\hat{\mathcal{S}} + \frac{1}{i\omega}d\hat{\mathcal{S}} = \mu(i\omega)^2\left[(\nabla\hat{\mathbf{u}})\Lambda_e + \Lambda_e(\nabla\hat{\mathbf{u}})^T\right] \\ + \mu\ i\omega\left[(\nabla\hat{\mathbf{u}})\Lambda_p + \Lambda_p(\nabla\hat{\mathbf{u}})^T\right] + \mu\left[(\nabla\hat{\mathbf{u}})\Lambda_w + \Lambda_w(\nabla\hat{\mathbf{u}})^T\right] \\ + \lambda(i\omega)^2\,\mathrm{div}(\Lambda_e\hat{\mathbf{u}})\mathcal{I} + \lambda\ i\omega\,\mathrm{div}(\Lambda_p\hat{\mathbf{u}})\mathcal{I} + \lambda\,\mathrm{div}(\Lambda_w\hat{\mathbf{u}})\mathcal{I}.\end{aligned} \tag{2.37}$$

Equations (2.34) and (2.37) constitute the corresponding frequency-domain governing equations in the stretched coordinate system. Then, to obtain the corresponding time-domain equations, we apply the inverse Fourier transform, to obtain:

$$\mathbf{div}\left[\dot{\mathcal{S}}^T\Lambda_e + \mathcal{S}^T\Lambda_p + \left(\int_0^t \mathcal{S}^T d\tau\right)\Lambda_w\right] = \rho\left(a\dddot{\mathbf{u}} + b\ddot{\mathbf{u}} + c\dot{\mathbf{u}} + d\mathbf{u}\right), \tag{2.38a}$$

$$\begin{aligned}&a\ddot{\mathcal{S}} + b\dot{\mathcal{S}} + c\mathcal{S} + d\left(\int_0^t \mathcal{S}d\tau\right) = \\ &\mu\left[(\nabla\ddot{\mathbf{u}})\Lambda_e + \Lambda_e(\nabla\ddot{\mathbf{u}})^T + (\nabla\dot{\mathbf{u}})\Lambda_p + \Lambda_p(\nabla\dot{\mathbf{u}})^T + (\nabla\mathbf{u})\Lambda_w + \Lambda_w(\nabla\mathbf{u})^T\right] + \\ &\lambda\left[\mathrm{div}(\Lambda_e\ddot{\mathbf{u}}) + \mathrm{div}(\Lambda_p\dot{\mathbf{u}}) + \mathrm{div}(\Lambda_w\mathbf{u})\right]\mathcal{I}.\end{aligned} \tag{2.38b}$$

We introduce again the auxiliary variable $\mathbf{S}(\mathbf{x},t)$, as previously defined in (2.38):

$$\mathbf{S}(\mathbf{x},t) = \int_0^t \mathcal{S}(\mathbf{x},\tau)d\tau. \tag{2.39a}$$

Clearly,

$$\dot{\mathbf{S}}(\mathbf{x},t) = \mathcal{S}(\mathbf{x},t), \qquad \ddot{\mathbf{S}}(\mathbf{x},t) = \dot{\mathcal{S}}(\mathbf{x},t), \qquad \dddot{\mathbf{S}}(\mathbf{x},t) = \ddot{\mathcal{S}}(\mathbf{x},t). \tag{2.39b}$$

Substituting (2.39) in (2.38), we obtain:

$$\mathbf{div}\left(\ddot{\mathbf{S}}^T\Lambda_e + \dot{\mathbf{S}}^T\Lambda_p + \mathbf{S}^T\Lambda_w\right) = \rho\left(a\dddot{\mathbf{u}} + b\ddot{\mathbf{u}} + c\dot{\mathbf{u}} + d\mathbf{u}\right), \tag{2.40a}$$

$$\begin{aligned} &a\dddot{\mathbf{S}} + b\ddot{\mathbf{S}} + c\dot{\mathbf{S}} + d\mathbf{S} = \\ &\mu\left[(\nabla\ddot{\mathbf{u}})\Lambda_e + \Lambda_e(\nabla\ddot{\mathbf{u}})^T + (\nabla\dot{\mathbf{u}})\Lambda_p + \Lambda_p(\nabla\dot{\mathbf{u}})^T + (\nabla\mathbf{u})\Lambda_w + \Lambda_w(\nabla\mathbf{u})^T\right] + \\ &\lambda\left[\mathrm{div}(\Lambda_e\ddot{\mathbf{u}}) + \mathrm{div}(\Lambda_p\dot{\mathbf{u}}) + \mathrm{div}(\Lambda_w\mathbf{u})\right]\mathcal{I}. \end{aligned} \tag{2.40b}$$

Equations (2.40) are the corresponding time-domain PML balance of momentum, and the combined constitutive and kinematic equations, respectively. The next step would be the spatial discretization using a Galerkin method to arrive at a third-order, continuous-in-time, system of ordinary differential equations.

Similarly to the two-dimensional model, it is possible to use (2.40) for the interior domain and the PML zone, which, in turn, amounts to considering stress and displacement components as unknowns in both the interior domain and the PML buffer zone. In order to reduce the computational cost, instead, we resort to a hybrid approach, originally developed in [180], where the interior domain is treated with a standard displacement-only formulation, coupled with the PML equations in the buffer zone. Accordingly, find $\mathbf{u}(\mathbf{x}, t)$ in $\Omega^{\mathrm{RD}} \cup \Omega^{\mathrm{PML}}$, and $\mathbf{S}(\mathbf{x}, t)$ in Ω^{PML} (see Figure 2.5 for domain and boundary designations), where $\mathbf{u}$ and $\mathbf{S}$ reside in

appropriate function spaces and:

$$\mathbf{div}\left\{\mu\left[\nabla\dot{\mathbf{u}}+(\nabla\dot{\mathbf{u}})^T\right]+\lambda(\operatorname{div}\dot{\mathbf{u}})\mathcal{I}\right\}=\rho\ddot{\mathbf{u}} \qquad \text{in } \Omega^{\mathrm{RD}}\times\mathsf{J}, \tag{2.41a}$$

$$\mathbf{div}\left(\ddot{\mathbf{S}}^T\Lambda_e+\dot{\mathbf{S}}^T\Lambda_p+\mathbf{S}^T\Lambda_w\right)=\rho\left(a\dddot{\mathbf{u}}+b\ddot{\mathbf{u}}+c\dot{\mathbf{u}}+d\mathbf{u}\right) \qquad \text{in } \Omega^{\mathrm{PML}}\times\mathsf{J}, \tag{2.41b}$$

$$\begin{aligned}&a\dddot{\mathbf{S}}+b\ddot{\mathbf{S}}+c\dot{\mathbf{S}}+d\mathbf{S}=\\&\mu\left[(\nabla\ddot{\mathbf{u}})\Lambda_e+\Lambda_e(\nabla\ddot{\mathbf{u}})^T+(\nabla\dot{\mathbf{u}})\Lambda_p+\Lambda_p(\nabla\dot{\mathbf{u}})^T+(\nabla\mathbf{u})\Lambda_w+\Lambda_w(\nabla\mathbf{u})^T\right]+\\&\lambda\left[\operatorname{div}(\Lambda_e\ddot{\mathbf{u}})+\operatorname{div}(\Lambda_p\dot{\mathbf{u}})+\operatorname{div}(\Lambda_w\mathbf{u})\right]\mathcal{I}\end{aligned} \qquad \text{in } \Omega^{\mathrm{PML}}\times\mathsf{J}. \tag{2.41c}$$

The system is initially at rest, and subject to the following boundary and interface conditions:

$$\left\{\mu\left[\nabla\dot{\mathbf{u}}+(\nabla\dot{\mathbf{u}})^T\right]+\lambda(\operatorname{div}\dot{\mathbf{u}})\mathcal{I}\right\}\mathbf{n}^+=\dot{\boldsymbol{g}}_n \qquad \text{on } \Gamma_N^{\mathrm{RD}}\times\mathsf{J}, \tag{2.42a}$$

$$(\ddot{\mathbf{S}}^T\Lambda_e+\dot{\mathbf{S}}^T\Lambda_p+\mathbf{S}^T\Lambda_w)\mathbf{n}^-=\mathbf{0} \qquad \text{on } \Gamma_N^{\mathrm{PML}}\times\mathsf{J}, \tag{2.42b}$$

$$\mathbf{u}=\mathbf{0} \qquad \text{on } \Gamma_D^{\mathrm{PML}}\times\mathsf{J}, \tag{2.42c}$$

$$\mathbf{u}^+=\mathbf{u}^- \qquad \text{on } \Gamma^{\mathrm{I}}\times\mathsf{J}, \tag{2.42d}$$

$$\begin{aligned}&\left\{\mu\left[\nabla\dot{\mathbf{u}}+(\nabla\dot{\mathbf{u}})^T\right]+\lambda(\operatorname{div}\dot{\mathbf{u}})\mathcal{I}\right\}\mathbf{n}^++\\&(\ddot{\mathbf{S}}^T\Lambda_e+\dot{\mathbf{S}}^T\Lambda_p+\mathbf{S}^T\Lambda_w)\mathbf{n}^-=0\end{aligned} \qquad \text{on } \Gamma^{\mathrm{I}}\times\mathsf{J}, \tag{2.42e}$$

where Ω^{RD} denotes the interior (regular) domain, Ω^{PML} represents the region occupied by the PML buffer zone, Γ^{I} is the interface boundary between the interior and PML domains, Γ_N^{RD} and Γ_N^{PML} denote the free (top surface) boundary of the interior domain and PML, respectively, and $\mathsf{J}=(0,T]$ is the time interval of interest.

Equation (2.42e) enforces the balance of tractions at the interface of the interior domain and the PML. Moreover, (2.42d) implies continuity of displacements

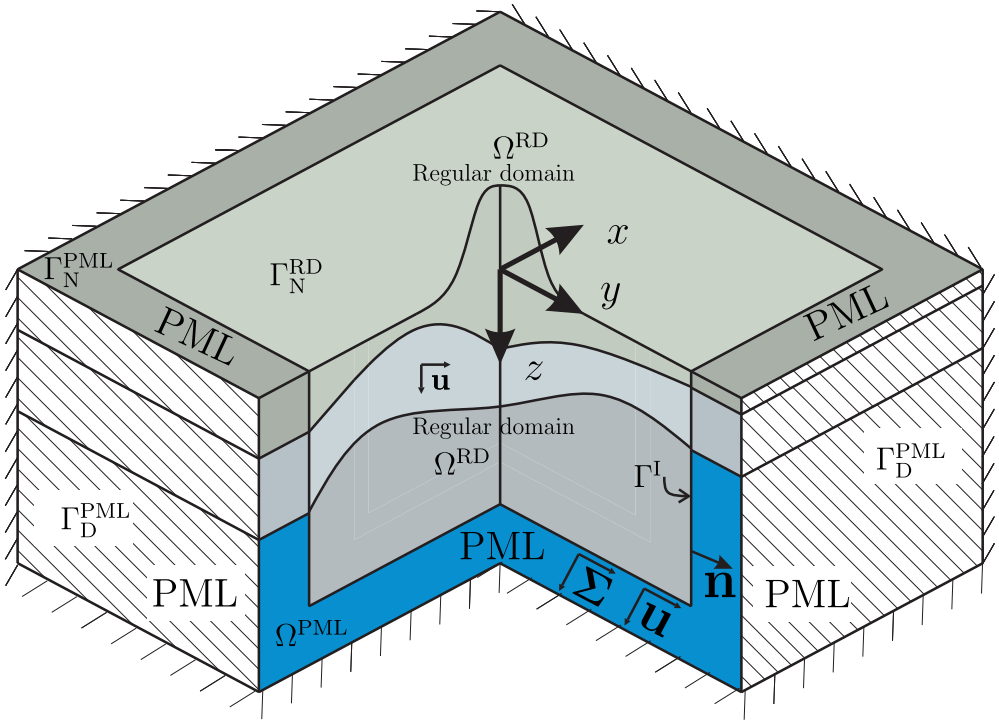

Figure 2.5: PML-truncated semi-infinite domain

at the interface; (2.42a) specifies tractions ($\boldsymbol{g}_n$) on the top surface of the interior domain, and (2.42b) implies traction-free boundary condition on the top PML surface. We consider fixed boundaries for the PML on the sides and at the bottom, as indicated by (2.42c).

Next, we seek a weak form, corresponding to the strong form of (2.41) and (2.42), in the Galerkin sense. Specifically, we take the inner products of (2.41a) and (2.41b) with (vector) test function $\mathbf{w}(\mathbf{x})$, and integrate by parts over their corresponding domains. Incorporating (2.42d)-(2.42e) eliminates the interface boundary terms and results in (2.43a). Next, we take the inner product of (2.41c) with (tensor) test function $\mathbf{T}(\mathbf{x})$; there results (2.43b).

Accordingly, find $\mathbf{u} \in \mathbf{H}^1(\Omega) \times \mathsf{J}$, and $\mathbf{S} \in \mathcal{L}^2(\Omega) \times \mathsf{J}$, such that:

$$\int_{\Omega^{\mathrm{RD}}} \nabla \mathbf{w} : \left\{ \mu \left[\nabla \dot{\mathbf{u}} + (\nabla \dot{\mathbf{u}})^T \right] + \lambda (\operatorname{div} \dot{\mathbf{u}}) \mathcal{I} \right\} \, \mathrm{d}\Omega + \int_{\Omega^{\mathrm{PML}}} \nabla \mathbf{w} : \left(\ddot{\mathbf{S}}^T \Lambda_e + \dot{\mathbf{S}}^T \Lambda_p + \mathbf{S}^T \Lambda_w \right) \mathrm{d}\Omega$$
$$+ \int_{\Omega^{\mathrm{RD}}} \mathbf{w} \cdot \rho \ddot{\mathbf{u}} \, \mathrm{d}\Omega + \int_{\Omega^{\mathrm{PML}}} \mathbf{w} \cdot \rho \left(a \dddot{\mathbf{u}} + b \ddot{\mathbf{u}} + c \dot{\mathbf{u}} + d \mathbf{u} \right) \mathrm{d}\Omega = \int_{\Gamma_N^{\mathrm{RD}}} \mathbf{w} \cdot \dot{\boldsymbol{g}}_n \, \mathrm{d}\Gamma + \int_{\Omega^{\mathrm{RD}}} \mathbf{w} \cdot \dot{\mathbf{b}} \, \mathrm{d}\Omega, \tag{2.43a}$$

$$\int_{\Omega^{\mathrm{PML}}} \mathbf{T} : \left(a \dddot{\mathbf{S}} + b \ddot{\mathbf{S}} + c \dot{\mathbf{S}} + d \mathbf{S} \right) \mathrm{d}\Omega$$
$$= \int_{\Omega^{\mathrm{PML}}} \mathbf{T} : \mu \left[(\nabla \ddot{\mathbf{u}}) \Lambda_e + \Lambda_e (\nabla \ddot{\mathbf{u}})^T + (\nabla \dot{\mathbf{u}}) \Lambda_p + \Lambda_p (\nabla \dot{\mathbf{u}})^T + (\nabla \mathbf{u}) \Lambda_w + \Lambda_w (\nabla \mathbf{u})^T \right]$$
$$+ \mathbf{T} : \lambda \left[\operatorname{div}(\Lambda_e \ddot{\mathbf{u}}) + \operatorname{div}(\Lambda_p \dot{\mathbf{u}}) + \operatorname{div}(\Lambda_w \mathbf{u}) \right] \mathcal{I} \mathrm{d}\Omega, \tag{2.43b}$$

for every $\mathbf{w} \in \mathbf{H}^1(\Omega)$ and $\mathbf{T} \in \mathcal{L}^2(\Omega)$, where $\boldsymbol{g}_n \in \mathbf{L}^2(\Omega) \times \mathsf{J}$, and $\mathbf{b} \in \mathbf{L}^2(\Omega) \times \mathsf{J}$. Function spaces for scalar- (v), vector- ($\mathbf{v}$), and tensor-valued ($\mathcal{A}$) functions are defined as:

$$L^2(\Omega) = \left\{ v : \int_\Omega |v|^2 d\mathbf{x} < \infty \right\}, \tag{2.44a}$$
$$\mathbf{L}^2(\Omega) = \left\{ \mathbf{v} : \mathbf{v} \in (L^2(\Omega))^3 \right\}, \tag{2.44b}$$
$$\mathcal{L}^2(\Omega) = \left\{ \mathcal{A} : \mathcal{A} \in (L^2(\Omega))^{3\times 3} \right\}, \tag{2.44c}$$
$$H^1(\Omega) = \left\{ v : \int_\Omega \left(|v|^2 + |\nabla v|^2 \right) d\mathbf{x} < \infty, \; v|_{\Gamma_D^{\mathrm{PML}}} = 0 \right\}, \tag{2.44d}$$
$$\mathbf{H}^1(\Omega) = \left\{ \mathbf{v} : \mathbf{v} \in (H^1(\Omega))^3 \right\}. \tag{2.44e}$$

In order to resolve (2.43) numerically, we use standard finite-dimensional subspaces. Specifically, we introduce finite-dimensional subspaces $\boldsymbol{\Xi}_h \subset \mathbf{H}^1(\Omega)$ and $\boldsymbol{\Upsilon}_h \subset \mathcal{L}^2(\Omega)$, with basis functions $\boldsymbol{\Phi}$ and $\boldsymbol{\Psi}$, respectively. We then approximate

$\mathbf{u}(\mathbf{x},t)$ with $\mathbf{u}_h(\mathbf{x},t) \in \boldsymbol{\Xi}_h \times \mathsf{J}$, and $\mathbf{S}(\mathbf{x},t)$ with $\mathbf{S}_h(\mathbf{x},t) \in \boldsymbol{\Upsilon}_h \times \mathsf{J}$, as detailed below:

$$\mathbf{u}_h(\mathbf{x},t) = \begin{bmatrix} \boldsymbol{\Phi}^T(\mathbf{x})\mathbf{u}_x(t) \\ \boldsymbol{\Phi}^T(\mathbf{x})\mathbf{u}_y(t) \\ \boldsymbol{\Phi}^T(\mathbf{x})\mathbf{u}_z(t) \end{bmatrix}, \tag{2.45a}$$

$$\mathbf{S}_h(\mathbf{x},t) = \begin{bmatrix} \boldsymbol{\Psi}^T(\mathbf{x})\mathbf{S}_{xx}(t) & \boldsymbol{\Psi}^T(\mathbf{x})\mathbf{S}_{xy}(t) & \boldsymbol{\Psi}^T(\mathbf{x})\mathbf{S}_{xz}(t) \\ \boldsymbol{\Psi}^T(\mathbf{x})\mathbf{S}_{yx}(t) & \boldsymbol{\Psi}^T(\mathbf{x})\mathbf{S}_{yy}(t) & \boldsymbol{\Psi}^T(\mathbf{x})\mathbf{S}_{yz}(t) \\ \boldsymbol{\Psi}^T(\mathbf{x})\mathbf{S}_{zx}(t) & \boldsymbol{\Psi}^T(\mathbf{x})\mathbf{S}_{zy}(t) & \boldsymbol{\Psi}^T(\mathbf{x})\mathbf{S}_{zz}(t) \end{bmatrix}. \tag{2.45b}$$

In a similar fashion, we approximate the test functions, $\mathbf{w}(\mathbf{x})$ with $\mathbf{w}_h(\mathbf{x}) \in \boldsymbol{\Xi}_h$, and $\mathbf{T}(\mathbf{x})$ with $\mathbf{T}_h(\mathbf{x}) \in \boldsymbol{\Upsilon}_h$; therefore:

$$\mathbf{w}_h(\mathbf{x}) = \begin{bmatrix} \mathbf{w}_x^T\boldsymbol{\Phi}(\mathbf{x}) \\ \mathbf{w}_y^T\boldsymbol{\Phi}(\mathbf{x}) \\ \mathbf{w}_z^T\boldsymbol{\Phi}(\mathbf{x}) \end{bmatrix}, \tag{2.46a}$$

$$\mathbf{T}_h(\mathbf{x}) = \begin{bmatrix} \mathbf{T}_{xx}^T\boldsymbol{\Psi}(\mathbf{x}) & \mathbf{T}_{xy}^T\boldsymbol{\Psi}(\mathbf{x}) & \mathbf{T}_{xz}^T\boldsymbol{\Psi}(\mathbf{x}) \\ \mathbf{T}_{yx}^T\boldsymbol{\Psi}(\mathbf{x}) & \mathbf{T}_{yy}^T\boldsymbol{\Psi}(\mathbf{x}) & \mathbf{T}_{yz}^T\boldsymbol{\Psi}(\mathbf{x}) \\ \mathbf{T}_{zx}^T\boldsymbol{\Psi}(\mathbf{x}) & \mathbf{T}_{zy}^T\boldsymbol{\Psi}(\mathbf{x}) & \mathbf{T}_{zz}^T\boldsymbol{\Psi}(\mathbf{x}) \end{bmatrix}. \tag{2.46b}$$

Incorporating (2.45) and (2.46) into (2.43), results in the following semi-discrete form:

$$\mathbf{M}\ddot{\mathbf{d}} + \mathbf{C}\ddot{\mathbf{d}} + \mathbf{K}\dot{\mathbf{d}} + \mathbf{G}\mathbf{d} = \dot{\mathbf{f}}, \tag{2.47}$$

where spatial and temporal dependencies are suppressed for brevity, and system matrices, $\mathbf{M}$, $\mathbf{C}$, $\mathbf{K}$, $\mathbf{G}$, and vectors $\mathbf{d}$ and $\mathbf{f}$, are defined as:

$$\mathbf{M} = \begin{bmatrix} \bar{\mathbf{M}}_{\mathrm{RD}} + \bar{\mathbf{M}}_a & \mathbf{0} \\ \mathbf{0} & \mathbf{N}_a \end{bmatrix}, \qquad \mathbf{C} = \begin{bmatrix} \bar{\mathbf{M}}_b & \bar{\mathbf{A}}_{eu} \\ -\bar{\mathbf{A}}_{el}^T & \mathbf{N}_b \end{bmatrix}, \tag{2.48a}$$

$$\mathbf{K} = \begin{bmatrix} \bar{\mathbf{K}}_{\mathrm{RD}} + \bar{\mathbf{M}}_c & \bar{\mathbf{A}}_{pu} \\ -\bar{\mathbf{A}}_{pl}^T & \mathbf{N}_c \end{bmatrix}, \qquad \mathbf{G} = \begin{bmatrix} \bar{\mathbf{M}}_d & \bar{\mathbf{A}}_{wu} \\ -\bar{\mathbf{A}}_{wl}^T & \mathbf{N}_d \end{bmatrix}, \tag{2.48b}$$

$$\mathbf{d} = \begin{bmatrix} \mathbf{U} \\ \boldsymbol{\Sigma} \end{bmatrix}, \qquad \mathbf{f} = \begin{bmatrix} \bar{\mathbf{f}}_{\mathrm{RD}} \\ \mathbf{0} \end{bmatrix}, \tag{2.48c}$$

where subscript RD refers to the interior (regular) domain, and $\mathbf{M}_{\mathrm{RD}}$, $\mathbf{K}_{\mathrm{RD}}$, and $\mathbf{f}_{\mathrm{RD}}$, correspond to the standard mass matrix, stiffness matrix, and vector of nodal forces in the interior domain, respectively, and a bar indicates their extension to encompass all the displacement degrees-of-freedom; $\mathbf{U}$ and $\mathbf{\Sigma}$ comprise the vector of nodal displacements and stresses. Moreover, $\mathbf{U}$ is partitioned such that its first entries belong solely to the interior domain, followed by those on the interface boundary between the interior domain and the PML buffer, and finally those that are located only within the PML. The rest of the submatrices in (2.48) correspond to the PML buffer zone (see Figure 2.6 for a schematic partitioning, and Appendix A.1.2 for submatrix definitions; the dotted line in Figure 2.6 separates displacement from stress degrees-of-freedom).

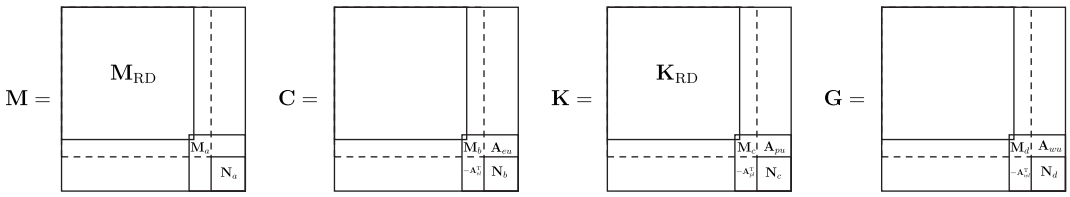

Figure 2.6: Partitioning of submatrices in (2.48)

We remark that the upper-left corner blocks of $\mathbf{M}$ and $\mathbf{K}$ correspond to the mass and stiffness matrices of a standard displacement-only formulation, as depicted in Figure 2.6. This implies that in order to accommodate PML capability into existing codes, one needs to account for the submatrices on the lower-right blocks of $\mathbf{M}$, $\mathbf{C}$, $\mathbf{K}$, and $\mathbf{G}$. Notice that the semi-discrete form (2.47) is not symmetric. In fact, a block-diagonal structure for $\mathbf{M}$ comes at the price of losing symmetry.

Alternatively, one may preserve symmetry of the matrices in the semi-discrete form at the expense of losing the block-diagonal form of $\mathbf{M}$, and thus the ability for explicit time-integration. For more information on the PML formulation see [89, 179, 180].

Time-integration can be accomplished by working with either (2.47) or one of its second- or first-order system counterparts, or, alternatively, one may (analytically) integrate (2.47) in time first, to obviate the temporal differentiation of the forcing vector. Assuming the system is initially at rest, there results:

$$\mathbf{M}\ddot{\mathbf{d}} + \mathbf{C}\dot{\mathbf{d}} + \mathbf{K}\mathbf{d} + \mathbf{G}\bar{\mathbf{d}} = \mathbf{f}, \tag{2.49a}$$

$$\bar{\mathbf{d}} = \int_0^t \mathbf{d}(\tau)|_{\mathrm{PML}}\, d\tau, \tag{2.49b}$$

where $\bar{\mathbf{d}}$ is the vector of displacement history. Equation (2.49) can be integrated via an extended Newmark method as outlined in Section 2.3.1. The scheme is implicit and requires matrix factorization. We remark that $\bar{\mathbf{d}}$ contains displacement and stress degrees-of-freedom that are associated with the PML buffer only; therefore, its size is much smaller than $\mathbf{d}$ (see Figure 2.6), which includes the displacement degrees-of-freedom of the entire domain.

Alternatively, (2.49) can be expressed as a second-order system:

$$\mathbf{M}\ddot{\mathbf{d}} + \mathbf{C}\dot{\mathbf{d}} + \mathbf{K}\mathbf{d} + \mathbf{G}\bar{\mathbf{d}} = \mathbf{f}, \tag{2.50a}$$

$$\dot{\bar{\mathbf{d}}} = \mathbf{d}|_{\mathrm{PML}}. \tag{2.50b}$$

In matrix notation, (2.50) reads

$$\begin{bmatrix} \mathbf{M} & \mathbf{0} \\ \mathbf{0} & \mathbf{0} \end{bmatrix} \begin{bmatrix} \ddot{\mathbf{d}} \\ \ddot{\bar{\mathbf{d}}} \end{bmatrix} + \begin{bmatrix} \mathbf{C} & \mathbf{0} \\ \mathbf{0} & \mathbf{I} \end{bmatrix} \begin{bmatrix} \dot{\mathbf{d}} \\ \dot{\bar{\mathbf{d}}} \end{bmatrix} + \begin{bmatrix} \mathbf{K} & \mathbf{G} \\ -\mathbf{I} & \mathbf{0} \end{bmatrix} \begin{bmatrix} \mathbf{d} \\ \bar{\mathbf{d}} \end{bmatrix} = \begin{bmatrix} \mathbf{f} \\ \mathbf{0} \end{bmatrix}, \tag{2.51}$$

where now a standard Newmark scheme may be utilized to integrate (2.51) or, alternatively:

$$\begin{bmatrix} \mathbf{M} & \mathbf{0} \\ \mathbf{0} & \mathbf{I} \end{bmatrix} \begin{bmatrix} \ddot{\mathbf{d}} \\ \ddot{\bar{\mathbf{d}}} \end{bmatrix} + \begin{bmatrix} \mathbf{C} & \mathbf{0} \\ -\mathbf{I} & \mathbf{0} \end{bmatrix} \begin{bmatrix} \dot{\mathbf{d}} \\ \dot{\bar{\mathbf{d}}} \end{bmatrix} + \begin{bmatrix} \mathbf{K} & \mathbf{G} \\ \mathbf{0} & \mathbf{0} \end{bmatrix} \begin{bmatrix} \mathbf{d} \\ \bar{\mathbf{d}} \end{bmatrix} = \begin{bmatrix} \mathbf{f} \\ \mathbf{0} \end{bmatrix}, \tag{2.52}$$

where the resulting system can be integrated explicitly, provided that $\mathbf{M}$ is diagonal, as we discuss in Section 2.3.2.2.

2.1.4 The M-PML in 3D-truncated domains [4]

The aforementioned derivations are based on using the classical stretching function discussed in (2.2), where stretching is enforced only in the direction perpendicular to the PML interface. It has been reported that, in two-dimensional models, and under certain parameterizations, this stretching function creates spurious growths when waves travel along the interface, thus leading to numerical instability. In an attempt to stabilize the PML for two-dimensional domains, Meza-Fajardo and Papageorgiou [206] proposed coordinate-stretching in all directions within the PML buffer, leading to the, so-called, Multi-axial PML (M-PML). We show in this section that our framework can also accommodate the M-PML. We focus on the right PML buffer zone first, i.e., the volume contained in $x_0 \leq x \leq x_t$ (see Figure 2.2 with s replaced by x); extending the ideas to the zones where two or three layers intersect is straightforward, and can be accomplished by using superposition. We stretch the

[4] The development in this section was first published in Fathi et al. (2015) [89]

physical coordinates according to:

$$\tilde{x} = x_0 + \int_{x_0}^{x} \left[\alpha_x(x') + \frac{1}{i\omega} \beta_x(x') \right] dx', \tag{2.53a}$$

$$\tilde{y} = y_0 + \int_{y_0}^{y} \left[\alpha_y(x) + \frac{1}{i\omega} \beta_y(x) \right] dy', \tag{2.53b}$$

$$\tilde{z} = z_0 + \int_{z_0}^{z} \left[\alpha_z(x) + \frac{1}{i\omega} \beta_z(x) \right] dz', \tag{2.53c}$$

where $\alpha_y, \alpha_z, \beta_y$, and β_z are functions of x only, and are defined as:

$$\alpha_y(x) = 1 + \varrho\ \alpha_o \left[\frac{(x - x_o) n_x}{L_{\text{PML}}} \right]^m, \qquad \beta_y(x) = \varrho\ \beta_x(x), \tag{2.54a}$$

$$\alpha_z(x) = 1 + \varrho\ \alpha_o \left[\frac{(x - x_o) n_x}{L_{\text{PML}}} \right]^m, \qquad \beta_z(x) = \varrho\ \beta_x(x), \tag{2.54b}$$

where ϱ is a proportionality constant, and n_x is the outward unit normal at the interface, similar to n_s in Figure 2.2; α_x and β_x are defined in (2.3). We remark that $\alpha_y, \alpha_z, \beta_y$, and β_z would have been identically zero in the right buffer had we used the classical stretching. Applying the fundamental theorem of calculus to Figure 2.53, results in:

$$\lambda_x := \frac{\partial \tilde{x}}{\partial x} = \alpha_x(x) + \frac{1}{i\omega} \beta_x(x), \tag{2.55a}$$

$$\lambda_y := \frac{\partial \tilde{y}}{\partial y} = \alpha_y(x) + \frac{1}{i\omega} \beta_y(x), \tag{2.55b}$$

$$\lambda_z := \frac{\partial \tilde{z}}{\partial z} = \alpha_z(x) + \frac{1}{i\omega} \beta_z(x). \tag{2.55c}$$

These are the stretching functions the authors used in [207]. However, the definition of the stretched gradient operator in equation (3) in [207] requires additional terms, which the authors had not included. For example, the derivative with respect to $\tilde{x}$

should read:

$$\frac{\partial(\ )}{\partial\tilde{x}} = \frac{\partial(\ )}{\partial x}\frac{\partial x}{\partial\tilde{x}} + \frac{\partial(\ )}{\partial y}\frac{\partial y}{\partial\tilde{x}} + \frac{\partial(\ )}{\partial z}\frac{\partial z}{\partial\tilde{x}} \tag{2.56a}$$

$$= \frac{1}{\lambda_x}\frac{\partial(\ )}{\partial x} - \frac{\lambda_{yx}}{\lambda_x\lambda_y}\frac{\partial(\ )}{\partial y} - \frac{\lambda_{zx}}{\lambda_x\lambda_z}\frac{\partial(\ )}{\partial z}, \tag{2.56b}$$

instead of the expression given in [207] reads:

$$\frac{\partial(\ )}{\partial\tilde{x}} = \frac{1}{\lambda_x}\frac{\partial(\ )}{\partial x}. \tag{2.57}$$

In (2.56), the cross-derivative terms are defined as:

$$\lambda_{yx} := \frac{\partial\tilde{y}}{\partial x} = \left(\frac{\partial}{\partial x}\alpha_y(x) + \frac{1}{i\omega}\frac{\partial}{\partial x}\beta_y(x)\right)(y - y_0), \tag{2.58a}$$

$$\lambda_{zx} := \frac{\partial\tilde{z}}{\partial x} = \left(\frac{\partial}{\partial x}\alpha_z(x) + \frac{1}{i\omega}\frac{\partial}{\partial x}\beta_z(x)\right)(z - z_0). \tag{2.58b}$$

In other words, it seems that in [206, 207], the authors have not accounted properly for the Jacobian. Thus, there are at least two possible forms of the M-PML: the *uncorrected* form in [206, 207], and the *corrected* form, which accounts for the cross-derivatives. Interestingly, numerical experiments we performed in two dimensions with the corrected form yielded small, but non-negligible reflections from the interface. By contrast, the *uncorrected* form yielded better results, despite its unsound mathematical foundation. This has led us to adopt the approach taken in [206, 207]; accordingly, the equation pertaining to the conservation of linear momentum in the stretched coordinate system becomes:

$$\mathbf{div}\left(\hat{\mathcal{S}}^T\Lambda\right) - \hat{\mathcal{S}}^T\,\mathbf{div}\,\Lambda = (i\omega)^2\rho\ \lambda_x\lambda_y\lambda_z\ \hat{\mathbf{u}}, \tag{2.59}$$

which results in the following strong form:

$$\mathbf{div}\left(\ddot{\mathbf{S}}^T\Lambda_e + \dot{\mathbf{S}}^T\Lambda_p + \mathbf{S}^T\Lambda_w\right) - \left(\ddot{\mathbf{S}}^T\,\mathbf{div}\,\Lambda_e + \dot{\mathbf{S}}^T\,\mathbf{div}\,\Lambda_p + \mathbf{S}^T\,\mathbf{div}\,\Lambda_w\right) = \rho\left(a\ddot{\mathbf{u}} + b\ddot{\mathbf{u}} + c\dot{\mathbf{u}} + d\mathbf{u}\right). \quad (2.60)$$

The structure of the formulation pertaining to the combined constitutive and kinematic equation in the stretched coordinate system remains unaltered. Hence, for accommodating the M-PML, one only needs to replace (2.41b) in the strong form of the equations with (2.60), which, in turn, changes the definition of submatrices $\mathbf{A}_{eu}$, $\mathbf{A}_{pu}$, and $\mathbf{A}_{wu}$ in (2.48). The new definition of these submatrices for the M-PML case are given in Appendix A.2.

2.2 Seismic input modeling

We consider three approaches for introducing seismic loads within the computational model: (i) simulating the seismic source as a double-couple; (ii) simulating the fault rupture as a double-couple sequence; and (iii) introducing indirectly the effects of seismic source to the model. The material presented in this section is the material that is mostly synthesized and recompiled for completeness from a few key references: they include the discussion and derivations for the double-couple in Sections 2.2.1 and 2.2.2; the material in Section 2.2.3.1 The material on the DRM-PML coupling in Sections 2.2.3.2 and 2.2.3.3 is new and has not been previously published.

2.2.1 Seismic source as a double-couple

Three modes are possible for a crack or rupture as stated by Bouchon et al. (2010) [44]: (i) Mode I, the opening mode, is when the slip is normal to the two faces of the rupture; (ii) Mode II, the sliding mode, implies a slip in the rupture surface normal to the crack front; and (iii) in Mode III, the tearing mode, the slip is parallel to the crack front. A seismic fault might be of Mode II, or Mode III, or a combination of both; however, Mode II is the most prevalent case.

Before we turn to the formulation, let us first review the seismic moment used to measure the earthquake strength, needed for the double-couple formulation. The *seismic moment* M_0 quantifies the earthquake energy according to:

$$M_0 = \int_A \mu D(A) dA, \tag{2.61}$$

where A is the area of fault rupture, D is the slip (the relative displacement of the formerly adjacent points on opposite sides of a fault surface), and μ is the shear modulus. The complex fault geometry with variable values of slip alongside the surface, shown typically in Figure 2.7(a), can be simplified as a rectangle with an average slip, as shown in Figure 2.7(b). Hence, the seismic moment would be:

$$M_0 = \mu DLW. \tag{2.62}$$

This simplified model is acceptable for aftershocks with relatively small rupture areas. We can claim now, according to [4, 276], that the seismic body forces generated from this model can be approximated through double-couple forces (Figure 2.7(c)). In the

remaining of the section, we outline first, the mathematical formulation for a single-couple and, then, we discuss how the simplified fault geometry can be formulated as double-couple forces.

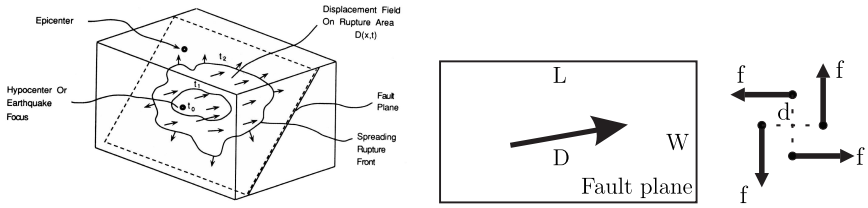

Figure 2.7: Fault model (a) schematic fault slip, (b) simplified fault plane with a constant slip, and (c) double-couple approximation of the fault (adapted from Stein and Wysession [276])

A single force couple, also known as a *vector dipole*, is composed of two equal opposite forces (thus the net force is zero) separated by a distance d, acting simultaneously on the surface of the seismic fault (see Figure 2.8). In a three-dimensional domain, a total number of nine vector dipoles exists as depicted in Figure 2.9. In this set, for instance, M_{xy} indicates a couple consisting of two forces of magnitude f, detached by a distance d along the y axis, and acting in the opposite $\pm x$ directions. The total moment, then, is fd, usually expressed in dyn $-$ m.

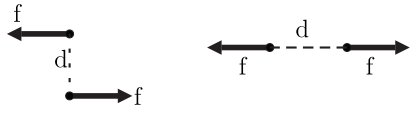

Figure 2.8: single-couple (redrawn from Stein and Wysession [276])

In order to attain a general form that represents all possible seismic scenarios,

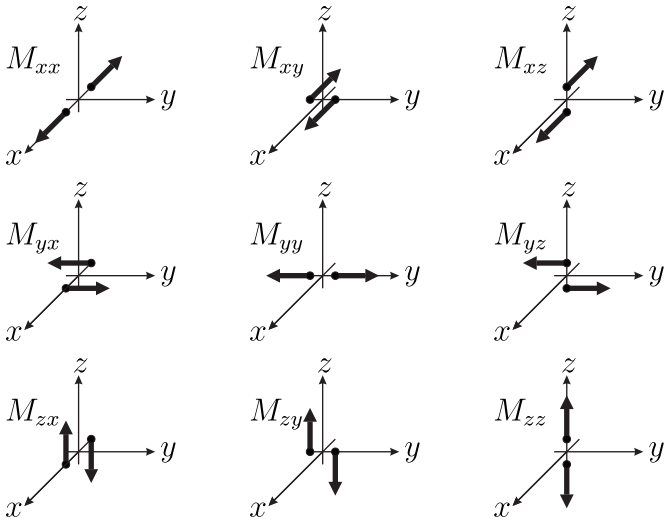

Figure 2.9: The nine possible couples that form the seismic moment tensor (redrawn from Stein and Wysession [276])

one can form a *seismic moment tensor*, which is a combination of all nine dipoles, as follows:

$$\mathbf{M} = M_0 \begin{bmatrix} M_{xx} & M_{xy} & M_{xz} \\ M_{yx} & M_{yy} & M_{yz} \\ M_{zx} & M_{zy} & M_{zz} \end{bmatrix}, \tag{2.63}$$

where, M_0 is the seismic moment. Therefore, one can utilize the seismic moment tensor to indicate the intensity of the fault, through the seismic moment M_0, and the fault orientation, through the dipoles. We also remark that owing to the conservation of angular momentum, the moment tensor is symmetric, hence, there are only six independent dipoles in the tensor.

Let us now focus on computing the moment tensor based on the fault orientation. Consider a typical planar seismic fault as illustrated in Figure 2.10. The

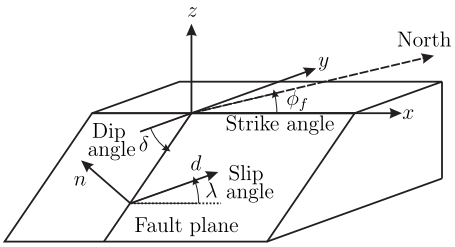

Figure 2.10: Simplified fault geometry (redrawn from Stein and Wysession [276])

normal vector of fault $\boldsymbol{n}$ is obtained as:

$$\boldsymbol{n} = \begin{bmatrix} -\sin\delta\sin\phi_f \\ -\sin\delta\cos\phi_f \\ \cos\delta, \end{bmatrix}, \tag{2.64}$$

where δ is the dip angle and ϕ_f is the strike angle. Likewise, the slip vector d, i.e., the unit vector in the slip direction, can be written as the following system:

$$\boldsymbol{d} = \begin{bmatrix} \cos\lambda\cos\phi_f + \sin\lambda\cos\delta\sin\phi_f \\ -\cos\lambda\sin\phi_f + \sin\lambda\cos\delta\cos\phi_f \\ \sin\lambda\sin\delta, \end{bmatrix}, \tag{2.65}$$

where λ is the slip angle. Accordingly, the components of the seismic moment tensor in an arbitrary coordinate system would be $M_{ij} = M_0(n_i d_j + n_j d_i)$. In other words, the full moment tensor is:

$$\mathbf{M} = M_0 \begin{bmatrix} 2n_x d_x & n_x d_y + n_y d_x & n_x d_z + n_z d_x \\ n_y d_x + n_x d_y & 2n_y d_y & n_y d_z + n_z d_y \\ n_z d_x + n_x d_z & n_z d_y + n_y d_z & 2n_z d_z \end{bmatrix}, \tag{2.66}$$

where n_i and d_i are the components of the normal and slip vectors, respectively, for $i = x, y, z$.

We mentioned earlier that an earthquake, in the simplest form, is a slip upon a flat fault surface. Maruyama (1963) [198] and Burridge and Knopoff (1964) [49] suggested that this slip can be modeled as a double-couple composed of four forces.

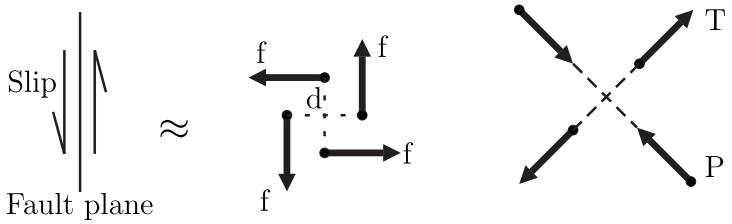

Figure 2.11: double-couples (redrawn from Stein and Wysession [276])

Figure 2.11 shows the relation between an earthquake fault geometry and the double-couple of equivalent forces [276].

Having the moment tensor $\mathbf{M}$, then, we need to convert the tensor to a set of body forces in the numerical model. According to Aki and Richards (2003) [4], the equivalent body force at location $\boldsymbol{\xi}$ is:

$$f_p(\mathbf{x}, t) = -\mathbf{M}_{pq}\frac{\partial}{\partial x_q}\delta(\mathbf{x}-\boldsymbol{\xi}). \tag{2.67}$$

The corresponding weak form as was shown in [21], is:

$$\begin{aligned}
\int_{\Omega^{\mathrm{RD}}} u_p f_p \,\mathrm{d}\Omega &= -\int_{\Omega^{\mathrm{RD}}} u_p \mathbf{M}_{pq}\frac{\partial}{\partial x_q}\delta(\mathbf{x}-\boldsymbol{\xi})\,\mathrm{d}\Omega \\
&= -\frac{1}{2}\int_{\Omega^{\mathrm{RD}}} \left[u_p \mathbf{M}_{qp}\frac{\partial}{\partial x_p}\delta(\mathbf{x}-\boldsymbol{\xi}) + u_p \mathbf{M}_{pq}\frac{\partial}{\partial x_q}\delta(\mathbf{x}-\boldsymbol{\xi})\right]\mathrm{d}\Omega \\
&= -\frac{1}{2}\int_{\Omega^{\mathrm{RD}}} \big[\frac{\partial}{\partial x_p}(u_p \mathbf{M}_{qp}\delta(\mathbf{x}-\boldsymbol{\xi})) - \frac{\partial u_p}{\partial x_p}\mathbf{M}_{qp}\delta(\mathbf{x}-\boldsymbol{\xi}) \\
&\quad + \frac{\partial}{\partial x_q}(u_p \mathbf{M}_{pq}\delta(\mathbf{x}-\boldsymbol{\xi})) - \frac{\partial u_p}{\partial x_q}\mathbf{M}_{pq}\delta(\mathbf{x}-\boldsymbol{\xi})\big]\,\mathrm{d}\Omega \\
&= -\frac{1}{2}\int_{\Gamma^{RD}} u_p \mathbf{M}_{qp}\delta(\mathbf{x}-\boldsymbol{\xi})\mathbf{n}_p dS + \frac{1}{2}\int_{\Omega^{\mathrm{RD}}} \frac{\partial u_p}{\partial x_p}\mathbf{M}_{qp}\delta(\mathbf{x}-\boldsymbol{\xi})\,\mathrm{d}\Omega \\
&\quad - \frac{1}{2}\int_{\Gamma^{RD}} u_p \mathbf{M}_{pq}\delta(\mathbf{x}-\boldsymbol{\xi})\mathbf{n}_q dS + \frac{1}{2}\int_{\Omega^{\mathrm{RD}}} \frac{\partial u_p}{\partial x_q}\mathbf{M}_{pq}\delta(\mathbf{x}-\boldsymbol{\xi})\,\mathrm{d}\Omega,
\end{aligned} \tag{2.68}$$

where u_p denotes the test function. The seismic moment tensor $\mathbf{M}$ is symmetric ($M_{pq} = M_{qp}$), hence, the first and third terms vanish if $\boldsymbol{\xi}$ is an interior point in Ω^{RD}. Finally, (2.68) reduces to:

$$\begin{aligned}\int_{\Omega^{\mathrm{RD}}} u_p f_p \,\mathrm{d}\Omega &= \int_{\Omega^{\mathrm{RD}}} \mathbf{M}_{pq}\delta(\mathbf{x}-\boldsymbol{\xi})\frac{1}{2}\big(\frac{\partial u_p}{\partial x_q}+\frac{\partial u_q}{\partial x_p}\big)\,\mathrm{d}\Omega \\ &= \int_{\Omega^{\mathrm{RD}}} \mathbf{M}_{pq}\delta(\mathbf{x}-\boldsymbol{\xi})\boldsymbol{\epsilon}_{pq}(\mathbf{x})\,\mathrm{d}\Omega \\ &= \mathbf{M}_{pq}\boldsymbol{\epsilon}_{pq}(\boldsymbol{\xi}) \\ &= \boldsymbol{\epsilon}^T\mathbf{M}, \end{aligned} \tag{2.69}$$

where $\boldsymbol{\epsilon}_{pq}$ is the virtual strain tensor associated with the displacement test function. To establish the element force vector $\mathbf{f}^e$ for the element that contains the source, we express the strain function using the defined basis function as (see (2.45a)):

$$\boldsymbol{\epsilon}^T\mathbf{M} = \big(\mathbf{Du}\big)^T\mathbf{M} = \big(\mathbf{D}\boldsymbol{\Phi}^T\mathbf{U}\big)^T\mathbf{M} = \mathbf{U}^T\big(\mathbf{D}\boldsymbol{\Phi}^T\big)^T\mathbf{M}, \tag{2.70}$$

where $\boldsymbol{\Phi}$ is the basis function, $\mathbf{D}$ is the differentiation matrix operator, and $\mathbf{U}$ is test function. Thus, the force becomes $\mathbf{f}^e = \big(\mathbf{D}\boldsymbol{\Phi}^T\big)^T\mathbf{M}$.

2.2.2 Seismic source as a double-couple sequence – fault rupture

To simulate a fault as an extended source, one can use the kinematic slip source model, also known as dynamic rupture model. In this model, slip initiates from the *hypocenter*, and propagates on the active fault plane with the *rupture velocity*, usually considered to be less than the shear velocity [21, 44]. The space-time distribution of the slip, i.e., the kinematic description of the rupture, is not uniform along the fault

plane, which may not be planar. However, to make the fault simulation feasible, most scientists consider a uniform slip in a perfectly planar fault with a constant strike and dip angle (dip is the angle that a planar fault form with the horizontal surface, see Figure 2.10). Note that this assumption, however unrealistic it may be, it is acceptable, since the kinematic description of a fault is, overall, fairly complex. Nonetheless, including the rupture geometry in simulations, as Käser and Gallovič (2008) [155] stated, may affect the seismic response.

According to the representation theorem (See Aki & Richards (2002) [4] and Käser and Gallovič 2008 [155]), for a rupture of surface S, the ith displacement component u_i, measured at location $\boldsymbol{r}$, is:

$$u_i(\boldsymbol{r},t) = \int_S G_{ip,q}(\boldsymbol{r},\boldsymbol{x},t) * \boldsymbol{M}_{pq}(\boldsymbol{x},t)dS, \tag{2.71}$$

where $\boldsymbol{M}_{pq}(\boldsymbol{x},t)$, is the moment tensor defined in the previous section, $G_{ip,q}(\boldsymbol{r},\boldsymbol{x},t)$ is the derivative of the elastodynamic Green's function with respect to x_q, and $*$ denotes the time convolution. The rupture surface can be broken into N_s equally-spaced elements S_n. There results:

$$u_i(\boldsymbol{r},t) = \sum_{n=1}^{N_s} \int_{S_n} G_{ip,q}(\boldsymbol{r},\boldsymbol{x},t) * \boldsymbol{M}_{pq}(\boldsymbol{x},t)dS. \tag{2.72}$$

We choose the rupture elements small enough such that the derivative of the Green's function remains constant. Hence, the displacement component can be

computed via:

$$u_i(\boldsymbol{r},t) \approx \sum_{n=1}^{N_s} G_{ip,q}(\boldsymbol{r},\boldsymbol{x}'_n,t) * \int_{S_n} \boldsymbol{M}_{pq}(\boldsymbol{x},t)dS$$
$$= \sum_{n=1}^{N_s} G_{ip,q}(\boldsymbol{r},\boldsymbol{x}'_n,t) * \boldsymbol{M}^n_{pq}(t), \tag{2.73}$$

where $\boldsymbol{x}'_n$ is the center of the nth rupture element. Since the rupture is assumed to be planar, the integral can be substituted by $M^n_{pq}(t)$.

To implement this latest formulation in the finite element model, first we need to locate the fault plane and identify all the elements that fall into the fault plane [21]. Next, we allocate the seismic moment for each element M^i_0, as follows:

$$M^i_0 = \mu_i D A_i, \tag{2.74}$$

where A_i is the intersected area of each element with the fault plane, μ_i is the shear modulus of element i, and D is the uniform slip. The total amount of seismic moment for the fault is the combination of all moments on each element:

$$M_0 = \sum_{n=1}^{N_s} \mu_i A_i D_i. \tag{2.75}$$

In summary, in order to numerically simulate a seismic scenario, we start by applying the seismic loads using the double-couple technique to the element where the hypocenter is located and then we activate the rupture elements alongside the fault plane with a time delay, calculated based on the rupture velocity. This, indeed, requires that the kinematic description of the fault is known.

2.2.3 Seismic source –indirect implementation

One primary interest in this project is the parametric investigation which, in turn, requires accommodation of incoming plane waves at various angles of incidence and frequencies, thus, simulating an earthquake originating from the far depth. To this end, we turn to the Domain Reduction Method (DRM) developed by Bielak et al. [33, 37, 70, 296]. The Domain Reduction Method is a two-step technique with a goal of reducing the computational cost by bringing the effects of seismic source closer to the domain of interest. In the first step, ground motion derives from a background model that consists of the source in the absence of the local geological features of the region of interest. In the second step, the ground motion derived in the first step is used to evaluate a set of localized equivalent earthquake forces applied as input in a computational domain that includes all the local features that were deleted form the first step domain. First, we briefly explain the DRM method, and then, we modify the formulation to couple it with the PML absorbing boundary conditions in two and three dimensions.

2.2.3.1 The Domain Reduction Method (DRM)

Figure 2.12(a) shows a semi-infinite domain with stratification and arbitrary geological features. The spatial discretization of the governing equations of motion, in either two or three dimensions, in the absence of the PML, is:

$$\mathbf{M}\ddot{\mathbf{d}} + \mathbf{C}\dot{\mathbf{d}} + \mathbf{K}\mathbf{d} = \mathbf{f}, \tag{2.76}$$

where $\mathbf{M}$, $\mathbf{C}$, and $\mathbf{K}$ are the mass, damping, and stiffness matrices, respectively, and $\mathbf{d}$ and $\mathbf{f}$ denote the displacement and load vectors, respectively. To eliminate the

necessity of including the source in the computational domain, we divide the domain using a fictitious surface Γ into two regions: (i) the domain of interest Ω, that contains all the features that are of interest; and (ii) the exterior domain Ω^+, which is a semi-infinite domain containing the seismic source, as shown in Figure 2.12(b).

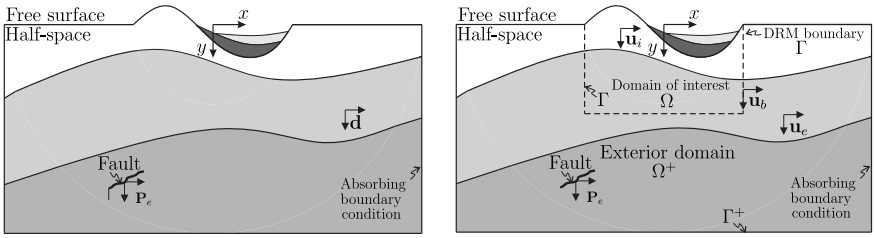

Figure 2.12: Domain Reduction Method configuration: (a) the original configuration of the semi-infinite domain, (b) the segregation of the domain of interest from the half-space (adapted from Bielak et al. [37])

Next, we partition (2.76) based on this division:

$$\begin{bmatrix} \mathbf{M}_{ii}^{\Omega} & \mathbf{M}_{ib}^{\Omega} & \mathbf{0} \\ \mathbf{M}_{bi}^{\Omega} & \mathbf{M}_{bb} & \mathbf{M}_{be}^{\Omega^+} \\ \mathbf{0} & \mathbf{M}_{eb}^{\Omega^+} & \mathbf{M}_{ee}^{\Omega^+} \end{bmatrix} \begin{bmatrix} \ddot{\mathbf{u}}_i \\ \ddot{\mathbf{u}}_b \\ \ddot{\mathbf{u}}_e \end{bmatrix} + \begin{bmatrix} \mathbf{C}_{ii}^{\Omega} & \mathbf{C}_{ib}^{\Omega} & \mathbf{0} \\ \mathbf{C}_{bi}^{\Omega} & \mathbf{C}_{bb} & \mathbf{C}_{be}^{\Omega^+} \\ \mathbf{0} & \mathbf{C}_{eb}^{\Omega^+} & \mathbf{C}_{ee}^{\Omega^+} \end{bmatrix} \begin{bmatrix} \dot{\mathbf{u}}_i \\ \dot{\mathbf{u}}_b \\ \dot{\mathbf{u}}_e \end{bmatrix} + \begin{bmatrix} \mathbf{K}_{ii}^{\Omega} & \mathbf{K}_{ib}^{\Omega} & \mathbf{0} \\ \mathbf{K}_{bi}^{\Omega} & \mathbf{K}_{bb} & \mathbf{K}_{be}^{\Omega^+} \\ \mathbf{0} & \mathbf{K}_{eb}^{\Omega^+} & \mathbf{K}_{ee}^{\Omega^+} \end{bmatrix} \begin{bmatrix} \mathbf{u}_i \\ \mathbf{u}_b \\ \mathbf{u}_e \end{bmatrix} = \begin{bmatrix} \mathbf{0} \\ \mathbf{0} \\ \mathbf{P}_e \end{bmatrix}, \tag{2.77}$$

where subscripts i, b, and e refer to the nodes in the domain of interest, on the fictitious surface Γ, and in the exterior domain, respectively. $\mathbf{P}_e$ is a vector containing the seismic loads from the fault and $\mathbf{u}$ is the solution/displacement. Note that the matrices on the fictitious interior boundary Γ, henceforth referred to as the DRM

boundary, receive contributions from both the interior and exterior domains:

$$\mathbf{M}_{bb} = \mathbf{M}_{bb}^{\Omega} + \mathbf{M}_{bb}^{\Omega^+}, \tag{2.78a}$$

$$\mathbf{C}_{bb} = \mathbf{C}_{bb}^{\Omega} + \mathbf{C}_{bb}^{\Omega^+}, \tag{2.78b}$$

$$\mathbf{K}_{bb} = \mathbf{K}_{bb}^{\Omega} + \mathbf{K}_{bb}^{\Omega^+}. \tag{2.78c}$$

We replace the domain of interest Ω with a simpler domain Ω_0, displayed in Figure 2.13, to have an *auxiliary model* where the exterior domain is exactly the same as the original model, however, the domain of interest is substituted with a modified domain Ω_0 which does not have any local features (flat surface) but follows the material properties of the exterior domain at the DRM boundary Γ.

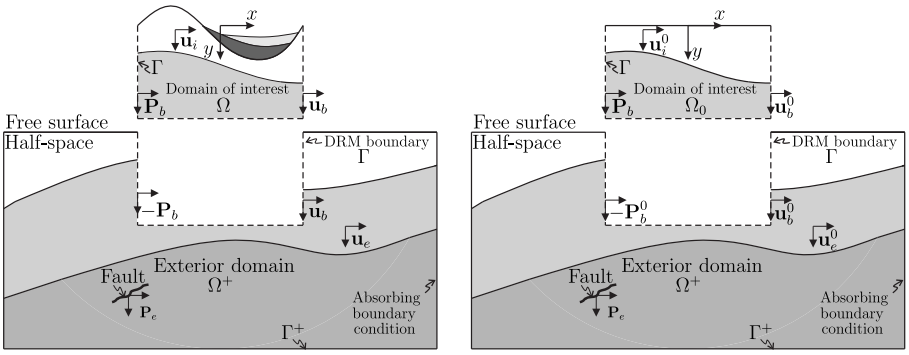

Figure 2.13: Auxiliary model: (a) segregation of the domain of interest from the half-space, (b) substituting the domain of interest with a simpler background (adapted from Bielak et al. [37])

Let us call the solution to the auxiliary model the free-field solution $\mathbf{u}^0$ to distinguish it from the solution to the original problem $\mathbf{u}$. Then, the partitioned

equation of motion for the auxiliary model as depicted in Figure 2.14 is:

$$\begin{bmatrix} \mathbf{M}_{ii}^{\Omega^0} & \mathbf{M}_{ib}^{\Omega^0} & \mathbf{0} \\ \mathbf{M}_{bi}^{\Omega^0} & \mathbf{M}_{bb} & \mathbf{M}_{be}^{\Omega^+} \\ \mathbf{0} & \mathbf{M}_{eb}^{\Omega^+} & \mathbf{M}_{ee}^{\Omega^+} \end{bmatrix} \begin{bmatrix} \ddot{\mathbf{u}}_i^0 \\ \ddot{\mathbf{u}}_b^0 \\ \ddot{\mathbf{u}}_e^0 \end{bmatrix} + \begin{bmatrix} \mathbf{C}_{ii}^{\Omega^0} & \mathbf{C}_{ib}^{\Omega^0} & \mathbf{0} \\ \mathbf{C}_{bi}^{\Omega^0} & \mathbf{C}_{bb} & \mathbf{C}_{be}^{\Omega^+} \\ \mathbf{0} & \mathbf{C}_{eb}^{\Omega^+} & \mathbf{C}_{ee}^{\Omega^+} \end{bmatrix} \begin{bmatrix} \dot{\mathbf{u}}_i^0 \\ \dot{\mathbf{u}}_b^0 \\ \dot{\mathbf{u}}_e^0 \end{bmatrix} + \begin{bmatrix} \mathbf{K}_{ii}^{\Omega^0} & \mathbf{K}_{ib}^{\Omega^0} & \mathbf{0} \\ \mathbf{K}_{bi}^{\Omega^0} & \mathbf{K}_{bb} & \mathbf{K}_{be}^{\Omega^+} \\ \mathbf{0} & \mathbf{K}_{eb}^{\Omega^+} & \mathbf{K}_{ee}^{\Omega^+} \end{bmatrix} \begin{bmatrix} \mathbf{u}_i^0 \\ \mathbf{u}_b^0 \\ \mathbf{u}_e^0 \end{bmatrix} = \begin{bmatrix} \mathbf{0} \\ \mathbf{0} \\ \mathbf{P}_e \end{bmatrix}. \tag{2.79}$$

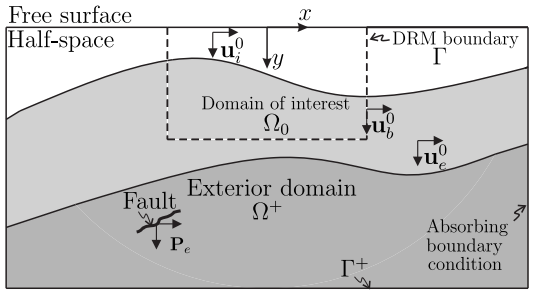

Figure 2.14: Auxiliary model (adapted from Bielak et al. [37])

From the last equation in (2.79), it can be seen that the seismic input $\mathbf{P}_e$ can be expressed in terms of the free-field solution $\mathbf{u}_e^0$ in the exterior domain as:

$$\mathbf{P}_e = \mathbf{M}_{eb}^{\Omega^+} \ddot{\mathbf{u}}_b^0 + \mathbf{M}_{ee}^{\Omega^+} \ddot{\mathbf{u}}_e^0 + \mathbf{C}_{eb}^{\Omega^+} \dot{\mathbf{u}}_b^0 + \mathbf{C}_{ee}^{\Omega^+} \dot{\mathbf{u}}_e^0 + \mathbf{K}_{eb}^{\Omega^+} \mathbf{u}_b^0 + \mathbf{K}_{ee}^{\Omega^+} \mathbf{u}_e^0. \tag{2.80}$$

This equation implies that the seismic load can be substituted by the displacement field in the exterior domain of the auxiliary model at each time-step. Clearly, this is only possible if we store the free-field solution in the entire exterior domain $\mathbf{u}_e^0$ for each time-step. However, due to the size of the exterior domain, this method is inefficient and requires substantial memory storage. To avoid this issue, we decompose the total displacement in the exterior domain of the original model $\mathbf{u}_e$ (Figure 2.12(b)) into the sum of the free-field displacement from the auxiliary model $\mathbf{u}_e^0$ and the residual

field $\mathbf{w}_e$ due to scattering at the localized features in the domain of interest:

$$\mathbf{u}_e = \mathbf{u}_e^0 + \mathbf{w}_e. \tag{2.81}$$

Bearing in mind (2.78), we introduce (2.81) to the last row of (2.77) and move the free-field solution terms to the right side of the equation, to obtain:

$$\begin{aligned} &\begin{bmatrix} \mathbf{M}_{ii}^{\Omega} & \mathbf{M}_{ib}^{\Omega} & \mathbf{0} \\ \mathbf{M}_{bi}^{\Omega} & \mathbf{M}_{bb}^{\Omega} + \mathbf{M}_{bb}^{\Omega^+} & \mathbf{M}_{be}^{\Omega^+} \\ \mathbf{0} & \mathbf{M}_{eb}^{\Omega^+} & \mathbf{M}_{ee}^{\Omega^+} \end{bmatrix} \begin{bmatrix} \ddot{\mathbf{u}}_i \\ \ddot{\mathbf{u}}_b \\ \ddot{\mathbf{w}}_e \end{bmatrix} + \begin{bmatrix} \mathbf{C}_{ii}^{\Omega} & \mathbf{C}_{ib}^{\Omega} & \mathbf{0} \\ \mathbf{C}_{bi}^{\Omega} & \mathbf{C}_{bb}^{\Omega} + \mathbf{C}_{bb}^{\Omega^+} & \mathbf{C}_{be}^{\Omega^+} \\ \mathbf{0} & \mathbf{M}_{eb}^{\Omega^+} & \mathbf{M}_{ee}^{\Omega^+} \end{bmatrix} \begin{bmatrix} \dot{\mathbf{u}}_i \\ \dot{\mathbf{u}}_b \\ \dot{\mathbf{w}}_e \end{bmatrix} \\ &+ \begin{bmatrix} \mathbf{K}_{ii}^{\Omega} & \mathbf{K}_{ib}^{\Omega} & \mathbf{0} \\ \mathbf{K}_{bi}^{\Omega} & \mathbf{K}_{bb}^{\Omega} + \mathbf{K}_{bb}^{\Omega^+} & \mathbf{K}_{be}^{\Omega^+} \\ \mathbf{0} & \mathbf{K}_{eb}^{\Omega^+} & \mathbf{K}_{ee}^{\Omega^+} \end{bmatrix} \begin{bmatrix} \mathbf{u}_i \\ \mathbf{u}_b \\ \mathbf{w}_e \end{bmatrix} = \begin{bmatrix} \mathbf{0} \\ -\mathbf{M}_{be}^{\Omega^+} \ddot{\mathbf{u}}_e^0 - \mathbf{C}_{be}^{\Omega^+} \dot{\mathbf{u}}_e^0 - \mathbf{K}_{be}^{\Omega^+} \mathbf{u}_e^0 \\ \mathbf{P}_e - \mathbf{M}_{ee}^{\Omega^+} \ddot{\mathbf{u}}_e^0 - \mathbf{C}_{ee}^{\Omega^+} \dot{\mathbf{u}}_e^0 - \mathbf{K}_{ee}^{\Omega^+} \mathbf{u}_e^0 \end{bmatrix}. \end{aligned} \tag{2.82}$$

We already derived an equivalent expression for the seismic load in (2.80) based on the free-field solution. Using this equivalent load in (2.82), results in:

$$\begin{aligned} &\begin{bmatrix} \mathbf{M}_{ii}^{\Omega} & \mathbf{M}_{ib}^{\Omega} & \mathbf{0} \\ \mathbf{M}_{bi}^{\Omega} & \mathbf{M}_{bb}^{\Omega} + \mathbf{M}_{bb}^{\Omega^+} & \mathbf{M}_{be}^{\Omega^+} \\ \mathbf{0} & \mathbf{M}_{eb}^{\Omega^+} & \mathbf{M}_{ee}^{\Omega^+} \end{bmatrix} \begin{bmatrix} \ddot{\mathbf{u}}_i \\ \ddot{\mathbf{u}}_b \\ \ddot{\mathbf{w}}_e \end{bmatrix} + \begin{bmatrix} \mathbf{C}_{ii}^{\Omega} & \mathbf{C}_{ib}^{\Omega} & \mathbf{0} \\ \mathbf{C}_{bi}^{\Omega} & \mathbf{C}_{bb}^{\Omega} + \mathbf{C}_{bb}^{\Omega^+} & \mathbf{C}_{be}^{\Omega^+} \\ \mathbf{0} & \mathbf{M}_{eb}^{\Omega^+} & \mathbf{M}_{ee}^{\Omega^+} \end{bmatrix} \begin{bmatrix} \dot{\mathbf{u}}_i \\ \dot{\mathbf{u}}_b \\ \dot{\mathbf{w}}_e \end{bmatrix} \\ &+ \begin{bmatrix} \mathbf{K}_{ii}^{\Omega} & \mathbf{K}_{ib}^{\Omega} & \mathbf{0} \\ \mathbf{K}_{bi}^{\Omega} & \mathbf{K}_{bb}^{\Omega} + \mathbf{K}_{bb}^{\Omega^+} & \mathbf{K}_{be}^{\Omega^+} \\ \mathbf{0} & \mathbf{K}_{eb}^{\Omega^+} & \mathbf{K}_{ee}^{\Omega^+} \end{bmatrix} \begin{bmatrix} \mathbf{u}_i \\ \mathbf{u}_b \\ \mathbf{w}_e \end{bmatrix} = \begin{bmatrix} \mathbf{0} \\ -\mathbf{M}_{be}^{\Omega^+} \ddot{\mathbf{u}}_e^0 - \mathbf{C}_{be}^{\Omega^+} \dot{\mathbf{u}}_e^0 - \mathbf{K}_{be}^{\Omega^+} \mathbf{u}_e^0 \\ +\mathbf{M}_{eb}^{\Omega^+} \ddot{\mathbf{u}}_b^0 + \mathbf{C}_{eb}^{\Omega^+} \dot{\mathbf{u}}_b^0 + \mathbf{K}_{eb}^{\Omega^+} \mathbf{u}_b^0 \end{bmatrix}. \end{aligned} \tag{2.83}$$

The last equation differs from (2.77) in the terms involved in the vector of the unknown. Specifically, the vector of total displacements in the exterior domain $\mathbf{u}_e$ has been replaced by the scattered motion vector $\mathbf{w}_e$. More importantly, the seismic load in the load vector has been replaced by effective nodal forces implicating only the free-field solution of the auxiliary model. The new load vector is superior to (2.80) because the free-field solution and its derivatives in the exterior domain are multiplied by $\mathbf{M}_{be}^{\Omega^+}$, $\mathbf{C}_{be}^{\Omega^+}$, and $\mathbf{K}_{be}^{\Omega^+}$, which are the contribution of the exterior domain in the

mass, damping, and stiffness matrices at the DRM boundary Γ. In other words, to introduce the effect of the seismic load, we only need to store the free-field solution in the auxiliary model on a single layer of elements in a finite element model, e.g. between Γ and an adjacent surface Γ_e, per Figure 2.15(b).

$$\mathbf{P}^{\mathit{eff}} = \begin{bmatrix} \mathbf{P}_i^{\mathit{eff}} \\ \mathbf{P}_b^{\mathit{eff}} \\ \mathbf{P}_e^{\mathit{eff}} \end{bmatrix} = \begin{bmatrix} \mathbf{0} \\ -\mathbf{M}_{be}^{\Omega^+}\ddot{\mathbf{u}}_e^0 - \mathbf{C}_{be}^{\Omega^+}\dot{\mathbf{u}}_e^0 - \mathbf{K}_{be}^{\Omega^+}\mathbf{u}_e^0 \\ +\mathbf{M}_{eb}^{\Omega^+}\ddot{\mathbf{u}}_b^0 + \mathbf{C}_{eb}^{\Omega^+}\dot{\mathbf{u}}_b^0 + \mathbf{K}_{eb}^{\Omega^+}\mathbf{u}_b^0 \end{bmatrix}. \tag{2.84}$$

In summary, the DRM proposes a two-step approach for incorporating the effects of the seismic source. In a first step, the free-field solution is obtained for a seismic source, e.g., a traveling plane wave, by subtracting the local heterogeneities or geometric irregularities of the region of interest, as depicted in Figure 2.15(a). In the second step as shown in Figure 2.15(b), the heterogeneities and/or topographic features are re-introduced and the equations of motion are appropriately modified to account for the incoming motion. The latter is accomplished by the introduction of the DRM boundaries -a one-element wide layer- separating the topographic feature, where the unknowns are the total displacements, and, secondly, the region between the DRM and the absorbing boundary, where the unknown is the scattered motion. It is on the DRM boundary that the incoming motion is prescribed.

We remark that when the free-field solution in the first step is readily available from analytical techniques, the method reduces to the second step only. Additionally, since we do not need to include the source in the second step, we can reduce the exterior domain Ω^+ as displayed in Figure 2.15(c) so that it only contains the DRM boundary. This is the reason this technique is called the Domain Reduction Method. In this study, we only consider the propagation of plane waves within a

homogeneous half-space, where the closed-form solution exists and will be presented in the verification chapter.

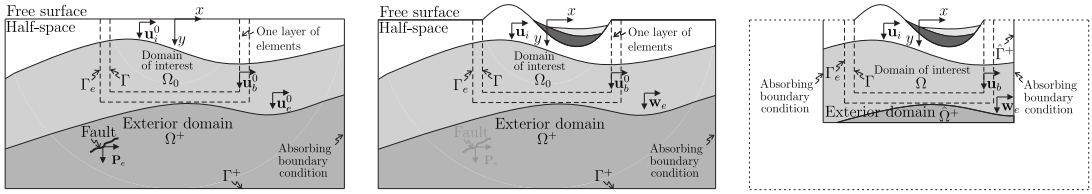

(a) (b) (c)

Figure 2.15: Steps of the Domain Reduction Method (a) step I: computational domain with a simpler background, (b) eliminating the seismic source, (c) step II: the reduced domain (adapted from Bielak et al. [37])

2.2.3.2 DRM-PML coupling in the time-domain

In deriving the DRM formulation, we assumed that the absorbing boundary conditions are already assigned to the global matrices. However, to accommodate the PML absorbing boundary, we need to modify the DRM equations for the second step of the method in (2.83). Figure 2.16 shows a schematic configuration of the second step of the DRM including the PML buffer zone.

Accordingly, the final equation of the DRM for a two-dimensional model is:

$$\tilde{\mathbf{M}}\ddot{\tilde{\mathbf{d}}} + \tilde{\mathbf{C}}\dot{\tilde{\mathbf{d}}} + \tilde{\mathbf{K}}\tilde{\mathbf{d}} = \tilde{\mathbf{f}}, \tag{2.85}$$

whereas for the three-dimensional model is:

$$\tilde{\mathbf{M}}\dddot{\tilde{\mathbf{d}}} + \tilde{\mathbf{C}}\ddot{\tilde{\mathbf{d}}} + \tilde{\mathbf{K}}\dot{\tilde{\mathbf{d}}} + \tilde{\mathbf{G}}\tilde{\mathbf{d}} = \dot{\tilde{\mathbf{f}}}, \tag{2.86}$$

where spatial and temporal dependencies are suppressed for brevity. The system

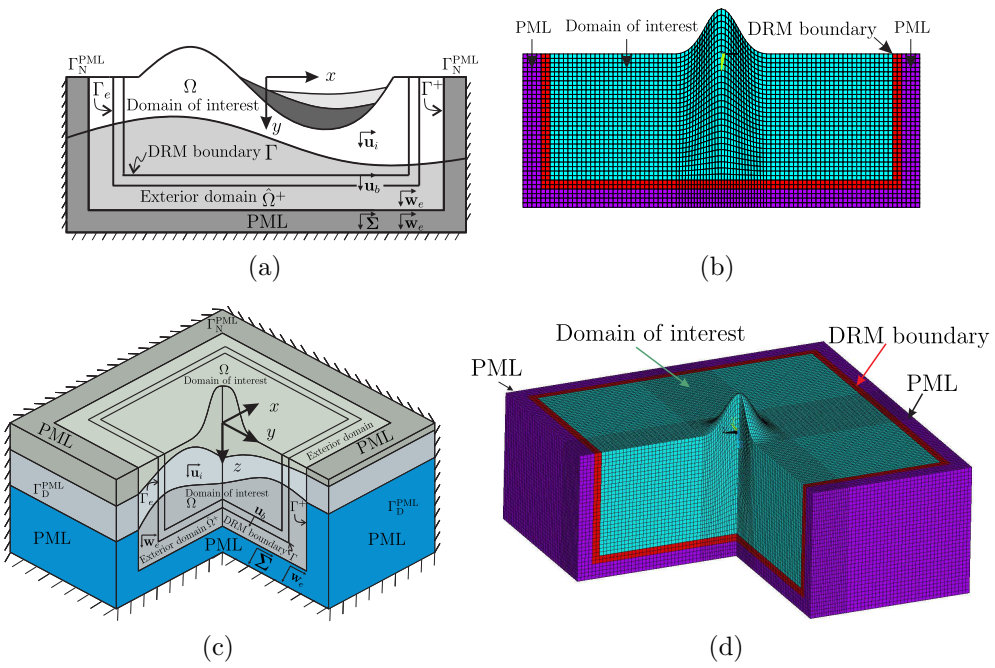

Figure 2.16: Schematic half-space (a) a typical 2D computational domain in the second step of the DRM technique with PML, (b) 2D half-space discretization, (c) 3D computational domain, and (d) 3D discretization

matrices, $\tilde{\mathbf{M}}$, $\tilde{\mathbf{C}}$, $\tilde{\mathbf{K}}$, and $\tilde{\mathbf{G}}$, and vectors $\tilde{\mathbf{d}}$ and $\tilde{\mathbf{f}}$, are defined as:

$$\tilde{\mathbf{M}} = \begin{bmatrix} \mathbf{M}_{ii}^{\Omega} & \mathbf{M}_{ib}^{\Omega} & \mathbf{0} & \mathbf{0} \\ \mathbf{M}_{bi}^{\Omega} & \mathbf{M}_{bb}^{\Omega} + \mathbf{M}_{bb}^{\Omega^+} & \bar{\mathbf{M}}_{be}^{\Omega^+} & \mathbf{0} \\ \mathbf{0} & \bar{\mathbf{M}}_{eb}^{\Omega^+} & \bar{\mathbf{M}}_{ee}^{\Omega^+} + \bar{\mathbf{M}}_a & \mathbf{0} \\ \mathbf{0} & \mathbf{0} & \mathbf{0} & \mathbf{N}_a \end{bmatrix}, \quad \tilde{\mathbf{C}} = \begin{bmatrix} \mathbf{0} & \mathbf{0} & \mathbf{0} & \mathbf{0} \\ \mathbf{0} & \mathbf{0} & \mathbf{0} & \mathbf{0} \\ \mathbf{0} & \mathbf{0} & \bar{\mathbf{M}}_b & \bar{\mathbf{A}}_{eu} \\ \mathbf{0} & \mathbf{0} & -\bar{\mathbf{A}}_{el}^T & \mathbf{N}_b \end{bmatrix},$$

$$\tilde{\mathbf{K}} = \begin{bmatrix} \mathbf{K}_{ii}^{\Omega} & \mathbf{K}_{ib}^{\Omega} & \mathbf{0} & \mathbf{0} \\ \mathbf{K}_{bi}^{\Omega} & \mathbf{K}_{bb}^{\Omega} + \mathbf{K}_{bb}^{\Omega^+} & \bar{\mathbf{K}}_{be}^{\Omega^+} & \mathbf{0} \\ \mathbf{0} & \bar{\mathbf{K}}_{eb}^{\Omega^+} & \bar{\mathbf{K}}_{ee}^{\Omega^+} + \bar{\mathbf{M}}_c & \bar{\mathbf{A}}_{pu} \\ \mathbf{0} & \mathbf{0} & -\bar{\mathbf{A}}_{pl}^T & \mathbf{N}_c \end{bmatrix}, \quad \tilde{\mathbf{G}} = \begin{bmatrix} \mathbf{0} & \mathbf{0} & \mathbf{0} & \mathbf{0} \\ \mathbf{0} & \mathbf{0} & \mathbf{0} & \mathbf{0} \\ \mathbf{0} & \mathbf{0} & \bar{\mathbf{M}}_d & \bar{\mathbf{A}}_{wu} \\ \mathbf{0} & \mathbf{0} & -\bar{\mathbf{A}}_{wl}^T & \mathbf{N}_d \end{bmatrix},$$

$$\tilde{\mathbf{f}} = \begin{bmatrix} \mathbf{0} \\ -\mathbf{M}_{be}^{\Omega^+}\ddot{\mathbf{u}}_e^0 - \mathbf{C}_{be}^{\Omega^+}\dot{\mathbf{u}}_e^0 - \mathbf{K}_{be}^{\Omega^+}\mathbf{u}_e^0 \\ +\mathbf{M}_{eb}^{\Omega^+}\ddot{\mathbf{u}}_b^0 + \mathbf{C}_{eb}^{\Omega^+}\dot{\mathbf{u}}_b^0 + \mathbf{K}_{eb}^{\Omega^+}\mathbf{u}_b^0 \\ \mathbf{0} \end{bmatrix}, \quad \tilde{\mathbf{d}} = \begin{bmatrix} \mathbf{u}_i \\ \mathbf{u}_b \\ \mathbf{w}_e \\ \boldsymbol{\Sigma} \end{bmatrix}. \tag{2.87}$$

The block matrices are identical to the ones defined in Appendix A.

2.2.3.3 DRM-PML coupling in the frequency-domain

Taking the Fourier transform of (2.85), the DRM formulation for the second step of the method in the frequency-domain, including the PML absorbing boundary, reads:

$$(-\omega^2\tilde{\mathbf{M}} + i\omega\tilde{\mathbf{C}} + \tilde{\mathbf{K}})\tilde{\mathbf{d}} = \tilde{\mathbf{f}}, \tag{2.88}$$

and for the three-dimensional domain:

$$(-i\omega^3\tilde{\mathbf{M}} - \omega^2\tilde{\mathbf{C}} + i\omega\tilde{\mathbf{K}} + \tilde{\mathbf{G}})\tilde{\mathbf{d}} = i\omega\tilde{\mathbf{f}}, \tag{2.89}$$

The definition of matrices in this equation are given in (2.87).

2.3 Numerical solvers

In this section, we discuss the numerical schemes that we used to solve the governing differential equations in time. These include: the implicit Newmark solver, the explicit Runge-Kutta method, and the Runge-Kutta-Fehlberg adaptive solver for the time-domain analyses.

Implicit transient analysis, where possible, is superior to explicit solvers because it has no inherent limit on the size of the time-step, whereas by contrast, the time-step in an explicit analysis must be less than the Courant limit, in order to have a numerically stable solution. As such, implicit time-steps are often larger than the explicit time-steps. On the other hand, explicit solvers are preferred in parallel implementations due to computational cost considerations, and could be quite efficient especially if one can improve/increase the time-step size. Therefore, we use the

implicit solver in this study mainly for verification purposes, while we reserve the explicit schemes for large three-dimensional simulations.

2.3.1 Time-domain implicit solver

We utilize the Newmark implicit time-integration scheme to march in time with the assumption that the system is initially at rest. The details of the method are described in the following sections for two- and three-dimensional systems.

2.3.1.1 Time integration for 2D problems

To discretize the two-dimensional equation in (2.26) (or similarly (2.85)) in time, we consider the following formulas to estimate displacement and velocity:

$$\mathbf{d}_{n+1} = \mathbf{d}_n + \Delta t \dot{\mathbf{d}} + \Delta t^2 [(\frac{1}{2} - \beta)\ddot{\mathbf{d}}_n + \beta \ddot{\mathbf{d}}_{n+1}], \tag{2.90a}$$

$$\dot{\mathbf{d}}_{n+1} = \dot{\mathbf{d}}_n + \Delta t [(1 - \gamma)\ddot{\mathbf{d}}_n + \gamma \ddot{\mathbf{d}}_{n+1}], \tag{2.90b}$$

where Δt denotes the time-step, and subscripts (n) and $(n+1)$ denote current and next time-steps, respectively. α and β are Newmark's parameters. In this study, we use the constant acceleration method, which requires that $(\beta, \gamma) = (\frac{1}{4}, \frac{1}{2})$. Introducing (2.90) to (2.26) written at $(n+1)$-th step, leads to:

$$\mathbf{K}^{\mathit{eff}} \ddot{\mathbf{d}}_{n+1} = \mathbf{f}^{\mathit{eff}}_{n+1}, \tag{2.91}$$

where $\mathbf{K}^{\mathit{eff}}$ and $\mathbf{f}_{n+1}^{\mathit{eff}}$ are effective stiffness matrix and effective force vector, respectively, defined as follows:

$$\mathbf{K}^{\mathit{eff}} = \mathbf{M} + \gamma\Delta t\mathbf{C} + \beta\Delta t^2\mathbf{K}, \tag{2.92a}$$

$$\begin{aligned}\mathbf{f}_{n+1}^{\mathit{eff}} &= \mathbf{f}_{n+1} - \mathbf{C}[\dot{\mathbf{d}}_n + (1-\gamma)\Delta t\ddot{\mathbf{d}}_n] \\ &\quad - \mathbf{K}[\mathbf{d}_n + \Delta t\dot{\mathbf{d}}_n + (\frac{1}{2} - \beta)\Delta t^2\ddot{\mathbf{d}}_n].\end{aligned} \tag{2.92b}$$

Equation (2.91) allows for the computation of the second-order terms at every $(n+1)$ step. Lower-order terms for the same time-step are then recoverable via (2.90) (see Algorithm 1).

2.3.1.2 Time integration for 3D problems

In this section, we are concerned with the time-integration of the following semi-discrete equation discussed in Section 2.1.3:

$$\mathbf{M}\ddot{\mathbf{d}} + \mathbf{C}\dot{\mathbf{d}} + \mathbf{K}\mathbf{d} + \mathbf{G}\bar{\mathbf{d}} = \mathbf{f}, \tag{2.49a revisited}$$

$$\bar{\mathbf{d}} = \int_0^t \mathbf{d}(\tau)|_{\mathrm{PML}}\, d\tau. \tag{2.49b revisited}$$

We discuss an extension of the Newmark method [178] for the time-integration of this equation. The scheme is implicit, and can be applied to problems with either symmetric or unsymmetric matrices. We start with Taylor series-like expansion of the following quantities:

$$\bar{\mathbf{d}}^{n+1} = \bar{\mathbf{d}}^n + \Delta t\ \mathbf{d}^n + \frac{\Delta t^2}{2}\dot{\mathbf{d}}^n + (\frac{1}{6} - \alpha)\Delta t^3\ \ddot{\mathbf{d}}^n + \alpha\ \Delta t^3\ \ddot{\mathbf{d}}^{n+1}, \tag{2.93a}$$

$$\mathbf{d}^{n+1} = \mathbf{d}^n + \Delta t\ \dot{\mathbf{d}}^n + (\frac{1}{2} - \beta)\Delta t^2\ \ddot{\mathbf{d}}^n + \beta\ \Delta t^2\ \ddot{\mathbf{d}}^{n+1}, \tag{2.93b}$$

$$\dot{\mathbf{d}}^{n+1} = \dot{\mathbf{d}}^n + (1-\gamma)\Delta t\ \ddot{\mathbf{d}}^n + \gamma\ \Delta t\ \ddot{\mathbf{d}}^{n+1}, \tag{2.93c}$$

where Δt denotes the time-step, superscripts (n) and $(n+1)$ indicate current and next time-steps, β and γ are the classic Newmark parameters, and α is a new parameter. Substitution of (2.93) in (2.92) at the $(n+1)$-th time-step, results in the following linear system of equations:

$$\hat{\mathbf{K}}\ \ddot{\mathbf{d}}^{n+1} = \hat{\mathbf{R}}^{n+1}, \tag{2.94a}$$

where

$$\hat{\mathbf{K}} = \mathbf{M} + \gamma\ \Delta t\ \mathbf{C} + \beta\ \Delta t^2\ \mathbf{K} + \alpha\ \Delta t^3\ \mathbf{G}, \tag{2.94b}$$

$$\begin{aligned}\hat{\mathbf{R}}^{n+1} = \mathbf{f}^{n+1} & \\ - \mathbf{C}\left[\dot{\mathbf{d}}^n + (1-\gamma)\ \Delta t\ \ddot{\mathbf{d}}^n\right] & \\ - \mathbf{K}\left[\mathbf{d}^n + \Delta t\ \dot{\mathbf{d}}^n + (\frac{1}{2} - \beta)\ \Delta t^2\ \ddot{\mathbf{d}}^n\right] & \\ - \mathbf{G}\left[\bar{\mathbf{d}}^n + \Delta t\ \mathbf{d}^n + \frac{\Delta t^2}{2}\mathbf{d}^n + (\frac{1}{6} - \alpha)\ \Delta t^3\ \ddot{\mathbf{d}}^n\right]. & \end{aligned} \tag{2.94c}$$

Upon solving for $\ddot{\mathbf{d}}^{n+1}$ from (2.94a), $\bar{\mathbf{d}}^{n+1}$, $\mathbf{d}^{n+1}$, and $\dot{\mathbf{d}}^{n+1}$ can be updated using (2.93). Average-, and linear-acceleration schemes correspond to taking (α, β, γ) equal to $(\frac{1}{12}, \frac{1}{4}, \frac{1}{2})$, and $(\frac{1}{24}, \frac{1}{6}, \frac{1}{2})$, respectively. The corresponding procedure is depicted in Algorithm 2.

2.3.2 Time-domain explicit solver

To solve the Cauchy problem of the following form:

$$\begin{cases} \dot{y}(t) &= f(t, y(t)), \qquad t \in I, \\ y(t_0) &= y_0, \end{cases} \tag{2.95}$$

we use a one-step Runge-Kutta method, which, in its most general form, can be written as:

$$u_{n+1} = u_n + \Delta t F(t_n, u_n, \Delta t; f), \qquad n \geq 0, \tag{2.96}$$

and the increment function F is:

$$F(t_n, u_n, \Delta t; f) = \sum_{i=1}^{s} b_i k_i, \tag{2.97a}$$

$$k_i = f(t_n + c_i \Delta t, u_n + \Delta t \sum_{j=1}^{s} a_{ij} k_j), \qquad i = 1, 2, \ldots, s. \tag{2.97b}$$

In these equations, u_n is the numerical approximation of the solution $y(t)$ at the time-step t_n, Δt is the step size, s determines the number of stages of the Runge-Kutta method, a_{ij}, b_i, and c_i are the coefficients that characterize the Runge-Kutta method. For more detailed information about Runge-Kutta method see [31, 46, 48, 134, 242].

To be able to use this solver, we need to first convert the second-order-in-time two-dimensional semi-discrete equation or the third-order-in-time three-dimensional semi-discrete equation to a first-order system. Once, we have the first-order system, we accommodate our formulations based on the Runge-Kutta method. Here, we favor three Runge-Kutta schemes that are discussed in the subsequent sections.

2.3.2.1 First-order system

The semi-discrete, second-order equation in (2.26), including the PML absorbing boundary condition (or similarly (2.85) that includes both DRM and PML), can be expressed as a first-order in time system, via the introduction of auxiliary variables.

$$\mathbf{M}\ddot{\mathbf{d}} + \mathbf{C}\dot{\mathbf{d}} + \mathbf{K}\mathbf{d} = \mathbf{f}. \tag{2.26 revisited}$$

Multiplying both sides by $\mathbf{M}^{-1}$, and rearranging the equation, yields:

$$\ddot{\mathbf{d}} = -\mathbf{M}^{-1}\mathbf{C}\dot{\mathbf{d}} - \mathbf{M}^{-1}\mathbf{K}\mathbf{d} + \mathbf{M}^{-1}\mathbf{f}. \tag{2.98}$$

We define two new variables as follows:

$$\begin{cases} \boldsymbol{d}_1 = \mathbf{d}, \\ \boldsymbol{d}_2 = \dot{\mathbf{d}}. \end{cases} \tag{2.99}$$

Substituting the new variables in (2.98), we can express (2.98) as:

$$\begin{bmatrix} \dot{\boldsymbol{d}}_1 \\ \dot{\boldsymbol{d}}_2 \end{bmatrix} = \begin{bmatrix} \mathbf{0} & \mathbf{I} \\ -\mathbf{M}^{-1}\mathbf{K} & -\mathbf{M}^{-1}\mathbf{C} \end{bmatrix} \begin{bmatrix} \boldsymbol{d}_1 \\ \boldsymbol{d}_2 \end{bmatrix} + \begin{bmatrix} \mathbf{0} \\ \mathbf{M}^{-1}\mathbf{f} \end{bmatrix}, \tag{2.100}$$

which is a system of first-order differential equations.

We need to perform a similar procedure for the third-order, semi-discrete system in (2.52):

$$\begin{bmatrix} \mathbf{M} & \mathbf{0} \\ \mathbf{0} & \mathbf{I} \end{bmatrix} \begin{bmatrix} \ddot{\mathbf{d}} \\ \ddot{\bar{\mathbf{d}}} \end{bmatrix} + \begin{bmatrix} \mathbf{C} & \mathbf{0} \\ -\mathbf{I} & \mathbf{0} \end{bmatrix} \begin{bmatrix} \dot{\mathbf{d}} \\ \dot{\bar{\mathbf{d}}} \end{bmatrix} + \begin{bmatrix} \mathbf{K} & \mathbf{G} \\ \mathbf{0} & \mathbf{0} \end{bmatrix} \begin{bmatrix} \mathbf{d} \\ \bar{\mathbf{d}} \end{bmatrix} = \begin{bmatrix} \mathbf{f} \\ \mathbf{0} \end{bmatrix}. \tag{2.52 revisited}$$

If we define new variables:

$$\begin{cases} \boldsymbol{d}_1 = \bar{\mathbf{d}}, \\ \boldsymbol{d}_2 = \mathbf{d}, \\ \boldsymbol{d}_3 = \dot{\mathbf{d}}, \end{cases} \tag{2.101}$$

we can rewrite the above second-order system, as a first-order system:

$$\begin{bmatrix} \dot{\boldsymbol{d}}_1 \\ \dot{\boldsymbol{d}}_2 \\ \dot{\boldsymbol{d}}_3 \end{bmatrix} = \begin{bmatrix} \mathbf{0} & \mathbf{I} & \mathbf{0} \\ \mathbf{0} & \mathbf{0} & \mathbf{I} \\ -\mathbf{M}^{-1}\mathbf{G} & -\mathbf{M}^{-1}\mathbf{K} & -\mathbf{M}^{-1}\mathbf{C} \end{bmatrix} \begin{bmatrix} \boldsymbol{d}_1 \\ \boldsymbol{d}_2 \\ \boldsymbol{d}_3 \end{bmatrix} + \begin{bmatrix} \mathbf{0} \\ \mathbf{0} \\ \mathbf{M}^{-1}\mathbf{f} \end{bmatrix}. \tag{2.102}$$

Thus, in the above, we transformed the second- and third-order semi-discrete forms to first-order systems for which we can use the the Runge-Kutta method to march in time. One potential difficulty in computing the first-order systems is the need to invert the mass matrix, which is computationally expensive, unless the matrix is diagonal. This concern will be addressed in the following section.

2.3.2.2 Spectral elements

In this section, we discuss techniques to diagonalize the mass matrix $\mathbf{M}$ in the semi-discrete form (2.26) and (2.47), thus enabling explicit time-stepping via the explicit solvers. The simplest way of obtaining diagonal mass-like matrices, is by mass-lumping, as was done in [22, 27] where the authors used linear elements. By contrast to classical Galerkin finite elements, a finite difference formulation automatically yields the diagonal mass-like matrices; see [84] for instance. To achieve high-order accuracy, however, one may use nodal spectral elements, where the numerical integration (quadrature rule) is based on the same nodes that polynomial interpolation is carried out [146, 176, 291]. This results in diagonal mass-like matrices, which are high-order accurate, depending on the degree of the interpolating polynomial. Herein, we use quadratic triangular (7-noded) and quadrilateral (9-noded) elements in 2D, and hexahedral (27-noded) elements with Legendre-Gauss-Lobatto quadrature rule (see Table 2.1).

Table 2.1: Legendre-Gauss-Lobatto quadrature rule

Element	Location of nodes	Location of integration points	Weights
Quadratic	± 1.0	± 1.0	1/3
(2D & 3D)	0.0	0.0	4/3
Triangular	$(0.0, 0.0), (1.0, 0.0), (0.0, 1.0)$	$(0.0, 0.0), (1.0, 0.0), (0.0, 1.0)$	1/40
(2D only)	$(0.5, 0.0), (0.5, 0.5), (0, 0.5)$	$(0.5, 0.0), (0.5, 0.5), (0, 0.5)$	1/15
	$(1/3, 1/3)$	$(1/3, 1/3)$	9/40

An m point Legendre-Gauss-Lobatto rule integrates polynomials of degree up to and including $2m - 3$, exactly [176]. However, to compute mass-like matrices, one needs to integrate terms with $\mathbf{\Phi}\mathbf{\Phi}^T$-like components, where $\mathbf{\Phi}$ is the vector of

Lagrange interpolating polynomials (see Appendix A). Having m interpolation nodes results in polynomials of degree $m-1$. The tensor products then involve terms of degree $2m-2$; thus, the approach relies on under-integration in order to return a diagonal mass-like matrix. Herein, we use the Legendre-Gauss-Lobatto rule to compute all the submatrices presented in (2.48).

2.3.2.3 Second-order Runge-Kutta (RK-2)

The coefficients corresponding to the 2-stage explicit Runge-Kutta method, known as the Runge-Kutta 2 (RK-2), to solve the first-order differential equation (2.95) are listed here:

$$k_1 = f(t_n, u_n), \tag{2.103a}$$

$$k_2 = f(t_n + \Delta t, u_n + \Delta t k_1). \tag{2.103b}$$

The approximate solution to the differential equation at time t_{n+1} is:

$$u_{n+1} = u_n + \frac{\Delta t}{2}(k_1 + k_2). \tag{2.104}$$

The details of this scheme for two- and three-dimensional domains and the computer algorithm are outlined in Appendix B.2.

2.3.2.4 Fourth-order Runge-Kutta (RK-4)

The coefficients corresponding to the 4-stage explicit Runge-Kutta method, known as the Runge-Kutta 4 (RK-4), to solve the first-order differential equation (2.95) are

listed here:

$$k_1 = f(t_n, u_n), \tag{2.105a}$$

$$k_2 = f(t_n + \frac{\Delta t}{2}, u_n + \frac{\Delta t}{2} k_1), \tag{2.105b}$$

$$k_3 = f(t_n + \frac{\Delta t}{2}, u_n + \frac{\Delta t}{2} k_2), \tag{2.105c}$$

$$k_4 = f(t_n + \Delta t, u_n + \Delta t k_3). \tag{2.105d}$$

The approximate solution to the differential equation at time t_{n+1} is:

$$u_{n+1} = u_n + \frac{\Delta t}{6}(k_1 + 2k_2 + 2k_3 + k_4). \tag{2.106}$$

The details of this scheme for two- and three-dimensional domains and the computer algorithm are outlined in Appendix B.3.

The Runge-Kutta 2 has the advantage of only two function evaluations k_i per step, which, in terms of the computational cost, might seem to be superior to the Runge-Kutta 4, that needs four function evaluations. Nevertheless, owing to the smaller region of absolute stability of the Runge-Kutta 2, to have a convergent solution, a smaller time-step is needed if we choose Runge-Kutta 2, which would entail a higher cost of computation in comparison with Runge-Kutta 4 [242].

Adjusting the appropriate time-step Δt to have a convergent solution is challenging in explicit solvers. A necessary condition for convergence according to the Courant-Friedrichs-Lewy (CFL) condition is that the maximum allowable time-step should be less than the required time for the elastic wave with the shortest wavelength to pass through the smallest grid points spacing in the entire model. This idea,

however, does not ensure a convergent solution, and finding the maximum possible time-step still needs a trial and error process, because, according to [170], there is no theoretical formulation on choosing the right time-step. Komatitsch et al. (2005) [170] and Casarotti et al. (2008) [55] made a heuristic rule of thumb to choose 50% of the maximum Courant condition for uniform grids and only 30% to 40% of the Courant condition for highly non-uniform grids. Fathi et al. (2015) [89] also suggest, based on numerical experiments in uniform meshes, to limit the time-step to less than 80% of the Courant number. Their suggestion is quite reasonable for uniform grids, however, for non-uniform grids, the optimal time-step is far below the CFL suggestion. In the following section, we address this issue thoroughly, and we use an adaptive technique to obviate the need for the trial and error process to find the optimal time-step.

2.3.2.5 Runge-Kutta-Fehlberg adaptive solver

The first step in developing an adaptive time solver is to evaluate the numerical error. The analysis for estimating the Global Truncation Error (GTE) is complex, instead, knowing the Local Truncation Error (LTE) (the error in one step of numerical integration), we can make an intuitive estimation of the GTE. Since LTE is more accessible, we will use the LTE as our principal measure of the accuracy of the numerical method.

The LTE varies for different step numbers results in different level of accuracy in time which is not welcoming. We have two options to maintain the LTE at a more or less a constant level. One way is to choose a step size based on an analysis near

the point where we have the largest error and use this fixed time-step during the whole simulation, similar to the fourth-order Runge-Kutta scheme. However, using a fixed time-step that is smaller than necessary over much of the interval results in unnecessary computations.

The other possibility to control the accuracy of the approximation is to adaptively modify the step-size in each time-step. This is only possible for one-step methods, for example Runge-Kutta, where only one previous approximation is required to approximate the solution in the next step. The difficult part of adaptivity is to find an efficient estimator of the local truncation error. An a posteriori error estimator is usually the tool that can be used in this case. Two options are available here [242]: (i) we use a Runge-Kutta time-integration scheme with two different step sizes Δt (typically $2h$ and h so that we can use the solution at the previous step), and (ii) we use two Runge-Kutta methods of different order, but with the same step-sizes and stages.

The first option requires that the method solves the system twice, which increases the computational effort. But, the second option to estimate the local error with no extra cost of functional evaluations is simultaneously using two Runge-Kutta methods with similar s-stages, but of orders p and $p+1$, such that they share the same values of k_i.

Let us assume that the first approximation is obtained from a pth-order Taylor method. Then, u_{n+1} the approximate solution at t_{n+1} with a local truncation error

of $\tau_{n+1}(h) = \mathcal{O}(h^p)$ would be:

$$u_{n+1} = u_n + hF(t_n, y_n, h; f), \qquad n > 0 \tag{2.107}$$

and y_{n+1} the exact solution at the same time-step is:

$$y_{n+1} = y_n + hF(t_n, y_n, h; f) + \mathcal{O}(h^{p+1}). \tag{2.108}$$

F is the increment function of the explicit solver. The second method is a $(p+1)$st-order Taylor method. Hence, the approximate solution $\widetilde{u}_{n+1}$ and the exact solution y_{n+1} would be:

$$\widetilde{u}_{n+1} = \widetilde{u}_n + h\widetilde{F}(t_n, y_n, h; f), \qquad n > 0 \tag{2.109a}$$

$$y_{n+1} = y_n + h\widetilde{F}(t_n, y_n, h; f) + \mathcal{O}(h^{p+2}). \tag{2.109b}$$

To estimate the local truncation error at time t_{n+1} for the scheme of order p (i.e., $\tau_{n+1}(h)$), we assume that the solution at the previous step is exact $y_n = u_n = \widetilde{u}_n$, and we use a fixed step size h to generate the approximations u_{n+1} and $\widetilde{u}_{n+1}$ to y_{n+1}. Having these assumptions, the local error can be computed as:

$$\tau_{n+1}(h) = \frac{1}{h}(y_{n+1} - u_{n+1}). \tag{2.110}$$

In a similar manner, the local truncation error at time t_{n+1} of the scheme with order $p+1$, $\widetilde{\tau}_{n+1}(h)$, is:

$$\widetilde{\tau}_{n+1}(h) = \frac{1}{h}(y_{n+1} - \widetilde{u}_{n+1}). \tag{2.111}$$

As a consequence, we have:

$$\begin{aligned}\tau_{n+1}(h) &= \frac{1}{h}(y_{n+1} - u_{n+1}) \\ &= \frac{1}{h}[(y_{n+1} - \widetilde{u}_{n+1}) + (\widetilde{u}_{n+1} - u_{n+1})] \\ &= \widetilde{\tau}_{n+1}(h) + \frac{1}{h}(\widetilde{u}_{n+1} - u_{n+1}). \end{aligned} \tag{2.112}$$

Since τ_{n+1} is of order h^p and $\widetilde{\tau}_{n+1}$ is of order h^{p+1}, $\frac{1}{h}(\widetilde{u}_{n+1} - u_{n+1})$ is the dominant term of $\tau_{n+1}(h)$ in (2.112). Hence, the local truncation error of the method of order p can be approximated via:

$$\tau_{n+1}(h) \approx \frac{1}{h}(\widetilde{u}_{n+1} - u_{n+1}). \tag{2.113}$$

Now, it remains to adjust the step size using this local truncation error. The fact that τ_{n+1} is of order h^p implies that there exists a number K, independent of h, such that $\tau_{n+1}(h) \approx Kh^p$. Therefore, the local truncation error due to applying the pth-order method with a new step size qh, can be estimated using the original approximations of u_{n+1} and $\widetilde{u}_{n+1}$:

$$\begin{aligned}\tau_{n+1}(qh) &\approx K(qh)^p = q^p(Kh^p) \\ &\approx q^p \tau_{n+1}(h) \\ &\approx \frac{q^p}{h}(\widetilde{u}_{n+1} - u_{n+1}). \end{aligned} \tag{2.114}$$

Thus, if we choose the appropriate q, we can force $\tau_{n+1}(qh)$ to be bounded by ε:

$$\frac{q^p}{h}|\widetilde{u}_{n+1} - u_{n+1}| \approx |\tau_{n+1}(qh)| \leq \varepsilon. \tag{2.115}$$

In other words, the modifier coefficient q can be evaluated from the following equation:

$$q \leq (\frac{\varepsilon h}{|\widetilde{u}_{n+1} - u_{n+1}|})^{\frac{1}{p}} = (\frac{\varepsilon}{\tau_{n+1}(h)})^{\frac{1}{p}}. \tag{2.116}$$

When the approximated error does not meet the allotted error criterion, the whole computation for this step should be repeated with the modified step size. Notice that if we deploy a p-th order scheme to initialize the solution at time-step $n+1$ the method has an order of p, as a whole. If conversely, the solution computed by the scheme of order $p+1$ is employed, the resulting scheme would have $p+1$-th order.

We apply the *Runge-Kutta-Fehlberg* (RKF) in this study that uses fourth-order Runge-Kutta coupled with a fifth-order Runge-Kutta method. Runge-Kutta-Fehlberg has the advantage of only six function evaluations k_i per step as opposed to arbitrary fourth- and fifth-order Runge-Kutta methods that require ten function evaluations, four for the fourth-order scheme and six for the fifth-order scheme. We choose q conservatively for the Runge-Kutta-Fehlberg method with $p = 4$, to avoid extra computations when the simulation in the current step has to be repeated, as follows:

$$q = (\frac{\varepsilon \Delta t}{2|\widetilde{u}_{n+1} - u_{n+1}|})^{1/4} = 0.84(\frac{\varepsilon}{\tau})^{1/4}. \tag{2.117}$$

The Runge-Kutta-Fehlberg coefficients are:

$$
\begin{aligned}
k_1 &= f(t_n, y_n), \\
k_2 &= f(t_n + \frac{1}{4}\Delta t, y_n + \frac{1}{4}\Delta t k_1), \\
k_3 &= f(t_n + \frac{3}{8}\Delta t, y_n + \frac{3}{32}\Delta t k_1 + \frac{9}{32}\Delta t k_2), \\
k_4 &= f(t_n + \frac{12}{13}\Delta t, y_n + \frac{1932}{2197}\Delta t k_1 - \frac{7200}{2197}\Delta t k_2 + \frac{7296}{2197}\Delta t k_3), \\
k_5 &= f(t_n + \Delta t, y_n + \frac{439}{216}\Delta t k_1 - 8\Delta t k_2 + \frac{3680}{513}\Delta t k_3 - \frac{845}{4104}\Delta t k_4), \\
k_6 &= f(t_n + \frac{1}{2}\Delta t, y_n - \frac{8}{27}\Delta t k_1 + 2\Delta t k_2 - \frac{3544}{2565}\Delta t k_3 + \frac{1859}{4104}\Delta t k_4 - \frac{11}{40}\Delta t k_5).
\end{aligned}
\tag{2.118}
$$

The fourth-order approximation for t_{n+1} would be:

$$
u_{n+1} = u_n + \Delta t(\frac{25}{216}k_1 + \frac{1408}{2565}k_3 + \frac{2197}{4104}k_4 - \frac{1}{5}k_5), \tag{2.119}
$$

and for the fifth-order approximation at t_{n+1} reads:

$$
\widetilde{u}_{n+1} = u_n + \Delta t(\frac{16}{135}k_1 + \frac{6656}{12825}k_3 + \frac{28561}{56430}k_4 - \frac{9}{50}k_5 + \frac{2}{55}k_6). \tag{2.120}
$$

Then, the difference between the two schemes $\widetilde{u}_{n+1} - u_{n+1}$ to be used in (2.117) to compute the modifier coefficient q, is obtained via:

$$
\tau_{n+1}(h) = \frac{\widetilde{u}_{n+1} - u_{n+1}}{\Delta t} = \frac{1}{360}k_1 - \frac{128}{4275}k_3 - \frac{2197}{75240}k_4 + \frac{1}{50}k_5 + \frac{2}{55}k_6. \tag{2.121}
$$

We remark that the total computational cost of the RK-4 (fixed time-step) is less than RKF (adaptive time-step) in each time-step because the number of function evaluations is greater in the latter scheme. To improve the efficiency of the adaptive scheme, we modify the original algorithm by combining RK-4 and RKF such that we march in time using the fixed time-step (RK-4) and check the local truncation error

every few steps to ensure that the error remains below the threshold. Additionally, according to our experiments, the performance (running time) of the algorithm increases if we still limit the maximum allowable time-step and also limit the time-step modifier q. We address the efficiency of the adaptive time-integration algorithm in Appendix D.

The details of this scheme for two- and three-dimensional models and the computer algorithm are outlined in Appendix B.4. See [46, 48, 242] for more details on the adaptive Runge-Kutta-Fehlberg.

Chapter 3

Verification[1]

In this chapter, we evaluate the validity of the formulation and numerical implementation by comparing the results against existing analytical and numerical solutions. Analytical solutions of wave propagation in a non-flat half-plane are scarce in the literature and are limited to only a few cases, mostly for SH-waves (see Section 1.2.2). Thus, to verify and assess the accuracy of our developed code, we resort to analytical solutions that are readily available for a flat homogeneous half-space, and to consider topography, we compare our results against those obtained from other numerical approaches. Moreover, analytical solutions are also needed for the parametric studies for which the imposition of the seismic input is done indirectly using the DRM.

In this chapter, we first discuss closed-form solutions of wave motion in a flat homogeneous domain, and, then, we compare our two- and three-dimensional numerical simulations with the exact solution. Afterwards, we compare our numerical results with a few published cases that take into account the effects of topography.

[1]Portion of this chapter has been published in: B. Poursartip, A. Fathi, L.F. Kallivokas, "Seismic wave amplification by topographic features: A parametric study," *Soil Dynamics and Earthquake Engineering*, 92, 503-527, 2017 [236]. The dissertation author had significant contribution to the article.

3.1 Analytical solutions for a homogeneous half-space in 2D and 3D

The analytical solution of wave propagation in a flat homogeneous half-plane is needed for three purposes: (i) to impose traveling incoming plane waves within the computational domain according to the DRM method, both in the time- and frequency-domains; (ii) to compare the motion amplification due to topography on the surface of a domain against the motion resulting from a flat surface consideration, used in the frequency-domain parametric study; (iii) to verify the numerical results against the exact solution in the time-domain simulations.

3.1.1 Frequency-domain solutions

Let $\boldsymbol{u}$ be the displacement vector in a two-dimensional flat-surface half-plane Figure 3.1:

$$\boldsymbol{u} = \begin{bmatrix} u_x(x,y) \\ u_y(x,y) \end{bmatrix}. \tag{3.1}$$

The exact frequency-domain solution of wave propagation can be obtained by decomposing the displacement field, using a Helmholtz decomposition, and substituting the results into Navier's equations [2, 108]. Accordingly, the displacement field due to SV-wave propagation in a half-plane can be written as:

$$\begin{bmatrix} u_x^s(x,y) \\ u_y^s(x,y) \end{bmatrix} = U_s^i \begin{bmatrix} +\cos\theta_s \\ +\sin\theta_s \end{bmatrix} e^{i\,k_s(x\,\sin\theta_s - y\,\cos\theta_s - c_s\,t)} + U_s^r \begin{bmatrix} -\cos\theta_s \\ +\sin\theta_s \end{bmatrix} e^{i\,k_s(x\,\sin\theta_s + y\,\cos\theta_s - c_s\,t)} + U_p^r \begin{bmatrix} +\sin\theta_p \\ +\cos\theta_p \end{bmatrix} e^{i\,k_p(x\,\sin\theta_p + y\,\cos\theta_p - c_p\,t)}, \tag{3.2}$$

where u_x^s and u_y^s are the displacements within the domain in the x and y directions, respectively; k_s and k_p are shear and compressional wavenumbers; θ_s is the angle of

SV incidence, which is also equal to the angle of reflected SV-wave; θ_p is the angle of reflected P-wave derived according to Snell's law:

$$\theta_p = \arcsin(\frac{c_p}{c_s}\sin\theta_s), \tag{3.3}$$

where c_s and c_p are shear and pressure wave velocities, respectively. $U_s^i = A_s^i k_s$ denotes the amplitude of the incoming SV-wave, and $U_s^r = A_s^r k_s$ and $U_p^r = A_p^r k_p$ are the amplitudes of the reflected SV- and P-waves, respectively; A_p^r and A_s^r are defined as:

$$A_p^r = \frac{-2\ k^2 \sin(2\theta_s)\ \cos(2\theta_s)}{\sin(2\theta_p)\ \sin(2\theta_s) + k^2\ \cos^2(2\theta_s)} A_s^i, \tag{3.4a}$$

$$A_s^r = \frac{\sin(2\theta_s)\ \sin(2\theta_p) - k^2\ \cos^2(2\theta_s)}{\sin(2\theta_p)\ \sin(2\theta_s) + k^2\ \cos^2(2\theta_s)} A_s^i, \tag{3.4b}$$

where $k = c_p/c_s$ [2].

In summary, leaving out special cases, according to this solution, a plane SV-wave reflects from the flat surface of a homogeneous half-plane as P- and SV-waves as depicted in Figure 3.1. The first term of (3.2) denotes the SV incident wave traveling at c_s and at an angle of incidence θ_s with an amplitude of $A_s^i k_s$; the second term indicates the reflected SV-wave traveling at the same velocity and reflection angle θ_s with an amplitude of $A_s^r k_s$; and the third term is the reflected P-wave which has an amplitude of $A_p^r k_p$ and traveling at c_p and angle of reflection θ_p.

A special case of particular interest in this study is the critical angle incidence,

[2]The notation follows [108], where a subscript p or s denotes P- or S-wave, and superscripts i and r denote incident and reflected waves, respectively.

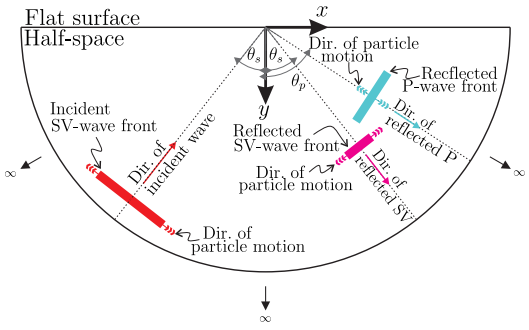

Figure 3.1: Schematic propagation of SV-wave in a flat homogeneous half-space for an angle of incidence less than the critical angle

where the P-wave reflects at grazing angle ($\theta = \pi/2$); the critical angle is:

$$\theta_{cr} = \sin^{-1}(\frac{c_s}{c_p}) = \sin^{-1}(\sqrt{\frac{1-2\nu}{2-2\nu}}). \tag{3.5}$$

Similarly, the displacement field due to P-wave propagation in a homogeneous flat half-plane can be expressed as:

$$\begin{bmatrix} u_x^p(x,y) \\ u_y^p(x,y) \end{bmatrix} = U_p^i \begin{bmatrix} +\sin\theta_p \\ -\cos\theta_p \end{bmatrix} e^{i\,k_p(x\,\sin\theta_p - y\,\cos\theta_p - c_p\,t)}$$
$$+ U_s^r \begin{bmatrix} +\cos\theta_s \\ -\sin\theta_s \end{bmatrix} e^{i\,k_s(x\,\sin\theta_s + y\,\cos\theta_s - c_s\,t)} + U_p^r \begin{bmatrix} +\sin\theta_p \\ +\cos\theta_p \end{bmatrix} e^{i\,k_p(x\,\sin\theta_p + y\,\cos\theta_p - c_p\,t)}. \tag{3.6}$$

u_x^p and u_y^p are the displacements within the domain in the x and y directions, respectively. $U_p^i = A_p^i k_p$ is the amplitude of the incoming P-wave, and $U_s^r = A_s^r k_s$ and $U_p^r = A_p^r k_p$ are the amplitudes of the reflected SV- and P-waves, respectively; A_p^r and A_s^r are computed as:

$$A_p^r = \frac{\sin(2\theta_p)\ \sin(2\theta_s) - k^2\ \cos^2(2\theta_s)}{\sin(2\theta_p)\ \sin(2\theta_s) + k^2\ \cos^2(2\theta_s)} A_p^i, \tag{3.7a}$$

$$A_s^r = \frac{2\ \sin(2\theta_p)\ \cos(2\theta_p)}{\sin(2\theta_p)\ \sin(2\theta_s) + k^2\ \cos^2(2\theta_s)} A_p^i. \tag{3.7b}$$

Figure 3.2 illustrates the typical reflection of a P-wave from a flat homogeneous half-space, excluding special cases. The first term of (3.6) is the incident P-wave traveling at c_p and at an angle of incidence θ_p with an amplitude of $A_p^i k_p$; the second term indicates the reflected SV-wave traveling at c_s and angle of reflection θ_s with an amplitude of $A_s^r k_s$; and the third term is the reflected P-wave which has an amplitude of $A_p^r k_p$ and traveling in the domain at c_p velocity and angle of reflection θ_p.

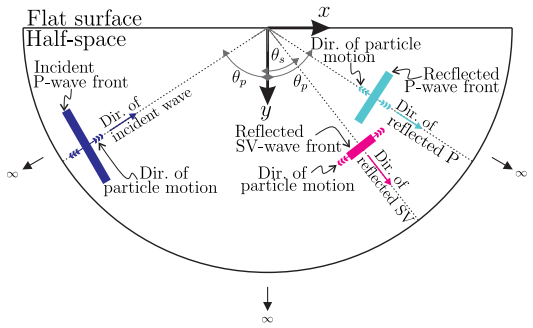

Figure 3.2: Schematic propagation of P-wave in a flat homogeneous half-space

3.1.2 Surface displacements

In this section, we provide expressions for the surface displacement due to plane waves in the frequency-domain. We use these results in Chapter 4 to measure the surface amplification due to topography.

The amplitude of the displacement components on the surface of a homogeneous flat half-plane ($y = 0$) for the SV wave incidence is computed from (3.2) as:

$$|u_x^{s,ff}| = | + A_s^i k_s \cos\theta_s - A_s^r k_s \cos\theta_s + A_p^r k_p \sin\theta_p|, \tag{3.8a}$$

$$|u_y^{s,ff}| = | + A_s^i k_s \sin\theta_s + A_s^r k_s \sin\theta_s + A_p^r k_p \cos\theta_p|, \tag{3.8b}$$

and similarly for the P-wave incidence:

$$|u_x^{p,ff}| = | + A_p^i k_p \sin\theta_p + A_s^r k_s \cos\theta_s + A_p^r k_p \sin\theta_p|, \tag{3.9a}$$

$$|u_y^{p,ff}| = | - A_p^i k_p \cos\theta_p - A_s^r k_s \sin\theta_s + A_p^r k_p \cos\theta_p|. \tag{3.9b}$$

(3.8) and (3.9) suggest the dependence of the surface motion on Poisson's ratio, and the angle of incidence.

Figure 3.3 depicts the surface displacement according to (3.8) and (3.9) for three Poisson's ratios that we use in this study (the material properties are discussed in detail in Chapter 4). Based on Figure 3.3(a) for a P-wave incidence, the horizontal displacement rises as the angle of incidence increases, from zero up to a certain angle, and reduces to zero again at the grazing angle, while the vertical displacement reduces steadily from 2.0 to zero as the angle of incidence climbs from zero to 90°. The SV incidence in Figure 3.3(b) shows a more complex pattern. The horizontal component reduces slightly from 2 and tends to increase sharply at the critical angle and drops to zero at the angle $\theta_s = 45°$. The vertical displacement rises as the angle of incidence increases until just before the critical angle and then suddenly plunges to zero at the critical angle. Notice that the horizontal displacement is always larger than the vertical displacement for angles of incidence less than the critical angle, because the particle motion for SV waves is normal to the direction of motion.

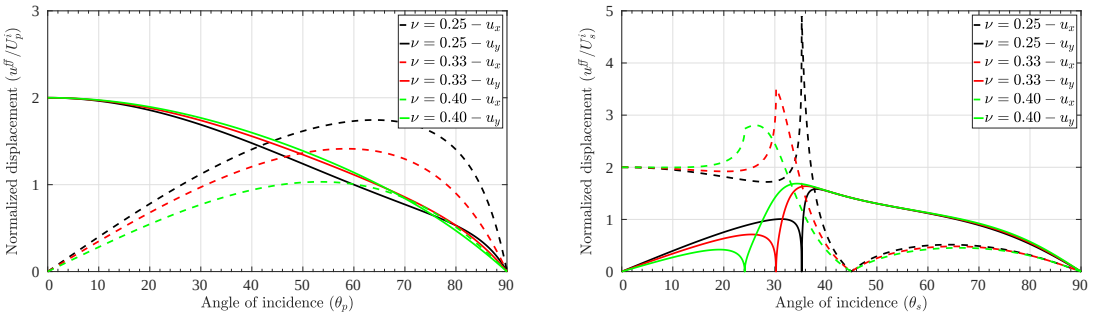

(a) (b)

Figure 3.3: Normalized displacement on the surface of a flat homogeneous half-plane due to the reflection of (a) P incident wave and (b) SV incident wave for three different Poisson's ratios used in this study against the angle of incidence

3.1.3 Time-domain solutions

The free-field solution of plane waves in a homogeneous, flat half-plane in the time-domain can be obtained from the frequency-domain solution using d'Alembert's method. The solution for SV incidence can be computed as:

$$\begin{bmatrix} u_x^s(x,y) \\ u_y^s(x,y) \end{bmatrix} = U_s^i \begin{bmatrix} +\cos\theta_s \\ +\sin\theta_s \end{bmatrix} f(-\frac{x}{c_s}\sin\theta_s + \frac{y}{c_s}\cos\theta_s + t) + U_s^r \begin{bmatrix} -\cos\theta_s \\ +\sin\theta_s \end{bmatrix} f(-\frac{x}{c_s}\sin\theta_s - \frac{y}{c_s}\cos\theta_s + t) + U_p^r \begin{bmatrix} +\sin\theta_p \\ +\cos\theta_p \end{bmatrix} f(-\frac{x}{c_p}\sin\theta_p - \frac{y}{c_p}\cos\theta_p + t), \tag{3.10}$$

and for the P incidence can be expressed as:

$$\begin{bmatrix} u_x^p(x,y) \\ u_y^p(x,y) \end{bmatrix} = U_p^i \begin{bmatrix} +\sin\theta_p \\ -\cos\theta_p \end{bmatrix} f(-\frac{x}{c_p}\sin\theta_p + \frac{y}{c_p}\cos\theta_p + t) + U_s^r \begin{bmatrix} +\cos\theta_s \\ -\sin\theta_s \end{bmatrix} f(-\frac{x}{c_s}\sin\theta_s - \frac{y}{c_s}\cos\theta_s + t) + U_p^r \begin{bmatrix} +\sin\theta_p \\ +\cos\theta_p \end{bmatrix} f(-\frac{x}{c_p}\sin\theta_p - \frac{y}{c_p}\cos\theta_p + t). \tag{3.11}$$

where c_s and c_p are the shear and pressure wave velocities, and θ_s and θ_p are the angles of shear wave and pressure wave (incidence or reflected), respectively. U is

the amplitude of wave fronts (see definitions in Section 3.1.1).

Function $f = f(\tau)$ is any single-variable function that determines the shape of the wave. In this study, we use both $f(\tau) = \sin(\tau)$ or a Ricker pulse time signature which is defined as:

$$f(u;\tau) = \frac{(0.25u^2 - 0.5)e^{-0.25u^2} - 13e^{-13.5}}{0.5 + 13e^{-13.5}}, \tag{3.12}$$

with u to be:

$$u(\tau) = \omega_r \tau - 3\sqrt{6}, \quad \text{with} \;\; 0 \leq t \leq \frac{6\sqrt{6}}{\omega_r}, \tag{3.13}$$

where ω_r $(= 2\pi f_r)$ denotes the characteristic central circular frequency of the pulse. For example, the pulse displacement time-history, and its corresponding Fourier spectrum are shown in Figure 3.4 for a central frequency $f_r = 2\,\text{Hz}$, and an amplitude of one.

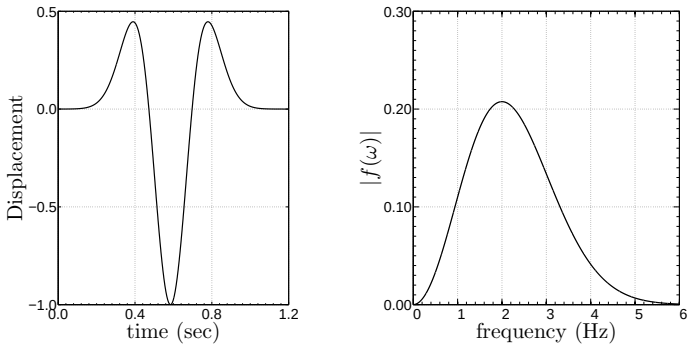

Figure 3.4: Ricker pulse (a) time history (b) its Fourier spectrum

3.2 Verification of two-dimensional wave motion in a half-plane in the time-domain

We compare the two-dimensional numerical simulation of wave motion in a homogeneous, flat half-plane with the analytical solutions obtained in Appendix 3.1.3. The homogeneous half-plane is truncated to a 800m $\times$ 300m computational domain, surrounded on its sides and bottom by a 25m-thick PML as shown in Figure 3.5. Quadratic quadrilateral spectral elements (9-noded) of edge size 2.5m are used to discretize the domain. The discretization results in a ten-element-thick PML with quadratic attenuation profile $m = 2$. The PML parameters α_0 and β_0 were set to 5.0 and 500m/s, respectively. The shear and pressure wave velocities are $c_s = 200$m/s and $c_p = 350$m/s, respectively, and no material damping is considered in the simulation. The frequency of the incident wave is 2Hz thus the shear wavelength is 100m and the pressure wavelength is 175m. The observation point to compare the analytical solution with the numerical results is located at $(0\text{m}, 150\text{m})$ (see Figure 3.5). This point is intentionally selected away from the surface so that we can see separate motion from waves. Wave motion is implemented in the model using (3.10) and (3.11) with $f(\tau) = \sin(\omega\tau)$ defined from 0 to π (half a cycle of a sinusoidal wave).

3.2.1 Reflection of P-wave

The first verification example tests the reflection of a P incident wave from the flat surface of a half-plane. Figure 3.6 depicts three snapshots of the displacement field in the x and y directions, in the half-plane for a P incident wave of amplitude 1 and angle of incidence 15°. The top figures display the P incident front just before it

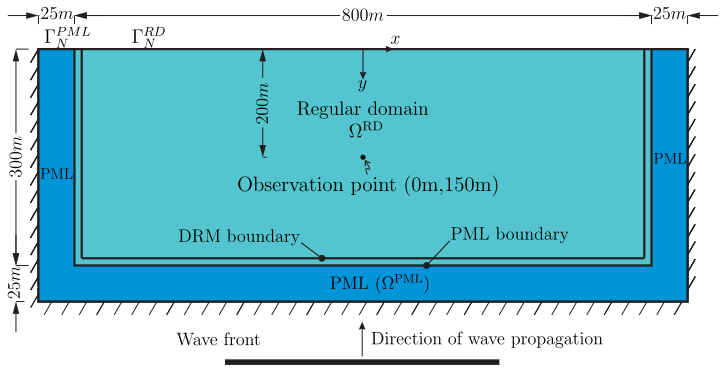

Figure 3.5: Geometry of the half-plane

hits the flat surface. The particle motion is in the direction of wave propagation (see Figure 3.2), hence, the x-direction motion is positive and the y-direction motion is negative. As the wave hits the surface, it reflects back into the domain as P- and SV-waves, shown in the middle snapshots.

The reflected P-wave appears first, owing to the larger pressure wave velocity, at the same angle as the angle of incidence, and with a lower amplitude compared to the amplitude of the incident wave, because of energy redistribution. Note that since the direction of motion has changed, both x and y displacements are negative in the reflected front. The SV-wave is following the P-wave with a shorter wavelength and slower motion. The last set of snapshots illustrates the moment that the reflected waves are leaving the domain. In these snapshots, the PML buffer zone combined with the DRM exterior domain are also visible on the sides and bottom of the model, where there is no motion at all. This is what we expect to see, because there are no irregularities on the surface, and the scattered motion should be zero.

The time history of displacements in the x and y directions for the analytical

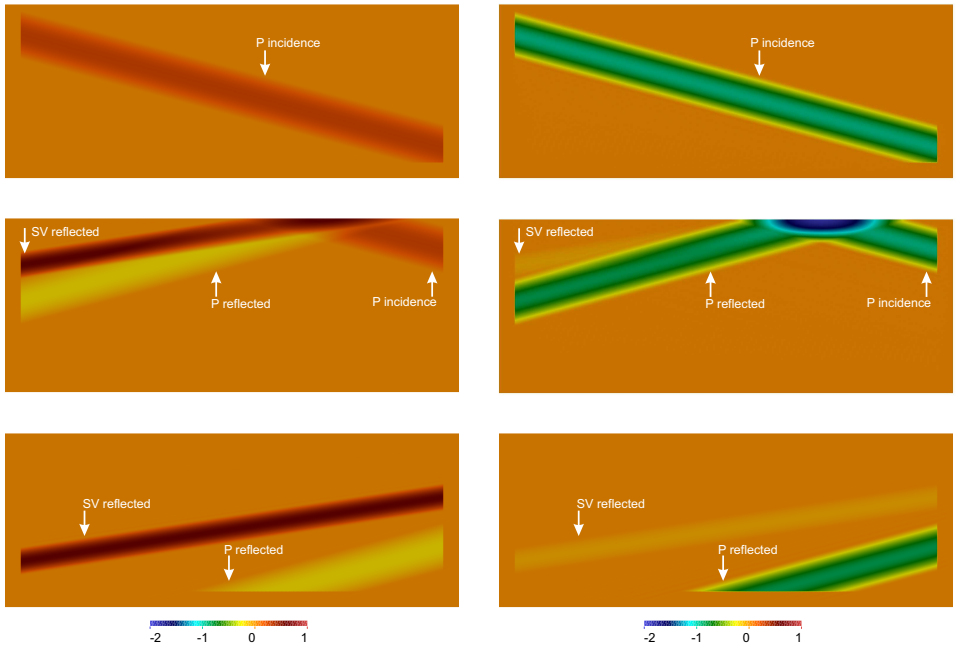

Figure 3.6: Propagation of P-wave in a flat half-plane with an angle of incidence 15°

and numerical solutions are displayed in Figure 3.7 for the observation point (see Figure 3.5). A total agreement between the two time histories implies the accuracy of the developed formulation and the numerical simulation. Notice that three bumps are visible in the time history; the first bump is for the P incident wave, the second bump is for the reflected P-wave, and the third bump is due to the reflected SV-wave which is slower than the P-wave.

3.2.2 Reflection of SV-wave

The second verification example is the reflection of a plane SV incident wave of amplitude 1 and an angle of incidence of 15°, from the flat surface. Figure 3.8 displays the displacement motion in the x and y directions after the incident wave

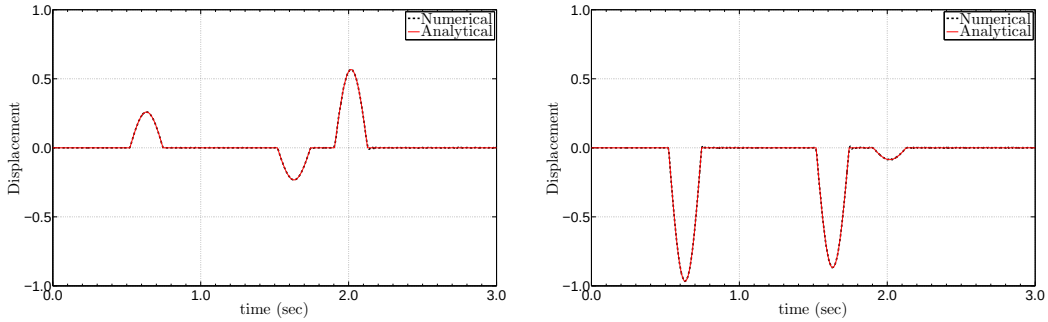

(a) x-direction (b) y-direction

Figure 3.7: Comparison of the time history of displacements at the observation point for the P incident wave

hits the flat surface. Three wave fronts can be seen in the displacement contour: the first one is the SV incidence, where the particle motion is normal to the direction of motion, thus, the x and y displacements are positive; the second one is the reflected P wave with positive displacements and greater angle of incidence and wavelength in comparison to the incidence; and the third one is the reflected SV wave with the same angle of incidence and wavelength.

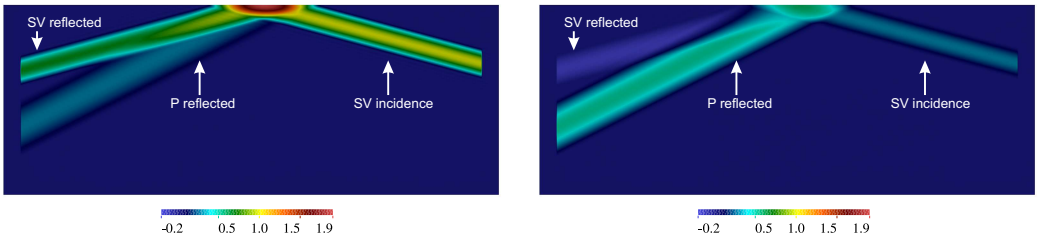

(a) x-direction (b) y-direction

Figure 3.8: Propagation of SV-wave in a half-plane with an angle of incidence less than the critical angle

The time history of displacement in the x and y directions for the propagation of SV-wave in the half-plane has been depicted in Figure 3.9 and is compared to the

analytical solution. There is a good agreement between the two results.

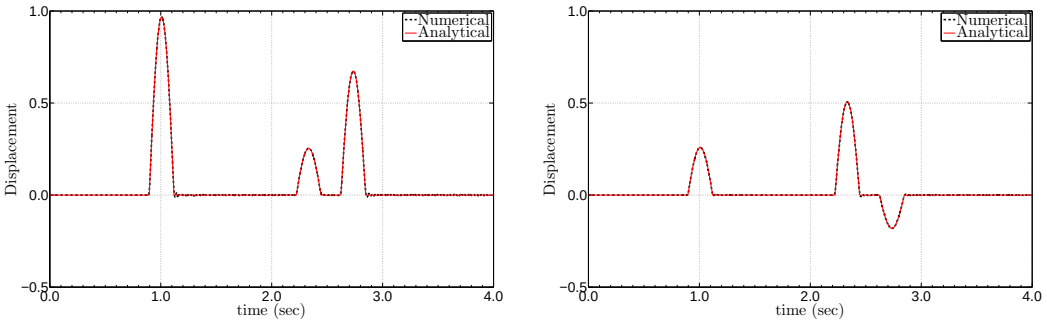

(a) x-direction (b) y-direction

Figure 3.9: The time history of displacement due to the propagation of SV-wave at angle of incidence less that the critical angle in a homogeneous flat half-plane

As an additional verification example, we study the propagation of SV-wave at the critical angle. The displacement contours are shown in Figure 3.10.

Notice that for this angle, P-wave reflects at grazing angle, hence, the vertical displacement for this wave front is zero because the particle motion for the P-wave is in the direction of the motion.

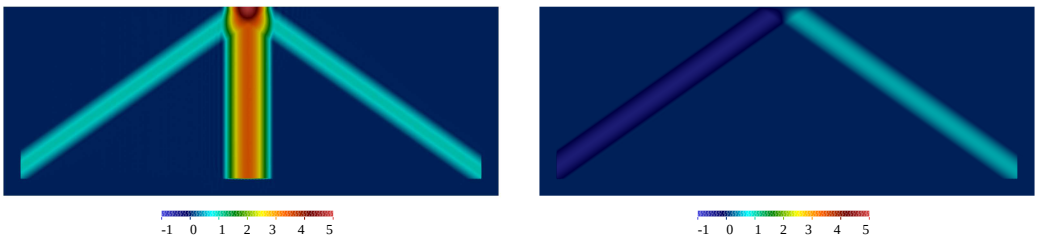

(a) x-direction (b) y-direction

Figure 3.10: Propagation of SV-wave in a half-plane at the critical angle

Figure 3.11 depicts the comparison of the time histories of displacements in

x and y directions at the observation point. In this time history, the x displacement shows three bumps, two for the incident and reflected SV-waves, and the middle one is for the reflected P-wave traveling at the grazing angle and exhibiting significant amplitude: 4.92 on the surface, and 3.25 at the observation point. The y component, on the other hand, experiences only two bumps, both for SV-waves. The analytical solution matches the numerical solution perfectly.

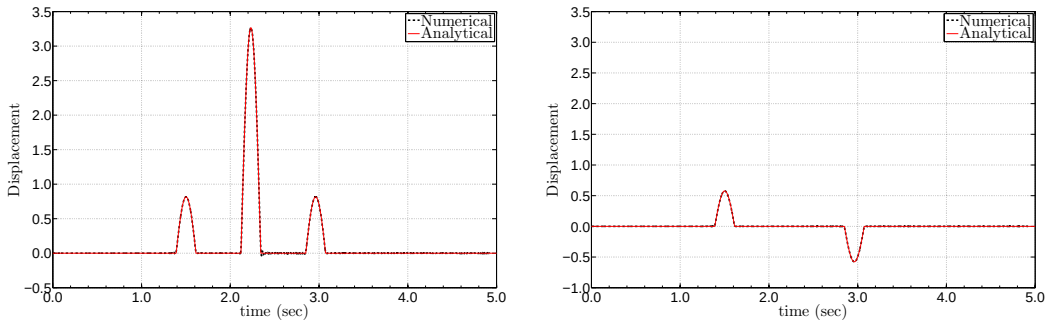

(a) x-direction (b) y-direction

Figure 3.11: The time history of displacement due to the propagation of SV-wave at critical angle in a homogeneous flat half-plane

3.3 Verification of three-dimensional wave motion in a half-space in the time-domain

We compare the numerical simulation of wave motion in a three-dimensional, homogeneous, flat half-space with the analytical solutions obtained in Section 3.1.3. The homogeneous half-space is truncated to a 800m $\times$ 800m $\times$ 300m computational domain, surrounded on its sides and bottom by a 50m-thick PML as shown in Figure 3.12. Quadratic hexahedral spectral elements (27-noded) of edge size 5m are used to discretize the domain. The discretization results in a ten-element-thick PML with

quadratic attenuation profile $m = 2$. The PML parameters α_0 and β_0 were set to 5.0 and 500m/s, respectively. The shear and pressure wave velocities are $c_s = 200$m/s and $c_p = 350$m/s, respectively, and no material damping mechanism is considered in the simulation. Wave motion is implemented in the model using (3.10) and (3.11)

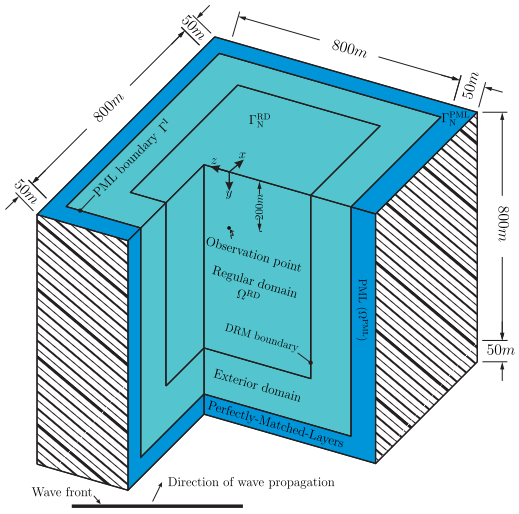

Figure 3.12: Geometry of the half-space

with $f(\tau) = sin(\omega\tau)$ defined from 0 to π (half a cycle of a sinusoidal wave). τ is the wave phase and ω is the cyclic frequency of the wave.

3.3.1 Reflection of P-wave

The first verification example tests the reflection of a plane P incident wave of unit amplitude and the angle of incidence 15° from the flat surface of a half-space according to (3.6). Figure 3.13 depicts the snapshot of displacement field in the x and y directions (the displacement in the z direction in zero). As the wave hits the surface, it reflects back into the domain as P- and SV-waves. The reflected P-wave,

which has the same angle as the incident wave, appears first due to the larger pressure velocity, with a reduction in the amplitude in comparison to the incident wave, owing to the redistribution of energy. Since the direction of motion has changed, both x and y displacements are negative. The SV-wave is following the P-wave with a shorter wavelength. In these snapshots, the PML buffer zone combined with the DRM exterior domain are also visible on the sides and bottom of the model, where there is no motion. The time history of displacements has been compared to the analytical solution and, as expected, is identical to Figure 3.7.

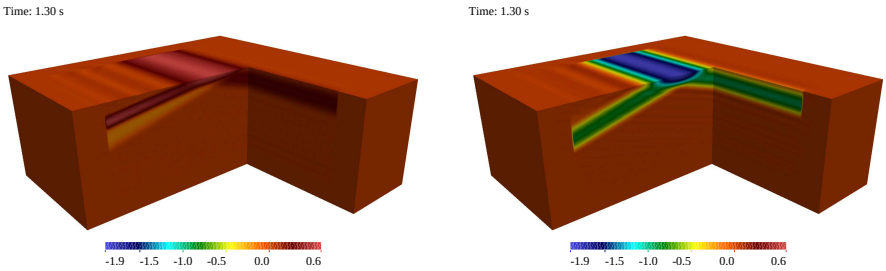

(a) x-direction (b) y-direction

Figure 3.13: Propagation of P-wave in a flat half-space with an angle of incidence 15°

3.3.2 Reflection of SV-wave

The second three-dimensional verification example is the reflection of a plane SV incident wave of amplitude one and an angle of incidence of 15°, from the flat surface of a homogeneous domain. Figure 3.14 displays the displacement field in the x and y directions within the domain after the incident wave hits the flat surface. Three wave fronts can be seen in the displacement contour; the first one is the SV incidence, where the particle motion is normal to the direction of motion, thus, the

x and y displacements are positive, the second one is the reflected P wave with positive displacements and greater angle of incidence and wavelength in comparison to the incidence, and the third one is the reflected SV wave with the same angle and wavelength as the incident wave. The time history of displacements corresponding to this example is identical to Figure 3.9.

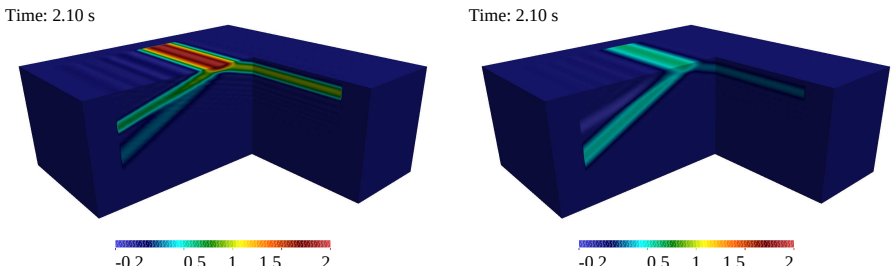

(a) x-direction (b) y-direction

Figure 3.14: Propagation of SV-wave in a flat half-plane with an angle of incidence 15°

As an additional verification example, we also consider the propagation of SV-wave at the critical angle. The displacement contours are shown in Figure 3.10. Notice that for this angle, the P-wave reflects at grazing angle, hence, since the particle motion of P-wave is in the direction of propagation, we expect the motion in the y direction to be zero. The comparison between the time history of displacements with the analytical solutions is identical to Figure 3.11.

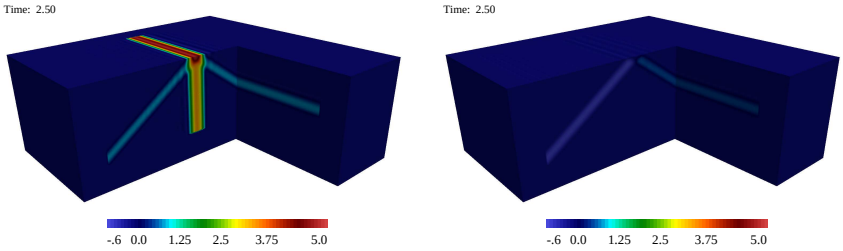

(a) x-direction (b) y-direction

Figure 3.15: Propagation of SV-wave in a flat half-plane at the critical angle

3.4 Verification of wave motion in a valley embedded in a half-plane in the frequency-domain

Analytical solutions of wave propagation in a non-flat half-plane are scarce in the literature and are limited to only a few cases, mostly for SH-waves. Thus, to assess the accuracy of our developed code, we compare our results against those obtained from other numerical approaches. To this end, we used the indirect boundary element method (IBEM)[3] to analyze a two-dimensional semi-circular valley embedded in a homogeneous half-plane subjected to plane P- and SV-waves. This particular geometry was first used by Trifunac [285] in 1973, to study topographic effects due to SH-wave propagation, and later in 1982 by Wong [292] for plane P- and SV-waves.

The configuration of the prototype semi-circular valley is shown in 3.16. The homogeneous half-plane is truncated to a 500m $\times$ 300m computational domain containing a cylindrical valley of radius $R_0 = 50$m, surrounded on its sides and bottom by a 25m-thick PML layer. The domain of interest and PML zone are discretized by quadratic quadrilateral spectral elements (9-node) of edge size 2.5m. The discretiza-

[3]IBEM results were provided by Dr. F. J. Sánchez-Sesma and N.C. Zamorate.

tion resulted in a ten-element-thick PML with a quadratic attenuation profile $m = 2$. The density of the medium is $\rho = 2000\text{kg/m}^3$ with shear modulus $G = 100\text{MPa}$, and Poisson's ratio $\nu = 0.33$. There is no material damping.

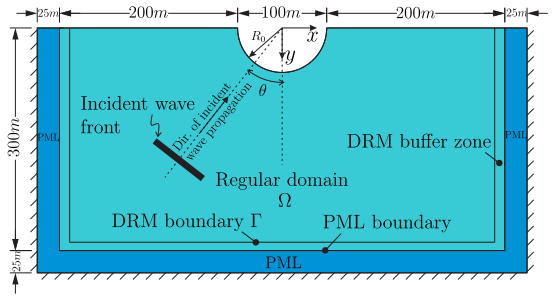

Figure 3.16: Geometry of the semi-circle valley in a half-plane

To quantify the size of the valley in comparison to the wavelength of the incoming wave, we define a dimensionless frequency $\eta = \frac{2R_0}{\lambda_s}$ that represents the ratio of the valley's diameter $2R_0$ to the shear wavelength of the incident wave λ_s. Hence, $\eta = 2.0$ represents a case where the shear wavelength is the same size as the valley's radius. To verify the results, the analysis is conducted for $\eta = 0.5, 1.0, 1.5,$ and 2.0 and two angles of incidence of $\theta_p = 0^\circ$ and 60° for P-wave and $\theta_s = 0^\circ$ and 30° for SV-wave. In the following figures, we plot horizontal and vertical surface displacements, normalized with respect to the amplitude of the incident wave A^i, against the normalized location x/R_0.

Figure 3.17 shows the surface displacement pattern caused by a vertically propagating P-wave. The IBEM results are well-matched with our Spectral-Element-Method (SEM) results in both directions. Minor differences exist mostly at the sharp corners of the edge of the valley. We mention that for this case, the free-field flat

surface displacements are $|u_x| = 0.0$ and $|u_y| = 2.0$ according to Section 3.1.1. The horizontal displacement is mostly caused by the Rayleigh waves generated at the corners of the valley and attains a maximum at the far end of the domain. The maximum vertical displacement occurs close to the edge of the valley, where the Rayleigh waves are combined with the reflected P-wave. The surface displacement exhibits a relatively high amplification on the surface of the valley and also away from it.

The scattering of P incidence with angle $\theta_p = 60°$ by the semi-circular valley is shown in Figure 3.18. The IBEM results are in a good agreement with our results with minor differences at the edges of the valley. The free-field solutions for this angle are $|u_x| = 1.39$ and $|u_y| = 1.12$.

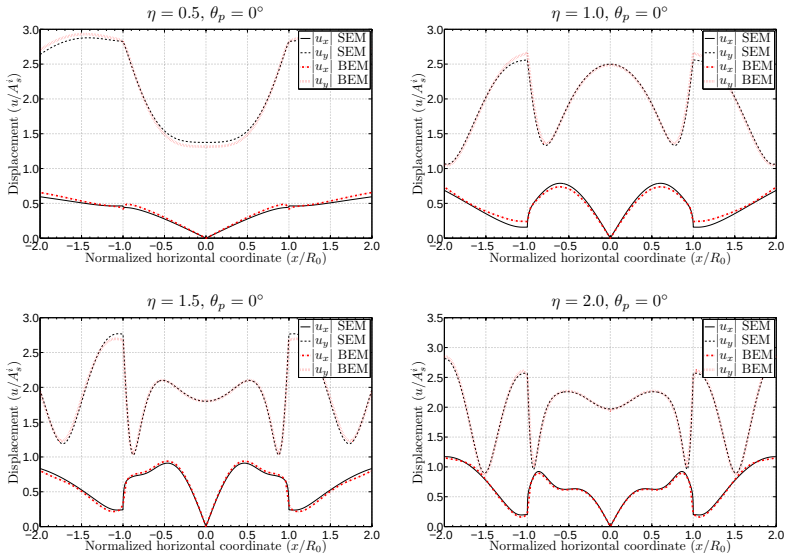

Figure 3.17: Displacement pattern on the surface of a semi-circular valley caused by a vertically propagating P incidence for four frequencies

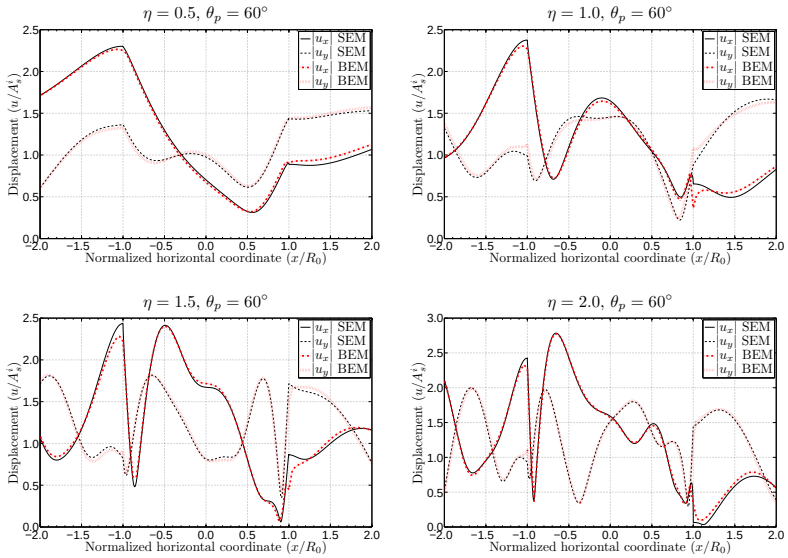

Figure 3.18: Displacement pattern on the surface of a semi-circular valley caused by a $\theta_p = 60°$ P incidence for four frequencies

The surface pattern for a vertically propagating SV incidence is plotted in Figure 3.19. Other than minor differences between SEM and IBEM results at the valley edges, the displacements are in excellent agreement.

The last angle of incidence that we explore for the study of SV propagation is the critical angle $\theta_s^{cr} = 30°$. The displacements from the two different methods are plotted in Figure 3.20 and also show good agreement.

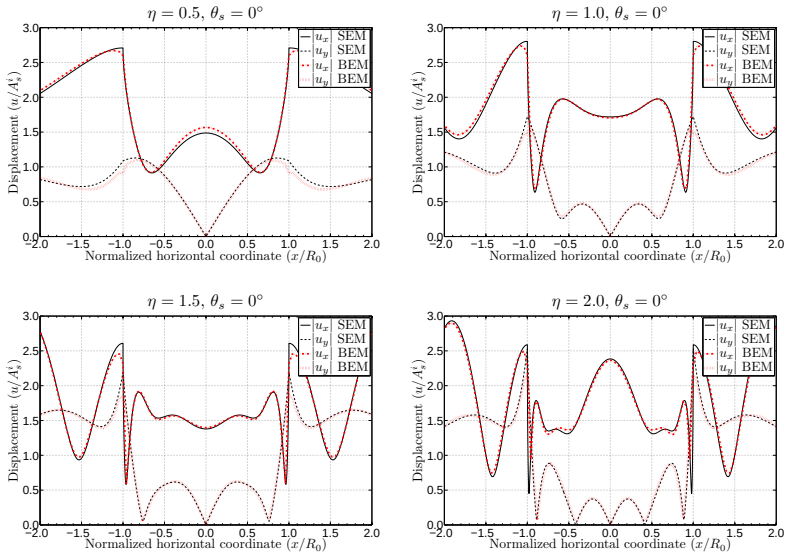

Figure 3.19: Displacement pattern on the surface of a semi-circular valley caused by a vertically propagating SV incidence for four frequencies

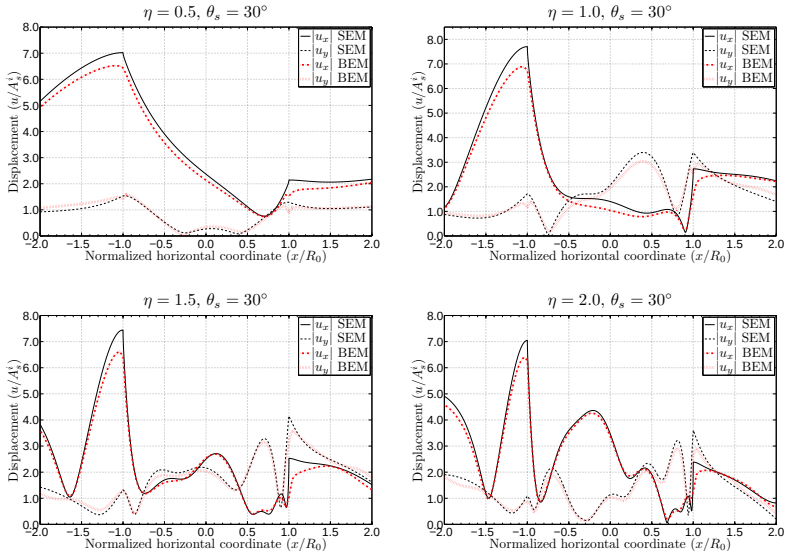

Figure 3.20: Displacement pattern on the surface of a semi-circular valley caused by a $\theta_s^{cr} = 30°$ SV incidence for four frequencies

Chapter 4

Frequency-domain parametric studies[1]

In this chapter, we discuss the results of an extensive parametric study aimed at understanding and quantifying the effect topography has in site response.

Three groups of parameters, in general, affect the motion amplification: (i) the geometry of the topographic feature; (ii) wave properties (wave type, wave frequency, and the angle of incidence); and (iii) material properties (shear modulus, Poisson's ratio, and density). We intend to investigate the effects of all three groups by simulating the scattering of in-plane P- and SV-waves due to various two-dimensional surface features, embedded in a linear elastic, homogeneous, isotropic half-plane, for different incident wave properties.

4.1 Description of study parameters

We consider a homogeneous medium with mass density $\rho = 2000\text{kg/m}^3$, shear modulus $G = 100\text{MPa}$, and Poisson's ratio $\nu = 0.25$.The majority of the simulations are based on this material model. Additionally, to study the effect of Poisson's ratio on

[1]Portion of this chapter has been published in: B. Poursartip, A. Fathi, L.F. Kallivokas, "Seismic wave amplification by topographic features: A parametric study," *Soil Dynamics and Earthquake Engineering*, 92, 503-527, 2017 [236]. The dissertation author had significant contribution to the article.

the wave motion, two additional material models are considered with Poisson's ratios $\nu = 0.33$ and $\nu = 0.40$, and otherwise identical mass density and shear modulus. The simulations are performed in the frequency-domain without any material damping.

We consider only symmetric hills and valleys to describe surface irregularities. The schematic configuration of the corresponding computational domains are plotted in Figure 4.1, where b denotes the base of the feature, and h is the height or depth of the hill or valley, respectively. We introduce the shape ratio $S_r = \arctan(h/b)$ to quantify the slenderness of each shape. We also introduce the dimensionless frequency:

$$\eta = \frac{h}{\lambda_s}, \tag{4.1}$$

which is the ratio of the feature's height/depth to the shear wavelength, in order to normalize the incident wave frequency.

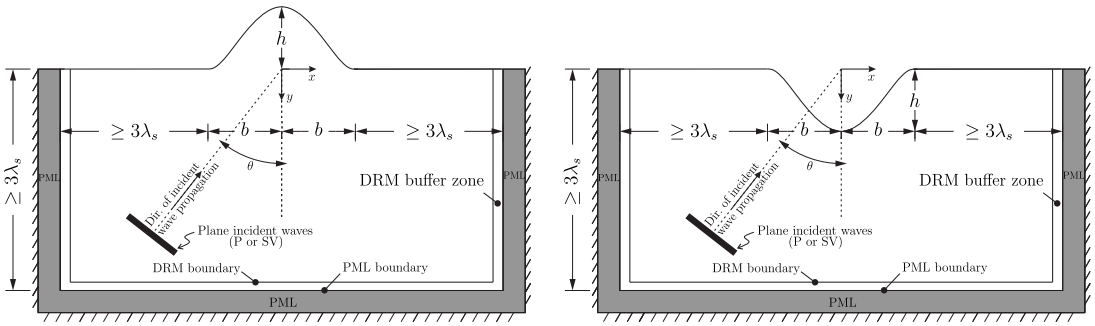

Figure 4.1: Typical geometry of topographic features used in this study (a) hills (b) valleys

We truncate the semi-infinite physical domain such that the distance from the feature to the truncation boundary is at least three times the shear wavelength λ_s.

The computational domain has been surrounded on its sides and bottom by a ten-element-thick PML. We discretize the computational domain using quadratic quadrilateral elements with element size that allows for at least 40 points per shear wavelength.

In summary, we perform the parametric study using the following parameters:

- wave types: plane P- and SV-waves.
- angle of incidence: 0° to 45° for P incidence, and 0° to 35° for SV incidence in 5° increments.
- incident wave frequency: η varies from 0.1 to 5.0, in 0.1 increments.
- topography: hills and valleys of different geometry.
- topography shape ratio: the inverse tangent of height to base ratio, $\arctan(h/b)$.

4.2 Parametric study on hills

In this section, we report the findings of the parametric study on the amplification and de-amplification of plane waves by a symmetric hill, as depicted in Figure 4.1(a). Numerical experiments were conducted to investigate the effects of the hill's geometry, the wave type, wave frequency, angle of incidence, and Poisson's ratio on the motion amplification.

4.2.1 Effects of feature's geometry

To investigate the influence of a feature's shape on the resulting motion, we consider: (i) the effect of the geometry idealization, i.e., how differences in similar shapes may

affect amplification, and (ii) the effect of shape ratio (the height to base ratio) for a fixed geometry. In this section, we focus on the former and discuss the latter in Section 4.2.2. We remark that geological features vary remarkably in shape, making the geometry classification a challenging task. For the purposes of this study, however, we consider only symmetric shapes that, nevertheless, cover a wide range of hills.

Four different hill geometries have been previously reported in the literature: (i) Semi-elliptical and semi-circular hills used in [255, 269, 292], (ii) Bell-shaped hills with an exponential function (Bell-e) proposed by [25, 269, 300], (iii) Bell-shaped hills described by a cosine function (Bell-c) [144], and (iv) triangular hills [254, 255, 252]. We perform the parametric study on all four shapes to review the effects of topography idealization on wave amplifications. The geometry and the area of these hills are described in Table 4.1 using a coordinate system whose origin is on the surface. Figure 4.2 depicts all four shapes for a common height $h = 100$m and a base $b = 100$m. Note that the semi-circular geometry has the largest area, and the Bell-e hill is the steepest idealized hill with the smallest area. The triangular and Bell-c hills have equal areas and, indeed, the Bell-c hill is a smoothened version of the triangular shape without sharp corners. In all cases, the half-space is homogeneous with a Poisson's ratio $\nu = 0.25$.

A sharp corner in the path of the plane waves on the surface would generate Rayleigh waves, whose amplitudes depend highly on the geometry of the hill and the sharpness of the corner. The maximum surface displacement in many cases occurs when the generated Rayleigh waves interfere constructively with each other

Table 4.1: The geometry of hills for $-b \leq x \leq b$, out of this range $y(x) = 0.0$.

Feature's name	**Geometry**	**Cross section area**
Semi-elliptical	$y(x) = h\sqrt{1 - (\frac{\|x\|}{b})^2}$	$\frac{\pi}{2}bh$
Bell-c	$y(x) = 0.5h(1 + \cos(\pi\frac{\|x\|}{b}))$	bh
Bell-e	$y(x) = h(1 - (\frac{\|x\|}{b})^2)\exp(-3(\frac{\|x\|}{b})^2)$	$0.86bh$
Triangle	$y(x) = h(1 - \frac{\|x\|}{b})$	bh

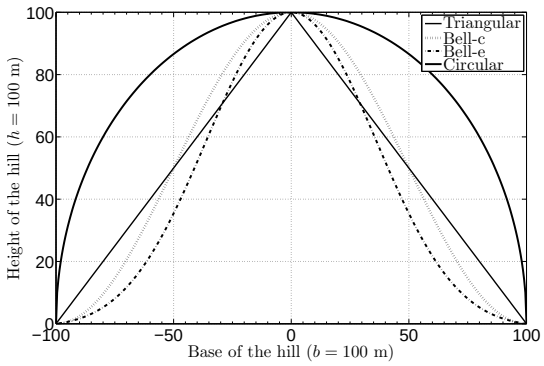

Figure 4.2: Geometry of four idealized hills considered in this study for a common height of $h = 100$m and a base $b = 100$m

within the feature. This is a key reason that different hill geometries show different amplifications, as we will see in this section.

Figure 4.3 compares the maximum displacements on the surface of the four idealized hills due to vertically propagating plane waves with frequencies ranging from $\eta = 0.1$ to 2.0, in increments of 0.1. The maximum displacement in this figure is normalized with respect to the flat surface solution u^{ff}, whenever the latter is non-zero (Section 3.1.1).

We note first the fluctuating amplification pattern of the semi-circular hill; for the other three shapes, the variation of amplification follows a smoother trend. For

example, the horizontal amplification of the semi-circular hill is 2.70 for an incident P-wave of frequency $\eta = 0.5$, while the amplification for the other geometries is around 1.20; by contrast, for $\eta = 1.5$ the semi-circular amplification is 1.52, while it is 2.55 for the triangular hill. We conjecture that at certain frequencies, the convexity of the semi-circular feature assists in the trapping of energy better than any other of the three shapes.

The other distinct pattern is the difference between the amplifications of the triangular hill and Bell-c hill, even though they have equal areas. For instance, the vertical displacement due to an incident SV with frequency $\eta = 1.5$ is only 2.01 on the surface of the triangular hill, however, it is 3.40 for the Bell-c hill. The difference can be attributed to the sharper corners that the triangular hill has in comparison to the Bell-c hill that leads to strong Rayleigh wave patterns within the feature. We also note that the two smooth Bell-shaped hills, though very close in shape, experience different amplifications, particularly for the horizontal component due to P incidence (Figure 4.3(c)). For example, the Bell-c hill horizontal amplification is 2.25 for $\eta = 0.8$, while it is 1.76 for the Bell-e hill. In summary, the observed differences between the amplifications indicate the strong effect the feature's idealization has on the amplification patterns.

Figure 4.4 displays the maximum surface amplifications of different geometries for plane waves with angle of incidence $\theta = 15^\circ$. Similar conclusions can be drawn for this angle of incidence, even though the amplifications are overall larger in comparison to the vertical incidence. The amplification pattern of the semi-circular hill is more rugged as opposed to the smoother amplification patterns of the other geometries.

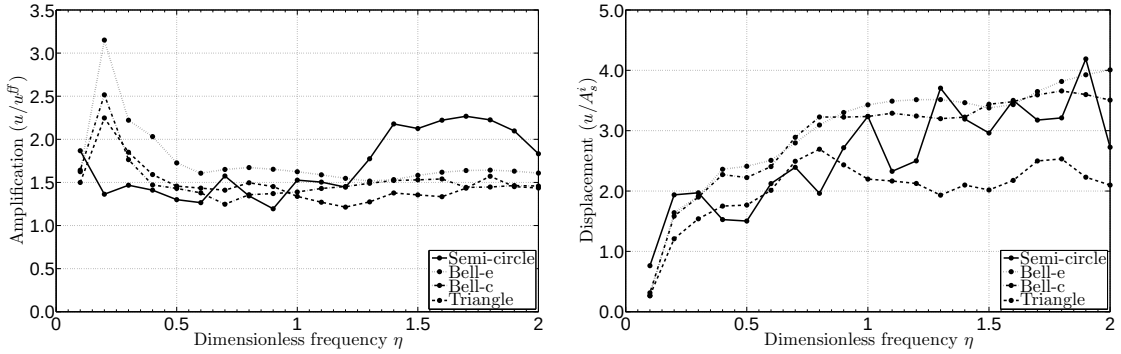

(a) Horizontal amplification due to SV-wave

(b) Vertical displacement due to SV-wave

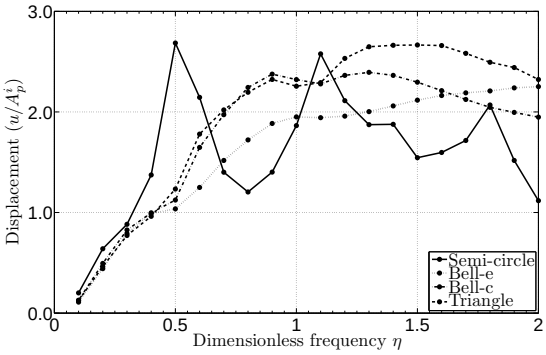

(c) Horizontal displacement due to P-wave

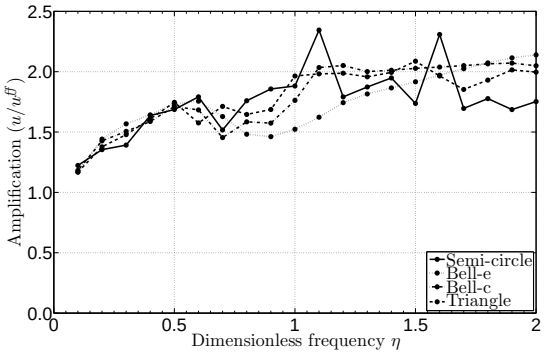

(d) Vertical amplification due to P-wave

Figure 4.3: Comparison of the maximum surface amplifications for four idealized topographies due to vertically propagating incident waves

For example, the horizontal amplification of the semi-circular hill is 4.40 for an incident P with frequency $\eta = 0.5$, while the amplification for the other geometries is around 2.70; the vertical amplification varies from 3.6 for the semi-circular hill to 5.35 for the Bell-c hill, 4.7 for triangular and 6.35 for the Bell-e for an incident SV with frequency $\eta = 1.0$, i.e., with a wavelength equal to the feature's height or, equal to half of the feature's base. There are again differences between the two Bell-shaped hills: for example, the vertical amplification due to SV incidence is 5.3 for the Bell-c shape at $\eta = 1.0$, but the corresponding Bell-e shape amplification is 6.2. For most

frequencies, the Bell-c hill yields larger amplifications for SV incidence and smaller amplifications for P incidence.

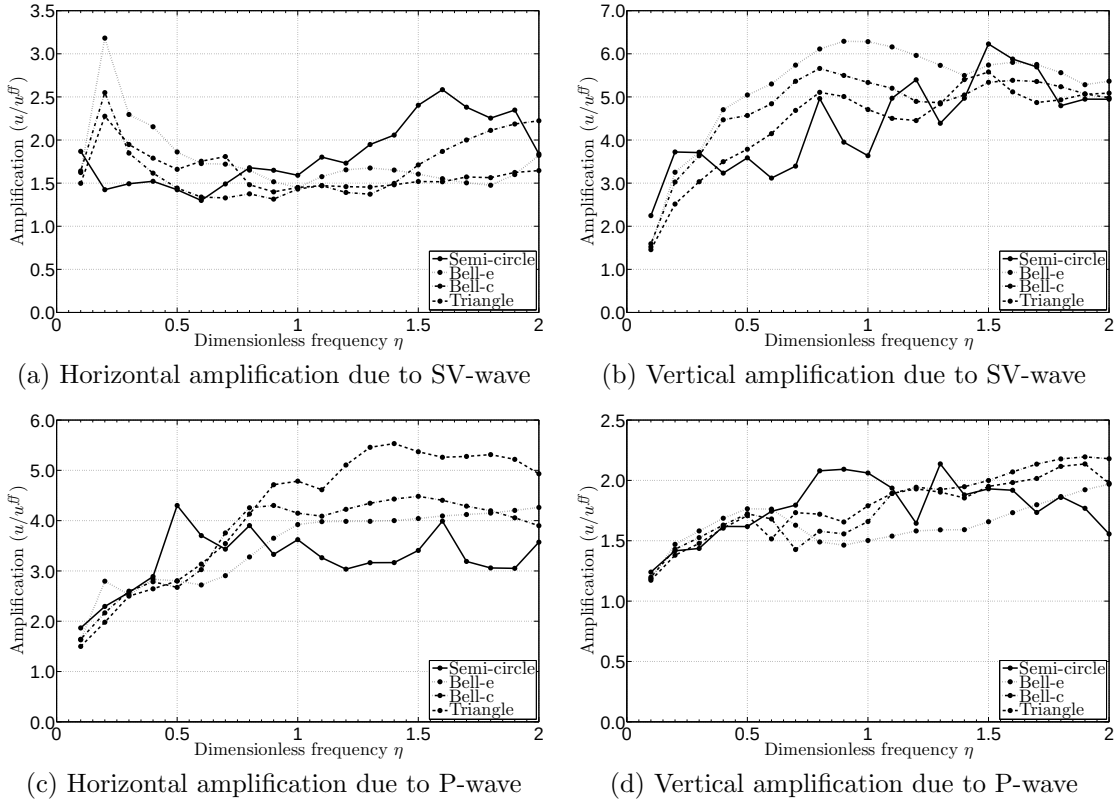

(a) Horizontal amplification due to SV-wave

(b) Vertical amplification due to SV-wave

(c) Horizontal amplification due to P-wave

(d) Vertical amplification due to P-wave

Figure 4.4: Comparison of the maximum surface amplifications for four idealized topographies due to incident waves of the angle $\theta = 15^{\circ}$

Not only the maximum surface amplification, but also the overall amplification pattern on the surface is affected by the geometry idealization. Figurs 4.5 and 4.6 depict the surface amplification patterns for four geometries due to SV and P incident waves, respectively. In these figures, the abscissa is the surface coordinate normalized with respect to the base of the feature b, i.e., the feature is always located

between -1 and 1, and the vertical axis is the normalized surface amplification with respect to the flat surface response u^{ff}, whenever $u^{ff} \neq 0$. Notice that, on the surface, the vertical displacement due to a vertically propagating SV, and also the horizontal displacement due to a vertically propagating P are zero. As a result, in these cases, we plot unnormalized surface displacements.

Figure 4.5 indicates that minor changes in the hill's geometry yield remarkable shifts in the amplification pattern on the surface. For example, the semi-circular hill shows larger amplitude oscillations on the flat surface away from the feature, however, the other geometries experience a large amplification mostly within the feature. The amplification patterns of the two Bell-shaped hills are quite similar, but are different in magnitude, even though the two hills are close in geometry. The geometry variation also causes the maximum amplifications to occur at different locations on the surface, particularly for the obliquely incident waves. For instance, the largest vertical amplification in the Bell-e hill occurs almost at the top of the hill with a magnitude 6.3, yet for the semi-circular hill the amplification is 3.6 and the location shifts away from the mid-point.

The role of geometry variation on the surface amplification pattern is even more noticeable for P incidence as shown in Figure 4.6. Not only the patterns and maximum amplifications are different but also the location of the maxima is different. For instance, the maximum displacement for the semi-circular hill occurs closer to the hill top for the horizontal component due to the oblique incidence (Figure 4.6(c)), but for other shapes it is closer to the foothill. The horizontal component is more sensitive to the geometry than the vertical component. For example, for $\theta_p = 0^\circ$, the

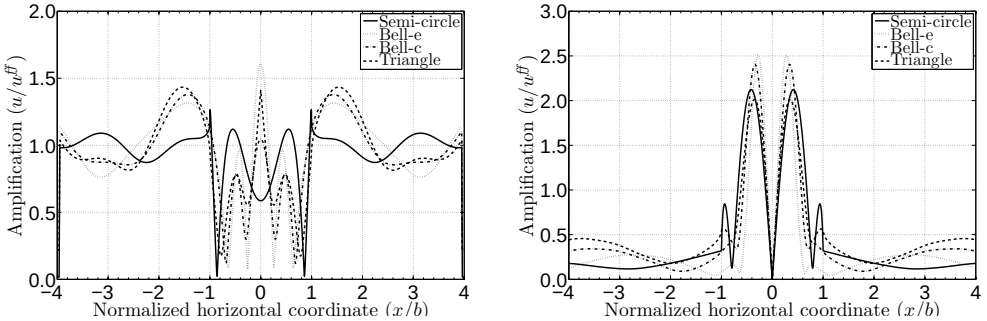

(a) x direction, $\eta = 0.6$, $\theta_s = 0°$ (b) y direction, $\eta = 0.6$, $\theta_s = 0°$

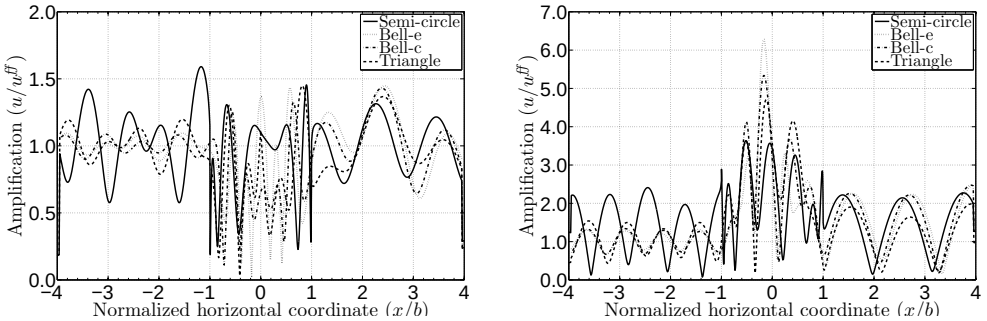

(c) x direction, $\eta = 1.0$, $\theta_s = 15°$ (d) y direction, $\eta = 1.0$, $\theta_s = 15°$

Figure 4.5: Amplification pattern on the surface of four idealized hill's geometries with Poisson's ratio $\nu = 0.25$ due to SV incidence for two different frequencies

horizontal amplification on the surface of the semi-circular hill at $\frac{x}{b} = 0.90$ is just 0.5, when it is 2.0 for the triangular hill; at the same location, the vertical amplification for both the semi-circular and triangular hills is 1.5.

We conclude that even a small change in the idealized model of the topographic feature has a noticeable effect in both the displacement magnitude and pattern. Thus, the idealization of the real topography should be done carefully so that the computational model remains as close as possible to the physical reality.

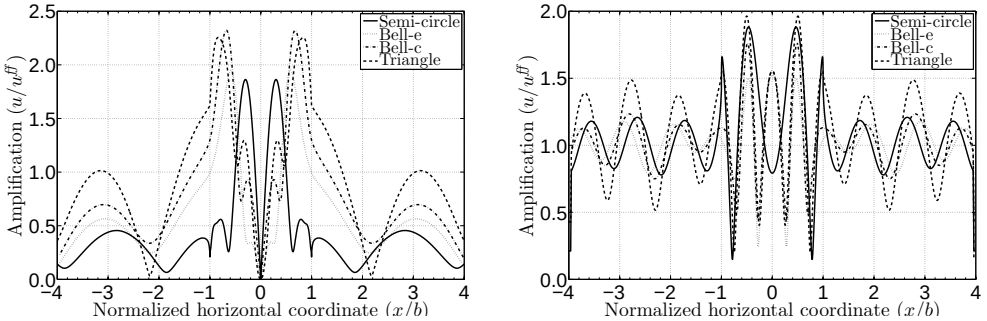

(a) x direction, $\eta = 1.0$, $\theta_p = 0°$ (b) y direction, $\eta = 1.0$, $\theta_p = 0°$

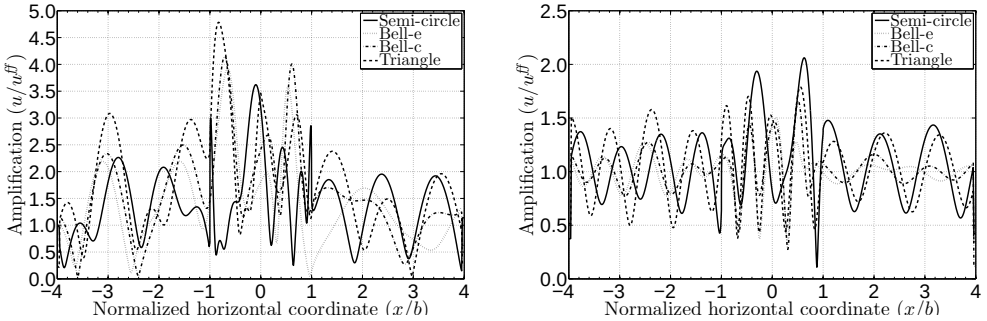

(c) x direction, $\eta = 1.0$, $\theta_p = 15°$ (d) y direction, $\eta = 1.0$, $\theta_p = 15°$

Figure 4.6: Amplification pattern on the surface of four idealized hill's geometries with Poisson's ratio $\nu = 0.25$ due to P incidence

4.2.2 Effects of incident wave frequency

The surface displacement in a flat-surface half-plane domain is independent of the incoming wave frequency, as shown in 3.1.1, while in a domain with surface irregularities, the wave frequency (or equivalently the wavelength) plays an important role on surface displacement. The interest in this section is to explore the dependence of the wave amplification on wave frequency through the dimensionless frequency parameter η defined earlier in (4.1). The influence of the shear wave velocity on the amplification can also be studied using the same parameter η. For example, for a fixed height h, a reduction in η is equivalent to an increase in the incident

shear wavelength (see (4.1)), which can be interpreted as either a reduction in the frequency or as an increase in the shear wave velocity.

We consider a Bell-e hill with a fixed height $h = 100$ and three different shape ratios $S_r = \arctan(h/b) = 15^\circ, 30^\circ$ and 45° (see Table 4.1). The domain is homogeneous with Poisson's ratio $\nu = 0.25$. We plot the normalized maximum amplification on the surface against η for different angles of incidence, irrespective of where the maximum displacement occurs on the surface. The amplification location will be discussed at the end of this section. We use a small frequency increment $\Delta\eta = 0.1$. Notice that the higher η is, the smaller the wavelength is in comparison to the height of the hill.

Figure 4.7 displays the maximum amplifications on the surface of a hill with shape ratio $\arctan(h/b) = 45^\circ$ for SV and P incident waves. The horizontal amplifications due to SV incidence are very close for the two smallest frequencies $\eta = 0.1$ and 0.2 (large incident wavelength in comparison to the hill's height) for all angles of incidence (Figure 4.7(a)). This is accompanied by a sharp jump from a horizontal amplification of 1.6 to 3.4 once the frequency increases from $\eta = 0.1$ to 0.2. As the dimensionless frequency η rises to almost 1.0, the amplification reduces and remains, eventually, almost constant for all angles and higher frequencies, i.e., for wavelengths smaller than the hill's height. The main exception here is for $\theta_s = 20^\circ$, where the amplification rises to 2.5 for $\eta = 3.7$. The least amplification is for $\theta_s = 35^\circ$, which is close to the critical angle $\theta_s^{cr} = 35.26^\circ$ for this material property.

Figure 4.7(b) shows the normalized maximum vertical amplifications due to SV incidence versus the wave frequency for various angles of incidence. The vertically

propagating SV-wave ($\theta_s = 0°$) is excluded from this graph because the vertical displacement on the surface of a flat domain vanishes for this angle (see 3.1.1). We note that the vertical amplifications are much larger than the horizontal ones. For example, the vertical amplification for $\eta = 2.0$ and $\theta_s = 5°$ is 18.2, while the corresponding horizontal amplification is only 1.6. The reason is that the vertical displacement on the flat domain, which we use to obtain the amplification, is much smaller than the horizontal displacement for angles of incidence less than the critical angle (see the free-field solution for a flat half-plane in Figure 3.3).

We remark that the overall amplification tends to reduce steadily as the angle of incidence increases, except for $\theta_s = 35°$. For example, the larger amplification for $\theta_s = 5°$ is 19.0 at $\eta = 1.1$, while the largest amplification for $\theta_s = 30°$ is only 2.0 at $\eta = 1.9$. The reason, as shown in Figure 3.3, is that the vertical displacement on the surface of a flat domain increases as the angle of incidence increases to $\theta_s = 30°$, and then drops quickly for $\theta_s = 35°$. Hence, we expect to see lower amplifications for higher angles of incidence except for $\theta_s = 35°$, which, by contrast, shows a larger amplification. Note again that, similar to the horizontal amplification, amplifications for each angle of incidence are almost constant for all frequencies, except for low frequencies ($\eta < 1.0$).

The horizontal and vertical amplifications for P incidence are plotted in Figurs 4.7(c) and 4.7(d), respectively. Since the horizontal displacement on a flat half-plane is zero for a vertically propagating wave, we do not report it for $\theta_p = 0°$. Similar to the SV incidence case, the horizontal amplification reduces as the angle of incidence rises, but for each angle, particularly for $\theta_p > 25°$, the amplification

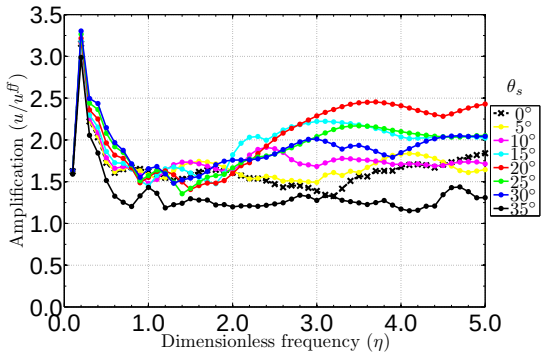

(a) Horizontal amplification due to SV-wave

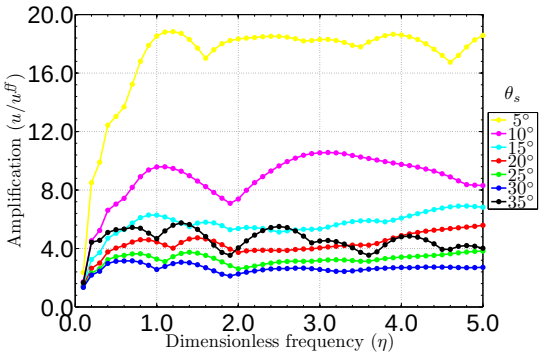

(b) Vertical amplification due to SV-wave

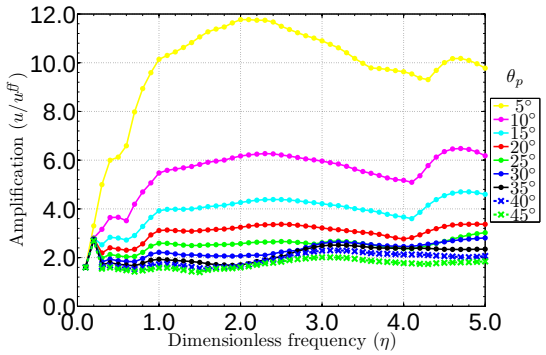

(c) Horizontal amplification due to P-wave

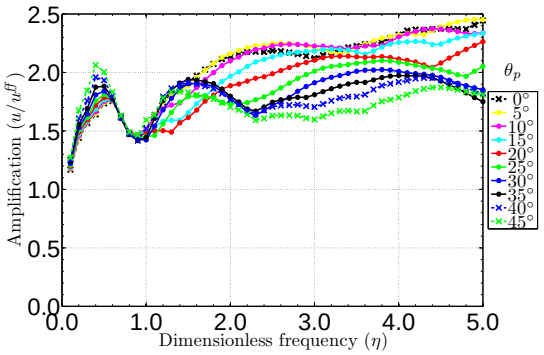

(d) Vertical amplification due to P-wave

Figure 4.7: Maximum amplification on the surface of the Bell-e hill of shape ratio 45°

remains almost constant for frequencies above 2.0, or equivalently for wavelengths half the hill's height or smaller. The largest horizontal amplification is about 12 for $\theta_p = 5°$, which is less than the amplification due to the SV incidence: the vertical amplifications are typically smaller than the horizontal ones. The variation of vertical amplification with frequency is more noticeable in the P incidence case, and becomes less prominent for higher frequencies. The angle of incidence does not seem to be playing a significant role for frequencies $\eta < 2$, but for higher frequencies the amplifications get smaller as the angle of incidence grows.

For a shape ratio of 45°, we note that even a small feature, i.e., a small η, causes significant amplification. The topography may amplify incident waves by as much as 19 times, particularly waves propagating at a vertical or close to a vertical direction. In general, as the angle of incidence increases, the amplification reduces. The only exception is the case of SV incidence at angles close to the critical angle.

Figure 4.8 is the counterpart of Figure 4.7 for a hill with a shape ratio of 30°. Overall, the findings are similar to those drawn for $S_r = 45°$, however, amplifications are overall smaller in comparison to the sharper shape ratio of 45°, for both horizontal and vertical components. The incident waves with smaller angles of incidence experience larger amplifications except for the SV incidence with $\theta_s = 35°$, where the amplification is greater than the one corresponding to $\theta_s = 15°$. Likewise, the vertical amplification of SV incidence is greater than the horizontal amplification. For instance, the largest vertical amplification is 15 at $\eta = 2.5$, and only 2.7 for the horizontal amplification at $\eta = 3.0$. By contrast, for P incidence, the horizontal amplifications are greater than the vertical ones. For the same wave, the horizontal amplification is almost constant for waves of incidence greater than 25°, but the amplification for smaller angles depends on the wave frequency, particularly if $\eta < 0.9$. For example, the amplification is almost 1.6 for $\theta_p = 45°$, regardless of the frequency, but varies from 2 to 12 for $\theta_p = 5°$ as the frequency increases. The vertical amplification is about the same for all angles of incidence, and remains the same for frequencies above 3.0.

The maximum amplification on the surface of the hill of shape ratio 15° is depicted in Figure 4.9 for P- and SV-wave incidence. We note the lower amplifications

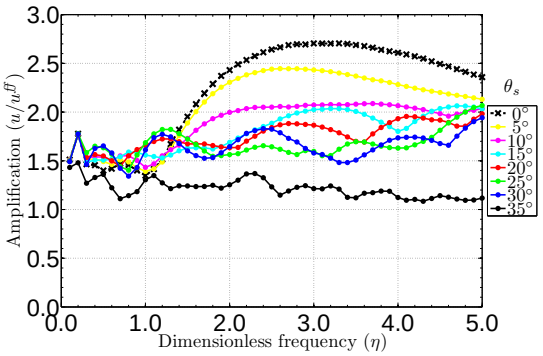

(a) Horizontal amplification due to SV-wave

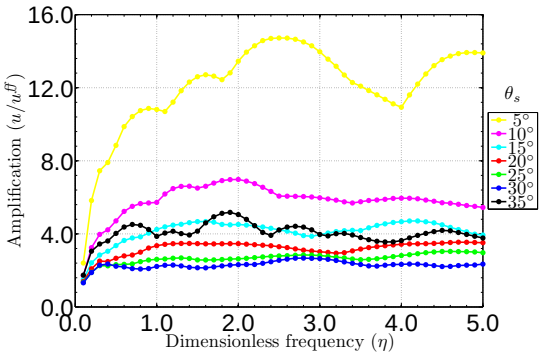

(b) Vertical amplification due to SV-wave

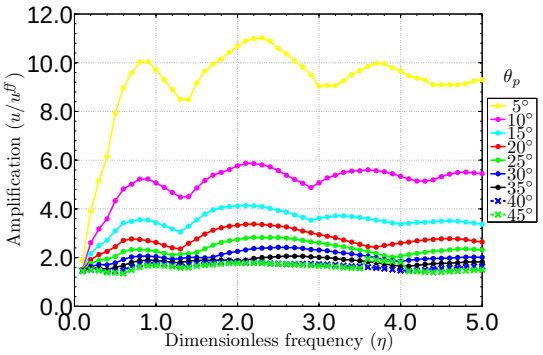

(c) Horizontal amplification due to P-wave

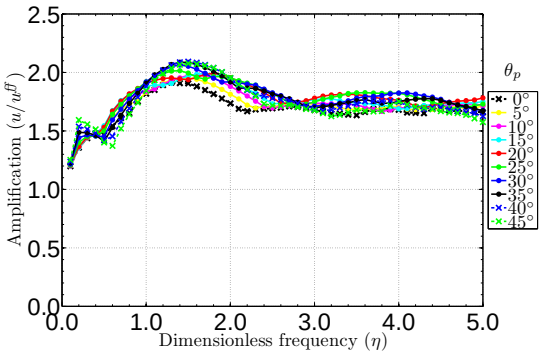

(d) Vertical amplification due to P-wave

Figure 4.8: Maximum amplification on the surface of the Bell-e hill of shape ratio 30°

in comparison to the other shape ratios. For example, the horizontal amplification due to SV incidence barely reaches 2.0 and the vertical amplification is only 4.6, while the same values for the sharpest hill are 3.4 and 18, respectively. The reason can be attributed to the flatter geometry of this shape ratio that allows the waves to escape the feature quickly, as opposed to the sharper hill case, where the energy gets trapped within the hill.

Amplifications of P-waves appear to be independent of the wave frequency and stay almost constant for each angle of incidence except for the low frequencies

($\eta < 1.5$). This implies that a flatter hill does not affect incident waves for which the wavelength is several times greater than the hill's height. Another noteworthy pattern for this shape ratio is that the largest vertical amplification is due to the largest angle of incidence $\theta_s = 35°$, while other incidence angles result in substantially smaller amplifications.

In conclusion, wave amplification depends on the incident wave frequency if the frequency is such that the wavelength is comparable to the feature's height, otherwise, if the hill's height is several times greater than the wavelength (large η), the amplification, while significant, is almost frequency independent. Additionally, a sharper hill tends to amplify waves more in comparison to a flatter hill owing to energy trapping within the feature.

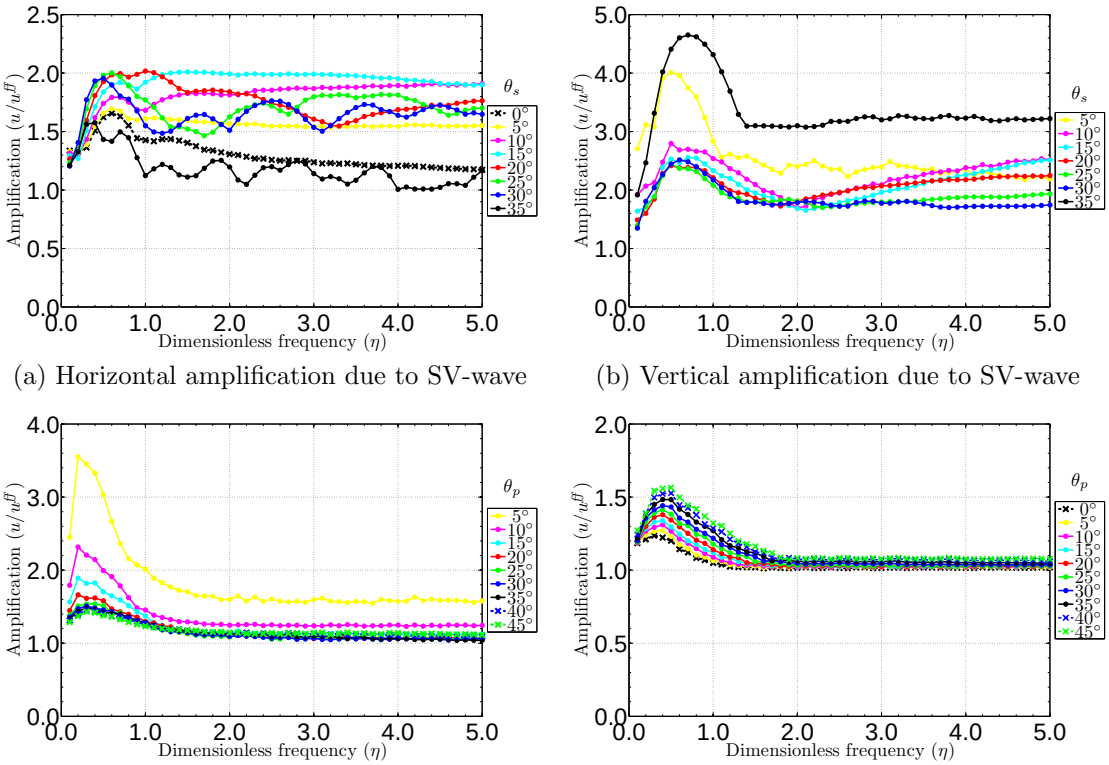

(a) Horizontal amplification due to SV-wave

(b) Vertical amplification due to SV-wave

(c) Horizontal amplification due to P-wave

(d) Vertical amplification due to P-wave

Figure 4.9: Maximum amplification on the surface of the Bell-e hill of shape ratio 15°

Location of the maximum amplification on the surface

In this section, we discuss the maximum amplification location. Figure 4.10 displays the location of maximum amplification on the surface of the Bell-e hill with shape ratio $\arctan(h/b) = 45°$ for various incidence angles of SV and P incidence. The hill is located between -1 and $+1$. The location of maximum amplification for SV incidence is primarily within the hill, not exactly at the top of the hill, but slightly shifted away toward the sides. This fact is in agreement with the previous observation that wave amplification is due to the trapped energy within the hill. The only major

exception here is the SV incidence at $\theta_s = 35°$, where, for several frequencies, the location of the maximum amplification is on the flat surface away from the feature. The location of maximum vertical amplification for P incidence is within the feature. For the horizontal amplification and at low frequencies, the maximum occurs away from the feature, however, as the frequency increases, the location shifts closer to the feature and finally falls within the feature for all frequencies above 2.5. Similar patterns are observed for hills with shape ratios other than $S_r = 45°$.

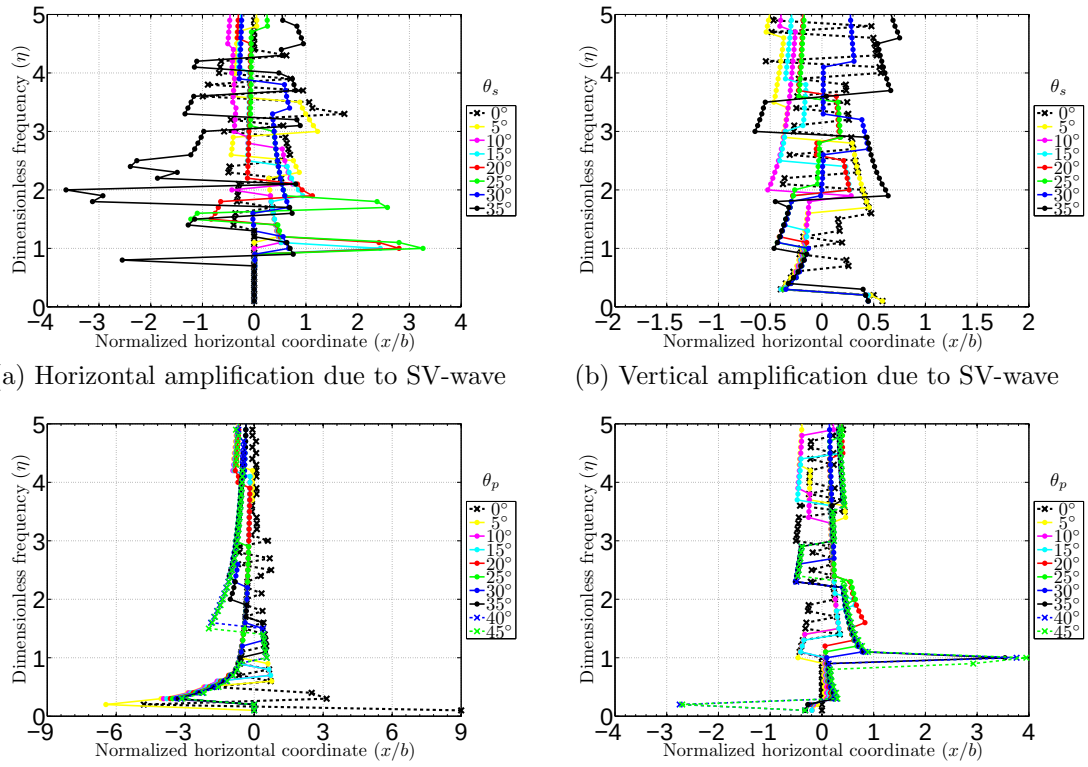

(a) Horizontal amplification due to SV-wave

(b) Vertical amplification due to SV-wave

(c) Horizontal amplification due to P-wave

(d) Vertical amplification due to P-wave

Figure 4.10: Location of the maximum amplification on the surface of the Bell-e hill with shape ratio 45°

4.2.3 Effects of angle of incidence

In this section, we consider the effects of the angle of incidence on the amplification. Toward this end, the scattering of plane waves by the Bell-e hill of shape ratio $\arctan(h/b) = 45^\circ$ embedded in a homogeneous medium of Poisson's ratio $\nu = 0.25$ is considered. We plot maximum surface amplifications, irrespective of location, against the angle of incidence, ranging from 0° to 35° for plane SV incidence, and from 0° through 45° for plane P incidence, for a few selected frequencies. The angle of incidence, as depicted in Figure 4.1, is measured from the vertical axis.

Figurs 4.11(a) and 4.11(b) display the maximum horizontal and vertical surface amplifications, respectively, for SV wave against the variation of angle of incidence in a Bell-e hill of shape ratio 45°. The horizontal amplification increases for frequencies higher than $\eta = 2.0$, as the angle of incidence increases to 20°, and then drops for higher angles. However, for smaller frequencies, i.e., small feature size in comparison to the wavelength, the amplification is almost independent of the incidence angle. The vertical amplification, on the other hand, falls sharply to 2.5 from 18 as the angle of incidence increases from 5° to 30°, and slightly increases to 4.0 at 35° for almost all frequencies. The very low frequencies, e.g., $\eta = 0.1$, are less affected by the incidence angle, similar to the horizontal amplification. In summary, the vertical displacement is more sensitive to the variation of incidence angle for the SV-wave.

According to Figure 4.11(c), the horizontal amplification continuously reduces for all frequencies as the angle of incidence increases, except at very low frequencies where it seems to be less affected by the angle of incidence. For example, the am-

plification reduces from 12 to 1.8 as the angle of incidence increases from 5° to 45° for frequencies higher than 1.5. The vertical amplifications in Figure 4.11(d) are not changing remarkably with the angle of incidence, staying almost constant for all angles.

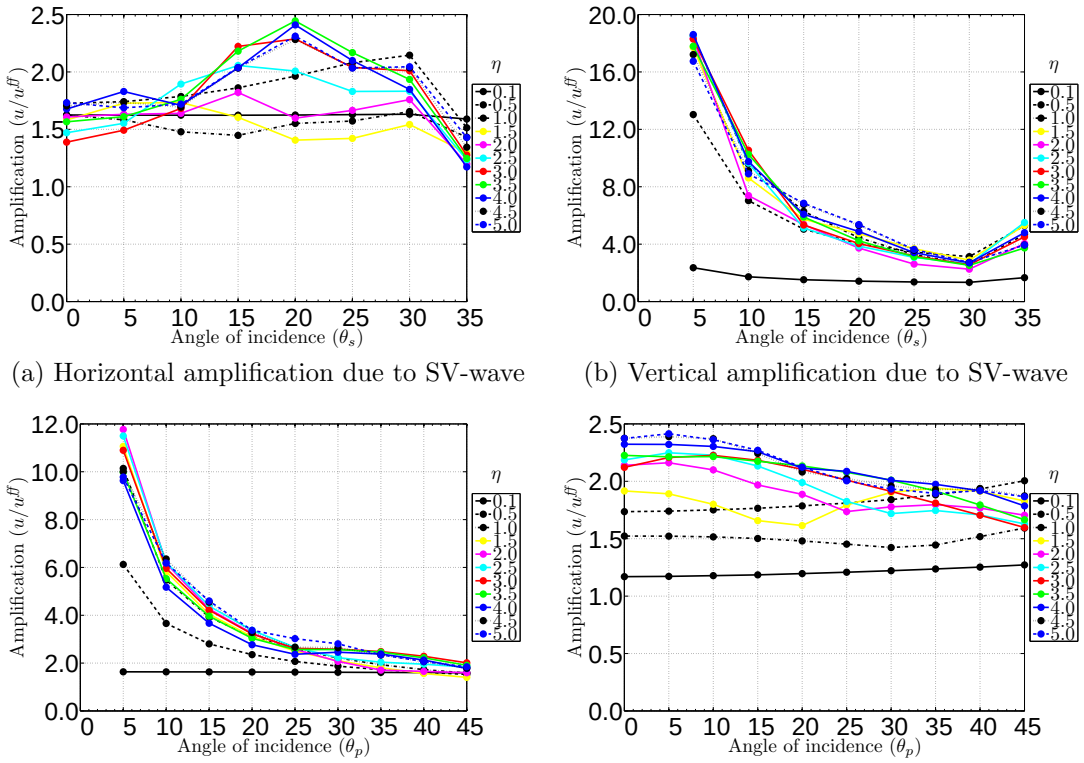

(a) Horizontal amplification due to SV-wave

(b) Vertical amplification due to SV-wave

(c) Horizontal amplification due to P-wave

(d) Vertical amplification due to P-wave

Figure 4.11: Maximum amplification on the surface of the Bell-e hill of shape ratio 45°. Angles of incidence are changing at 5° increment

Figure 4.12 shows the amplification for a Bell-e hill of shape ratio 30° and $\nu = 0.25$. Similar conclusions can be obtained for this shape ratio. In comparison with the steeper hill, $\arctan(h/b) = 45°$, amplifications are smaller for this feature,

except for the horizontal amplification of SV incidence, where amplifications are slightly larger for $\theta_s < 15°$. The reason for smaller amplifications might be attributed to the wider character of this shape ratio, which allows the waves to leave the feature with less reflections from the sides, thus reducing the likelihood of amplification.

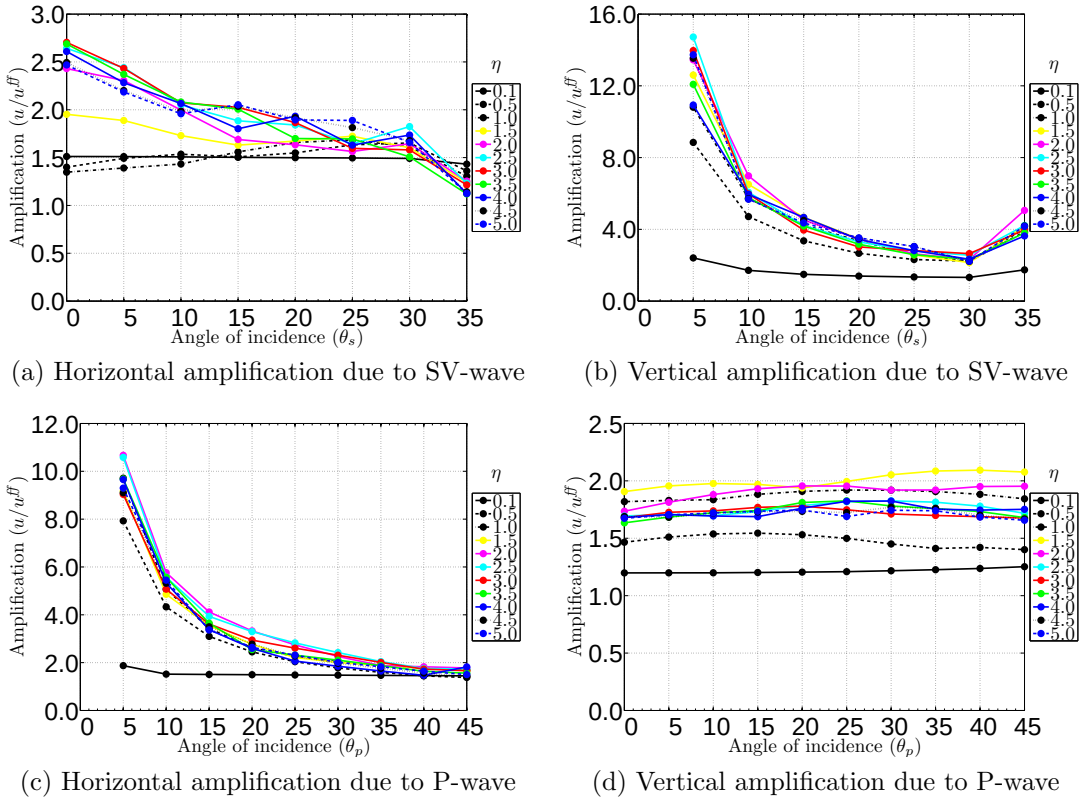

(a) Horizontal amplification due to SV-wave

(b) Vertical amplification due to SV-wave

(c) Horizontal amplification due to P-wave

(d) Vertical amplification due to P-wave

Figure 4.12: Maximum amplification on the surface of the Bell-e hill of shape ratio 30°

Figure 4.13 depicts the maximum surface amplification for the very wide hill of shape ratio $\arctan(h/b) = 15°$. The variation of amplification with respect to the angle of incidence is minor and the maximum amplifications for all angles of incidence are significantly smaller than those of the steeper hills.

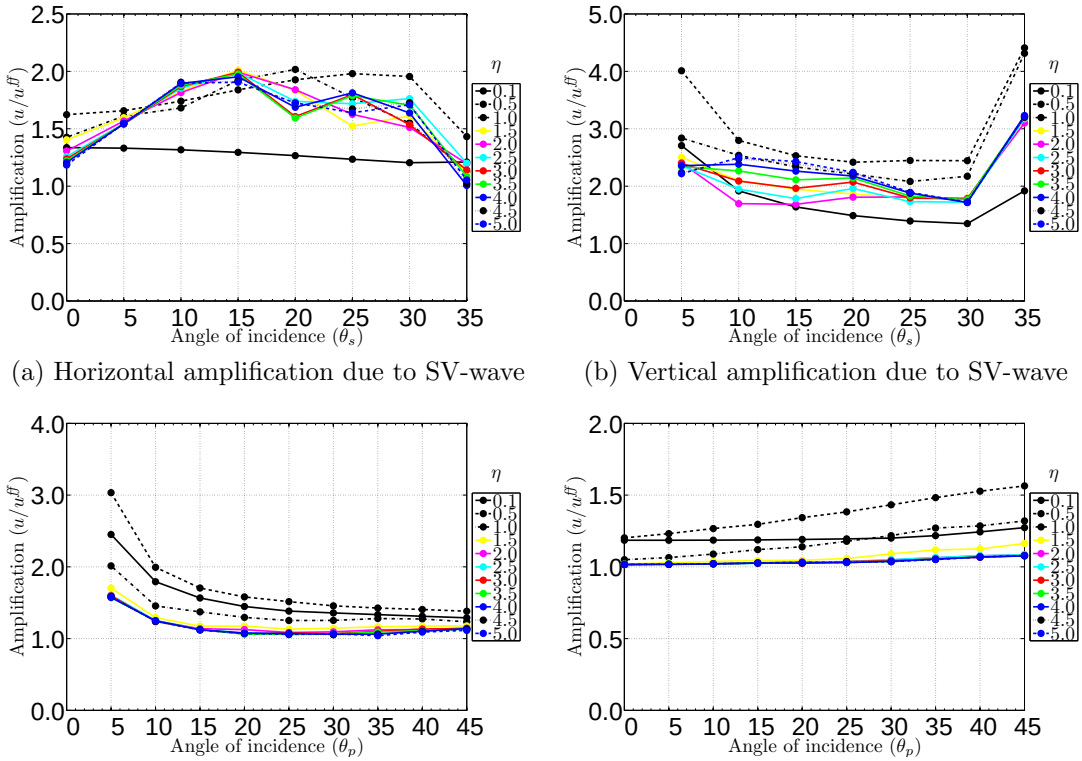

(a) Horizontal amplification due to SV-wave

(b) Vertical amplification due to SV-wave

(c) Horizontal amplification due to P-wave

(d) Vertical amplification due to P-wave

Figure 4.13: Maximum amplification on the surface of the Bell-e hill of shape ratio 15°

We note that larger amplifications can be reached for vertically or near-vertically propagating waves. As the angle of incidence increases, the amplification, overall, reduces. The only exception here is the SV incidence, where the amplification rises again just before the critical angle.

4.2.4 Poisson's ratio effects

We consider the Bell-e hill of shape ratio $\arctan(h/b) = 45°$ embedded in a homogeneous domain with mass density $\rho = 2000\text{kg/m}^3$, shear modulus $G = 100\text{MPa}$, and

use three Poisson's ratios $\nu = 0.25$, 0.33, and 0.40 to examine the effects of Poisson's ratio on the surface amplification. In this section, we consider the amplification of P- and SV-waves with only two angles of incidence, $\theta = 0^\circ$ and 15°, and the dimensionless frequency ranging from $\eta = 0.1$ to 5.0. Similar to the previous sections, the surface displacements have been normalized with respect to the flat-surface displacements, whenever the latter are non-zero.

We recall that the dimensionless frequency η is normalized with respect to the shear wavelength (see Figure 4.1), thus, a change in Poisson's ratio, while the mass density and shear modulus are fixed, does not change this dimensionless frequency, but does affect the P-wave velocity/wavelength.

Figure 4.14 shows the maximum amplification on the surface of the Bell-e hill for vertically propagating P and SV incident waves. The results suggest that for SV incidence, the horizontal amplification and the vertical displacement are not significantly affected by changes in Poisson's ratio, for all frequencies. The reason is a vertically propagating SV wave reflects from the flat surface as SV only, without any P-wave generated. Thus, as explained earlier in this section, since a change in Poisson's ratio only does not alter the SV wave, the amplifications remain the same for all frequencies. Even though, the reflection from the feature leaves a P-wave in the domain, that does not contribute noticeably to the amplification. By contrast, the variation of Poisson's ratio causes noticeable changes for a P incident wave. The effects of Poisson's ratio are different for horizontal amplification (Figure 4.14(c)) than for vertical (Figure 4.14(d)): an increase in Poisson's ratio results in a larger amplification for the horizontal component and a smaller amplification for the vertical

component. For example, the horizontal amplification for $\eta = 3.0$ increases from 2.0 to 2.5 as ν changes from 0.25 to 0.4, while the vertical amplification reduces from 2.2 to 1.6.

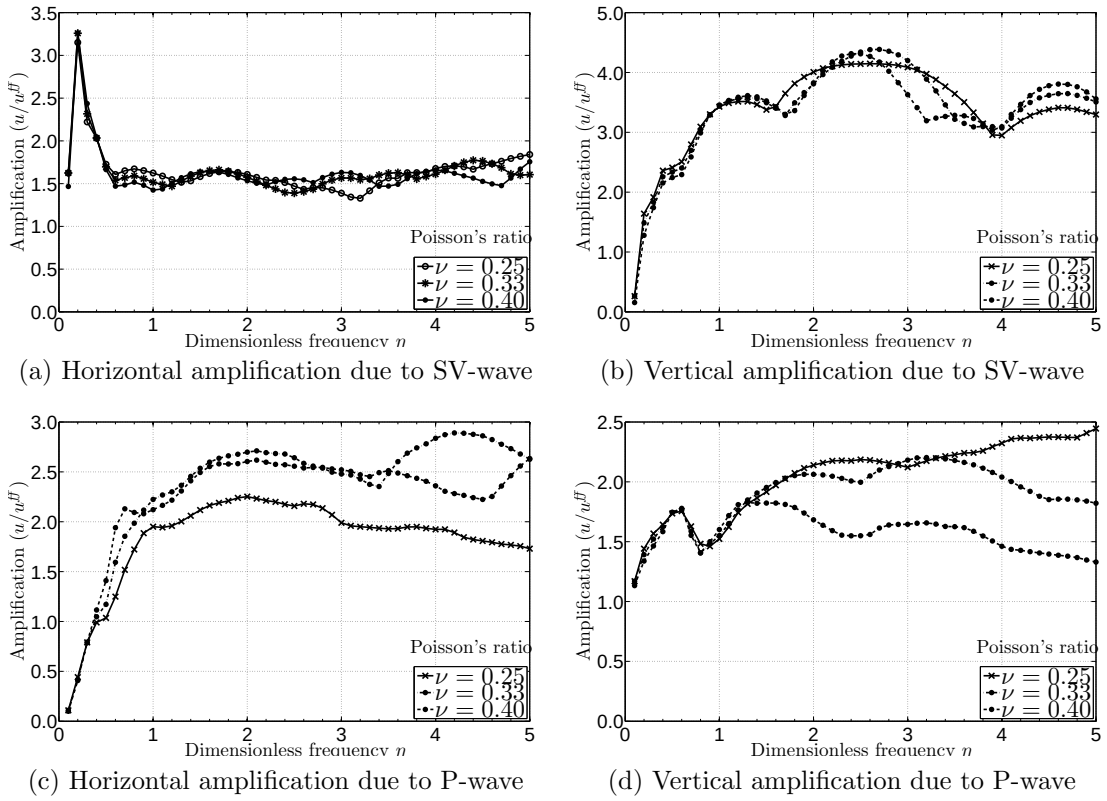

(a) Horizontal amplification due to SV-wave

(b) Vertical amplification due to SV-wave

(c) Horizontal amplification due to P-wave

(d) Vertical amplification due to P-wave

Figure 4.14: Maximum amplification on the surface of a Bell-e hill of shape ratio 45° due to vertically propagating waves

We plotted the maximum surface amplification on the Bell-e hill due to the plane P- and SV-waves, propagating at the incidence angle of 15°, in Figure 4.15. The apparent change, compared to the vertically propagating waves, is the variation of the vertical amplification with Poisson's ratio for SV-wave (Figure 4.15(b)). For

example, the amplification for frequency $\eta = 3.0$ is 10.1 for Poisson's ratio $\nu = 0.40$, while the amplification for $\nu = 0.25$ is 5.1, however, for the same frequency the vertical amplifications are about 3.8 for all Poisson's ratios for a vertically propagating SV-wave (Figure 4.14(b)). The reason is that an oblique SV-wave results in a P-wave reflection from the surface that will have a different wavelength as Poisson's ratio varies. Notice as well that the vertical component of the P wave is more prominent compared to the horizontal component, consequently, the variation of amplification with Poisson's ratio is more significant for the vertical amplification for SV incidence. For the oblique P incidence, the amplification pattern remains the same as the vertical propagation in a way that a rise in Poisson's ratio will lead to a climb in the horizontal amplification and a drop in the vertical ones. The Poisson's ratio variation affects oblique waves more strongly than vertical waves. For instance, the horizontal amplification of the oblique P wave for frequency $\eta = 3$ increases from 4.1 to 7.7 as Poisson's ratio increases from 0.25 to 0.4, whereas for the vertical wave the same values are 2.0 and 2.51, respectively.

We remark that total amplification reduces as Poisson's ratio increases for the P incidence, particularly for frequencies above $\eta = 1.5$, because the vertical surface displacement is larger than the horizontal one. Consequently, even though the horizontal amplification increases sharply, the vertical amplification, which has a larger amplitude, drops, and the result is a total surface amplification reduction. This amplification reduction is expected because as Poisson's ratio increases, the wavelength of the P incidence increases; hence, the feature appears smaller to the incoming wave. The amplification exhibits minor changes for lower frequencies as

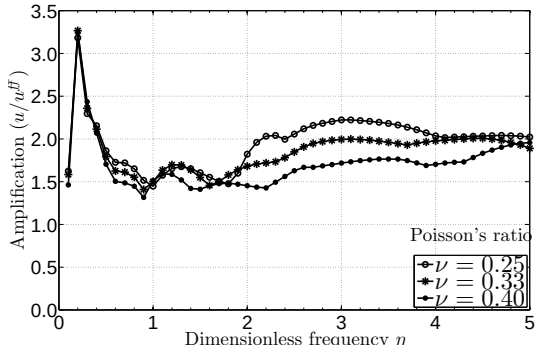

(a) Horizontal amplification due to SV-wave

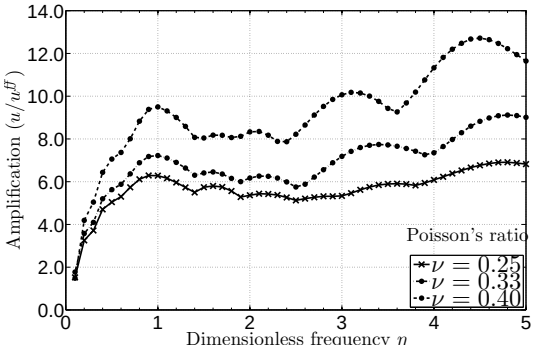

(b) Vertical amplification due to SV-wave

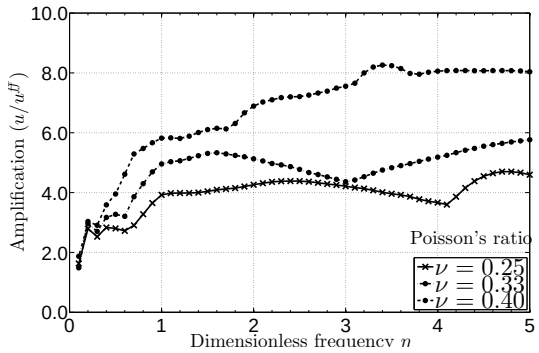

(c) Horizontal amplification due to P-wave

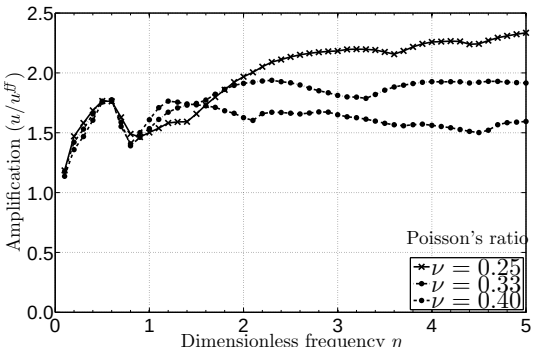

(d) Vertical amplification due to P-wave

Figure 4.15: Maximum amplification on the surface of a Bell-c hill of shape ratio 45° and an angle of incidence of 15°

Poisson's ratio varies, because, in general, the feature is almost invisible to low-frequency incident waves. The trend is quite different for the SV incidence where an increase in Poisson's ratio results in a slightly larger total amplification, because the horizontal displacement, which is greater in magnitude, exhibits a minor change, while the vertical component is amplified. Yet, the total variation remains small, because the magnitude of the vertical component is small.

The variation of Poisson's ratio induces modifications in the amplification pattern on the surface of the domain. To show these effects, we plot the amplification

patterns for three different Poisson's ratios in Figurs 4.16 and 4.17 due to oblique SV and P incident waves, respectively, for a dimensionless frequency $\eta = 2.0$. The horizontal and vertical amplifications caused by the SV incident wave for all three Poisson's ratios are very similar except at the hilltops. The difference is more significant for the vertical amplification. The shift in the amplification is more prominent for the incident P-wave. The difference between the patterns is significant within the feature, yet, mostly the same away from the feature on the flat surface.

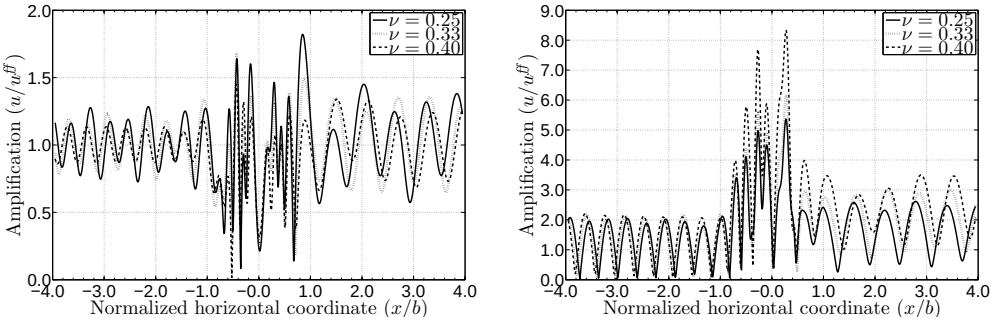

(a) Horizontal amplification

(b) Vertical amplification

Figure 4.16: Amplification pattern on the surface of the Bell-e hill of shape ratio 45° results from an inclined SV incident wave of angle $\theta_s = 15°$ for different Poisson's ratios. The dimensionless frequency is $\eta = 2.0$.

4.2.5 Spatial amplification patterns

In this section, we report the effects the presence of a hill has on the displacement pattern on the surface surrounding the topographic feature.

Figurs 4.18(a) and 4.18(b) show the amplification on the surface of the Bell-e hill with shape ratio $\arctan(h/b) = 45°$ for a vertically propagating SV incidence with frequencies $\eta = 0.6$ and $\eta = 2.0$, respectively. The horizontal axis is normalized

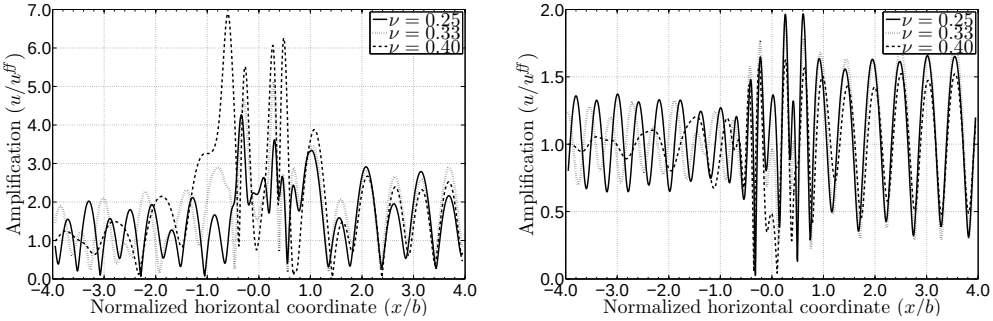

(a) Horizontal amplification (b) Vertical amplification

Figure 4.17: Amplification pattern on the surface of the Bell-e hill of shape ratio 45° results from an inclined P incident wave of angle $\theta_p = 15°$ for different Poisson's ratios. The dimensionless frequency is $\eta = 2.0$.

with respect to the base of the hill such that the feature is located between -1 and $+1$. We only normalize the horizontal amplification with respect to the free-field solution in a flat domain, because the vertical component in the flat domain is zero. The vertical displacement within the feature is quite significant, 2.5 times of the amplitude of the incident wave for $\eta = 0.6$ and 4.0 times of the amplitude of the incident wave for $\eta = 2.0$. However, the amplification on the flat surface around the feature is negligible. More interestingly, stationary points, where the displacement is zero or close to zero, exist on the surface because of the destructive interference of plane and surface waves. The number of stationary points increases as the frequency increases. The symmetry of model and load imposes a symmetric pattern on the surface for both horizontal and vertical displacements. Overall, the strongest amplification occurs mostly within the feature, while it oscillates around one away from the feature.

The surface amplifications for the oblique SV incidence with angle of incidence

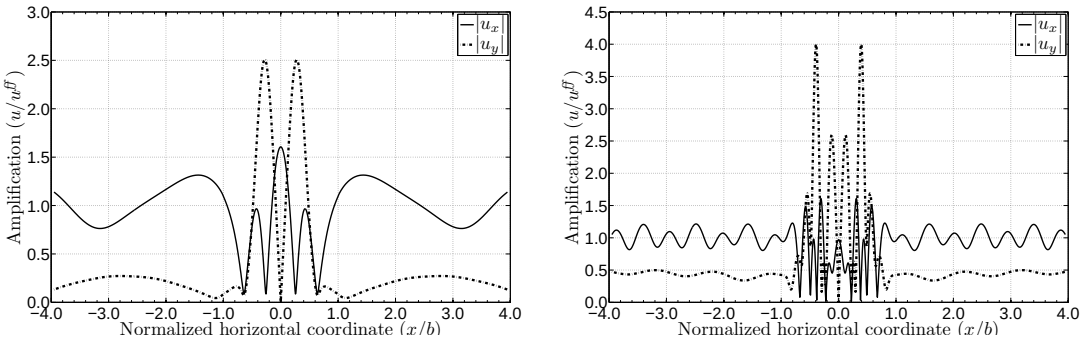

(a) $\eta = 0.6$ (b) $\eta = 2.0$

Figure 4.18: Amplification on the surface of the Bell-e hill of shape ratio 45° for a vertically propagating SV-wave

35° are plotted in Figurs 4.19(a) and 4.19(b) for frequencies $\eta = 0.6$ and $\eta = 1.0$, respectively. The oblique incident wave enters the domain and impinges upon the feature from the left (negative x). Accordingly, the amplification on the flat surface on the left side of the feature exhibits a smaller amplification, while the flat surface on the right side experiences a large amplification. For example, for $\eta = 0.6$, the maximum vertical amplification is only 1.6, whereas it is 2.6 on the right side. For $\eta = 1.0$, the difference is even more prominent, 1.7 versus 3.6. Note, however, the maximum amplification occurs on the left slope of the feature. In summary, the presence of a hill in the propagation path of an oblique SV incident wave results in surface amplification on the hill, and on the forward scatter region of the feature. We conducted similar experiments with oblique P-waves and reached analogous conclusions.

Thus far, we only focused on the amplification effects that topography causes on the surface displacement. Indeed, in some cases, de-amplification may also develop. For example, the surface amplification due to the propagation of P-wave with

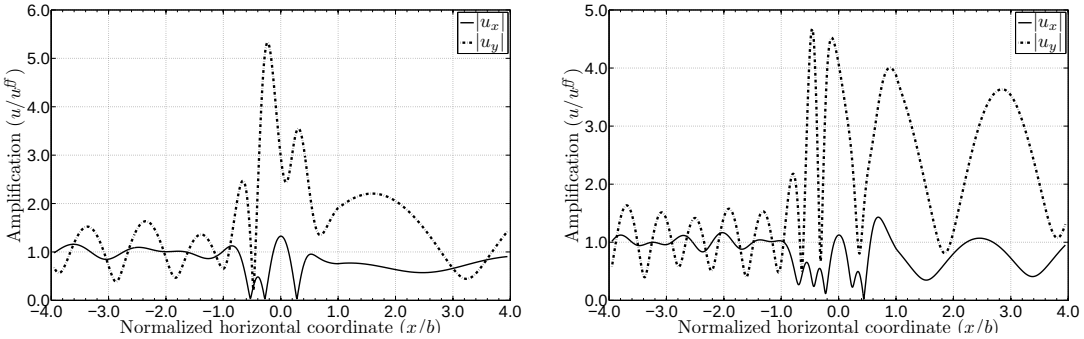

(a) $\eta = 0.6$ (b) $\eta = 1.0$

Figure 4.19: Amplification on the surface of the Bell-e hill of shape ratio 45° for the oblique SV-wave with angle $\theta_s = 35°$

angle $\theta_p = 45°$ in a hill with shape ratio $\arctan(h/b) = 45°$ shows de-amplification at some locations (see Figure 4.20). The horizontal amplification for $\eta = 0.6$ de-amplifies within the entire feature to the extent that it reduces to 0.2 at one point. A remarkable de-amplification of the vertical component occurs as well on the left side of the hill. For the higher frequency, as shown in Figure 4.20(b), de-amplification is less prominent.

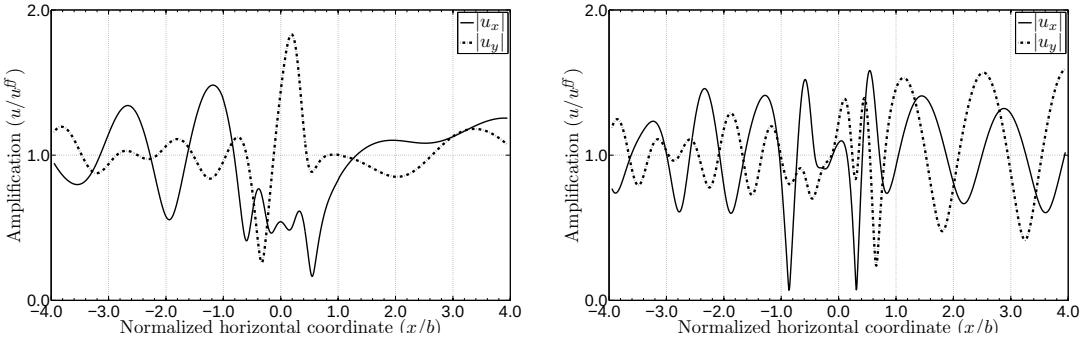

(a) $\eta = 0.6$ (b) $\eta = 1.0$

Figure 4.20: Amplification on the surface of the Bell-e hill of shape ratio 45° for the oblique P-wave with angle $\theta_p = 45°$

Figure 4.21 displays the surface amplification on the surface of a hill with shape ratio of $\arctan(h/b) = 15^\circ$ due to SV incidence. A flat hill, as expected, leads to small amplifications in comparison to a steep hill. For the vertically propagating SV incidence shown in Figure 4.21(a), the horizontal amplification oscillates rapidly around one, while the magnitude barely reaches to 1.25. The vertical displacement is almost negligible. For an oblique SV incidence, as shown in Figure 4.21(b), with an angle $\theta_s = 35^\circ$, no amplification occurs on the flat surface on the left side of the feature where the wave hits the domain first, however, there is a significant amplification on the feature and also on the forward scatter region. By contrast, the horizontal component experiences a de-amplification within and away from the feature on the flat surface to the right.

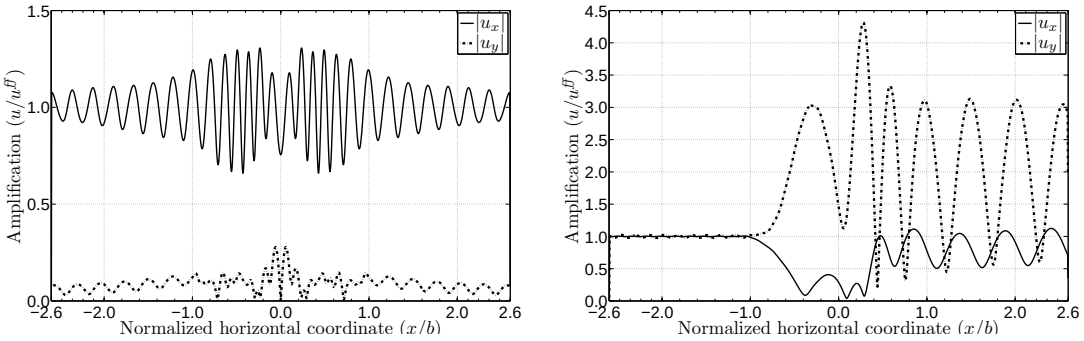

(a) $\theta_s = 0^\circ$, $\eta = 2.0$ (b) $\theta_s = 35^\circ$ and $\eta = 1.0$

Figure 4.21: Amplification on the surface of the Bell-e hill of shape ratio 15° due to the plane SV wave

4.3 Parametric study on valleys

In this section, we report parametric studies on the effect valleys have on the amplification/de-amplification of seismic waves. We use a two-dimensional linear elastic, homogeneous half-plane with Poisson's ratio $\nu = 0.25$, mass density $\rho = 2000\text{kg/m}^3$, and shear modulus $G = 100\text{MPa}$. The only shape ratio that we consider for this section is $\arctan(h/b) = 45^\circ$, where b is the base and h is the depth of the valley, as depicted in Figure 4.1(b). The dimensionless frequency for the incident wave is again defined as $\eta = h/\lambda_s$, which is the ratio of the valley's depth to the shear wavelength.

4.3.1 Effects of feature's geometry

This section discusses the effect the idealization of the valley's geometry has on the surface amplification. Here, we use again the same four geometry functions defined previously in Table 4.1, but flip the geometry with respect to the x axis to idealize valleys. We use a single dimensionless frequency $\eta = 1.0$, and two angles of incidence $\theta = 0^\circ$ and 15° for P- and SV-waves.

Figure 4.22 displays the surface displacement, normalized with respect to the free-field solution, whenever the displacement is non-zero, for vertically propagating SV- and P-waves. The horizontal axis of this figure runs along the surface, and is normalized with respect to the base of the valley such that the valley is always located between -1 and $+1$. The maximum horizontal amplification due to SV wave occurs on the flat surface away from the valley; it is around 1.5 for all four geometries, with the triangular valley showing the largest amplification. The difference between the amplification pattern of the various geometries is more interesting within the feature:

the semi-circular valley exhibits a small amplification, whereas all other geometries show de-amplification. Conversely, the semi-circular valley shows the least vertical amplification (Figure 4.22(b)) within the valley, but the largest on the flat surface, i.e., 2.8 versus 1.95. In terms of the surface pattern, all geometries are quite similar with the exception of the semi-circular valley, which shows a sharp drop and rise at the valley ends, for both horizontal and vertical displacements.

The contribution of the valley idealization is more prominent for the P incidence as shown in Figurs 4.22(c) and 4.22(d). The amplification patterns for the various geometries are relatively different, with the Bell-e valley showing the largest amplifications, both horizontal and vertical, while the smallest amplification is associated with the triangular valley. Seemingly, for P- and SV-waves, the amplification within the valley is less than the amplification on the flat surface, and at a few locations de-amplification occurs.

Figure 4.23 shows the amplification pattern on the surface of the four geometries for oblique incident waves with $\theta = 15^{\circ}$. Similar conclusions can be drawn here. Among them is the apparent difference between the amplification of the semi-circular valley with the Bell-shaped valleys, mainly because of the sharp corners of this geometry.

In summary, small changes in the geometry of the valley result in significant changes in the surface pattern and in the maximum amplification. Overall, it is very likely that amplification on the flat surface away from the feature is larger than the amplification within the valley. Clearly, for higher wave frequencies, the difference between the amplification of various geometries is bigger. Hence, when

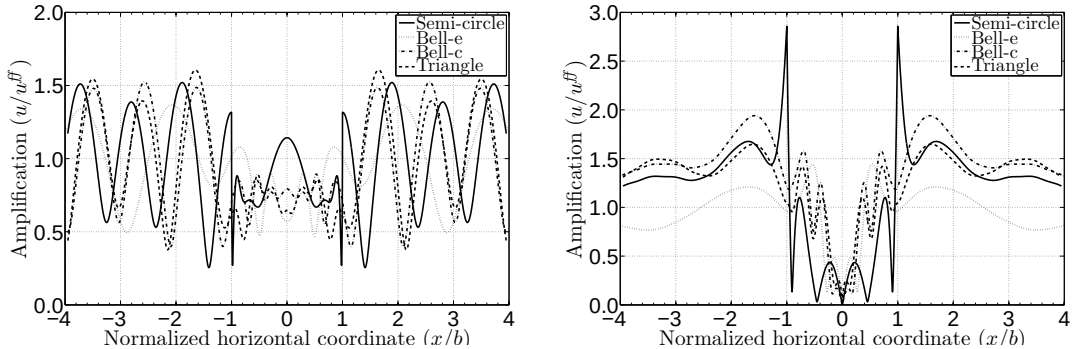

(a) Horizontal amplification due to SV-wave (b) Vertical amplification due to SV-wave

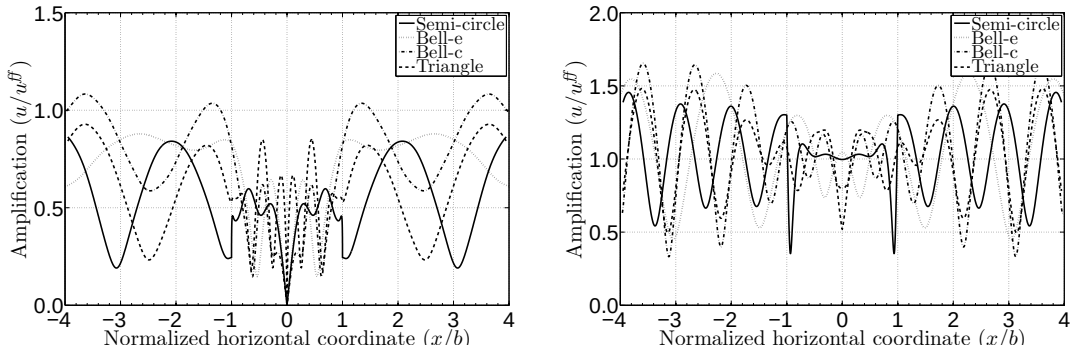

(c) Horizontal amplification due to P-wave (d) Vertical amplification due to P-wave

Figure 4.22: Amplification pattern on the surface of four idealized valley's geometries due to the vertically propagating incident wave

idealizing valleys, it is important that the computational geometry stays as close to the physical as possible for accurate predictions of the amplification patterns.

4.3.2 Effects of incident wave frequency

We study parametrically the dependence of the valleys' surface amplification on the dimensionless frequency parameter η. Figurs 4.24(a) and 4.24(b) show the maximum horizontal and vertical amplification, respectively, on the surface of the Bell-e valley of shape ratio 45° against the frequency for SV incidence. We note that the ampli-

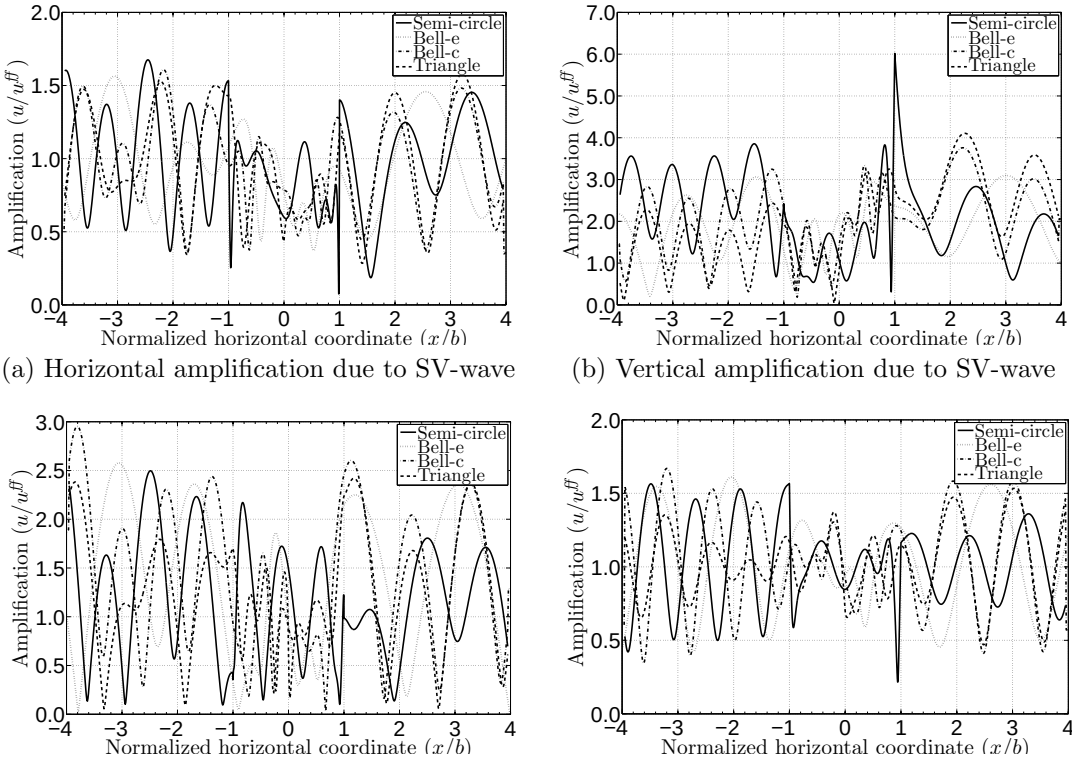

(a) Horizontal amplification due to SV-wave

(b) Vertical amplification due to SV-wave

(c) Horizontal amplification due to P-wave

(d) Vertical amplification due to P-wave

Figure 4.23: Amplification pattern on the surface of four idealized valley's geometries due to a propagating incident wave of $\theta = 15^{\circ}$

fication is quite constant for frequencies above $\eta = 1.5$ for all angles of incidence, which implies that the amplification depends on the frequency if the incident shear wavelength is almost the same size as the valley's depth, otherwise, if the wavelength is more than 1.5 times the depth of the valley, the presence of the valley amplifies the wave at each angle of incidence with the same magnitude. The only exception is the vertical amplification of SV incidence at angle $\theta_s = 5^{\circ}$, where the amplification reduces to 7.5 at $\eta = 2.90$ from its peak value 11.6, and increases again to 9.6 at $\eta = 5.0$. Overall, analogous to the hill topography, the vertical amplifications

are greater that the horizontal ones, though they are, in general, smaller than the amplifications caused by hills.

P incidence results in a larger horizontal amplification in comparison to the vertical amplification, as depicted in Figurs 4.24(c) and 4.24(d). Overall, for frequencies above $\eta = 0.5$, the horizontal and vertical amplifications reduce slightly as the frequency increases. Notice that the vertical amplifications for all angles are quite the same, however, the horizontal amplifications are well separated in a way that the higher angles yield smaller amplifications. In conclusion, surface amplification caused by a valley is less sensitive to the frequency in comparison to the hill topography.

Location of the maximum amplification on the surface

Figure 4.25 depicts the location of the maximum displacement for P- and SV-waves on the surface of a half-plane, including the valley. The maximum horizontal amplification due to SV incidence is outside of the valley, mostly for lower angles of incidence and frequencies, and gradually moves toward the valley as the frequency increases. This trend is, in general, the same for the vertical amplification. For the P incidence, the location of the maximum horizontal and vertical amplifications is outside of the valley. As the frequency increases, the location moves toward the valley, but still remains outside for the majority of the cases. We note that in most cases, the maximum amplification occurs away from the topographic feature, which implies that the presence of a valley results in an amplification on the flat surface away from the feature and that the valley itself may even experience a de-amplification.

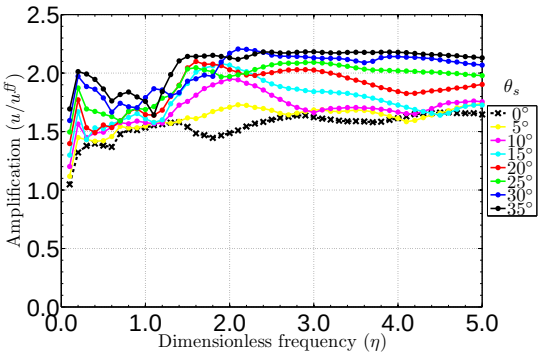

(a) Horizontal amplification due to SV-wave

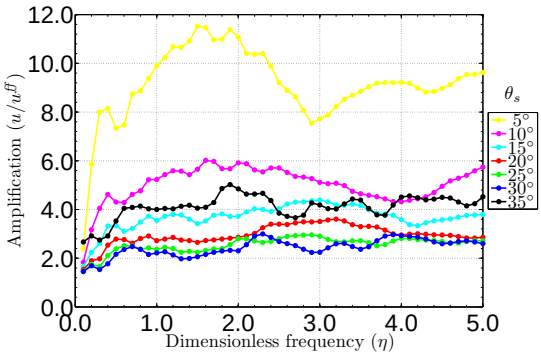

(b) Vertical amplification due to SV-wave

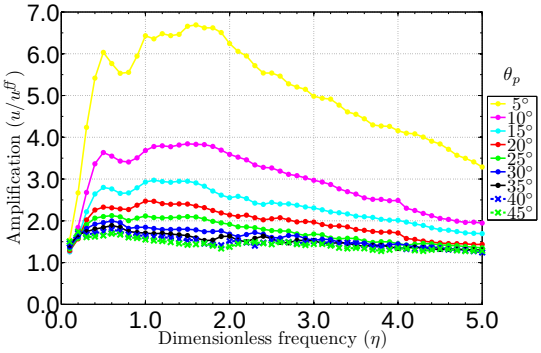

(c) Horizontal amplification due to P-wave

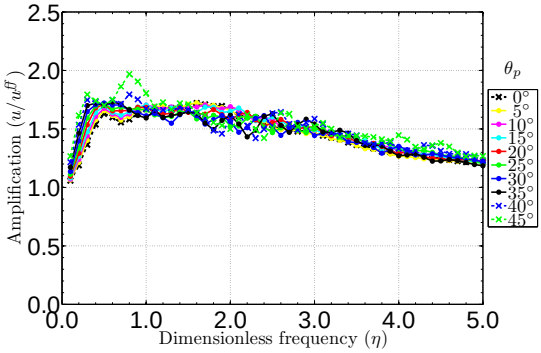

(d) Vertical ampl. due to P-wave

Figure 4.24: Maximum amplification on the surface of the Bell-e valley

4.3.3 Effects of angle of incidence

Figure 4.26 illustrates the effects of incidence angle on the surface amplification of the Bell-e valley of shape ratio $\arctan(h/b) = 45°$ for a few selected frequencies. The horizontal amplification due to SV incidence and the vertical amplification due to P incidence seem to be independent of the angle of incidence, whereas the other components are substantially affected by this parameter. For example, the vertical amplification of SV incidence reduces drastically as the angle of incidence increases up to $\theta_s = 30°$, and increases only slightly for higher angles. The reason, as we

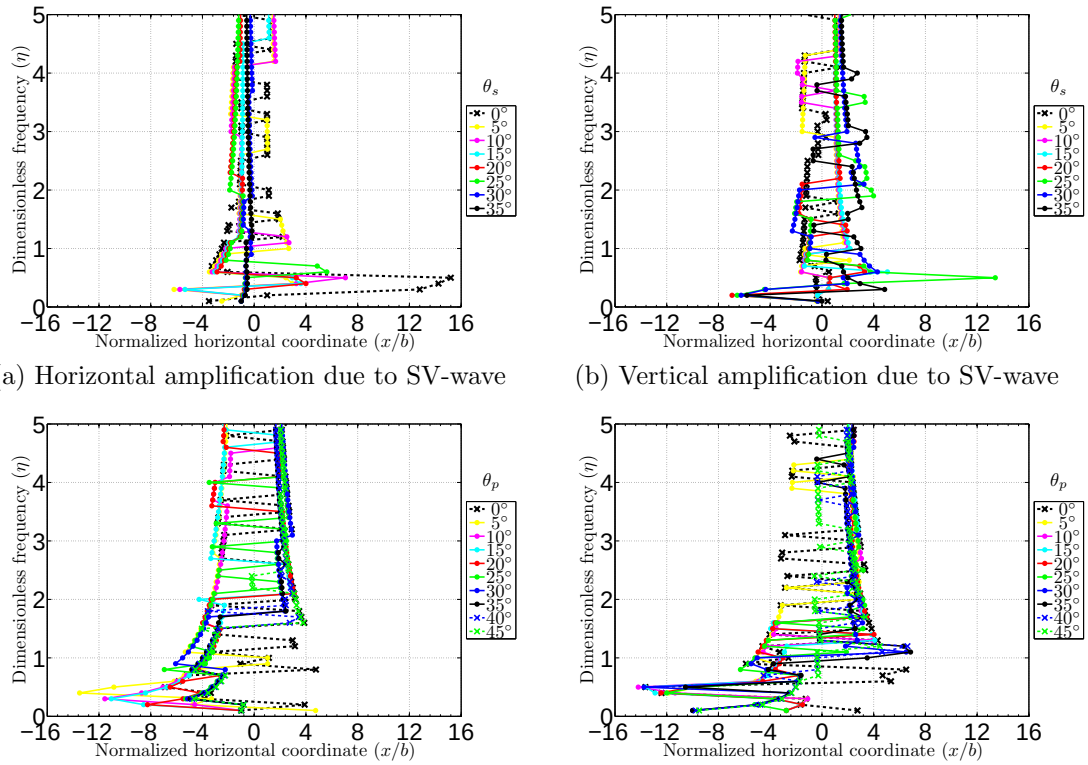

(a) Horizontal amplification due to SV-wave

(b) Vertical amplification due to SV-wave

(c) Horizontal amplification due to P-wave

(d) Vertical amplification due to P-wave

Figure 4.25: Location of the maximum amplification on the surface of the Bell-e valley with shape ratio 45°

discussed earlier, is that the vertical displacement of SV incidence on the surface of a flat homogeneous half-plane, used to compute the amplification, is minimum at $\theta_s = 30°$ and rises to the maximum amount at the critical angle (see Figure 3.3). The horizontal amplification of P wave is steadily decreasing as the angle of incidence increases to the point that the amplifications for all frequencies at $\theta_p = 45°$ are almost identical. We add that the vertical displacement due to the SV incidence and the horizontal displacement due to the P incidence are fairly small in comparison to the other components; hence, even though the amplification of these components seems

to be prominent, the total amplification is still not that big. We also note that the dependence of the amplification on the angle of incidence reduces as the frequency of the incident wave becomes smaller.

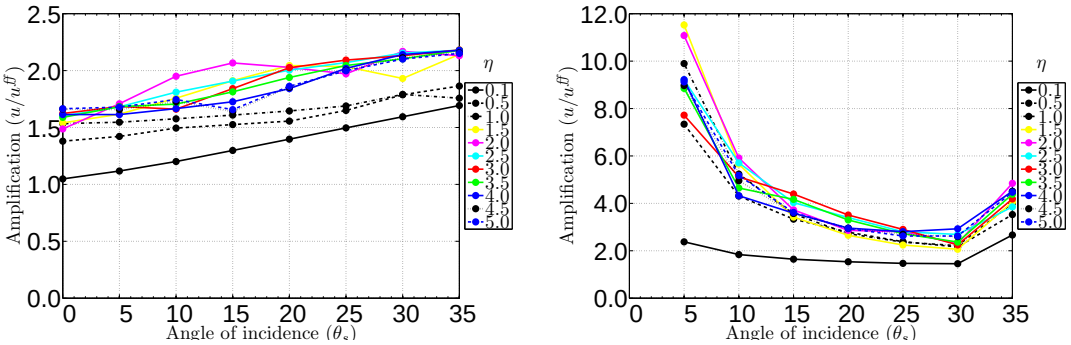

(a) Horizontal amplification due to SV-wave

(b) Vertical amplification due to SV-wave

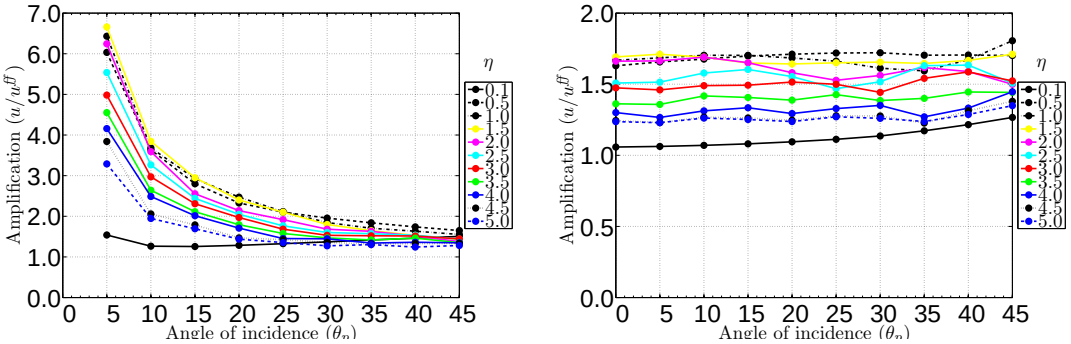

(c) Horizontal amplification due to P-wave

(d) Vertical amplification due to P-wave

Figure 4.26: Maximum amplification on the surface of the Bell-e valley with shape ratio 45°

4.3.4 Spatial amplification patterns

The presence of a feature induces substantial changes on the amplification pattern not only on the surface of the feature but also on the flat surface away from it. In this section, we study the effects the presence of the valley has on the surface patterns

for a few cases.

Figure 4.27(a) shows the amplification pattern on the surface of a Bell-e valley of shape ratio $\arctan(h/b) = 45^\circ$ due to a vertically propagating SV incidence with $\eta = 1.0$. The horizontal component is de-amplified on the entire surface of the valley, but it is amplified on the flat surface away from the feature. This pattern is the opposite of the hill's pattern, where the maximum amplification normally occurs on the surface of the hill. The reason is that the valley de-focuses the energy by diffracting waves away from the feature. The vertical displacement in this case is due to the reflection of waves from the valley, since a vertical SV incidence does not develop any vertical displacement on a flat half-plane. The amplitude of the vertical component is quite large in comparison to the amplitude of the incoming SV incidence and reaches its largest value next to the edge of the valley on the flat surface.

Figure 4.27(b) depicts surface amplification for P incoming waves with $\eta = 2.0$. The horizontal amplification, which is generated by the reflection of waves from the valley, is maximum outside the feature and has the smallest values within the valley. The vertical amplification on the surface of the valley is negligible, while away from the valley it increases remarkably. Since the frequency of the incident wave is twice the frequency of the previous case, we expect to see more ripples in the solution.

Figure 4.28 displays the amplification pattern for obliquely incoming plane P and SV waves with $\theta = 15^\circ$. The amplification is larger on the flat surface, and de-amplification occurs within the valley, particularly in the x direction. Moreover,

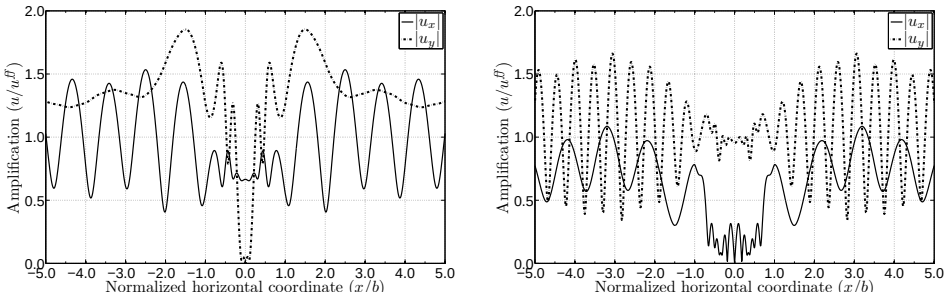

(a) SV incidence, $\eta = 1.0$ (b) P incidence, $\eta = 2.0$

Figure 4.27: Amplification on the surface of the Bell-e valley due to vertically propagating waves

significant amplification occurs on both sides of the valley, which implies that the presence of a canyon drastically changes the displacement everywhere on the surface of the half-plane.

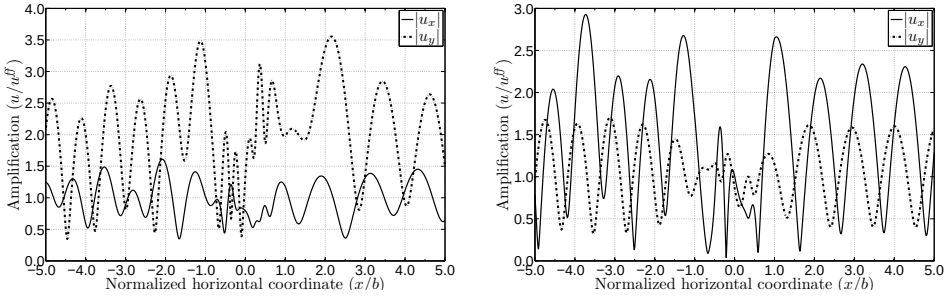

(a) SV incidence (b) P incidence

Figure 4.28: Amplification on the surface of the Bell-e valley due to the incident wave with $\theta = 15^\circ$ and $\eta = 1.0$

Chapter 5

Time-domain parametric studies

The interest in understanding and quantifying seismic motion effects, particularly in regions with surface irregularities, such as hills, valleys, and alluvial basins, is strong, especially in light of the reported discrepancies between recorded surface strong motion data and numerical simulations. Even though the uncertainty in the velocity model remains a primary source of the discrepancies, the pervasive flat-surface assumption and the expediency-driven reduction of model dimensionality contribute decidedly to the discrepancies.

We are concerned with the effects of physical domain representation, particularly model dimensionality and topography modeling, on the seismic response. In this chapter, we focus on numerical experiments in two and three dimensions, for various prototype hills and valleys embedded within layered domains, and compare the results with one-dimensional simulations and flat-surface earth models.

5.1 Effects of model dimensionality on seismic amplification

Owing to the complexity of simulations and the lack of convenient or widely adopted computational tools, the use of one-dimensional analysis remain is pervasive, despite its inherent inability to account for various site effects that greatly affect ground

motion.

We study model dimensionality effects on the amplification of waves via synthetic cases in order to quantify the differences between 1D, 2D, and 3D models, and to highlight the importance of considering the three-dimensional simulations in seismic studies. We claim that while the one- and two-dimensional models may offer preliminary estimates, a complete quantitative understanding of strong motion requires simultaneous consideration of topography and stratigraphy in a three-dimensional model that includes ideally, the seismic source. Toward this end, we report on model dimensionality effects: (i) in the presence of topography; and (ii) in the presence of heterogeneity.

5.1.1 Effects of model dimensionality on topographic amplification

We report the effects model dimensionality has on the surface motion in the presence of a hill. The corresponding one-, two-, and three-dimensional models are plotted in Figure 5.1. Notice that the two-dimensional model of the hill represents a hill range rather than an isolated hill, and that the one-dimensional model is unable to account for the topography effects at all.

We consider a smooth bell-e shaped hill; its geometry is described in Table 5.2. The medium is homogeneous with mass density $\rho = 2000\ \mathrm{kg/m^3}$, Poisson's ratio $\nu = 0.25$, shear wave velocity $c_s = 200$ m/s, and pressure wave velocity $c_p = 350$ m/s. The semi-infinite domain is truncated to an $800 \times 300\ \mathrm{m}^2$ for the two-dimensional domain and to $800 \times 800 \times 300\ \mathrm{m}^3$ for the three-dimensional computational domain, surrounded on its sides and bottom by a 50 m-thick PML, as shown in Figure 5.1.

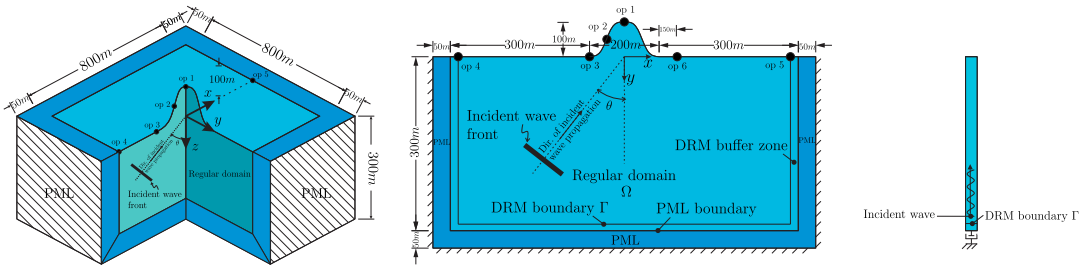

Figure 5.1: Schematic figure of the hills with observation points

The incident excitations are plane P- and SV-waves in the form of a Ricker pulse with a central frequency of 2.0Hz (Figure 3.4), resulting in a shear wavelength of 100m, which is equal to the height of the hill. The simulations are performed in the time-domain with no material damping. We compare the time histories of displacement and their spectra for various models at various observation points (op i, $i = 1, 2, ..., 6$) on the surface (Figure 5.1). Notice that for the one-dimensional model, there is only one observation point.

Figure 5.2 shows the displacement time history at observation point op1 (hilltop), normalized with respect to the amplitude of the incident wave u_i, due to a vertically propagating P-wave. The horizontal component of the displacement is zero, owing to the symmetry of the model and of the seismic load. The largest amplification, 4.78, results from the three-dimensional model, and is 2.4 times larger than the amplification predicted by the one-dimensional model. The amplification of the two-dimensional model is 3.11, roughly 1.56 times greater than that of the one-dimensional model. The larger amplification in the three-dimensional model is mostly due to wave focusing at the hilltop. Notice also that in reality, a large am-

plification at the hilltop or any other corners, such as the edge of a cliff, is likely but it is localize and, as we will see later, we don't expect such large amplifications at other points on the surface.

We also remark that the total motion duration (until near silence) has almost doubled for the two- and three-dimensional models compared to the one-dimensional simulation (1 second versus 2 seconds), due to the trapping of the waves within the topographic feature.

The displacement time-histories in all three models contain similar frequencies, as depicted in Figure 5.2, however, the three-dimensional model shows the largest amplitudes: while for the central frequency of the wave 2 Hz, the one- and two-dimensional amplitudes barely reach 0.37 and 0.65, respectively, the amplitude of the three-dimensional model is 1.0. Notice also that at the hilltop, all frequencies in the signal have been uniformly amplified.

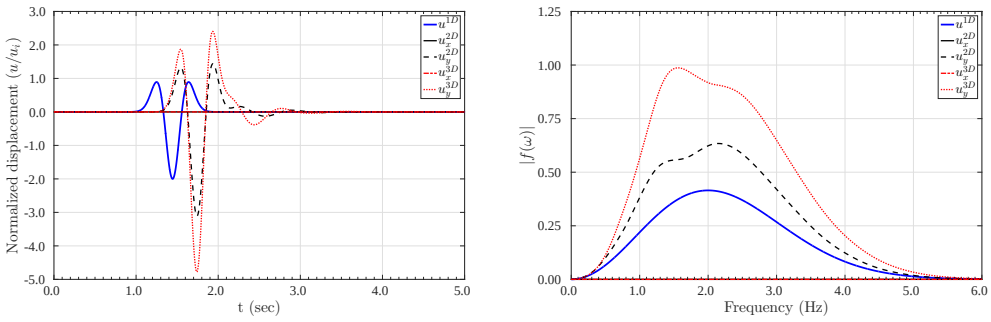

(a) (b)

Figure 5.2: Comparison of (a) displacement time histories and (b) their frequency spectra at *observation point 1* due to a vertically propagating P-wave for the one-, two-, and three-dimensional hill models

If we repeat the same experiment with an SV incident wave, as shown in Figure 5.3, the amplification for the three-dimensional model increases to 8.78. The maximum amplification that a one-dimensional model can predict is 2. The SV-wave motion in the two-dimensional model results in an amplification of 2.96. The frequency spectrum for the three-dimensional model shows greater amplification for all frequencies when compared to the P-wave incidence (Figure 5.3(b)) .

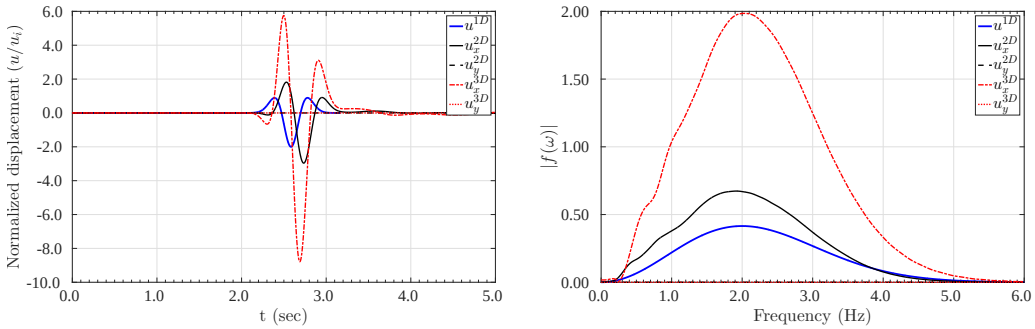

(a) (b)

Figure 5.3: Comparison of (a) displacement time histories and (b) their frequency spectra at *observation point 1* due to a vertically propagating SV-wave for the one-, two-, and three-dimensional hill models

The displacement time history for observation point 2, located at the middle of the slope, 50 m away from the hilltop, is shown in Figure 5.4. By contrast to the displacement waveform at the hilltop, the waveform mid-slope shows multiple peaks for both the two- and three-dimensional models, owing to complex wave interference that is more pronounced at mid-slope than at the hilltop. Even though the maximum displacement in each component is not remarkably greater than that of the one-dimensional model, the combination of the two components shows a relatively

strong motion than the one-dimensional case. The total ground motion duration has increased to more than three seconds, which is more than three times the duration of motion in the one-dimensional model and 50% longer than the motion duration at the hilltop.

The Fourier spectrum of the time history (Figure 5.4) reveals more information about the effects of topography: by contrast to the one-dimensional model, certain frequencies exhibit greater amplification than what we observed at the hilltop, while at other frequencies the motion is de-amplified.

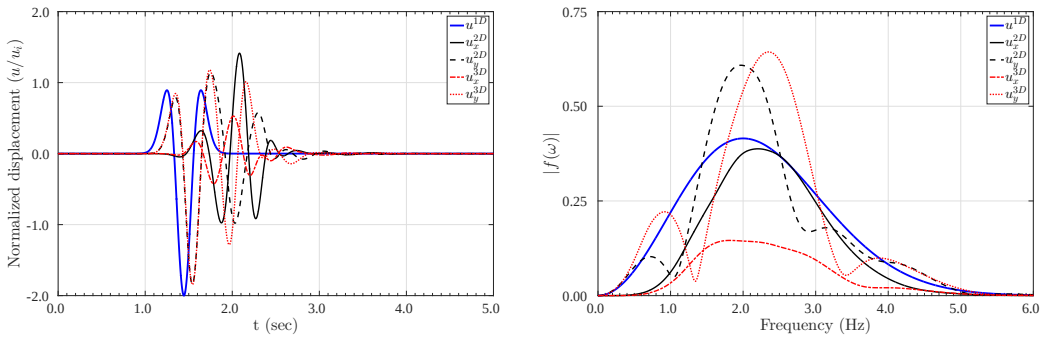

(a) (b)

Figure 5.4: Comparison of (a) displacement time histories and (b) their frequency spectra at *observation point 2* due to a vertically propagating P-wave for the one-, two-, and three-dimensional hill models

Figure 5.5 shows the displacement time history at observation point 3, located at the foot of the hill. We can distinguish two separate motions in the time history of the two- and three-dimensional models: the first one, whose waveform resembles the incident wave, is the reflection of the incident wave from the flat surface, and the second part captures waves reflected from the topography. Interestingly

enough, the first part of the time history is quite similar for the two- and three-dimensional models, however, the displacement amplitude is smaller in comparison to the one-dimensional model, because of the immediate destructive interaction between the incident and the reflected waves, in the 1D case. In the second part of the time history, the two-dimensional model shows a larger amplitude than the three-dimensional model because the two-dimensional model represents a hill range, thus, trapping more energy within the range, than that trapped within the isolated hill. The motion duration at this point is longer than the one-dimensional simulation, but quite similar to other observation points on the surface. The frequency spectrum of this signal shows some minor fluctuations at some frequencies, however, the overall content is similar to the one-dimensional simulation.

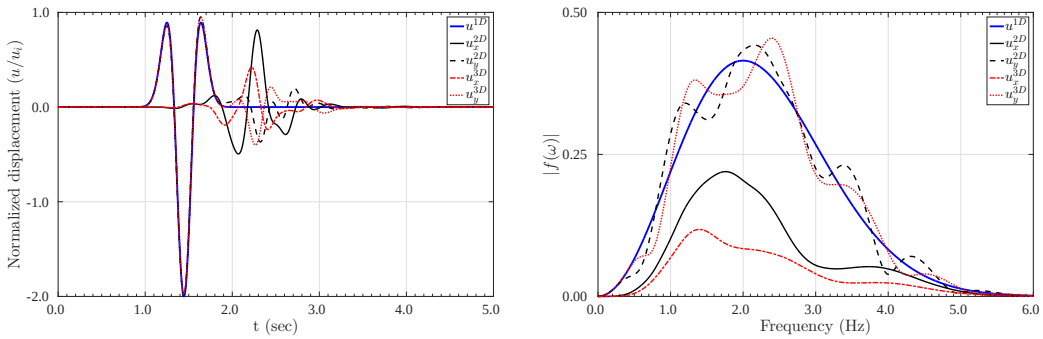

(a) (b)

Figure 5.5: Comparison of (a) displacement time histories and (b) their frequency spectra at *observation point 3* due to a vertically propagating P-wave for the one-, two-, and three-dimensional hill models

The displacement time history for observation point 4, located at the farthest point from the feature, is shown in Figure 5.6. We can clearly observe the

incident wave during the first part of the waveform, followed by the reflections from the topography, that reach the point after some delay. Notice that not only the displacements for the two- and three-dimensional models are identical in the first part, but they are also identical to the one-dimensional simulation. That implies that if the main shock is not polluted by the reflected waves from the topography, the time histories of displacement on the flat surface for all models are identical, as also expected from the closed-form solutions. The rest of the motion on the flat surface followed by the main shock is the result of wave reflections and mode conversions in the hill and also mostly due to the Rayleigh waves, which are not accounted for in a one-dimensional simulation. Even though the amplitude of the reflected waves is not significant in comparison to the main shock, but the total vibration duration is increased. Moreover, due to the symmetry of the load and the model, the vertical displacement of the main shock is zero, but the vertical component of the reflected waveform does not vanish and the motion amplitude is greater for the two-dimensional model compared to the three-dimensional model, because, the two-dimensional model resembles a hill range which produces wave reflections from the entire range, while in the three-dimensional simulation, there is reflection only from the isolated hill.

We also remark that the total duration of the incident wave is only 1.2 seconds, which does not allow sufficient time for any interactions –constructive or destructive– between the incident and the reflected waves generated from the topography. In a real earthquake event, with long duration, interference of the incident and reflected waves is very likely and would result in amplification/de-amplification within the

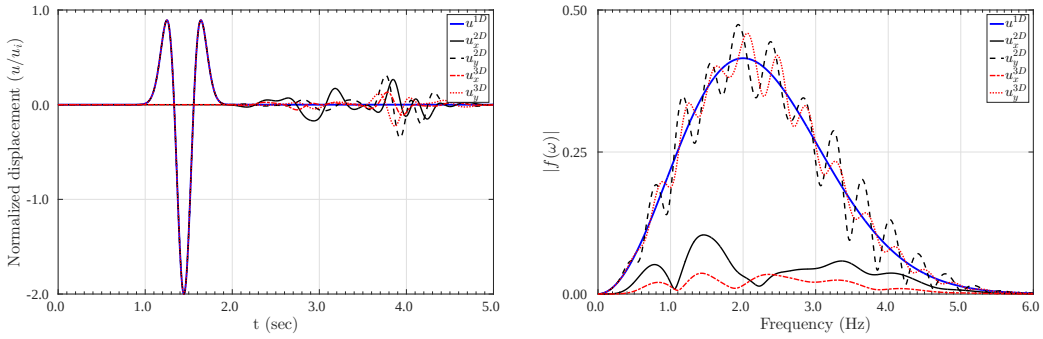

(a) (b)

Figure 5.6: Comparison of (a) the time histories of displacement and (b) the frequency spectra at the *observation point 4* due to a vertically propagating P-wave for two- and three-dimensional hills

hill within the hill as well as on the flat surface away from the hill. To study this particular case, we transmit five consecutive and alternating Ricker pulses in the two-dimensional model. The displacement time history at observation point 6 is plotted in Figure 5.7(a), which shows that the displacement on the flat surface amplifies to 2.38 – a 19% increase in comparison to the maximum displacement of the single Ricker pulse case. The flat surface amplification occurs at multiple locations away from the hill as shown Figure 5.7(b).

In conclusion, the presence of topography not only affects the total duration of the motion on the flat surface, but also increases the maximum displacement. As a result, the region around the topography is prone to experiencing displacement amplification if the motion duration is long enough[1].

[1]In general, a prolonged ground shaking due to a moderate number of cycles causes more damage to the structure than a single pulse, because the continued motion weakens the structure and reduces its resistance to withstand dynamic loads. A more devastating case is the combination of several strong pulses with longer duration, as shown in this example. This behavior cannot be predicted

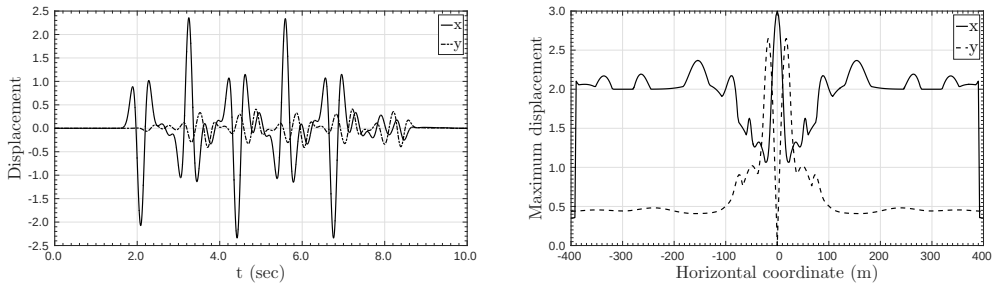

(a) (b)

Figure 5.7: (a) Displacement time history at observation point 6 for a longer duration incident wave, and (b) maximum surface displacement due to a vertically propagating SV-wave

Figurs 5.8 and 5.9 display the contours of total displacement in the two- and three-dimensional simulations for a vertically propagating SV-wave, respectively. The first snapshot shows the propagation of the incident wave just before it hits the surface. The second snapshot shows the displacement after the incident wave hits the surface. Then, the incident wave enters the hill and reflects multiple times on the hillsides. Notice that the Rayleigh waves are generated in the domain due to the foot of the hill. The third snapshot shows the moment the maximum displacement is recorded, when the generated Rayleigh waves from the two sides of the hill arrive at the hilltop. The last snapshot displays the displacement contour right before the incident wave leaves the domain. Notice the wave that has been trapped within the hill due to multiple reflections from the hillsides. The Rayleigh waves are also responsible for motion on the flat surface after the incident wave hits the surface. We remark that the PML buffer zone is clearly visible on the sides and bottom of the

through a one-dimensional simulation.

models, and, as it can be seen, there is no reflection from the truncation boundaries.

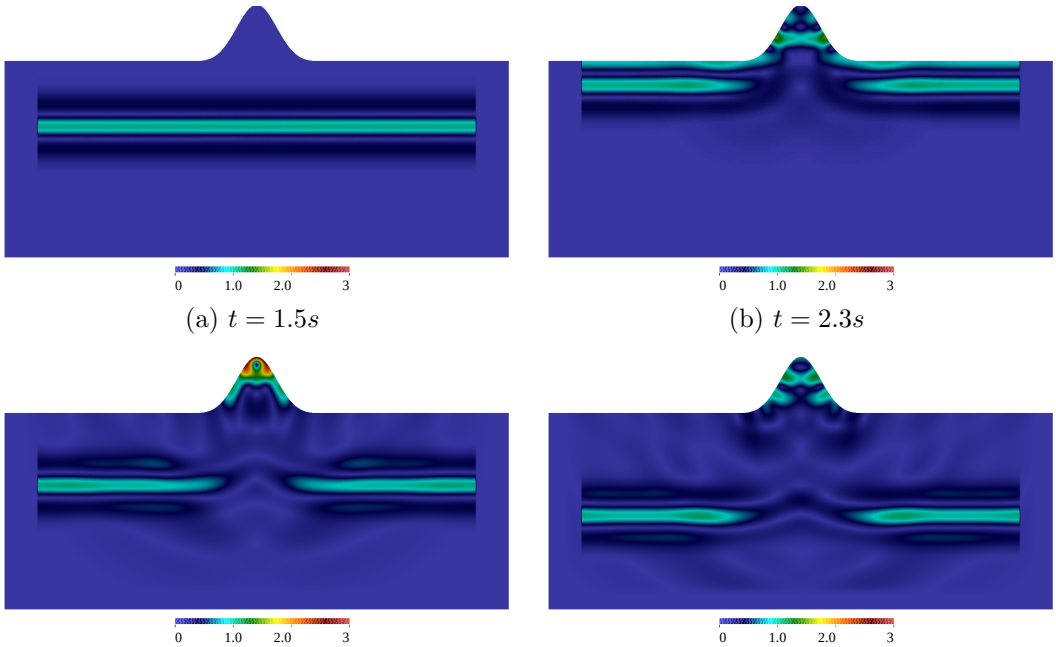

(a) $t = 1.5s$ (b) $t = 2.3s$

(c) $t = 2.73s$ (d) $t = 3.0s$

Figure 5.8: Contours of displacement due to a vertically propagating SV wave in the two-dimensional model

In another experiment, we transmit an oblique SV-wave of an angle of incidence $\theta_s = 15°$. We remark that it is not possible to consider an oblique wave motion in a one-dimensional simulation, hence, we only compare two- and three-dimensional model results. Figure 5.10 illustrates the displacement time history at observation point 1. The horizontal displacement in the three-dimensional model is greater than that of the two-dimensional model, 7.24 vs. 1.93, respectively, while the vertical displacements are almost the same, 1.29 vs 1.96. Even though the max-

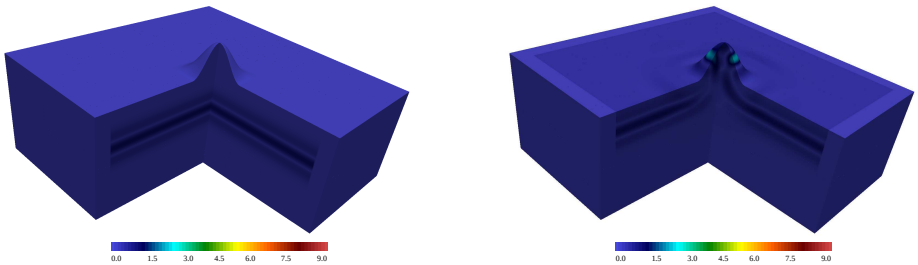

(a) $t = 1.5s$ (b) $t = 2.3s$

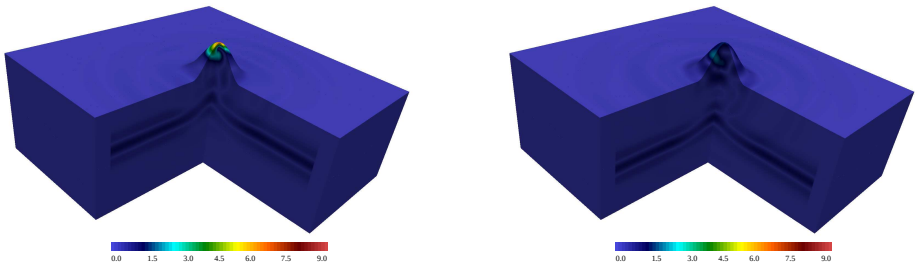

(c) $t = 2.73s$ (d) $t = 3.0s$

Figure 5.9: Displacement contours due to a vertically propagating SV wave in the three-dimensional model

imum displacements for the obliquely incident wave are smaller in comparison to the vertically propagating wave, they are still greater than those corresponding to the one-dimensional model. The frequency spectra of the signals indicate that the largest amplification occurs at frequencies that are less than the central frequency of the seismic input.

Figure 5.11 shows the displacement time history at observation points 4 and 5, on the two sides of the hill for the obliquely incident wave. The first part of the time histories, i.e., the reflection of the incident from the flat surface, is identical. However, the amplitude of the reflected waves at observation point 4, on the left side of the hill where the plane wave hits first, is less than the other point, 0.2 vs. 0.4.

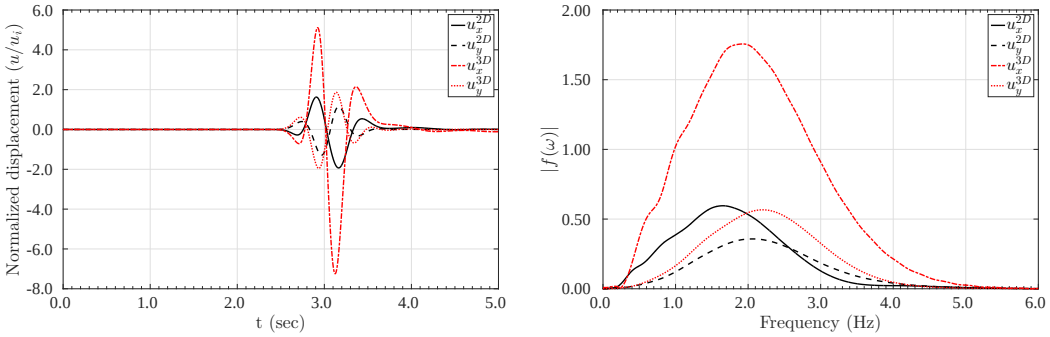

(a) (b)

Figure 5.10: Comparison of (a) displacement time histories of displacement and (b) their frequency spectra at *observation point 1* due to the SV incidence at $\theta_s = 15°$ for the two- and three-dimensional hill models

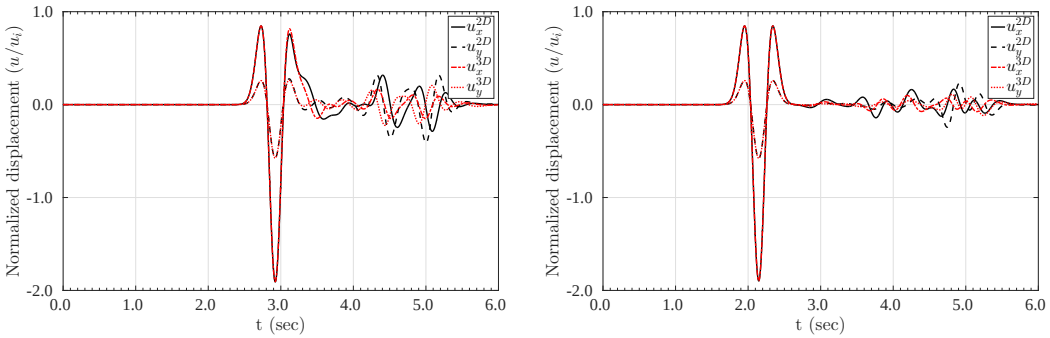

(a) (b)

Figure 5.11: Comparison of displacement time histories of displacements at (a) *observation point 4*, and (b) *observation point 5* due to SV incidence at $\theta_s = 15°$ for the two- and three-dimensional hill models

5.1.2 Effects of model dimensionality on the response of heterogeneous domains

A one-dimensional seismic model might be a good approximation for a layered domain only if the soil structure is horizontally layered without any surface irregularities, as shown, for example, in Figure 5.12(a). However, observations from

past earthquakes show that this assumption might not lead to accurate results for sediment-filled valleys. For example, King and Tucker (1985) [161] showed via experiments that a seismic amplification of ten is possible within the sedimentary valleys, but the surface amplification depends highly on the distance from the edge of the valley, to the extent that, for example, the ground motion at the edge of the valley may differ from the motion at mid-valley, by as much as a factor of five, even though the sites may be separated from each other by as little as 100m. This behavior cannot be predicted with one-dimensional models.

The goal of this section is to use one-, two-, and three-dimensional models of two synthetic, sediment-filled valleys to investigate the dimensionality effects on seismic motion amplification.

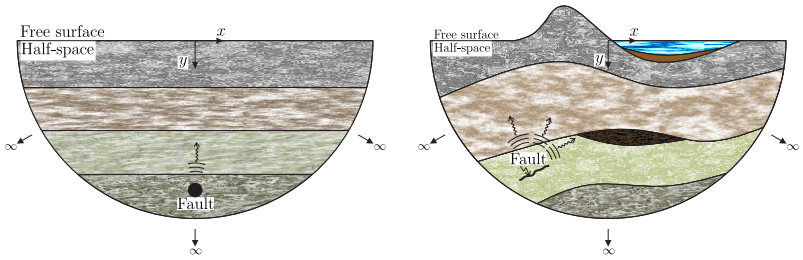

Figure 5.12: Ground idealization: simplified seismic model versus reality

5.1.2.1 Example 1: Homogeneous valley, 1D vs. 2D

Let us consider a two-dimensional, homogeneous, semi-circular, sediment-filled valley, with radius 100 m, as shown in Figure 5.13. The valley is embedded within a stiffer host. The semi-infinite domain is truncated to an 800×300 m^2, surrounded

on its sides and bottom by a 25 m-thick PML. The mass density of the stiff material is $\rho = 2000$ kg/m^3, shear wave velocity is $c_s = 300$ m/s, and pressure wave velocity is $c_p = 489.9$ m/s. We define the soft material such that the shear and pressure wave velocities are $c_s = 150$ m/s and $c_p = 280.6$ m/s, respectively, with mass density $\rho = 1500$ kg/m^3. The medium is linear elastic with no material damping. The equivalent one-dimensional models for the two soil column beneath observation points 1 and 2 (Figure 5.13(a)) are plotted in Figurs 5.13(b) and 5.13(c).

The PML absorbing layer and the regular domain with the stiff material are discretized by quadratic elements with an element size of 2.5m, resulting in a ten-element-thick PML. The soft sedimentary valley is discretized with element of size 1.25 m. The excitation is an incident P-wave[2] in the form of a Ricker pulse with a central frequency of $f_r = 3.0$ Hz.

The time histories of the vertical displacements, normalized with respect to the amplitude of the incident wave, and their Fourier spectra at observation point 1 are shown in Figure 5.14 along with the equivalent one-dimensional model results. Notice that, owing to the symmetry of the domain and the load, the horizontal displacement in the two-dimensional simulation vanishes at this point. The maximum displacements are 2.54 versus 3.54, for the one- and two-dimensional simulations, respectively. In other words, the two-dimensional simulation results in 40% larger

[2]Notice that we are only able to simulate pressure and anti-plane shear (SH) waves in a layered, one-dimensional model, but not SV waves. Therefore, in this section, to have a fair comparison and also consider the effects of mode conversion that occur in two- and three-dimensional domains, we resort to P wave rather than the shear wave, even though in general, as we will discuss later in this section, the shear incidence is more realistic.

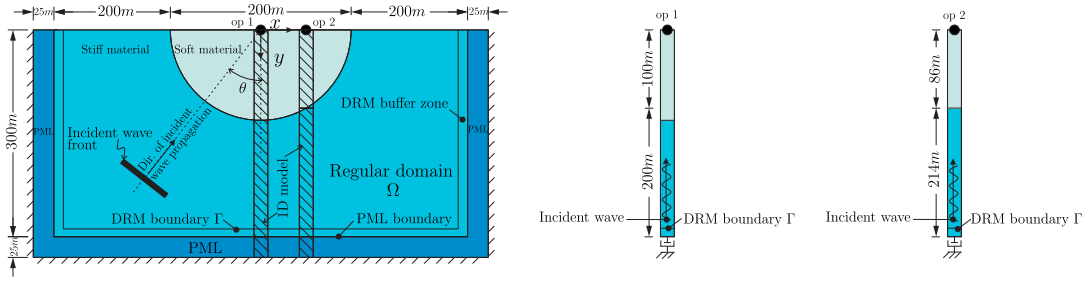

(a) (b) (c)

Figure 5.13: The computational domain for example 1: (a) the two-dimensional, sediment-filled valley, (b) equivalent one-dimensional model (soil column below observation point 1), and (c) equivalent one-dimensional model (soil column below observation point 2)

displacement at that particular point. Additionally, while the motion in the one-dimensional simulation consists of a few isolated pulses, the two-dimensional model exhibits a longer lasting motion with large amplitudes. In other words, the one-dimensional simulation substantially underestimates the surface motion.

Let us turn our attention to the frequency spectra of the displacements at this observation point, depicted in Figure 5.14(b). The first 3 theoretical amplification frequencies[3] for the 1D model are 0.702 Hz, 2.105 Hz, and 3.508 Hz; they are clearly recovered in the 1D spectrum of Figure 5.14(b). However, Notice that the two-dimensional amplification frequencies are different from those of the one-dimensional model. However, the largest amplification in the one-dimensional model is only 0.46 (at 3.508 Hz), while for the two-dimensional model, the maximum amplification is 1.015 at 2.7 Hz. The two spectra are fundamentally different, both in terms of the

[3]It can be shown that the amplification frequencies of the one-dimensional soft layer over half-space are the same as the natural frequencies of the layer with fixed base, given as $\frac{2n-1}{4H}c_p$ for $n = 1, 2, ...$ and H the height of the layer.

amplification frequencies and the amplitudes.

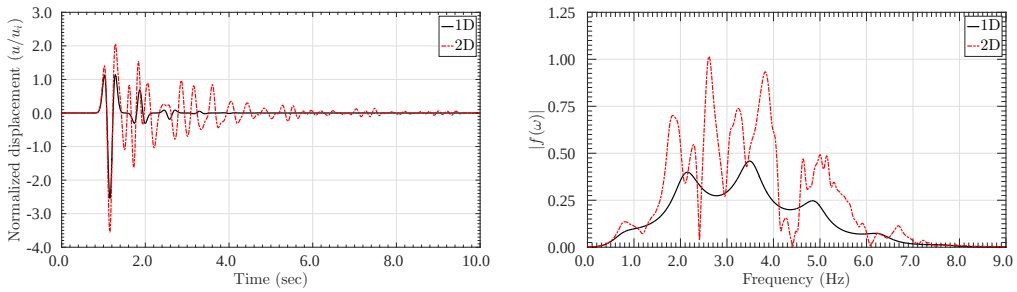

(a) (b)

Figure 5.14: Comparison between (a) displacement time histories, and (b) their frequency spectra of the one- and two-dimensional models at observation point 1

The time histories of the horizontal and vertical displacements for observation point 2, located 50 m away from the midpoint of the valley, are shown in Figure 5.15(a). At this point (op2), the maximum displacement of the two-dimensional model is smaller in comparison to the first observation point (op1), while the maximum displacement of the one-dimensional simulation has remained the same. The maxima are comparable, 2.30 versus 2.54 for the one- and two-dimensional models, respectively. The main difference here is the presence of horizontal motion in the two-dimensional model, which cannot be predicted by the one-dimensional model. The horizontal displacement is as large as 1.85, and if it is combined with the vertical displacement, the total displacement would be greater than the one predicted by the one-dimensional model. The frequency spectra of the displacements from the two simulations, shown in Figure 5.15(b), differ both in amplitude and in the dominant frequencies.

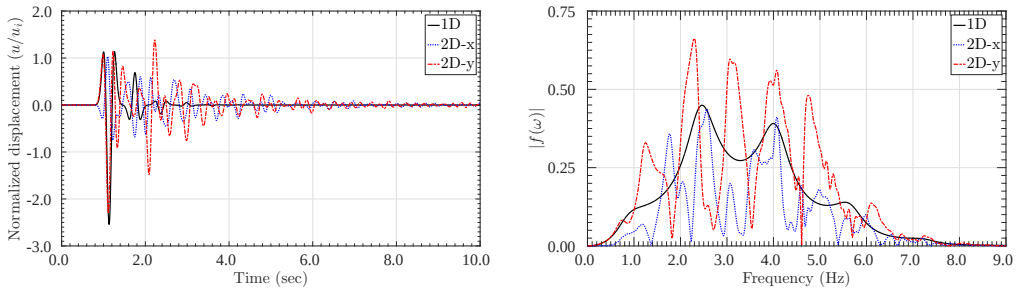

(a) (b)

Figure 5.15: Comparison between (a) displacement time histories, and (b) their frequency spectra of the one- and two-dimensional models at observation point 2

We note that the maximum displacement in the one-dimensional simulation is constant, regardless of the depth of the soft layer and the frequency of the signal, yet, the amplification frequencies are different for each depth. By contrast, the maximum surface displacement for the two-dimensional model, depicted in Figure 5.16, varies by surface location, owing to the wave interactions within the soft sediment (the valley extends between -100m and 100m). The maximum horizontal displacement is 3.54, occurs at the midpoint of the sediment valley, while the maximum vertical displacement is 1.73 and occurs closer to the edge of valley. If we consider the total displacement on the surface, the one-dimensional model underestimates the amplification at the middle of the valley in comparison to the two-dimensional model, while it overestimates the amplification closer to the edge of the valley. The difference between the maximum displacements on the surface is indicative of the valley edge effects.

It is worth observing the surface amplification due to a vertically propagating SV wave in the two-dimensional model, as shown in Figure 5.17: the maximum

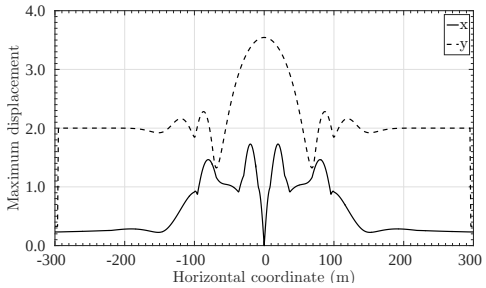

Figure 5.16: Maximum surface displacement in the two-dimensional, homogeneous, sediment-filled valley due to a vertically propagating P wave

horizontal displacement is 4.31, occurs at the middle of the valley, while that of the P-wave is only 1.73, and the corresponding vertical displacements are 2.57 versus 3.54.

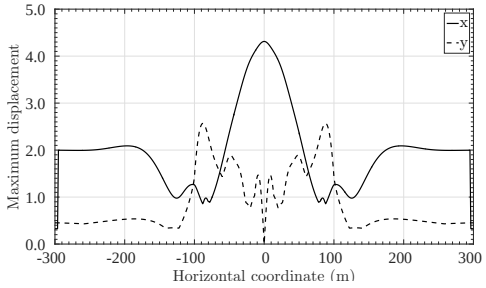

Figure 5.17: Maximum surface displacement in the two-dimensional, homogeneous, sediment-filled valley due to a vertically propagating SV wave

One can possibly use either P or SH incident waves in a one-dimensional wave simulation, i.e., using either the constrained or the shear modulus in the wave equation. We conducted an experiment using the one-dimensional model at observation point 1 to investigate the effects of wave type on the surface amplification. Figure 5.18 shows the displacement time histories on the surface and their Fourier

transforms for P- and SH-waves. Apparently, the surface amplification due to the SH wave is slightly greater than that of the P-wave, which, in turn, is closer to the two-dimensional approximation.

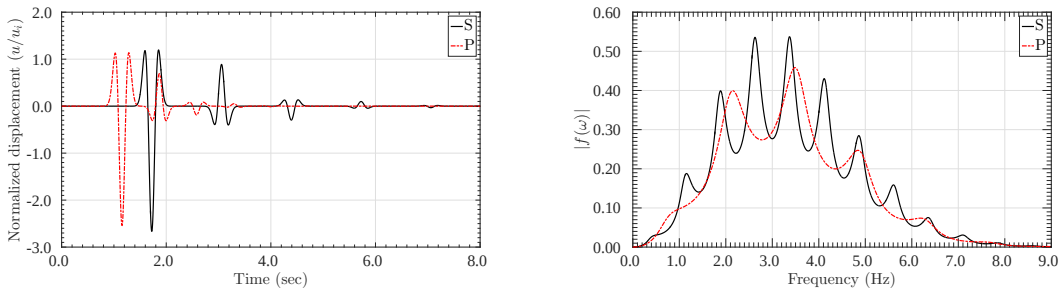

(a) (b)

Figure 5.18: Comparison between the (a) displacement time histories, and (b) their frequency spectra for the vertical propagation of pressure and shear waves in the one-dimensional model at observation point 1

We would like to compare the one-dimensional model results for the two observation points (plotted in Figurs 5.13(b) and 5.13(c)). The time histories of displacement for the two models are depicted in Figure 5.19(a). The two signals are, literally, identical, both in terms of the maximum displacement and the shape of different pulses. The only difference is that the timings of the signals are shifted because of the different depths of the soft layers. In other words, a structure would experience identical loads based on this one-dimensional time-domain simulation at two different locations on the surface, even though the depth of the soft layers is different. By contrast, the frequency content of the two signals, if we consider the entire signal at once, i.e., the frequency-domain results, as indicated in Figure 5.20(b), implies remarkable differences in the amplification frequencies of the two models, just

because of different timings. Indeed, the actual spectrum that the structure would experience is from the two separate signals, as shown in Figure 5.19(b) for the first two pulses in the displacement time history. The reader may ask then, why the amplification frequencies appear in the frequency spectrum of the entire signal? The reason is the interaction of different pulses in the frequency-domain, which due to the different timing, may happen at different frequencies.

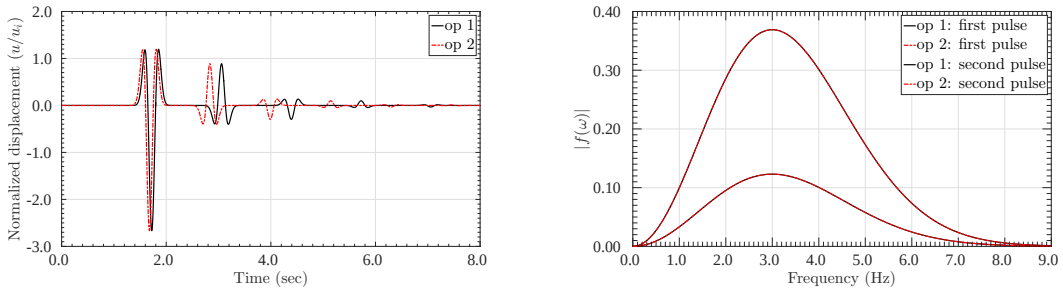

(a) (b)

Figure 5.19: Comparison between (a) displacement time histories, and (b) their frequency spectra of the isolated pulses at observation points 1 and 2 for a vertically propagating shear wave

We also remark that in this particular example, the incoming incident wave was only a short pulse. In fact, in the absence of any interaction between the incident wave and reflected waves, i.e., short signal/deep soft layer, the soft layer amplifies all frequencies unanimously with the same magnitude (see Figure 5.19(b)). By contrast, if the incoming signal is long enough, or equivalently the depth of the soft layer is small enough, such that the reflected waves from the interface of layers interact with the reflected incident wave from the surface, the behavior will change, either in favor of amplification, for example at the cut-off frequencies, or in fewer of de-amplification

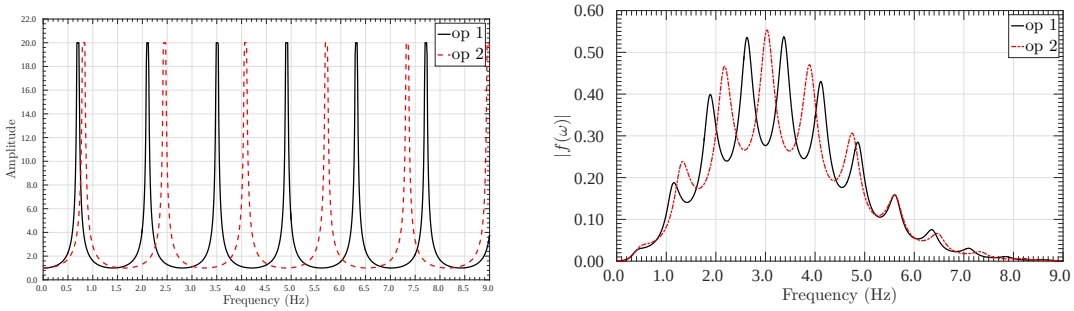

(a) (b)

Figure 5.20: (a) Transfer functions via frequency-domain analysis (without damping), (b) The frequency spectra of the entire displacement time histories at observation points 1 and 2

at most other frequencies. Accordingly, we can conclude that the presence of the soft layer, no matter how deep the layer is/how long the signal is, is enough to initially amplify the incident wave to a certain level, and later, due to wave interactions, the amplification may increase or decrease to even de-amplification.

The complexity of time-domain analysis encourages most engineers to use a one-dimensional, frequency-domain simulation to predict behavior under particular events (for example, using SHAKE). The transfer function obtained from a frequency-domain simulations, by nature, yields the steady state solution. The downside of this simulation is that because, on one side, the frequency-domain analysis is unable to predict the initial amplification at most frequencies prior to any wave interaction, it underestimates the actual amplification due to the soft layer. For example, a frequency-domain analysis predicts an amplification of 2 for the frequency of 1.41Hz at observation point 1, while the same value in a one-dimensional, time-domain simulation is 2.54. On the other hand, the large amplifications at the cut-off frequencies

may not happen in reality because the seismic event might be short enough, especially for deep sediment layers. In short, judging the amplifications based on a transfer function, one may overestimate the amplification at the cut-off frequencies, and underestimate the amplifications at other frequencies.

We plot the displacement contours due to a vertically propagating SV-wave at various instances in the two-dimensional model in Figure 5.21. Notice that the particle motion for the SV incidence is normal to the direction of motion, thus, in the first snapshot, taken right after the plane wave enters the soft layer, the vertical displacement outside the soft soil is zero. The wave velocity, and consequently the wavelength, is smaller in the soft layer. Therefore, to preserve the wave energy, the wave amplitude increases. Vertical displacements are generated within the domain, the moment the wave hits the soft soil. The maximum surface displacement occurs when the incident wave within the soft soil reflects back from the surface. The wave get trapped within the soft soil and bounces back from the interface of the two materials and also from the surface. Even though the main incident front has left the domain in the last snapshot, there is still some motion in the soft soil. The DRM boundary is also visible in the last snapshot, where there is a jump between the total motion in the regular domain and the scattered motion in the buffer between the DRM and the PML.

The displacement contour for the one-dimensional model at observation point 1 is depicted in Figure 5.22. The first snapshot shows the incident wave in the first layer, just before it hits the soft soil. The incident wave enters the second layer, (the second snapshot) and causes the displacement to rise, while the wavelength

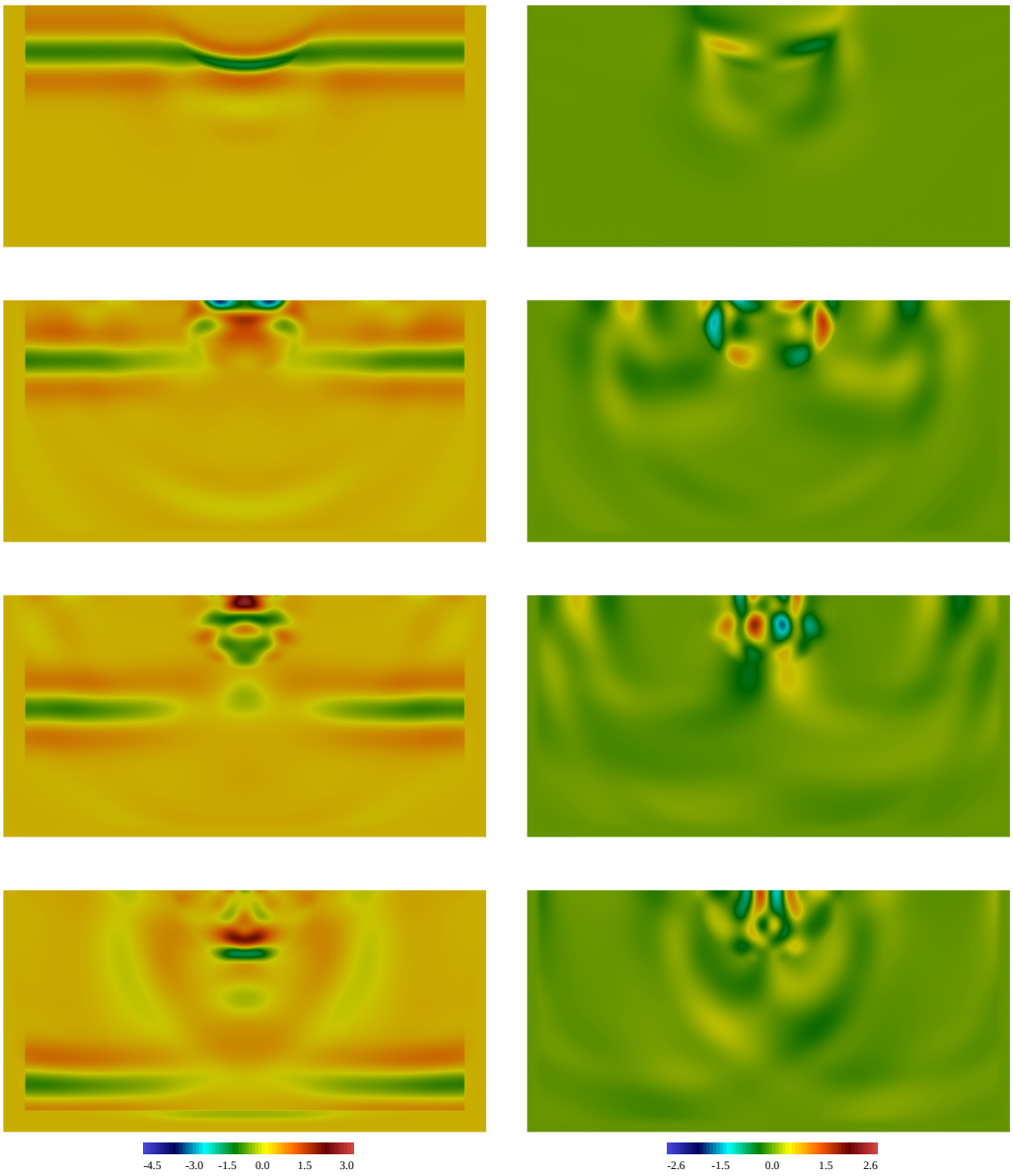

(a) displacement in the X direction (b) displacement in the Y direction

Figure 5.21: Displacement contours in the x and y directions due to a vertically propagating SV-wave

decreases. The third snapshot indicates the moment, where the incident wave is in the second layer and it has also been reflected back into the first layer. The last snapshot shows the moment of maximum displacement on the surface.

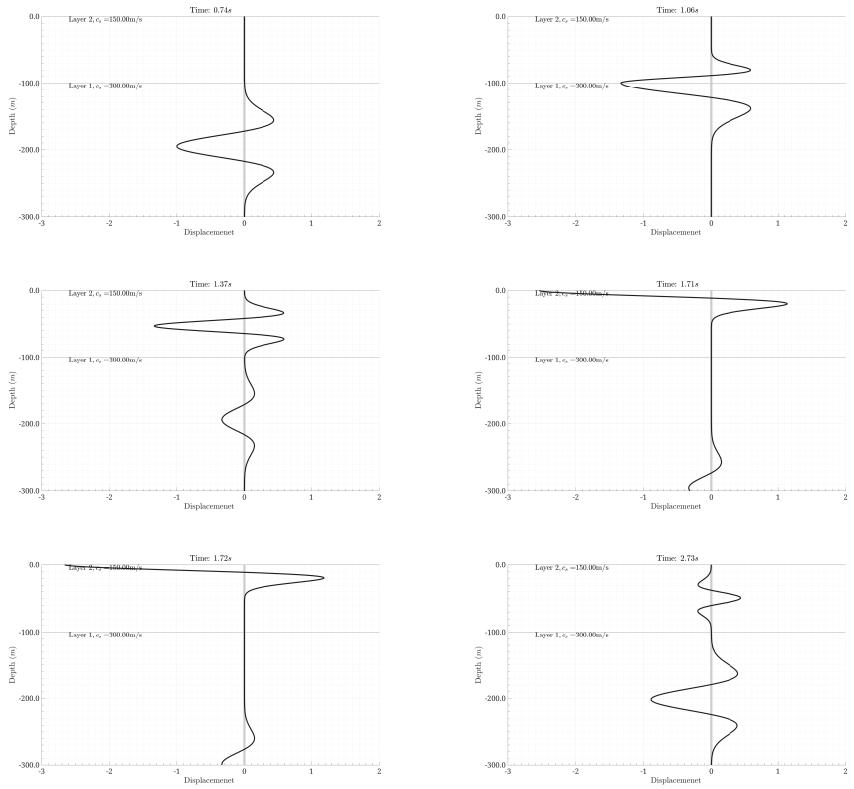

Figure 5.22: Displacement contours in the one-dimensional domain due to a shear incident wave

5.1.2.2 Example 2: A layered sedimentary valley, 1D vs. 2D vs. 3D

A number of densely populated areas, including Manhattan, NY, the San Fernando Valley, CA, or Seattle, WA [96, 271], are situated on large, relatively low-velocity, basins, and are prone to strong earthquakes, due to their proximity to active seismic faults. Figure 5.23 shows, for example, the sediment thickness and velocity model of the Seattle basin. There are several reports on the discrepancies between recorded motion and numerical computations due to complex site effects in heterogeneous geological configurations [23, 93, 121].

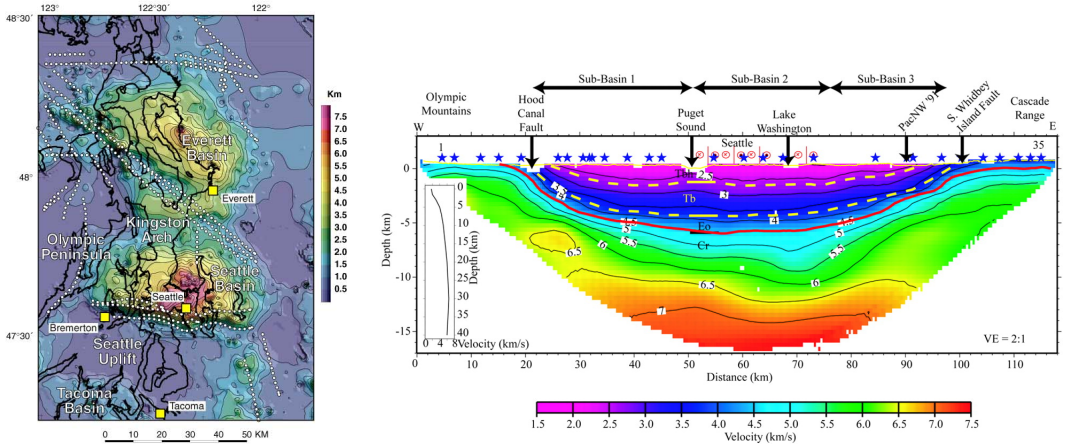

(a) (b)

Figure 5.23: Seattle sedimentary basin: (a) Sediment thickness at the Seattle basin, (b) Cross-section of the Seattle basin [271]

In this section, we attempt to numerically assess model dimensionality effects on the seismic response, using a typical multi-layered, sediment-filled, valley. Toward this end, we compare the displacement time history on the surface using one-, two, and three-dimensional models, for a vertically propagating P wave. We also compare

the amplification of SV-wave between the two- and three-dimensional models.

Let us consider a typical sediment-filled valley, similar to the Seattle basin, as shown in Figure 5.24. The material properties and the depth of each layer have been summarized in Table 5.1. The semi-infinite domain is truncated to a 1700 $\times$ 1700 $\times$ 1200 m^3, surrounded on its sides and bottom by a 120m-thick PML. The medium is linear elastic with no material damping. The PML absorbing layer and the stiff half-space were discretized by quadratic elements with an element size of 20m, resulting in six-element-thick PML. In the soft sediments, we use an element size of 15m. The excitation is a plane incident wave (P or SV) in the form of a Ricker pulse with a central frequency of $f_r = 1.0$Hz.

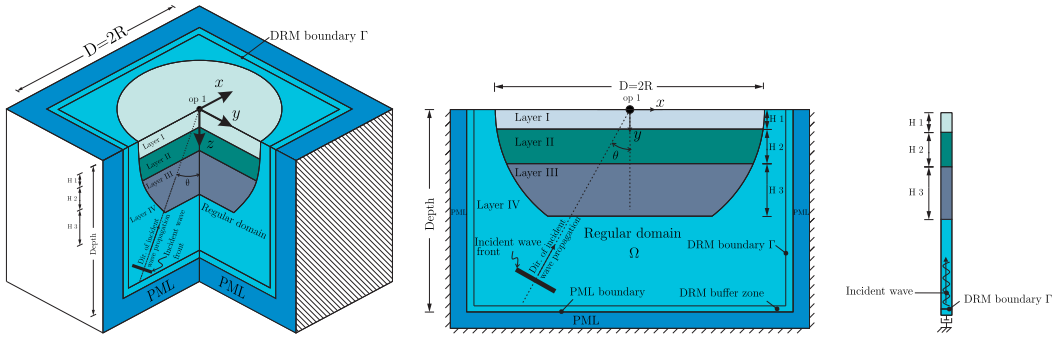

Figure 5.24: Sedimentary valley models: (a) three-dimensional model, (b) two-dimensional model, and (c) equivalent one-dimensional model at observation point 1 (op1)

Figure 5.25 shows the displacement time histories and their frequency content at observation point 1, located in the middle of the domain (Figure 5.24). The maximum displacements are 3.50, 4.41, and 13.99, for the one-, two-, and three-

Table 5.1: Depths and material properties of the layered domain

Layer	mass density ρ(kg/m^3)	Poisson's ratio ν	shear velocity c_s(m/s)	pressure velocity c_p(m/s)	depth (H)
I	1800	0.25	200	346.41	30
II	2000	0.25	450	779.42	120
III	2200	0.25	600	1039.23	400
IV	2800	0.25	900	1558.85	550

dimensional models, respectively, i.e., the three-dimensional model yields a response 4 times greater than that of the one-dimensional model. Notice that if we look at the time history signal closely, we observe that the first pulse in all models is near identical in shape and magnitude, which in fact, represents the first reflection of the incident wave from the surface before the response gets polluted by the reflected waves from the layer interfaces. The maximum displacements for the one- and two-dimensional models both arise during the first pulse phase, and the rest of the response is characterize by smaller amplitudes. Interestingly, however, the maximum displacement in the three-dimensional model arises later in time as a result of the interference of Rayleigh waves generated from the edges of the sedimentary valley, with the reflected waves [93]. In summary, the main reason for having such a large difference between the maximum displacement obtained from the one-dimensional model and the two- or three-dimensional models is the inability of the one-dimensional model to capture mode conversions and Rayleigh waves. The total motion duration is over 25 seconds for the three-dimensional model, while the motion in the one- and two-dimensional models last only 3.5 and 10 seconds, respectively.

The frequency spectra of the three time histories in Figure 5.25(b) show that all models amplify the frequencies between 0.7 to 1.5Hz, though at different rates,

while the three-dimensional model, exhibits another set of frequency amplifications between 1.5 to 2.1Hz with higher amplitudes than those of the lower frequencies. Recall that the central frequency of the incident wave is 1Hz, but, owing to the presence of the soft layers, amplification shifts to other frequencies.

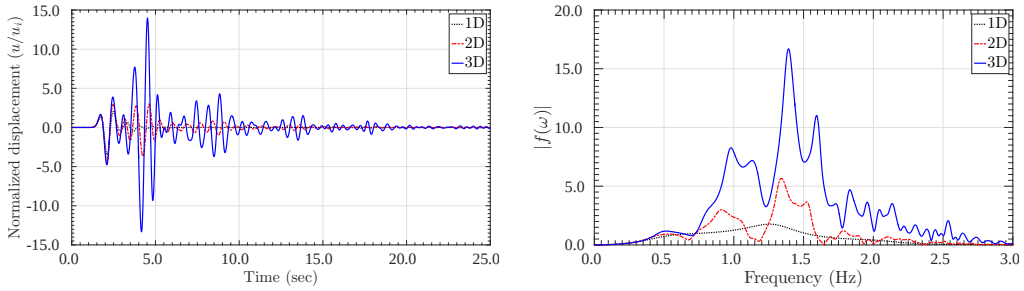

(a) (b)

Figure 5.25: (a) Displacement time histories and (b) their frequency spectra at observation point 1, for the one-, two-, and three-dimensional models due to the vertically propagating P-wave

Figure 5.26 displays the maximum surface displacement for all three models. While a one-dimensional simulation predicts a constant amplification over the entire layered domain, the two- and three-dimensional models show variable amplifications. Particularly, the constructive interaction of waves in the middle of the domain in the three-dimensional modal yields a large amplification, which cannot be seen even in the two-dimensional model. We remark again that the total duration of the incoming signal in this example is quire short, only 1.2 seconds, thus, the constructive interference of incoming and surface waves, which cannot be predicted by the one-dimensional model, may (very likely) lead to even larger amplifications if the input duration were to increase.

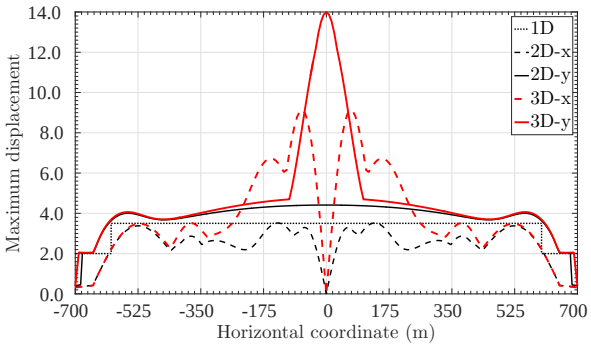

Figure 5.26: The maximum displacement on the surface for all three models due to a vertically propagating P-wave

In a subsequent numerical experiment, we study the dimensionality effects on the propagation of SV waves using the two- and three-dimensional models only. Figure 5.27(a) displays the displacement time histories at observation point 1. The maximum displacements are 5.59 and 11.14, for the two- and three-dimensional models, respectively, i.e., the three-dimensional model yields a maximum displacement 2 times as large as that of the two-dimensional model. The total motion duration is over 30 seconds for the three-dimensional model, while the two-dimensional motion lasts no more than 15 seconds.

We would like to know whether the difference between the maximum displacements in the two- and three-dimensional models is localized (a small area in the middle of basin) or can be observed at other points on the surface as well. Toward this end, we plot (Figure 5.1.2.2) the total maximum displacement on the surface of the two models in Figure 5.1.2.2. The graph clearly shows that the interference of the waves in a large area in the middle of the three-dimensional domain results in a remarkable amplification, which cannot be predicted via a one- or even a two-

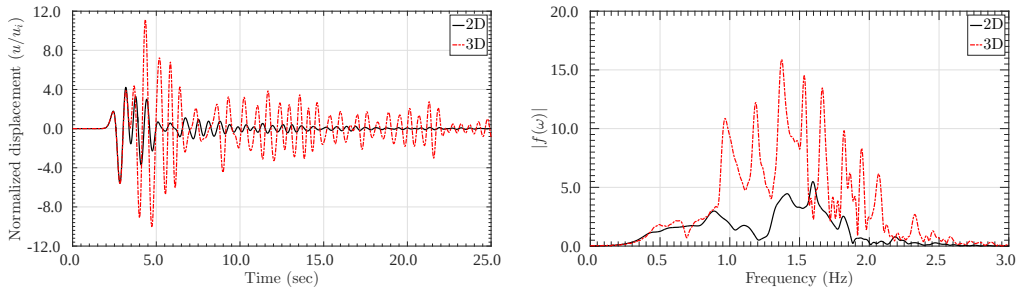

(a) (b)

Figure 5.27: Comparison of (a) displacement time histories and (b) their frequency spectra at observation point 1, for two- and three-dimensional domains due to vertically propagating SV wave

dimensional model.

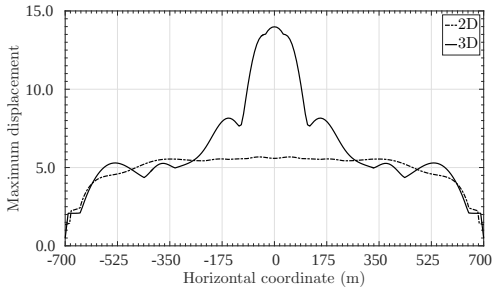

Figure 5.28: The maximum surface displacement of the two- and three-dimensional models due to a vertically propagating SV-wave

The displacement contours for the three-dimensional model is depicted in Figure 5.29 at various instances. The first snapshot shows the moment where the waves enter the soft layer. The second snapshot shows the first reflection of the incident wave from the surface of the soft layers and the third one is at the moment when the maximum displacement occurs. The contours show how the amplification occurs within the layered domain due to energy being trapped within the soft layers.

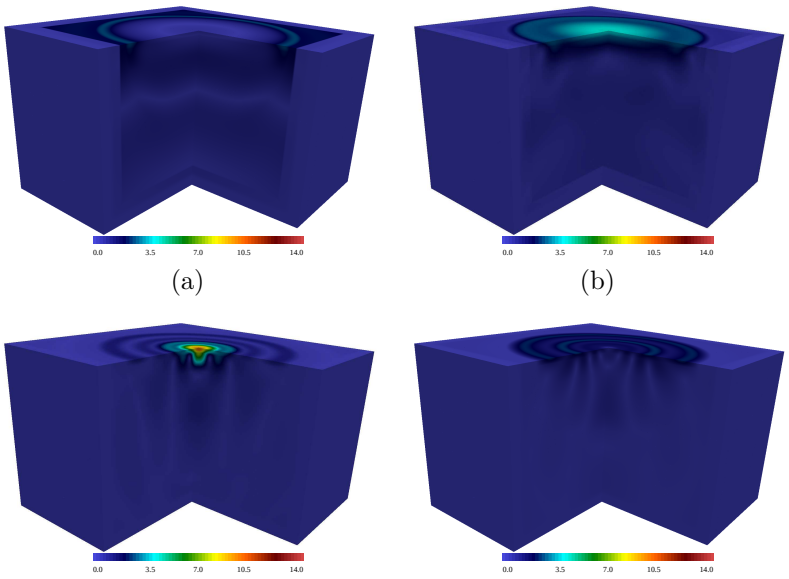

Figure 5.29: Displacement contours at various instances due to a vertically propagating P-wave

5.2 Effects of geometry idealization on seismic amplification

We are interested in studying the effects the geometry idealization has on the surface motion by considering three different hills, whose geometries differ only slightly, for both the two- and three-dimensional models. Figure 5.30 depicts all shapes for a common height $h = 100$m and a base $b = 100$m and Table 5.2 summarizes their definitions. The geometries are intentionally defined very close to each other to study whether small perturbations in geometry affect the response.

Table 5.2: The geometry of hills for $-b \leq x \leq b$

Feature's name	**Geometry**	**Cross section area**
Bell-c	$y(x) = 0.5h(1 + \cos(\pi \frac{\lvert x \rvert}{b}))$	bh
Bell-e	$y(x) = h(1 - (\frac{\lvert x \rvert}{b})^2) \exp(-3(\frac{\lvert x \rvert}{b})^2)$	$0.86bh$
Triangle	$y(x) = h(1 - \frac{\lvert x \rvert}{b})$	bh

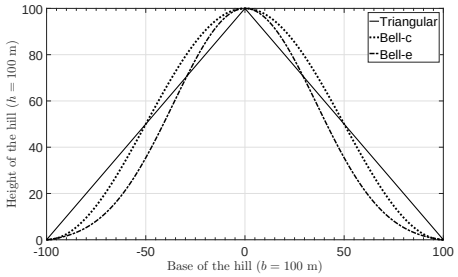

Figure 5.30: Geometry of three idealized hills with common height $h = 100$m and base $b = 100$m

We consider a homogeneous medium with mass density $\rho = 2000$ kg/m^3, Poisson's ratio $\nu = 0.25$, shear wave velocity $c_s = 200$ m/s, and pressure wave velocity $c_p = 350$ m/s. The semi-infinite domain is truncated to an 800×300 m^2 for the two-dimensional and to $800 \times 300 \times 300$ m^3 for the three-dimensional computational

domains, surrounded on their sides and bottom by a 50 m-thick PML, as shown in Figure 5.31 for a bell-shaped hill. The PML absorbing layer and the regular domain were discretized by quadratic elements of size 5 m, resulting in ten-element-thick PML for both the two- and three-dimensional domains. The incident excitation is a plane SV-wave in the form of a Ricker pulse with a central frequency of 2.0 Hz, resulting in a shear wavelength of 100 m, the same as the height of the hills. The simulations are performed in the time-domain with no material damping.

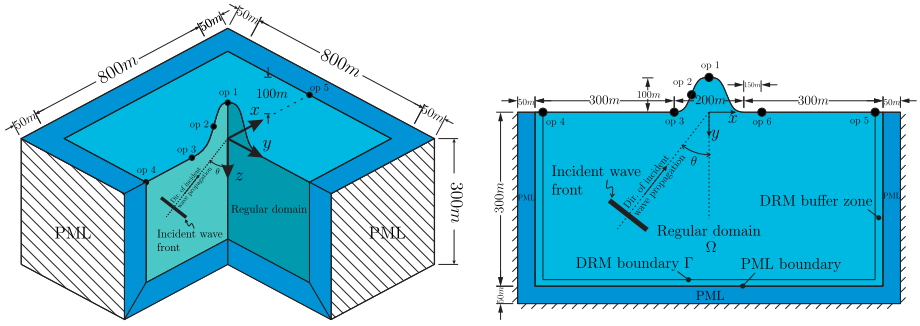

Figure 5.31: Schematic figure of the hills with observation points

To study the effects of dimensionality and geometry idealization, we plot the displacement time history for different models at the observation points on the surface (Figure 5.1).

5.2.1 Two-dimensional models

Figure 5.32 displays the time history of horizontal displacement (normalized with respect to the amplitude of the incident wave u_i) and its Fourier transform at observation point 1, located at the hilltop, for three two-dimensional hills. Even though

the difference in the geometry of the hills is subtle, there is a remarkable difference in the maximum amplitude. The maximum displacement for the Bell-e hill is 2.97, while the same value is only 1.68 for the triangular, and 1.79 for the Bell-c hills. Notice that the triangular hill is the typical geometry used in the literature to model a hill. The total duration of simulation is quite the same for all cases. The frequency content of the signal shows that the Bell-e hill amplifies all frequencies rather uniformly, while the triangular hill, de-amplifies the main frequency of the incident wave (2.0 Hz) and amplifies slightly other frequencies.

The effect of geometry idealization on the displacement is less prominent at observation point 2 as shown in Figure 5.33. The displacement on the flat surface at the foot of the hill, observation point 3, is depicted in Figure 5.34, where the maximum displacement is due to the reflection of the main signal from the surface, followed by the reflections from the hills. All three geometries, more or less, produce similar response, with some observable departure for the triangular hill, which we attribute to Rayleigh waves off of the foot of the triangular hill.

Table 5.3 summarizes the maximum surface displacement for the three hill geometries and the location where the maximum displacement occurs. The maximum horizontal displacement is 2.96 for the Bell-e hill that happens at the hilltop, however, the corresponding values for the Bell-c and triangular hills are 2.08 and 2.09 located on the flat surface at -152.5 and -160.0, respectively. Additionally, the maximum displacement happens at different times as well. The difference between the maximum vertical displacements is even larger, 2.65 for the Bell-e hill, versus 1.67 for the triangular hill, and 2.47 for the Bell-c hill, but they occur at almost the

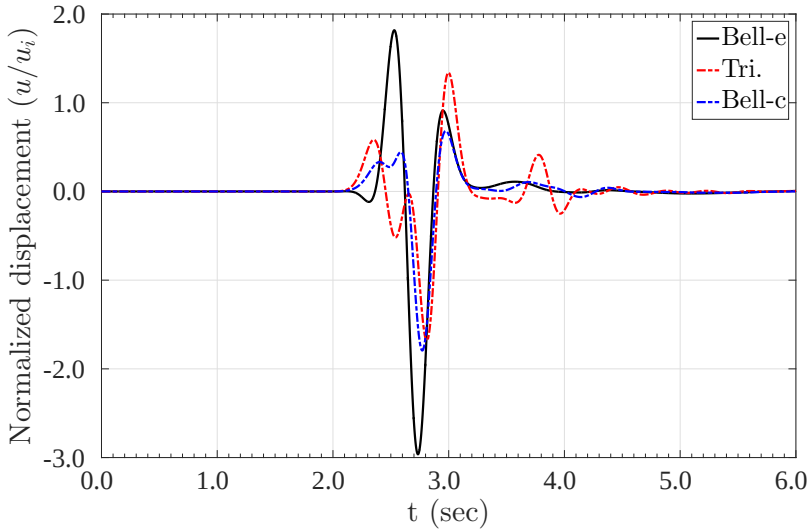

(a)

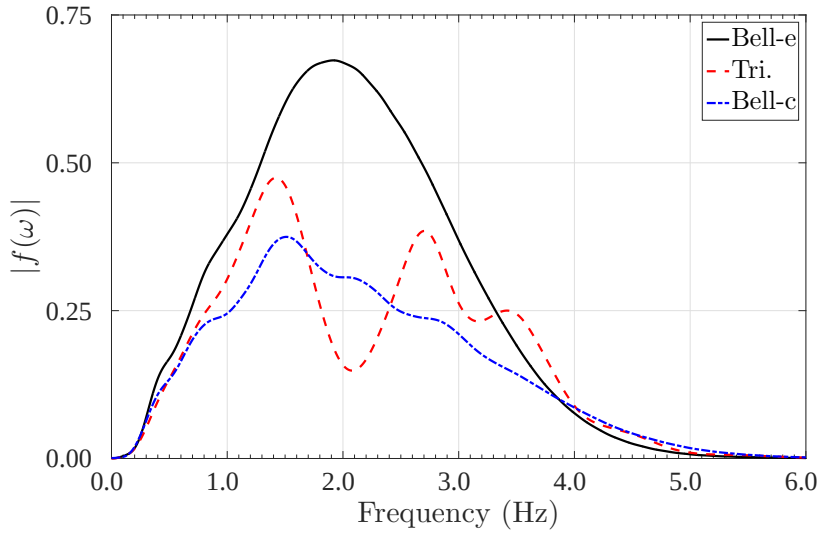

(b)

Figure 5.32: Comparison of (a) displacement time histories and (b) their frequency spectra at *observation point 1* due to a vertically propagating SV wave for three different two-dimensional hills

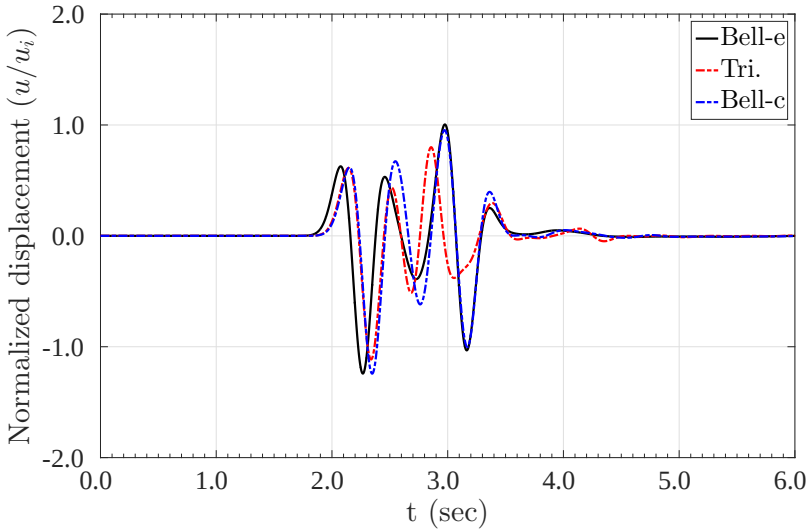

(a) Horizontal displacement

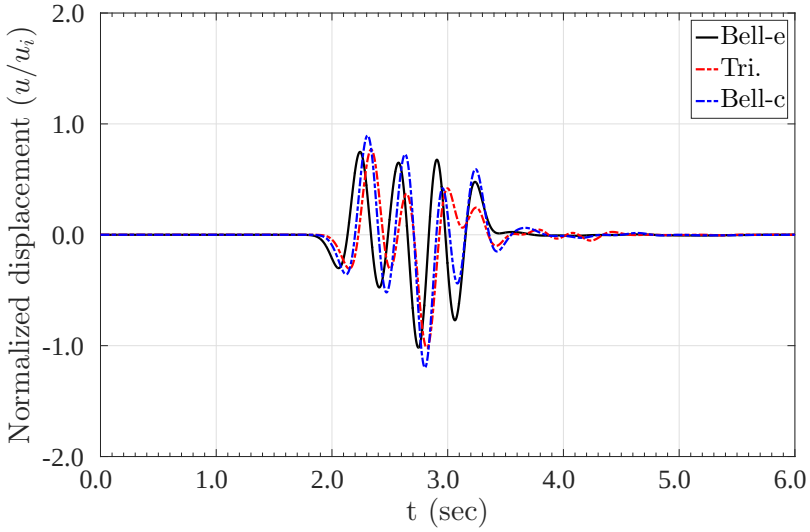

(b) Vertical displacement

Figure 5.33: The displacement time histories at *observation point 2* due to a vertically propagating SV wave for three two-dimensional hills

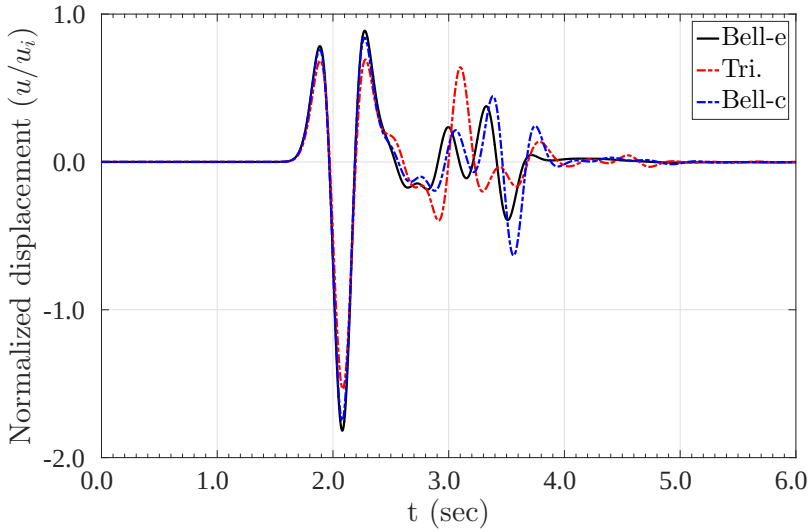

(a) Horizontal displacement

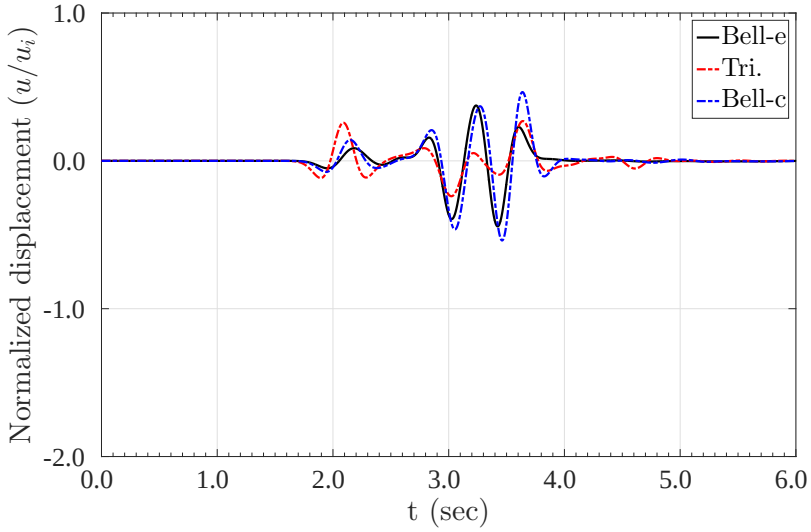

(b) Vertical displacement

Figure 5.34: The displacement time histories at *observation point 3* due to a vertically propagating SV wave for three two-dimensional hills

same location and time. The maximum total surface displacement for each geometry is also listed in Table 5.3, which shows that the Bell-e hill experiences the largest total amplification at the hilltop.

Table 5.3: Table of maximum displacements and its location

Feature's name	x-direction			y-direction			Total displacement		
	max.	loc.	time	max.	loc.	time	max.	loc.	time
Bell-e	2.96	0.0	2.73	2.65	17.80	2.71	2.96	0.0	2.73
Bell-c	2.08	−152.5	2.09	2.47	−19.73	2.75	2.47	20.64	2.75
Triangle	2.09	−160.0	5.09	1.67	−23.33	2.71	2.15	−18.33	2.51

Figure 5.35 compares the maximum surface displacements of all three geometries for a vertically propagating SV-wave. The abscissa indicates the surface of the domain, where the hill extends between −100m to 100m. On the flat surface away from the feature, the maximum displacement in the x-direction is 2.0, equivalent to the maximum displacement in the one-dimensional model. However, the presence of the hill, disrupts the pattern on the surface of the hill and also on the flat surface close to the feature. For this particular case, the displacement is de-amplified on the surface of the hill for the triangular and Bell-c hill, while the displacement increases around the hilltop for the Bell-e hill. Overall, the displacement increases for all three geometries around the hilltop, but notice that the triangular and Bell-c hill patterns are more similar. The vertical motion, which is zero in the one-dimensional model, is quite significant, particularly on the surface of the hill for all geometries. At the hilltop, due to the symmetry of the model and the load, the displacement is zero, but just around the hilltop, the displacement reaches 2.7 for both bell-shaped hills, however, the triangular hill experiences a smaller displacement. Overall, the

displacement on the surface of the hill, except for the hilltop, has been amplified for all geometries.

5.2.2 Three-dimensional models

The effect of the geometry idealization on the surface motion in three-dimensional models is studied in this section, using the three hill geometries described in Table 5.2. Figure 5.36 shows the maximum surface displacement in the x- and y-directions. Overall, the same conclusions can be made for the three-dimensional simulations: on the flat surface, the horizontal displacements for all geometries are identical to the one-dimensional motion, however, on the hill surface, the difference is significant. The Bell-e hill exhibits the highest amplitude of 8.78, while the Bell-c hill is 6.02 and the triangular hill is only 3.5. The overall patterns are similar, but the amplitudes are different on the surface of the hill. The maximum vertical displacement for the triangular hill is the lowest (2.3), while for the other two hills, the maxima are almost twice as that of triangular hill (4.6). By contrast, on the flat surface, the triangular hill produces the largest amplitude in comparison to the other hills.

5.3 Levee simulation –a topography and heterogeneity case

Levees are widely used all over the world, primarily for flood management. In this section, we study, through a time-domain simulation, the effects of seismic loads on a typical levee.

Figure 5.37 displays a typical levee. In our simulation, we consider a levee with a height of 10m, 6m crest, 8m core height, and a core crest of 2m, with equal

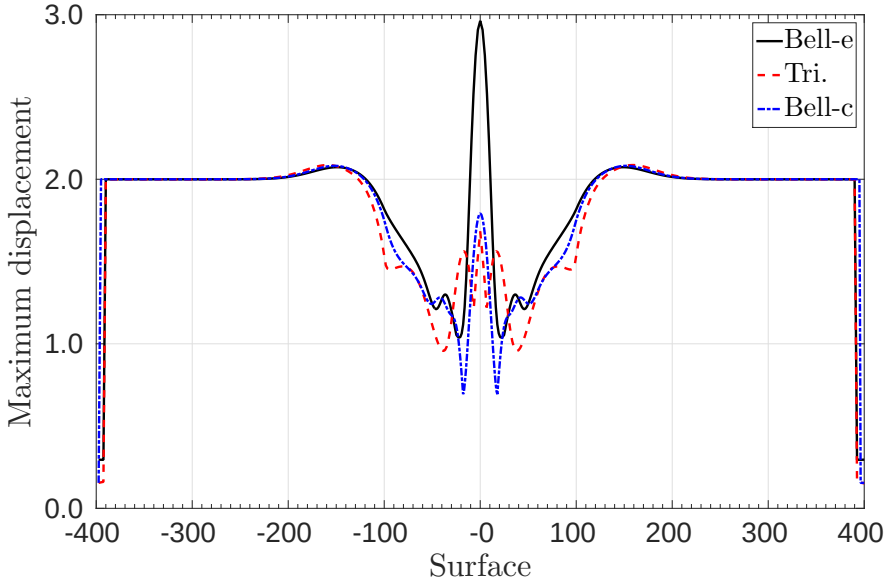

(a) x direction

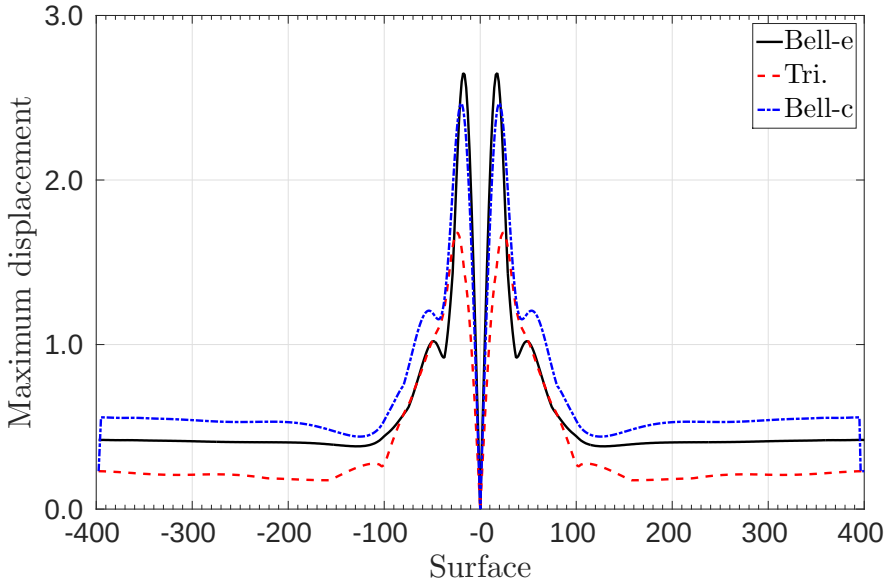

(b) y direction

Figure 5.35: Maximum surface displacement for the two-dimensional geometries due to a vertically propagating SV wave

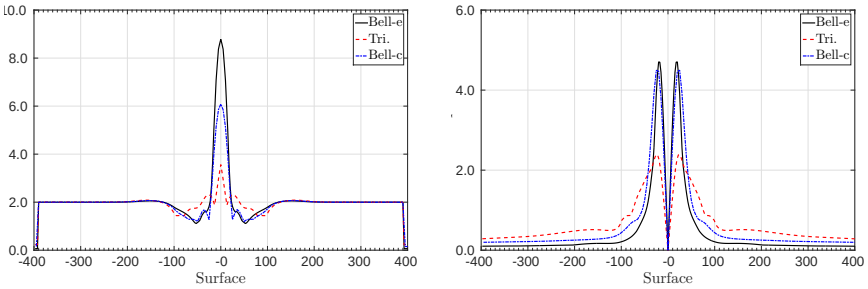

(a) x direction (b) y direction

Figure 5.36: Maximum displacement on the surface of three-dimensional hills for a vertically propagating SV wave

upstream and downstream slope of $U = D = 2$. We define the material properties of the core such that the shear and pressure wave velocities are $c_s = 200$ m/s and $c_p = 326.6$ m/s, respectively, and the corresponding values for the embankment are $c_s = 150$ m/s and $c_p = 224.95$ m/s, respectively. We consider a homogeneous medium for the foundation with mass density $\rho = 2000$ kg/m^3, shear wave velocity $c_s = 400$ m/s, and pressure wave velocity $c_p = 653.2$ m/s.

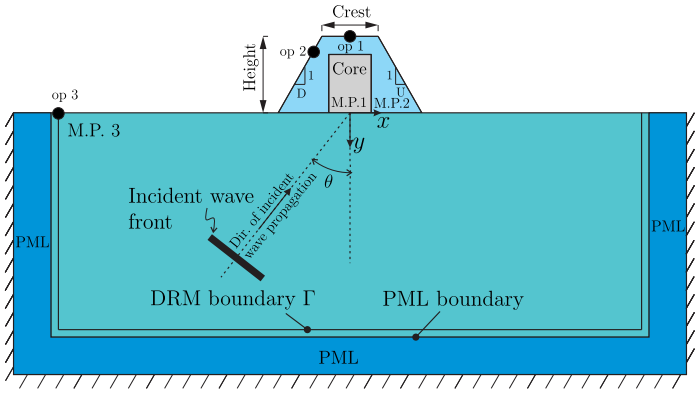

Figure 5.37: Schematic configuration of a typical levee

The extent of the semi-infinite physical domain has been truncated such that

the distance from the levee to the truncation boundary is about three times the shear wavelength. The computational domain has been surrounded on its sides and bottom by a ten-element-thick PML. We discretize the computational domain using quadratic quadrilateral elements with element size that allows for at least 40 points per shear wavelength. The simulation is performed in the time-domain with no material damping. The incident wave is a plane SV-wave in the form of a Ricker pulse with central frequency $f_r = 5$ Hz.

Figure 5.38 shows the displacement time histories (normalized with respect to the amplitude of the incident wave u_i) and the frequency content of the signals at four observation points (Figure 5.37). The first set of results corresponds to the first observation point located at the middle of the crest of the levee. The displacement amplification, which is roughly equal to 5.0, is remarkable in comparison with what we would expect in a one-dimensional simulation (2). The frequency spectrum of this signal also shows remarkable amplification at certain frequencies: for example, the displacement amplitude for frequencies 3.9 Hz and 4.6 Hz is more than one, while under a flat-surface assumption, the corresponding amplitudes are only 0.3. The displacement at the second observation point, located on the side of the levee, does not show as strong an amplification as the mid-crest point, but, includes both horizontal and vertical displacements, which would have not been seen in a one-dimensional model. The frequency spectra of the signals still show large amplifications in comparison to the incident wave. Notice that the amplification is larger for frequencies above the central frequency $f_r = 5$ Hz for the vertical displacement, as opposed to the horizontal displacement. The last observation point is located on the flat surface

away from the levee. The displacement time history at this point shows that the presence of a levee, with loose material, on a stiff foundation, does not affect the motion significantly on the flat surface away from the levee. The amplitude of the reflected waves from the levee, followed by the main shock, are smaller than the main shock. Also Notice that due to the contrast between the material properties of the levee and the foundation, waves get trapped within the loose material, resulting in a distinctive amplification pattern.

Figure 5.39 shows the maximum surface amplification for the entire simulation for a normalized coordinate such that the levee extends between -1 and $+1$. We expect to observe a horizontal amplification of magnitude 2 for a flat homogeneous domain, however, at the levee the wave amplification is 240% larger than the flat surface. Based on this simulation, the maximum horizontal displacement is 4.80 and occurs at 0.705s at the middle of the crest, while the maximum vertical displacement is 2.69 and occurs at 0.816s, 5.4m away from the mid-point, on the slope. We observe that amplification happens in the entire levee, but amplification on the flat surface away from the levee remains constant. Notice that in this simulation, we only considered a short incident wave signal, thus, the reflected waves from the levee do not interfere strongly with the incident wave, leading to a localized amplification only within the levee. Longer duration incident waves would result in a different amplification or de-amplification pattern.

Figure 5.40 shows the displacement contours in the x and y directions at various time-steps. The first snapshot, taken at time 0.40s, shows the plane incident wave propagating in the domain before it hits the surface. Notice that the vertical

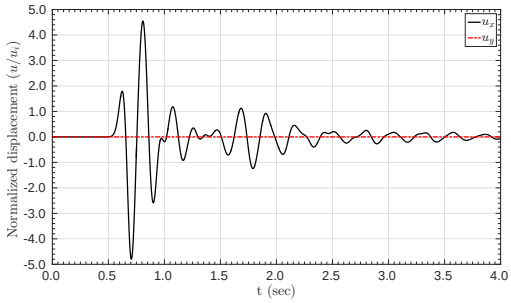

(a) Displacement time history at op 1

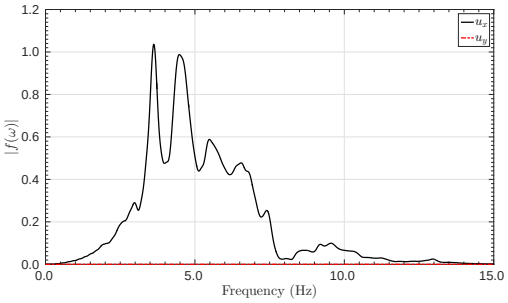

(b) Frequency spectrum at op 1

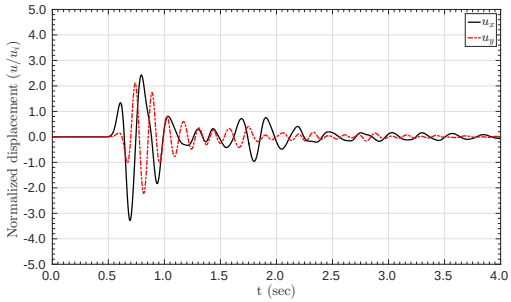

(c) Displacement time history at op 2

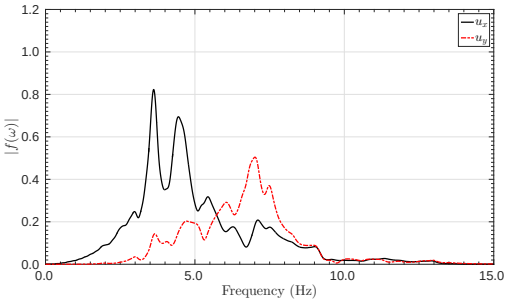

(d) Frequency spectrum at op 2

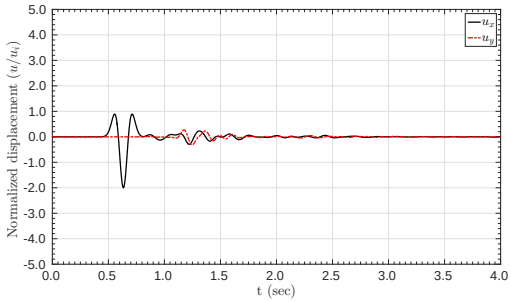

(e) Displacement time history at op 3

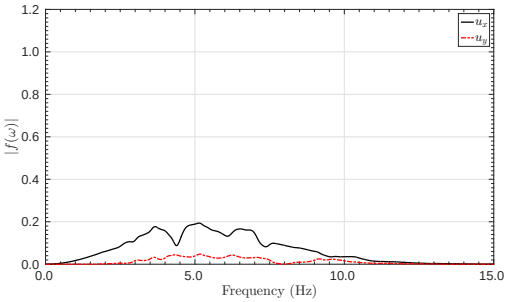

(f) Frequency spectrum at op 3

Figure 5.38: (a) Displacement time histories and (b) their frequency spectra at various observation points, for the levee model due to a vertically propagating SV-wave

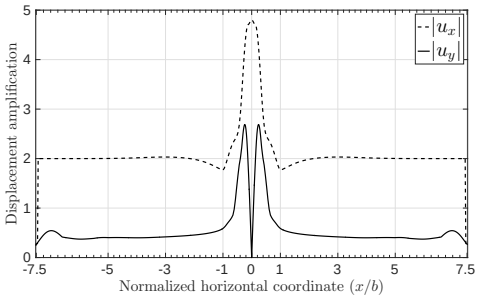

Figure 5.39: Maximum surface displacement on the surface of the levee

displacement is zero because the particle motion is only in the x direction for a vertically propagating SV-wave. The next set of snapshots shows the displacement field at time 0.71s, the moment the wave hits the surface. Notice the trapped wave within the levee in the x direction and also the wave generated in the y direction. The next two snapshots show the motion after the main wave reflected from the surface. The wave focusing, due to the constructive interference of the reflected and surface waves, even though the main shock has long passed, is noticeable and the displacement is still as large as 3 times the amplitude of the incident wave. The motion focus, and as a result the stresses, at the sharp corners of the levee is significant.

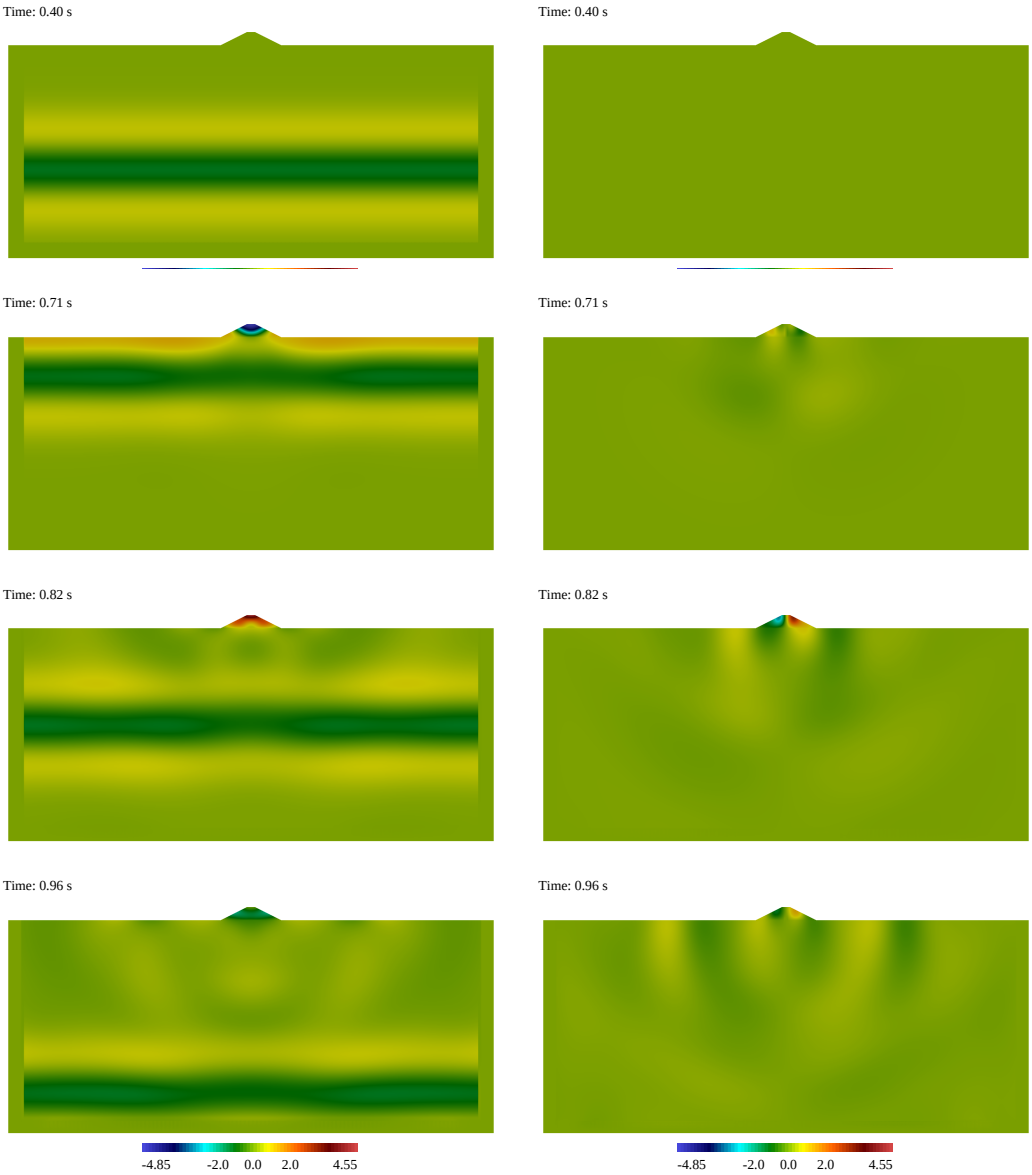

(a) displacement in the y direction (b) displacement in the y direction

Figure 5.40: Displacement contours along the x and y directions in the levee due to a vertically propagating SV-wave

Chapter 6

Conclusions

Seismic hazard assessment studies rely increasingly on wave motion simulations, which, when provided with reliable material properties (velocity models), would yield the surface motion for given seismic input scenarios. Most developments to date do not account for topographical features, making the assumption of a flat earth surface model. Observations from strong earthquakes, however, have shown that the presence of topographic features can significantly aggravate the catastrophic consequences of strong seismic motion. The effects of topography on site response may not be predicted by the widely employed flat surface models.

It is the aim of this work to fill the modeling gap, and advance the state-of-the art in available tools for seismic hazard mitigation: (i) by developing computational tools that fully account for the effects of topography in seismic motion simulations; (ii) by validating the numerical models/predictions using existing analytical solutions; and (iii) by identifying the critical parameters that govern the intensity of topographic amplification.

Figure 6.1 depicts the computational framework developed in this work that made possible the study of wave motion amplifications. In short, the developed toolchain accounts systematically for model input, meshing (using METIS [152]) and

partitioning. The main computational engine was build on top of PETSc [19, 18, 20] and includes spectral elements in 2D and 3D for wave propagation, PMLs for domain truncation, DRM for seismic input, and explicit solvers for time marching. The post-processing/visualization step includes an interface with ParaView [122]. This computational framework has been also implemented to a full-waveform inversion approach for high-fidelity subsurface imaging of the soil. This inverse approach commonly arises in geotechnical site characterization, for example [86, 87, 88, 142] and geophysical explorations [137, 147, 148, 149, 150, 151, 174, 175].

We deployed the developed computational tool to systematically simulate wave motion for different scenarios. In this chapter, we summarize the main observations.

6.1 Summary of the results

6.1.1 Topography effects

We conducted parametric studies that provided insight on the amplification of plane P- and SV-waves by idealized topographic features. The results of this research can be combined with the soil-structure interaction studies to obtain the impedance functions for foundations located on hills and valleys [80, 81, 82, 83, 102, 136].

Overall, the feature's geometry and its relation to the characteristics of the propagating waves affect decidedly the severity of the motion amplification in terms of magnitude and location.

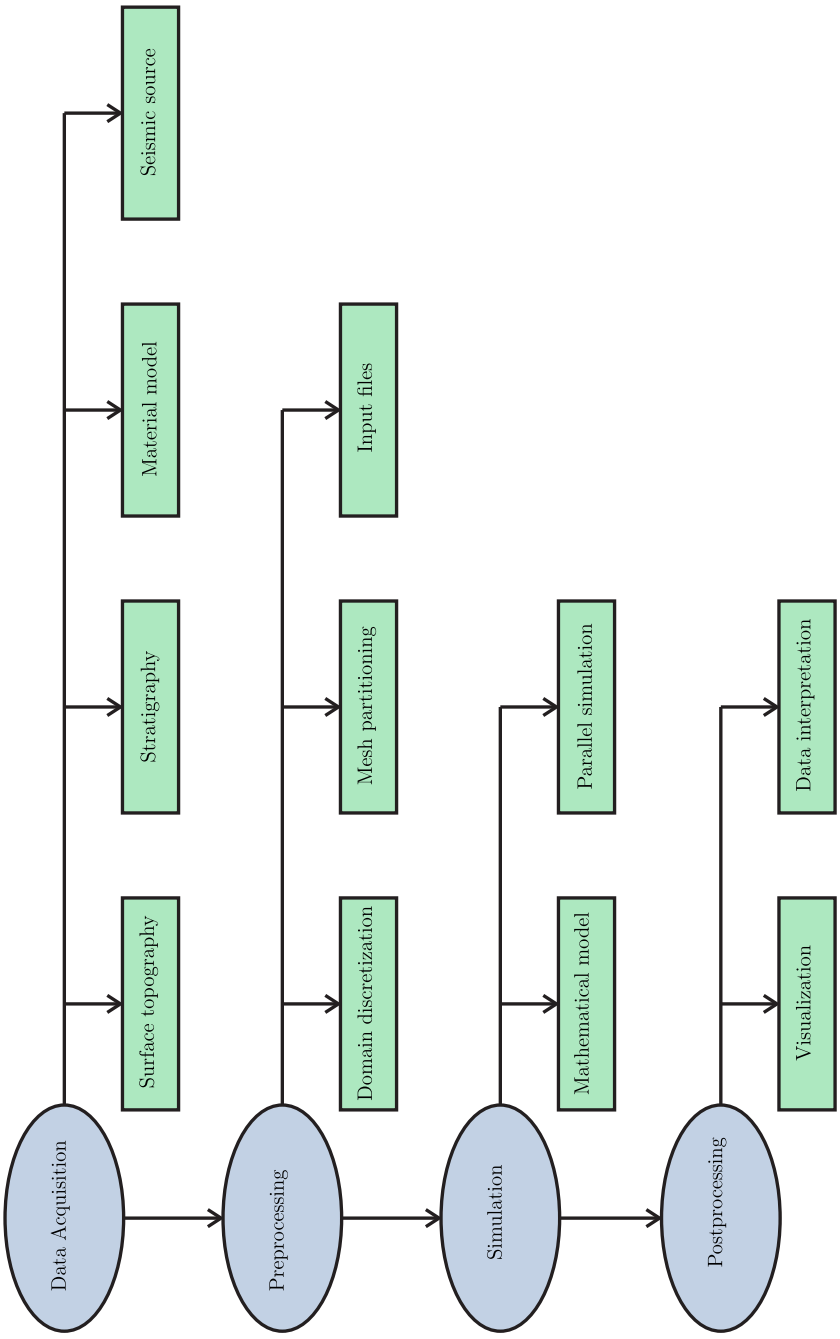

Figure 6.1: Schematic procedure to perform a seismic simulation

For events characterized by frequencies resulting in wavelengths longer than a characteristic dimension of the topographic feature, the feature appears nearly transparent to the incoming wave, and the resulting surface motion pattern is almost unaffected by the presence of the feature. But, in all other cases, a complex motion pattern emerges, resulting in significant amplification.

As expected, the strongest amplification is observed within the topographic feature, owing to the constructive interference of both body and surface waves inside and on the feature. But, the occurrence of strong amplification away from the feature cannot be excluded, as special cases reported herein demonstrate.

An interesting observation emerging from the present study refers to the importance of maintaining as faithful a geometric representation of the physical terrain as is possible, especially in light of the growing reliance on digital elevation data: two fairly close geometries may result in significantly different amplification patterns, as the numerical studies demonstrated.

We also reported on amplification patterns related to idealized valleys: overall, the amplification is weaker when dealing with terrain depressions than with proud topographic features.

Specific observations include:

- The approximation of a topographic feature's geometry affects the amplification in the SV incidence case, regardless of the angle and frequency of the incident wave. By contrast, for P incidence, the amplification at low frequencies is affected less by geometric variations.

- The surface pattern on a hill is affected significantly by the feature's geometry. There are noticeable differences in the amplification pattern between the semi-circular feature, and any of the other three considered geometries. Differences can be observed even between the triangular feature and any of the two bell-shaped circumscribing geometries, both within the feature, as well as on the flat surface exterior to the feature. Differences in the overall amplification pattern between the two bell-shaped geometries are less pronounced, but become significant in the region within the feature, indicating again the importance of geometric representation.

- In general, for low frequencies, or equivalently, for incident wavelengths that are several times the size of the feature's height, the effect of the feature's geometry tends to diminish, leading to smaller amplification values.

- The angle of incidence tends to impact more the amplification for higher frequencies. For very low frequencies ($\eta < 0.5$), which are tantamount to a small feature in comparison to the incident wavelength, the angle of incidence does not change the amplification significantly.

- The interplay between the angle of incidence and the feature's geometry suggests that when waves become trapped within the feature in such manner that a constructive interface pattern is developed, the amplification can become large. By contrast, when the feature is wide enough, reflected waves from the hillsides leave the feature without being trapped, resulting in smaller amplification. We observed amplifications larger than 10 for a shape ratio of 45° (steeper), when,

by contrast for a shape ratio of 15° (flatter) amplifications are barely larger than 4.

- The study of the surface amplification patterns in hills indicates that de-amplification is possible to occur within or away from the feature. De-amplification stems from the destructive interference of incoming, reflected, and Rayleigh waves generated at the bottom of the hill.

- In almost all cases, the maximum amplification occurs on the surface of the hill. Exceptions are associated with very small frequencies, where the incident shear wavelength is several times the feature's height.

- Even though, in general, the strongest motion will arise within the feature, the amplification pattern away from the feature, i.e., on the flat surface to the sides of the feature, may be significantly affected. Compared to a flat-surface model, the presence of a feature may amplify or de-amplify the motion on the flat part of the surface, where the amplification may reach 2.5 to 3. Similarly, de-amplification may also occur on parts of the flat surroundings, even leading to near-silent zones.

- Surface amplifications due to the presence of a valley are overall smaller than in the case of hill topography. The main reason is that a valley scatters the incoming waves in a way that energy disperses away from the feature, as opposed to the hill, where the energy focuses within the feature.

- The influence of wave frequency is less prominent for valleys than for hills. For SV incidence, the amplification remains almost constant for frequencies higher than $\eta = 1.5$. The P-wave amplification shows a minor rise up to roughly $\eta = 0.5$, when the wavelength of the incoming wave is twice the depth of the valley, and reduces as the frequency increases.

- For valleys the angle of incidence hardly affects the strong displacement components on the surface (horizontal displacement for SV wave, and vertical displacement for P-wave). By contrast, the weak displacement components are highly affected by the angle of incidence. The amplification decreases sharply as the angle of incidence increases for P incidence and remains constant for angles above $\theta_p = 30°$. The SV incidence shows an increase once the angle comes closer to the critical angle.

- In most cases, the location of the maximum amplification is on the flat surface to the sides of the valley.

6.1.2 Model dimensionality effects

We studied model dimensionality effects on the seismic motion via time-domain numerical experiments in domains with irregular surfaces and in layered media. We concluded that a one-dimensional model underestimates the amplification, compared to the two- and three-dimensional models. Additionally, in some cases, the one-dimensional model may overestimate the motion by not considering the destructive interference of waves. In other words, the results from the equivalent one-dimensional model, in the majority of cases, are fundamentally different from the actual two- or

three-dimensional models. We encourage rigorous, full three-dimensional simulations, including surface topography, soil layers, and the seismic source, for sensitive structures, such as nuclear power plants, high rise buildings, and others, especially in seismic prone areas.

6.1.3 Geometry idealization

We studied the effects geometry idealization has on the surface displacement via parametric studies in the frequency- and time-domains. Our results indicate that small changes in the geometry of the topography could affect the amplification as well as the location of the maximum surface displacement. Thus, in order to have a more realistic approximation, we need to model the topography as close as possible to reality. We also remark that it is not possible to isolate the effects of topography on amplification from those the stratigraphy.

6.2 Contributions

Key contributions of the present development are listed below:

- We have extended the Perfectly-Matched-Layers (PMLs) and the Multi-axial Perfectly-Matched-Layers (M-MPL) to three-dimensional models.
- We have coupled the Domain Reduction Method (DRM) with the PMLs; the resulting methodology can fully account for seismic wave motion simulation in two- and three-dimensional heterogeneous domains.
- To improve the efficiency of the time-domain simulations, we implemented the

Runge-Kutta-Fehlberg adaptive time solver, in addition to the Runge-Kutta 4 fixed time-step scheme, to obviate the necessity of several trial and error simulations for arriving at an optimal time-step.

- A parallel wave motion numerical simulator has been developed, which includes: (1) a mesh partitioner interface on top of the METIS library; (2) main simulation engine, which is capable of simulating two- and three-dimensional wave propagation in the time- and frequency-domains, using either structured or unstructured discretizations; and (3) data visualization interface for ParaView based on the VTK toolkit.

- We conducted extensive parametric studies to explore the effects of topography on seismic wave amplification.

- We studied model dimensionality effects on the seismic response heterogeneous domains.

6.3 Improvements –future research

In order to improve the accuracy of seismic simulations, we highlight the following future research topics, that we found to have notable impact on the results, but were out of the scope of this work:

- Material damping was not included in our models. The computational engine we developed can readily accommodate any number of linear material attenuation models.

- Coupling of the soil to structures for a comprehensive seismic risk assessment of cities and sensitive infrastructure components.

- An important goal of computational seismology is to simulate dynamic earthquake rupture and strong ground motion in realistic models that include crustal heterogeneities and complex fault geometries. Mathematical models for seismic fault modeling is an area that requires attention. The available models to simulate faults, due to the complexity of the the rupture, introduce uncertainty in the computations. More rigorous seismic fault models such as dynamic or kinematic models may be considered.

- We excluded any nonlinearity in our simulations, assuming that seismic waves propagate as linear elastic waves, include nonlinear behavior, modifications will be required to the main engine, but we remark that the DRM/PML framework need to change.

- In our numerical simulations, we assumed that the material and geometric properties of the domain of interest are known with confidence. The effect of uncertainty associated with our knowledge of material and geometric properties on wave motion amplification can be quantified by conducting sensitivity and reliability analyses.

Appendices

Appendix A

PML discrete forms

This appendix provides details for the submatrices used in the PML and M-PML absorbing boundary conditions for two- and three-dimensional domains.

A.1 PML matrices

A.1.1 Submatrices for (2.27) –in 2D

Subscripts in the shape functions indicate derivatives.

$$\mathbf{K}_{\mathrm{RD}} = \int_{\Omega^{\mathrm{RD}}} \begin{bmatrix} (\lambda+2\mu)\boldsymbol{\Phi}_x\boldsymbol{\Phi}_x^T + \mu(\boldsymbol{\Phi}_y\boldsymbol{\Phi}_y^T) & \lambda\boldsymbol{\Phi}_x\boldsymbol{\Phi}_y^T + \mu\boldsymbol{\Phi}_y\boldsymbol{\Phi}_x^T \\ \lambda\boldsymbol{\Phi}_y\boldsymbol{\Phi}_x^T + \mu\boldsymbol{\Phi}_x\boldsymbol{\Phi}_y^T & (\lambda+2\mu)\boldsymbol{\Phi}_y\boldsymbol{\Phi}_y^T + \mu(\boldsymbol{\Phi}_x\boldsymbol{\Phi}_x^T) \end{bmatrix} \mathrm{d}\Omega. \quad \text{(A.1)}$$

$$\mathbf{M}_{\mathrm{RD}} = \int_{\Omega^{\mathrm{RD}}} \rho \ \mathrm{diag}(\boldsymbol{\Phi}\boldsymbol{\Phi}^T, \boldsymbol{\Phi}\boldsymbol{\Phi}^T)\, \mathrm{d}\Omega. \quad \text{(A.2a)}$$

$$\mathbf{M}_i = \int_{\Omega^{\mathrm{RD}}} i \ \rho \ \mathrm{diag}(\boldsymbol{\Phi}\boldsymbol{\Phi}^T, \boldsymbol{\Phi}\boldsymbol{\Phi}^T)\, \mathrm{d}\Omega, \quad i = a, b, c. \quad \text{(A.2b)}$$

$$\mathbf{N}_i = \int_{\Omega^{\mathrm{PML}}} i \ \mathrm{diag}(\boldsymbol{\Psi}\boldsymbol{\Psi}^T, \boldsymbol{\Psi}\boldsymbol{\Psi}^T, 2\boldsymbol{\Psi}\boldsymbol{\Psi}^T)\mathrm{d}\Omega, \quad i = a, b, c. \quad \text{(A.2c)}$$

$$a = \alpha_x \ \alpha_y, \quad b = \alpha_x \ \beta_y + \alpha_y \ \beta_x, \quad c = \beta_x \ \beta_y.$$

α and β are scaling and attenuation functions according to the PML stretching function.

$$\mathbf{A}_{iu} = \int_{\Omega^{\mathrm{PML}}} \begin{bmatrix} \boldsymbol{\Phi}_x \boldsymbol{\Psi}^T \hat{\lambda}_y^i & & \boldsymbol{\Phi}_y \boldsymbol{\Psi}^T \hat{\lambda}_x^i \\ & \boldsymbol{\Phi}_y \boldsymbol{\Psi}^T \hat{\lambda}_x^i & \boldsymbol{\Phi}_x \boldsymbol{\Psi}^T \hat{\lambda}_y^i \end{bmatrix} \mathrm{d}\Omega, \tag{A.3}$$

$$i = e, p, \quad \hat{\lambda}_j^e = \alpha_j, \qquad \hat{\lambda}_j^p = \beta_j.$$

$$\mathbf{A}_{il} = \int_{\Omega^{\mathrm{PML}}} \begin{bmatrix} (\lambda + 2\mu)\boldsymbol{\Phi}_x \boldsymbol{\Psi}^T \hat{\lambda}_y^i & \lambda \boldsymbol{\Phi}_x \boldsymbol{\Psi}^T \hat{\lambda}_y^i & 2\mu \boldsymbol{\Phi}_y \boldsymbol{\Psi}^T \hat{\lambda}_x^i \\ \lambda \boldsymbol{\Phi}_y \boldsymbol{\Psi}^T \hat{\lambda}_x^i & (\lambda + 2\mu)\boldsymbol{\Phi}_y \boldsymbol{\Psi}^T \hat{\lambda}_x^i & 2\mu \boldsymbol{\Phi}_x \boldsymbol{\Psi}^T \hat{\lambda}_y^i \end{bmatrix} \mathrm{d}\Omega, \tag{A.4}$$

$$i = e, p, \qquad \hat{\lambda}_j^e = \alpha_j, \qquad \hat{\lambda}_j^p = \beta_j.$$

$$\mathbf{f}_{\mathrm{RD}} = \int_{\Gamma_N^{\mathrm{RD}}} \begin{bmatrix} \boldsymbol{\Phi}\ g_x(\mathbf{x}, t) \\ \boldsymbol{\Phi}\ g_y(\mathbf{x}, t) \end{bmatrix} \mathrm{d}\Gamma + \int_{\Omega^{\mathrm{RD}}} \begin{bmatrix} \boldsymbol{\Phi}\ b_x(\mathbf{x}, t) \\ \boldsymbol{\Phi}\ b_y(\mathbf{x}, t) \end{bmatrix} \mathrm{d}\Omega. \tag{A.5}$$

A.1.2 Submatrices for (2.48) –in 3D

$$\mathbf{K}_{\mathrm{RD}} = \int_{\Omega^{\mathrm{RD}}} \begin{bmatrix} \mathbf{K}_{xx} & \mathbf{K}_{xy} & \mathbf{K}_{xz} \\ \mathbf{K}_{yx} & \mathbf{K}_{yy} & \mathbf{K}_{yz} \\ \mathbf{K}_{zx} & \mathbf{K}_{zy} & \mathbf{K}_{zz} \end{bmatrix} \mathrm{d}\Omega, \tag{A.6}$$

$$\mathbf{K}_{xx} = (\lambda + 2\mu)\mathbf{\Phi}_x\mathbf{\Phi}_x^T + \mu(\mathbf{\Phi}_y\mathbf{\Phi}_y^T + \mathbf{\Phi}_z\mathbf{\Phi}_z^T),$$

$$\mathbf{K}_{xy} = \lambda\mathbf{\Phi}_x\mathbf{\Phi}_y^T + \mu\mathbf{\Phi}_y\mathbf{\Phi}_x^T,$$

$$\mathbf{K}_{xz} = \lambda\mathbf{\Phi}_x\mathbf{\Phi}_z^T + \mu\mathbf{\Phi}_z\mathbf{\Phi}_x^T,$$

$$\mathbf{K}_{yx} = \lambda\mathbf{\Phi}_y\mathbf{\Phi}_x^T + \mu\mathbf{\Phi}_x\mathbf{\Phi}_y^T,$$

$$\mathbf{K}_{yy} = (\lambda + 2\mu)\mathbf{\Phi}_y\mathbf{\Phi}_y^T + \mu(\mathbf{\Phi}_x\mathbf{\Phi}_x^T + \mathbf{\Phi}_z\mathbf{\Phi}_z^T),$$

$$\mathbf{K}_{yz} = \lambda\mathbf{\Phi}_y\mathbf{\Phi}_z^T + \mu\mathbf{\Phi}_z\mathbf{\Phi}_y^T,$$

$$\mathbf{K}_{zx} = \lambda\mathbf{\Phi}_z\mathbf{\Phi}_x^T + \mu\mathbf{\Phi}_x\mathbf{\Phi}_z^T,$$

$$\mathbf{K}_{zy} = \lambda\mathbf{\Phi}_z\mathbf{\Phi}_y^T + \mu\mathbf{\Phi}_y\mathbf{\Phi}_z^T,$$

$$\mathbf{K}_{zz} = (\lambda + 2\mu)\mathbf{\Phi}_z\mathbf{\Phi}_z^T + \mu(\mathbf{\Phi}_x\mathbf{\Phi}_x^T + \mathbf{\Phi}_y\mathbf{\Phi}_y^T).$$

$$\mathbf{M}_{\mathrm{RD}} = \int_{\Omega^{\mathrm{RD}}} \rho\ \mathrm{diag}(\mathbf{\Phi}\mathbf{\Phi}^T, \mathbf{\Phi}\mathbf{\Phi}^T, \mathbf{\Phi}\mathbf{\Phi}^T)\ \mathrm{d}\Omega. \tag{A.7a}$$

$$\mathbf{M}_i = \int_{\Omega^{\mathrm{RD}}} i\ \rho\ \mathrm{diag}(\mathbf{\Phi}\mathbf{\Phi}^T, \mathbf{\Phi}\mathbf{\Phi}^T, \mathbf{\Phi}\mathbf{\Phi}^T)\ \mathrm{d}\Omega, \quad i = a, b, c, d. \tag{A.7b}$$

$$\mathbf{N}_i = \int_{\Omega^{\mathrm{PML}}} i\ \mathrm{diag}(\mathbf{\Psi}\mathbf{\Psi}^T, \mathbf{\Psi}\mathbf{\Psi}^T, \mathbf{\Psi}\mathbf{\Psi}^T, 2\mathbf{\Psi}\mathbf{\Psi}^T, 2\mathbf{\Psi}\mathbf{\Psi}^T, 2\mathbf{\Psi}\mathbf{\Psi}^T)\mathrm{d}\Omega, \quad i = a, b, c, d. \tag{A.7c}$$

$$\mathbf{A}_{iu} = \int\limits_{\Omega^{\mathrm{PML}}} \begin{bmatrix} \boldsymbol{\Phi}_x\boldsymbol{\Psi}^T\hat{\lambda}^i_{yz} & & & \boldsymbol{\Phi}_y\boldsymbol{\Psi}^T\hat{\lambda}^i_{xz} & \boldsymbol{\Phi}_z\boldsymbol{\Psi}^T\hat{\lambda}^i_{xy} & \\ & \boldsymbol{\Phi}_y\boldsymbol{\Psi}^T\hat{\lambda}^i_{xz} & & \boldsymbol{\Phi}_x\boldsymbol{\Psi}^T\hat{\lambda}^i_{yz} & & \boldsymbol{\Phi}_z\boldsymbol{\Psi}^T\hat{\lambda}^i_{xy} \\ & & \boldsymbol{\Phi}_z\boldsymbol{\Psi}^T\hat{\lambda}^i_{xy} & & \boldsymbol{\Phi}_x\boldsymbol{\Psi}^T\hat{\lambda}^i_{yz} & \boldsymbol{\Phi}_y\boldsymbol{\Psi}^T\hat{\lambda}^i_{xz} \end{bmatrix} \mathrm{d}\Omega, \tag{A.8}$$

$$i = e, w, p, \qquad \hat{\lambda}^e_{jk} = \alpha_j\alpha_k, \qquad \hat{\lambda}^p_{jk} = \alpha_j\beta_k + \beta_j\alpha_k, \qquad \hat{\lambda}^w_{jk} = \beta_j\beta_k, \qquad j, k = x, y, z.$$

$$\mathbf{A}_{il} = \int\limits_{\Omega^{\mathrm{PML}}} \begin{bmatrix} \mathbf{A}_{x1} & \mathbf{A}_{x2} & \mathbf{A}_{x3} & \mathbf{A}_{x4} & \mathbf{A}_{x5} & \\ \mathbf{A}_{y1} & \mathbf{A}_{y2} & \mathbf{A}_{y3} & \mathbf{A}_{y4} & & \mathbf{A}_{y6} \\ \mathbf{A}_{z1} & \mathbf{A}_{z2} & \mathbf{A}_{z3} & & \mathbf{A}_{z5} & \mathbf{A}_{z6} \end{bmatrix} \mathrm{d}\Omega, \tag{A.9}$$

$$\begin{aligned}
&\mathbf{A}_{x1} = (\lambda + 2\mu)\boldsymbol{\Phi}_x\boldsymbol{\Psi}^T\hat{\lambda}^i_{yz}, && \mathbf{A}_{y1} = \lambda\boldsymbol{\Phi}_y\boldsymbol{\Psi}^T\hat{\lambda}^i_{xz}, && \mathbf{A}_{z1} = \lambda\boldsymbol{\Phi}_z\boldsymbol{\Psi}^T\hat{\lambda}^i_{xy}, \\
&\mathbf{A}_{x2} = \lambda\boldsymbol{\Phi}_x\boldsymbol{\Psi}^T\hat{\lambda}^i_{yz}, && \mathbf{A}_{y2} = (\lambda + 2\mu)\boldsymbol{\Phi}_y\boldsymbol{\Psi}^T\hat{\lambda}^i_{xz}, && \mathbf{A}_{z2} = \lambda\boldsymbol{\Phi}_z\boldsymbol{\Psi}^T\hat{\lambda}^i_{xy}, \\
&\mathbf{A}_{x3} = \lambda\boldsymbol{\Phi}_x\boldsymbol{\Psi}^T\hat{\lambda}^i_{yz},, && \mathbf{A}_{y3} = \lambda\boldsymbol{\Phi}_y\boldsymbol{\Psi}^T\hat{\lambda}^i_{xz}, && \mathbf{A}_{z3} = (\lambda + 2\mu)\boldsymbol{\Phi}_z\boldsymbol{\Psi}^T\hat{\lambda}^i_{xy}, \\
&\mathbf{A}_{x4} = 2\mu\boldsymbol{\Phi}_y\boldsymbol{\Psi}^T\hat{\lambda}^i_{xz}, && \mathbf{A}_{y4} = 2\mu\boldsymbol{\Phi}_x\boldsymbol{\Psi}^T\hat{\lambda}^i_{yz}, && \mathbf{A}_{z5} = 2\mu\boldsymbol{\Phi}_x\boldsymbol{\Psi}^T\hat{\lambda}^i_{yz}, \\
&\mathbf{A}_{x5} = 2\mu\boldsymbol{\Phi}_z\boldsymbol{\Psi}^T\hat{\lambda}^i_{xy}, && \mathbf{A}_{y6} = 2\mu\boldsymbol{\Phi}_z\boldsymbol{\Psi}^T\hat{\lambda}^i_{xy}, && \mathbf{A}_{z6} = 2\mu\boldsymbol{\Phi}_y\boldsymbol{\Psi}^T\hat{\lambda}^i_{xz}, \\
&\hat{\lambda}^e_{jk} = \alpha_j\alpha_k, && \hat{\lambda}^p_{jk} = \alpha_j\beta_k + \beta_j\alpha_k, && \hat{\lambda}^w_{jk} = \beta_j\beta_k, \\
&\quad i = e, w, p, && j, k = x, y, z.
\end{aligned}$$

$$\mathbf{f}_{\mathrm{RD}} = \int\limits_{\Gamma_N^{\mathrm{RD}}} \begin{bmatrix} \boldsymbol{\Phi}\ g_x(\mathbf{x}, t) \\ \boldsymbol{\Phi}\ g_y(\mathbf{x}, t) \\ \boldsymbol{\Phi}\ g_z(\mathbf{x}, t) \end{bmatrix} \mathrm{d}\Gamma + \int\limits_{\Omega^{\mathrm{RD}}} \begin{bmatrix} \boldsymbol{\Phi}\ b_x(\mathbf{x}, t) \\ \boldsymbol{\Phi}\ b_y(\mathbf{x}, t) \\ \boldsymbol{\Phi}\ b_z(\mathbf{x}, t) \end{bmatrix} \mathrm{d}\Omega. \tag{A.11}$$

A.2 M-PML matrices

$$\begin{aligned}
\mathbf{A}_{iu} = &\int\limits_{\Omega^{\mathrm{PML}}} \begin{bmatrix} \boldsymbol{\Phi}_x\boldsymbol{\Psi}^T\hat{\lambda}^i_{yz} & & & \boldsymbol{\Phi}_y\boldsymbol{\Psi}^T\hat{\lambda}^i_{xz} & \boldsymbol{\Phi}_z\boldsymbol{\Psi}^T\hat{\lambda}^i_{xy} & \\ & \boldsymbol{\Phi}_y\boldsymbol{\Psi}^T\hat{\lambda}^i_{xz} & & \boldsymbol{\Phi}_x\boldsymbol{\Psi}^T\hat{\lambda}^i_{yz} & & \boldsymbol{\Phi}_z\boldsymbol{\Psi}^T\hat{\lambda}^i_{xy} \\ & & \boldsymbol{\Phi}_z\boldsymbol{\Psi}^T\hat{\lambda}^i_{xy} & & \boldsymbol{\Phi}_x\boldsymbol{\Psi}^T\hat{\lambda}^i_{yz} & \boldsymbol{\Phi}_y\boldsymbol{\Psi}^T\hat{\lambda}^i_{xz} \end{bmatrix} \mathrm{d}\Omega \\
&+ \int\limits_{\Omega^{\mathrm{PML}}} \begin{bmatrix} \boldsymbol{\Phi}\boldsymbol{\Psi}^T\frac{\partial\hat{\lambda}^i_{yz}}{\partial x} & & & \boldsymbol{\Phi}\boldsymbol{\Psi}^T\frac{\partial\hat{\lambda}^i_{xz}}{\partial y} & \boldsymbol{\Phi}\boldsymbol{\Psi}^T\frac{\partial\hat{\lambda}^i_{xy}}{\partial z} & \\ & \boldsymbol{\Phi}\boldsymbol{\Psi}^T\frac{\partial\hat{\lambda}^i_{xz}}{\partial y} & & \boldsymbol{\Phi}\boldsymbol{\Psi}^T\frac{\partial\hat{\lambda}^i_{yz}}{\partial x} & & \boldsymbol{\Phi}\boldsymbol{\Psi}^T\frac{\partial\hat{\lambda}^i_{xy}}{\partial z} \\ & & \boldsymbol{\Phi}\boldsymbol{\Psi}^T\frac{\partial\hat{\lambda}^i_{xy}}{\partial z} & & \boldsymbol{\Phi}\boldsymbol{\Psi}^T\frac{\partial\hat{\lambda}^i_{yz}}{\partial x} & \boldsymbol{\Phi}\boldsymbol{\Psi}^T\frac{\partial\hat{\lambda}^i_{xz}}{\partial y} \end{bmatrix} \mathrm{d}\Omega,
\end{aligned} \tag{A.12}$$

$$\hat{\lambda}^e_{jk} = \alpha_j\alpha_k, \quad \hat{\lambda}^p_{jk} = \alpha_j\beta_k + \beta_j\alpha_k, \quad \hat{\lambda}^w_{jk} = \beta_j\beta_k, \quad i = e, w, p, \quad j, k = x, y, z.$$

Appendix B

Time integration implementation details

This appendix discusses the details of the time integration algorithms for the two- and three-dimensional formulations.

B.1 Newmark method

The implicit time integration algorithm based on the Newmark method for two-dimensional models, described in Section 2.3.1.1, is presented in Algorithm 1.

Algorithm 1 Implicit time integration scheme by Newmark method

Newmark's algorithm to solve the two-dimensional system initially at rest:
$\mathbf{M}\ddot{\mathbf{d}} + \mathbf{C}\dot{\mathbf{d}} + \mathbf{K}\mathbf{d} = \mathbf{f}$ ▷ eq.2.26

inputs
$\mathbf{M}, \mathbf{C}, \mathbf{K}$: global matrices
β, γ: Newmark's parameters
Δt: time-step
N: total number of steps (total simulation time = $N\Delta t$)

output
approximation of y at i-th step

steps

initialization
$t \longleftarrow \emptyset$
$\mathbf{d}_0 \longleftarrow \emptyset$
$\dot{\mathbf{d}}_0 \longleftarrow \emptyset$
$\ddot{\mathbf{d}}_0 \longleftarrow \emptyset$
assemble $\mathbf{K}^{\mathit{eff}}$ ▷ eq.2.92a
for $i \leftarrow 1 : N + 1$ **do** ▷ loop over the time-steps
    $t \longleftarrow (i-1)\Delta t$ ▷ update time
    update the effective force
    $\mathbf{f}_{n+1}^{\mathit{eff}} \leftarrow$ update $\mathbf{f}_{n+1}^{\mathit{eff}}$ ▷ eq.2.92b
    compute $\ddot{\mathbf{d}}_{n+1}$ ▷ eq.2.91
    $\mathbf{d}_{n+1}, \dot{\mathbf{d}}_{n+1} \leftarrow$ update $\mathbf{d}_{n+1}, \dot{\mathbf{d}}_{n+1}$ ▷ eq.2.90
    print the results (displacement, velocity, and acceleration)
end for

The implicit time integration algorithm by extended Newmark method for three-dimensional models, described in Section 2.3.1.2, is presented in Algorithm 2.

Algorithm 2 Implicit time integration scheme by extended Newmark method

Newmark's algorithm to solve the three-dimensional system initially at rest:
$\mathbf{M}\ddot{\mathbf{d}} + \mathbf{C}\dot{\mathbf{d}} + \mathbf{K}\mathbf{d} + \mathbf{G}\bar{\mathbf{d}} = \mathbf{f}$ ▷ eq.2.49
$\dot{\mathbf{d}} = \mathbf{d}|_{\text{PML}}$

inputs
$\mathbf{M}, \mathbf{C}, \mathbf{K}, \mathbf{G}$: global matrices
α, β, γ: Newmark's parameters
Δt: time-step
N: total number of steps (total simulation time $= N\Delta t$)
output
approximation of y at i-th step
steps

initialization
$t \longleftarrow \emptyset$
$\bar{\mathbf{d}}_0 \longleftarrow \emptyset$
$\mathbf{d}_0 \longleftarrow \emptyset$
$\dot{\mathbf{d}}_0 \longleftarrow \emptyset$
assemble $\mathbf{K}^{\mathit{eff}}$ ▷ eq.2.94a
for $i \leftarrow 1 : N + 1$ **do** ▷ loop over the time-steps
    $t \longleftarrow (i-1)\Delta t$ ▷ update time
    update the effective force
    $\mathbf{f}_{n+1}^{\mathit{eff}} \leftarrow$ update $\mathbf{f}_{n+1}^{\mathit{eff}}$ ▷ eq.2.94c
    compute $\ddot{\mathbf{d}}_{n+1}$ ▷ eq.2.94a
    $\bar{\mathbf{d}}, \mathbf{d}_{n+1}, \dot{\mathbf{d}}_{n+1} \leftarrow$ update $\bar{\mathbf{d}}, \mathbf{d}_{n+1}, \dot{\mathbf{d}}_{n+1}$ ▷ eq.2.93
    print the results (displacement, velocity, and acceleration)
end for

B.2 Second-order Runge-Kutta (RK-2) formulations

This section explains the accommodation of the second-order Runge-Kutta (RK-2) for the two- and three-dimensional formulations.

B.2.1 For two-dimensional problems

Comparing (2.100) with (2.95), we have:

$$\boldsymbol{y}(t) = \begin{bmatrix} \boldsymbol{d}_1 \\ \boldsymbol{d}_2 \end{bmatrix}, \tag{B.1a}$$

$$\boldsymbol{f}(\boldsymbol{y}(t), t) = \begin{bmatrix} \mathbf{0} & \mathbf{I} \\ -\mathbf{M}^{-1}\mathbf{K} & -\mathbf{M}^{-1}\mathbf{C} \end{bmatrix} \begin{bmatrix} \boldsymbol{d}_1 \\ \boldsymbol{d}_2 \end{bmatrix} + \begin{bmatrix} \mathbf{0} \\ \mathbf{M}^{-1}\mathbf{f} \end{bmatrix}. \tag{B.1b}$$

Hence, according to (2.103):

$$\begin{aligned} \boldsymbol{k}_1 = \begin{bmatrix} \boldsymbol{k}_{11} \\ \boldsymbol{k}_{12} \end{bmatrix} &= \begin{bmatrix} \mathbf{0} & \mathbf{I} \\ -\mathbf{M}^{-1}\mathbf{K} & -\mathbf{M}^{-1}\mathbf{C} \end{bmatrix} \begin{bmatrix} \boldsymbol{d}_1(t_n) \\ \boldsymbol{d}_2(t_n) \end{bmatrix} + \begin{bmatrix} \mathbf{0} \\ \mathbf{M}^{-1}\mathbf{f}(t_n) \end{bmatrix} \\ &= \begin{bmatrix} \boldsymbol{d}_2(t_n) \\ -\mathbf{M}^{-1}\mathbf{K}\boldsymbol{d}_1(t_n) - \mathbf{M}^{-1}\mathbf{C}\boldsymbol{d}_2(t_n) + \mathbf{M}^{-1}\mathbf{f}(t_n) \end{bmatrix}, \end{aligned} \tag{B.2a}$$

$$\begin{aligned} \boldsymbol{k}_2 = \begin{bmatrix} \boldsymbol{k}_{21} \\ \boldsymbol{k}_{22} \end{bmatrix} &= \begin{bmatrix} \mathbf{0} & \mathbf{I} \\ -\mathbf{M}^{-1}\mathbf{K} & -\mathbf{M}^{-1}\mathbf{C} \end{bmatrix} \begin{bmatrix} \boldsymbol{d}_1(t_n) + \Delta t\boldsymbol{k}_{11} \\ \boldsymbol{d}_2(t_n) + \Delta t\boldsymbol{k}_{12} \end{bmatrix} + \begin{bmatrix} \mathbf{0} \\ \mathbf{M}^{-1}\mathbf{f}(t_n + \Delta t) \end{bmatrix} \\ &= \begin{bmatrix} \boldsymbol{d}_2(t_n) + \Delta t\boldsymbol{k}_{12} \\ -\mathbf{M}^{-1}\mathbf{K}(\boldsymbol{d}_1(t_n) + \Delta t\boldsymbol{k}_{11}) - \mathbf{M}^{-1}\mathbf{C}(\boldsymbol{d}_2(t_n) + \Delta t\boldsymbol{k}_{12}) + \mathbf{M}^{-1}\mathbf{f}(t_n + \Delta t) \end{bmatrix}. \end{aligned} \tag{B.2b}$$

Having the functions updated at $n+1$-th time-step, the updated solution at $n+1$-th step results in:

$$\boldsymbol{u}_{n+1} = \boldsymbol{u}_n + \frac{\Delta t}{2}(\boldsymbol{k}_1 + \boldsymbol{k}_2). \tag{B.3}$$

B.2.2 For three-dimensional problems

Comparing (2.102) with (2.95), we have:

$$\boldsymbol{y}(t) = \begin{bmatrix} \boldsymbol{d}_1 \\ \boldsymbol{d}_2 \\ \boldsymbol{d}_3 \end{bmatrix}, \tag{B.4a}$$

$$\boldsymbol{f}(\boldsymbol{y}(t), t) = \begin{bmatrix} \mathbf{0} & \mathbf{I} & \mathbf{0} \\ \mathbf{0} & \mathbf{0} & \mathbf{I} \\ -\mathbf{M}^{-1}\mathbf{G} & -\mathbf{M}^{-1}\mathbf{K} & -\mathbf{M}^{-1}\mathbf{C} \end{bmatrix} \begin{bmatrix} \boldsymbol{d}_1 \\ \boldsymbol{d}_2 \\ \boldsymbol{d}_3 \end{bmatrix} + \begin{bmatrix} \mathbf{0} \\ \mathbf{0} \\ \mathbf{M}^{-1}\mathbf{f} \end{bmatrix}. \tag{B.4b}$$

Hence, according to (2.103):

$$\begin{aligned} \boldsymbol{k}_1 = \begin{bmatrix} \boldsymbol{k}_{11} \\ \boldsymbol{k}_{12} \\ \boldsymbol{k}_{13} \end{bmatrix} &= \begin{bmatrix} \mathbf{0} & \mathbf{I} & \mathbf{0} \\ \mathbf{0} & \mathbf{0} & \mathbf{I} \\ -\mathbf{M}^{-1}\mathbf{G} & -\mathbf{M}^{-1}\mathbf{K} & -\mathbf{M}^{-1}\mathbf{C} \end{bmatrix} \begin{bmatrix} \boldsymbol{d}_1(t_n) \\ \boldsymbol{d}_2(t_n) \\ \boldsymbol{d}_3(t_n) \end{bmatrix} + \begin{bmatrix} \mathbf{0} \\ \mathbf{0} \\ \mathbf{M}^{-1}\mathbf{f}(t_n) \end{bmatrix} \\ &= \begin{bmatrix} \boldsymbol{d}_2(t_n) \\ \boldsymbol{d}_3(t_n) \\ -\mathbf{M}^{-1}\mathbf{G}\boldsymbol{d}_1(t_n) - \mathbf{M}^{-1}\mathbf{K}\boldsymbol{d}_2(t_n) - \mathbf{M}^{-1}\mathbf{C}\boldsymbol{d}_3(t_n) + \mathbf{M}^{-1}\mathbf{f}(t_n) \end{bmatrix}, \end{aligned} \tag{B.5a}$$

$$\begin{aligned} \boldsymbol{k}_2 = \begin{bmatrix} \boldsymbol{k}_{21} \\ \boldsymbol{k}_{22} \\ \boldsymbol{k}_{23} \end{bmatrix} &= \begin{bmatrix} \mathbf{0} & \mathbf{I} & \mathbf{0} \\ \mathbf{0} & \mathbf{0} & \mathbf{I} \\ -\mathbf{M}^{-1}\mathbf{G} & -\mathbf{M}^{-1}\mathbf{K} & -\mathbf{M}^{-1}\mathbf{C} \end{bmatrix} \begin{bmatrix} \boldsymbol{d}_1(t_n) + \Delta t\boldsymbol{k}_{11} \\ \boldsymbol{d}_2(t_n) + \Delta t\boldsymbol{k}_{12} \\ \boldsymbol{d}_3(t_n) + \Delta t\boldsymbol{k}_{13} \end{bmatrix} + \begin{bmatrix} \mathbf{0} \\ \mathbf{0} \\ \mathbf{M}^{-1}\mathbf{f}(t_n + \Delta t) \end{bmatrix} \\ &= \begin{bmatrix} \boldsymbol{d}_2(t_n) + \Delta t\boldsymbol{k}_{12} \\ \boldsymbol{d}_3(t_n) + \Delta t\boldsymbol{k}_{13} \\ \{-\mathbf{M}^{-1}\mathbf{G}(\boldsymbol{d}_1(t_n) + \Delta t\boldsymbol{k}_{11}) - \mathbf{M}^{-1}\mathbf{K}(\boldsymbol{d}_2(t_n) + \Delta t\boldsymbol{k}_{12}) - \mathbf{M}^{-1}\mathbf{C}(\boldsymbol{d}_3(t_n) + \Delta t\boldsymbol{k}_{13}) \\ +\mathbf{M}^{-1}\mathbf{f}(t_n + \Delta t)\} \end{bmatrix}. \end{aligned} \tag{B.5b}$$

Having the functions updated at $n+1$-th time-step, the updated solution at $n+1$-th step results in:

$$\boldsymbol{u}_{n+1} = \boldsymbol{u}_n + \frac{\Delta t}{2}(\boldsymbol{k}_1 + \boldsymbol{k}_2). \tag{B.6}$$

B.2.3 Algorithm

Algorithm 3 shows the second-order Runge-Kutta procedure.

Algorithm 3 Explicit time integration by second-order Runge-Kutta method

numerical solution of the initial-value problem:
$\dot{\boldsymbol{y}} = \boldsymbol{f}(t, \boldsymbol{y}), \quad 0 \leq t \leq T, \quad \boldsymbol{y}(0) = \boldsymbol{0}$ ▷ 2.98

inputs
$\boldsymbol{f}$: initial value problem
Δt: time-step
N: total number of steps (total simulation time = $N\Delta t$)

output
approximation of y at i-th step

steps

initialization
$t \longleftarrow \emptyset$
$\boldsymbol{u} \longleftarrow \emptyset$
for $i \leftarrow 1 : N + 1$ **do** ▷ loop over the time-steps
    $t \longleftarrow (i-1)\Delta t$; ▷ update time
    update the functions
    $\boldsymbol{k}_1 \leftarrow$ update $\boldsymbol{k}_1$ ▷ 2D:B.2a-3D:B.5a
    $\boldsymbol{k}_2 \leftarrow$ update $\boldsymbol{k}_2$ ▷ 2D:B.2b-3D:B.5b
    update the results at the i-th time step
    $\boldsymbol{u} \leftarrow \boldsymbol{u} + \dfrac{\Delta t}{2}(\boldsymbol{k}_1 + \boldsymbol{k}_2)$ ▷ B.6
    print the results (displacement, velocity, and acceleration)
end for

B.3 Fourth-order Runge-Kutta (RK-4) formulations

This section explains the accommodation of the fourth-order Runge-Kutta (RK-4) for the two- and three-dimensional formulations.

B.3.1 For two-dimensional problems

Comparing (2.100) with (2.95), we have:

$$\boldsymbol{y}(t) = \begin{bmatrix} \boldsymbol{d}_1 \\ \boldsymbol{d}_2 \end{bmatrix}, \tag{B.7a}$$

$$\boldsymbol{f}(\boldsymbol{y}(t), t) = \begin{bmatrix} \mathbf{0} & \mathbf{I} \\ -\mathbf{M}^{-1}\mathbf{K} & -\mathbf{M}^{-1}\mathbf{C} \end{bmatrix} \begin{bmatrix} \boldsymbol{d}_1 \\ \boldsymbol{d}_2 \end{bmatrix} + \begin{bmatrix} \mathbf{0} \\ \mathbf{M}^{-1}\mathbf{f} \end{bmatrix}. \tag{B.7b}$$

Hence, according to (2.105):

$$\begin{aligned} \boldsymbol{k}_1 &= \begin{bmatrix} \boldsymbol{k}_{11} \\ \boldsymbol{k}_{12} \end{bmatrix} = \begin{bmatrix} \mathbf{0} & \mathbf{I} \\ -\mathbf{M}^{-1}\mathbf{K} & -\mathbf{M}^{-1}\mathbf{C} \end{bmatrix} \begin{bmatrix} \boldsymbol{d}_1(t_n) \\ \boldsymbol{d}_2(t_n) \end{bmatrix} + \begin{bmatrix} \mathbf{0} \\ \mathbf{M}^{-1}\mathbf{f}(t_n) \end{bmatrix} \\ &= \begin{bmatrix} \boldsymbol{d}_2(t_n) \\ -\mathbf{M}^{-1}\mathbf{K}\boldsymbol{d}_1(t_n) - \mathbf{M}^{-1}\mathbf{C}\boldsymbol{d}_2(t_n) + \mathbf{M}^{-1}\mathbf{f}(t_n) \end{bmatrix}, \end{aligned} \tag{B.8a}$$

$$\begin{aligned} \boldsymbol{k}_2 &= \begin{bmatrix} \boldsymbol{k}_{21} \\ \boldsymbol{k}_{22} \end{bmatrix} = \begin{bmatrix} \mathbf{0} & \mathbf{I} \\ -\mathbf{M}^{-1}\mathbf{K} & -\mathbf{M}^{-1}\mathbf{C} \end{bmatrix} \begin{bmatrix} \boldsymbol{d}_1(t_n) + \frac{\Delta t}{2}\boldsymbol{k}_{11} \\ \boldsymbol{d}_2(t_n) + \frac{\Delta t}{2}\boldsymbol{k}_{12} \end{bmatrix} + \begin{bmatrix} \mathbf{0} \\ \mathbf{M}^{-1}\mathbf{f}(t_n + \frac{\Delta t}{2}) \end{bmatrix} \\ &= \begin{bmatrix} \boldsymbol{d}_2(t_n) + \frac{\Delta t}{2}\boldsymbol{k}_{12} \\ -\mathbf{M}^{-1}\mathbf{K}(\boldsymbol{d}_1(t_n) + \frac{\Delta t}{2}\boldsymbol{k}_{11}) - \mathbf{M}^{-1}\mathbf{C}(\boldsymbol{d}_2(t_n) + \frac{\Delta t}{2}\boldsymbol{k}_{12}) + \mathbf{M}^{-1}\mathbf{f}(t_n + \frac{\Delta t}{2}) \end{bmatrix}, \end{aligned} \tag{B.8b}$$

$$\begin{aligned} \boldsymbol{k}_3 &= \begin{bmatrix} \boldsymbol{k}_{31} \\ \boldsymbol{k}_{32} \end{bmatrix} = \begin{bmatrix} \mathbf{0} & \mathbf{I} \\ -\mathbf{M}^{-1}\mathbf{K} & -\mathbf{M}^{-1}\mathbf{C} \end{bmatrix} \begin{bmatrix} \boldsymbol{d}_1(t_n) + \frac{\Delta t}{2}\boldsymbol{k}_{21} \\ \boldsymbol{d}_2(t_n) + \frac{\Delta t}{2}\boldsymbol{k}_{22} \end{bmatrix} + \begin{bmatrix} \mathbf{0} \\ \mathbf{M}^{-1}\mathbf{f}(t_n + \frac{\Delta t}{2}) \end{bmatrix} \\ &= \begin{bmatrix} \boldsymbol{d}_2(t_n) + \frac{\Delta t}{2}\boldsymbol{k}_{22} \\ -\mathbf{M}^{-1}\mathbf{K}(\boldsymbol{d}_1(t_n) + \frac{\Delta t}{2}\boldsymbol{k}_{21}) - \mathbf{M}^{-1}\mathbf{C}(\boldsymbol{d}_2(t_n) + \frac{\Delta t}{2}\boldsymbol{k}_{22}) + \mathbf{M}^{-1}\mathbf{f}(t_n + \frac{\Delta t}{2}) \end{bmatrix}, \end{aligned} \tag{B.8c}$$

$$\begin{aligned} \boldsymbol{k}_4 &= \begin{bmatrix} \boldsymbol{k}_{41} \\ \boldsymbol{k}_{42} \end{bmatrix} = \begin{bmatrix} \mathbf{0} & \mathbf{I} \\ -\mathbf{M}^{-1}\mathbf{K} & -\mathbf{M}^{-1}\mathbf{C} \end{bmatrix} \begin{bmatrix} \boldsymbol{d}_1(t_n) + \boldsymbol{k}_{31} \\ \boldsymbol{d}_2(t_n) + \boldsymbol{k}_{32} \end{bmatrix} + \begin{bmatrix} \mathbf{0} \\ \mathbf{M}^{-1}\mathbf{f}(t_n + \Delta t) \end{bmatrix} \\ &= \begin{bmatrix} \boldsymbol{d}_2(t_n) + \boldsymbol{k}_{32} \\ -\mathbf{M}^{-1}\mathbf{K}(\boldsymbol{d}_1(t_n) + \boldsymbol{k}_{31}) - \mathbf{M}^{-1}\mathbf{C}(\boldsymbol{d}_2(t_n) + \boldsymbol{k}_{32}) + \mathbf{M}^{-1}\mathbf{f}(t_n + \Delta t) \end{bmatrix}. \end{aligned} \tag{B.8d}$$

Having the functions updated at $n+1$-th time-step, the updated solution at $n+1$-th step results in:

$$\boldsymbol{u}_{n+1} = \boldsymbol{u}_n + \frac{\Delta t}{6}(\boldsymbol{k}_1 + 2\boldsymbol{k}_2 + 2\boldsymbol{k}_3 + \boldsymbol{k}_4). \tag{B.9}$$

B.3.2 For three-dimensional problems

Comparing (2.102) with (2.95), we have:

$$\boldsymbol{y}(t) = \begin{bmatrix} \boldsymbol{d}_1 \\ \boldsymbol{d}_2 \\ \boldsymbol{d}_3 \end{bmatrix}, \tag{B.10a}$$

$$\boldsymbol{f}(\boldsymbol{y}(t), t) = \begin{bmatrix} \mathbf{0} & \mathbf{I} & \mathbf{0} \\ \mathbf{0} & \mathbf{0} & \mathbf{I} \\ -\mathbf{M}^{-1}\mathbf{G} & -\mathbf{M}^{-1}\mathbf{K} & -\mathbf{M}^{-1}\mathbf{C} \end{bmatrix} \begin{bmatrix} \boldsymbol{d}_1 \\ \boldsymbol{d}_2 \\ \boldsymbol{d}_3 \end{bmatrix} + \begin{bmatrix} \mathbf{0} \\ \mathbf{0} \\ \mathbf{M}^{-1}\mathbf{f} \end{bmatrix}. \tag{B.10b}$$

Hence, according to (2.105):

$$\boldsymbol{k}_1 = \begin{bmatrix} \boldsymbol{k}_{11} \\ \boldsymbol{k}_{12} \\ \boldsymbol{k}_{13} \end{bmatrix} = \begin{bmatrix} \mathbf{0} & \mathbf{I} & \mathbf{0} \\ \mathbf{0} & \mathbf{0} & \mathbf{I} \\ -\mathbf{M}^{-1}\mathbf{G} & -\mathbf{M}^{-1}\mathbf{K} & -\mathbf{M}^{-1}\mathbf{C} \end{bmatrix} \begin{bmatrix} \boldsymbol{d}_1(t_n) \\ \boldsymbol{d}_2(t_n) \\ \boldsymbol{d}_3(t_n) \end{bmatrix} + \begin{bmatrix} \mathbf{0} \\ \mathbf{0} \\ \mathbf{M}^{-1}\mathbf{f}(t_n) \end{bmatrix}$$
$$= \begin{bmatrix} \boldsymbol{d}_2(t_n) \\ \boldsymbol{d}_3(t_n) \\ -\mathbf{M}^{-1}\mathbf{G}\boldsymbol{d}_1(t_n) - \mathbf{M}^{-1}\mathbf{K}\boldsymbol{d}_2(t_n) - \mathbf{M}^{-1}\mathbf{C}\boldsymbol{d}_3(t_n) + \mathbf{M}^{-1}\mathbf{f}(t_n) \end{bmatrix}, \tag{B.11a}$$

$$\boldsymbol{k}_2 = \begin{bmatrix} \boldsymbol{k}_{21} \\ \boldsymbol{k}_{22} \\ \boldsymbol{k}_{23} \end{bmatrix} = \begin{bmatrix} \mathbf{0} & \mathbf{I} & \mathbf{0} \\ \mathbf{0} & \mathbf{0} & \mathbf{I} \\ -\mathbf{M}^{-1}\mathbf{G} & -\mathbf{M}^{-1}\mathbf{K} & -\mathbf{M}^{-1}\mathbf{C} \end{bmatrix} \begin{bmatrix} \boldsymbol{d}_1(t_n) + \frac{\Delta t}{2}\boldsymbol{k}_{11} \\ \boldsymbol{d}_2(t_n) + \frac{\Delta t}{2}\boldsymbol{k}_{12} \\ \boldsymbol{d}_3(t_n) + \frac{\Delta t}{2}\boldsymbol{k}_{13} \end{bmatrix} + \begin{bmatrix} \mathbf{0} \\ \mathbf{0} \\ \mathbf{M}^{-1}\mathbf{f}(t_n + \frac{\Delta t}{2}) \end{bmatrix}$$
$$= \begin{bmatrix} \boldsymbol{d}_2(t_n) + \frac{\Delta t}{2}\boldsymbol{k}_{12} \\ \boldsymbol{d}_3(t_n) + \frac{\Delta t}{2}\boldsymbol{k}_{13} \\ \{-\mathbf{M}^{-1}\mathbf{G}(\boldsymbol{d}_1(t_n) + \frac{\Delta t}{2}\boldsymbol{k}_{11}) - \mathbf{M}^{-1}\mathbf{K}(\boldsymbol{d}_2(t_n) + \frac{\Delta t}{2}\boldsymbol{k}_{12}) - \mathbf{M}^{-1}\mathbf{C}(\boldsymbol{d}_3(t_n) + \frac{\Delta t}{2}\boldsymbol{k}_{13}) \\ +\mathbf{M}^{-1}\mathbf{f}(t_n + \frac{\Delta t}{2})\} \end{bmatrix}, \tag{B.11b}$$

$$\boldsymbol{k}_3 = \begin{bmatrix} \boldsymbol{k}_{31} \\ \boldsymbol{k}_{32} \\ \boldsymbol{k}_{33} \end{bmatrix} = \begin{bmatrix} \mathbf{0} & \mathbf{I} & \mathbf{0} \\ \mathbf{0} & \mathbf{0} & \mathbf{I} \\ -\mathbf{M}^{-1}\mathbf{G} & -\mathbf{M}^{-1}\mathbf{K} & -\mathbf{M}^{-1}\mathbf{C} \end{bmatrix} \begin{bmatrix} \boldsymbol{d}_1(t_n) + \frac{\Delta t}{2}\boldsymbol{k}_{21} \\ \boldsymbol{d}_2(t_n) + \frac{\Delta t}{2}\boldsymbol{k}_{22} \\ \boldsymbol{d}_3(t_n) + \frac{\Delta t}{2}\boldsymbol{k}_{23} \end{bmatrix} + \begin{bmatrix} \mathbf{0} \\ \mathbf{0} \\ \mathbf{M}^{-1}\mathbf{f}(t_n + \frac{\Delta t}{2}) \end{bmatrix}$$
$$= \begin{bmatrix} \boldsymbol{d}_2(t_n) + \frac{\Delta t}{2}\boldsymbol{k}_{22} \\ \boldsymbol{d}_3(t_n) + \frac{\Delta t}{2}\boldsymbol{k}_{23} \\ \{-\mathbf{M}^{-1}\mathbf{G}(\boldsymbol{d}_1(t_n) + \frac{\Delta t}{2}\boldsymbol{k}_{21}) - \mathbf{M}^{-1}\mathbf{K}(\boldsymbol{d}_2(t_n) + \frac{\Delta t}{2}\boldsymbol{k}_{22}) - \mathbf{M}^{-1}\mathbf{C}(\boldsymbol{d}_3(t_n) + \frac{\Delta t}{2}\boldsymbol{k}_{23}) \\ +\mathbf{M}^{-1}\mathbf{f}(t_n + \frac{\Delta t}{2})\} \end{bmatrix}, \tag{B.11c}$$

$$\boldsymbol{k}_4 = \begin{bmatrix} \boldsymbol{k}_{41} \\ \boldsymbol{k}_{42} \\ \boldsymbol{k}_{43} \end{bmatrix} = \begin{bmatrix} \mathbf{0} & \mathbf{I} & \mathbf{0} \\ \mathbf{0} & \mathbf{0} & \mathbf{I} \\ -\mathbf{M}^{-1}\mathbf{G} & -\mathbf{M}^{-1}\mathbf{K} & -\mathbf{M}^{-1}\mathbf{C} \end{bmatrix} \begin{bmatrix} \boldsymbol{d}_1(t_n) + \boldsymbol{k}_{31} \\ \boldsymbol{d}_2(t_n) + \boldsymbol{k}_{32} \\ \boldsymbol{d}_3(t_n) + \boldsymbol{k}_{33} \end{bmatrix} + \begin{bmatrix} \mathbf{0} \\ \mathbf{0} \\ \mathbf{M}^{-1}\mathbf{f}(t_n + \Delta t) \end{bmatrix}$$
$$= \begin{bmatrix} \boldsymbol{d}_2(t_n) + \boldsymbol{k}_{32} \\ \boldsymbol{d}_2(t_n) + \boldsymbol{k}_{33} \\ \{-\mathbf{M}^{-1}\mathbf{G}(\boldsymbol{d}_1(t_n) + \boldsymbol{k}_{31}) - \mathbf{M}^{-1}\mathbf{K}(\boldsymbol{d}_2(t_n) + \boldsymbol{k}_{32}) - \mathbf{M}^{-1}\mathbf{C}(\boldsymbol{d}_3(t_n) + \boldsymbol{k}_{33}) \\ +\mathbf{M}^{-1}\mathbf{f}(t_n + \Delta t)\} \end{bmatrix}. \tag{B.11d}$$

Having the functions updated at $n+1$-th time-step, the updated solution at $n+1$-th step results in:

$$\boldsymbol{u}_{n+1} = \boldsymbol{u}_n + \frac{\Delta t}{6}(\boldsymbol{k}_1 + 2\boldsymbol{k}_2 + 2\boldsymbol{k}_3 + \boldsymbol{k}_4). \tag{B.12}$$

B.3.3 Algorithm

Algorithm 4 shows the fourth-order Runge-Kutta procedure.

Algorithm 4 Explicit time integration by fourth-order Runge-Kutta method

numerical solution of the initial-value problem:
$\dot{\boldsymbol{y}} = \boldsymbol{f}(t, \boldsymbol{y}), \quad 0 \leq t \leq T, \quad \boldsymbol{y}(0) = \boldsymbol{0}$ ▷ 2.98

inputs
$\boldsymbol{f}$: initial value problem
Δt: time-step
N: total number of steps (total simulation time = $N\Delta t$)

output
approximation of y at i-th step

steps

initialization
$t \longleftarrow \emptyset$
$\boldsymbol{u} \longleftarrow \emptyset$
for $i \leftarrow 1 : N + 1$ **do** ▷ loop over the time-steps
    $t \longleftarrow (i-1)\Delta t$; ▷ update time
    update functions
    $\boldsymbol{k}_1 \leftarrow$ update $\boldsymbol{k}_1$ ▷ 2D:B.8a-3D:B.11a
    $\boldsymbol{k}_2 \leftarrow$ update $\boldsymbol{k}_2$ ▷ 2D:B.8b-3D:B.11b
    $\boldsymbol{k}_3 \leftarrow$ update $\boldsymbol{k}_3$ ▷ 2D:B.8c-3D:B.11c
    $\boldsymbol{k}_4 \leftarrow$ update $\boldsymbol{k}_4$ ▷ 2D:B.8d-3D:B.11d
    update the results at the i-th time step
    $\boldsymbol{u} \leftarrow \boldsymbol{u} + \dfrac{\Delta t}{6}(\boldsymbol{k}_1 + 2\boldsymbol{k}_2 + 2\boldsymbol{k}_3 + \boldsymbol{k}_4)$
    print the results (displacement, velocity, and acceleration)
end for

B.4 Runge-Kutta-Fehlberg formulations

This section explains the accommodation of the adaptive Runge-Kutta-Fehlberg (RKF) for the two- and three-dimensional formulation.

B.4.1 For two-dimensional problems

Comparing (2.100) with (2.95), we have:

$$\boldsymbol{y}(t) = \begin{bmatrix} \boldsymbol{d}_1 \\ \boldsymbol{d}_2 \end{bmatrix}, \tag{B.13a}$$

$$\boldsymbol{f}(\boldsymbol{y}(t), t) = \begin{bmatrix} \mathbf{0} & \mathbf{I} \\ -\mathbf{M}^{-1}\mathbf{K} & -\mathbf{M}^{-1}\mathbf{C} \end{bmatrix} \begin{bmatrix} \boldsymbol{d}_1 \\ \boldsymbol{d}_2 \end{bmatrix} + \begin{bmatrix} \mathbf{0} \\ \mathbf{M}^{-1}\mathbf{f} \end{bmatrix}. \tag{B.13b}$$

Hence, according to (2.118):

$$\boldsymbol{k}_1 = \begin{bmatrix}\boldsymbol{k}_{11}\\ \boldsymbol{k}_{12}\end{bmatrix} = \begin{bmatrix}\mathbf{0} & \mathbf{I}\\ -\mathbf{M}^{-1}\mathbf{K} & -\mathbf{M}^{-1}\mathbf{C}\end{bmatrix}\begin{bmatrix}\boldsymbol{d}_1(t_n)\\ \boldsymbol{d}_2(t_n)\end{bmatrix} + \begin{bmatrix}\mathbf{0}\\ \mathbf{M}^{-1}\mathbf{f}(t_n)\end{bmatrix}$$
$$= \begin{bmatrix}\boldsymbol{d}_2(t_n)\\ -\mathbf{M}^{-1}\mathbf{K}\boldsymbol{d}_1(t_n) - \mathbf{M}^{-1}\mathbf{C}\boldsymbol{d}_2(t_n) + \mathbf{M}^{-1}\mathbf{f}(t_n)\end{bmatrix}, \tag{B.14a}$$

$$\boldsymbol{k}_2 = \begin{bmatrix}\boldsymbol{k}_{21}\\ \boldsymbol{k}_{22}\end{bmatrix} = \begin{bmatrix}\mathbf{0} & \mathbf{I}\\ -\mathbf{M}^{-1}\mathbf{K} & -\mathbf{M}^{-1}\mathbf{C}\end{bmatrix}\begin{bmatrix}\boldsymbol{d}_1(t_n) + \frac{\Delta t}{4}\boldsymbol{k}_{11}\\ \boldsymbol{d}_2(t_n) + \frac{\Delta t}{4}\boldsymbol{k}_{12}\end{bmatrix} + \begin{bmatrix}\mathbf{0}\\ \mathbf{M}^{-1}\mathbf{f}(t_n + \frac{1}{4}\Delta t)\end{bmatrix}$$
$$= \begin{bmatrix}\boldsymbol{d}_2(t_n) + \frac{\Delta t}{4}\boldsymbol{k}_{12}\\ -\mathbf{M}^{-1}\mathbf{K}(\boldsymbol{d}_1(t_n) + \frac{\Delta t}{4}\boldsymbol{k}_{11}) - \mathbf{M}^{-1}\mathbf{C}(\boldsymbol{d}_2(t_n) + \frac{\Delta t}{4}\boldsymbol{k}_{12}) + \mathbf{M}^{-1}\mathbf{f}(t_n + \frac{1}{4}\Delta t)\end{bmatrix}, \tag{B.14b}$$

$$\boldsymbol{k}_3 = \begin{bmatrix}\boldsymbol{k}_{31}\\ \boldsymbol{k}_{32}\end{bmatrix} = \begin{bmatrix}\mathbf{0} & \mathbf{I}\\ -\mathbf{M}^{-1}\mathbf{K} & -\mathbf{M}^{-1}\mathbf{C}\end{bmatrix}\begin{bmatrix}\boldsymbol{d}_1(t_n) + \frac{3\Delta t}{32}\boldsymbol{k}_{11} + \frac{9\Delta t}{32}\boldsymbol{k}_{21}\\ \boldsymbol{d}_2(t_n) + \frac{3\Delta t}{32}\boldsymbol{k}_{12} + \frac{9\Delta t}{32}\boldsymbol{k}_{22}\end{bmatrix} + \begin{bmatrix}\mathbf{0}\\ \mathbf{M}^{-1}\mathbf{f}(t_n + \frac{3}{8}\Delta t)\end{bmatrix}$$
$$= \begin{bmatrix}\boldsymbol{d}_2(t_n) + \frac{3\Delta t}{32}\boldsymbol{k}_{12} + \frac{9\Delta t}{32}\boldsymbol{k}_{22}\\ \{-\mathbf{M}^{-1}\mathbf{K}(\boldsymbol{d}_1(t_n) + \frac{3\Delta t}{32}\boldsymbol{k}_{11} + \frac{9\Delta t}{32}\boldsymbol{k}_{21}) - \mathbf{M}^{-1}\mathbf{C}(\boldsymbol{d}_2(t_n) + \frac{3\Delta t}{32}\boldsymbol{k}_{12} + \frac{9\Delta t}{32}\boldsymbol{k}_{22})\\ +\mathbf{M}^{-1}\mathbf{f}(t_n + \frac{3}{8}\Delta t)\}\end{bmatrix}, \tag{B.14c}$$

$$\boldsymbol{k}_4 = \begin{bmatrix}\boldsymbol{k}_{41}\\ \boldsymbol{k}_{42}\end{bmatrix} = \begin{bmatrix}\mathbf{0} & \mathbf{I}\\ -\mathbf{M}^{-1}\mathbf{K} & -\mathbf{M}^{-1}\mathbf{C}\end{bmatrix}\begin{bmatrix}\boldsymbol{d}_1(t_n) + \frac{1932}{2197}\boldsymbol{k}_{11} - \frac{7200}{2197}\boldsymbol{k}_{21} + \frac{7296}{2197}\boldsymbol{k}_{31}\\ \boldsymbol{d}_2(t_n) + \frac{1932}{2197}\boldsymbol{k}_{12} - \frac{7200}{2197}\boldsymbol{k}_{22} + \frac{7296}{2197}\boldsymbol{k}_{32}\end{bmatrix}$$
$$+ \begin{bmatrix}\mathbf{0}\\ \mathbf{M}^{-1}\mathbf{f}(t_n + \frac{12}{13}\Delta t)\end{bmatrix}$$
$$= \begin{bmatrix}\boldsymbol{d}_2(t_n) + \frac{1932}{2197}\boldsymbol{k}_{12} - \frac{7200}{2197}\boldsymbol{k}_{22} + \frac{7296}{2197}\boldsymbol{k}_{32}\\ \{-\mathbf{M}^{-1}\mathbf{K}(\boldsymbol{d}_1(t_n) + \frac{1932}{2197}\boldsymbol{k}_{11} - \frac{7200}{2197}\boldsymbol{k}_{21} + \frac{7296}{2197}\boldsymbol{k}_{31})\\ -\mathbf{M}^{-1}\mathbf{C}(\boldsymbol{d}_2(t_n) + \frac{1932}{2197}\boldsymbol{k}_{12} - \frac{7200}{2197}\boldsymbol{k}_{22} + \frac{7296}{2197}\boldsymbol{k}_{32}) + \mathbf{M}^{-1}\mathbf{f}(t_n + \frac{12}{13}\Delta t)\}\end{bmatrix}, \tag{B.14d}$$

$$\boldsymbol{k}_5 = \begin{bmatrix}\boldsymbol{k}_{51}\\ \boldsymbol{k}_{52}\end{bmatrix} = \begin{bmatrix}\mathbf{0} & \mathbf{I}\\ -\mathbf{M}^{-1}\mathbf{K} & -\mathbf{M}^{-1}\mathbf{C}\end{bmatrix}\begin{bmatrix}\boldsymbol{d}_1(t_n) + \frac{439}{216}\boldsymbol{k}_{11} - 8\boldsymbol{k}_{21} + \frac{3680}{513}\boldsymbol{k}_{31} - \frac{845}{4104}\boldsymbol{k}_{41}\\ \boldsymbol{d}_2(t_n) + \frac{439}{216}\boldsymbol{k}_{12} - 8\boldsymbol{k}_{22} + \frac{3680}{513}\boldsymbol{k}_{32} - \frac{845}{4104}\boldsymbol{k}_{42}\end{bmatrix}$$
$$+ \begin{bmatrix}\mathbf{0}\\ \mathbf{M}^{-1}\mathbf{f}(t_n + \Delta t)\end{bmatrix}$$
$$= \begin{bmatrix}\boldsymbol{d}_2(t_n) + \frac{439}{216}\boldsymbol{k}_{12} - 8\boldsymbol{k}_{22} + \frac{3680}{513}\boldsymbol{k}_{32} - \frac{845}{4104}\boldsymbol{k}_{42}\\ \{-\mathbf{M}^{-1}\mathbf{K}(\boldsymbol{d}_1(t_n) + \frac{439}{216}\boldsymbol{k}_{11} - 8\boldsymbol{k}_{21} + \frac{3680}{513}\boldsymbol{k}_{31} - \frac{845}{4104}\boldsymbol{k}_{41})\\ -\mathbf{M}^{-1}\mathbf{C}(\boldsymbol{d}_2(t_n) + \frac{439}{216}\boldsymbol{k}_{12} - 8\boldsymbol{k}_{22} + \frac{3680}{513}\boldsymbol{k}_{32} - \frac{845}{4104}\boldsymbol{k}_{42}) + \mathbf{M}^{-1}\mathbf{f}(t_n + \Delta t)\}\end{bmatrix}, \tag{B.14e}$$

$$\boldsymbol{k}_6 = \begin{bmatrix}\boldsymbol{k}_{61}\\ \boldsymbol{k}_{62}\end{bmatrix} = \begin{bmatrix}\mathbf{0} & \mathbf{I}\\ -\mathbf{M}^{-1}\mathbf{K} & -\mathbf{M}^{-1}\mathbf{C}\end{bmatrix}\begin{bmatrix}\boldsymbol{d}_1(t_n) - \frac{8}{27}\boldsymbol{k}_{11} + 2\boldsymbol{k}_{21} - \frac{3544}{2565}\boldsymbol{k}_{31} + \frac{1859}{4104}\boldsymbol{k}_{41} - \frac{11}{40}\boldsymbol{k}_{51}\\ \boldsymbol{d}_2(t_n) - \frac{8}{27}\boldsymbol{k}_{12} + 2\boldsymbol{k}_{22} - \frac{3544}{2565}\boldsymbol{k}_{32} + \frac{1859}{4104}\boldsymbol{k}_{42} - \frac{11}{40}\boldsymbol{k}_{52}\end{bmatrix}$$
$$+ \begin{bmatrix}\mathbf{0}\\ \mathbf{M}^{-1}\mathbf{f}(t_n + \frac{1}{2}\Delta t)\end{bmatrix}$$
$$= \begin{bmatrix}\boldsymbol{d}_2(t_n) - \frac{8}{27}\boldsymbol{k}_{12} + 2\boldsymbol{k}_{22} - \frac{3544}{2565}\boldsymbol{k}_{32} + \frac{1859}{4104}\boldsymbol{k}_{42} - \frac{11}{40}\boldsymbol{k}_{52}\\ \{-\mathbf{M}^{-1}\mathbf{K}(\boldsymbol{d}_1(t_n) - \frac{8}{27}\boldsymbol{k}_{11} + 2\boldsymbol{k}_{21} - \frac{3544}{2565}\boldsymbol{k}_{31} + \frac{1859}{4104}\boldsymbol{k}_{41} - \frac{11}{40}\boldsymbol{k}_{51}) -\\ \mathbf{M}^{-1}\mathbf{C}(\boldsymbol{d}_2(t_n) - \frac{8}{27}\boldsymbol{k}_{12} + 2\boldsymbol{k}_{22} - \frac{3544}{2565}\boldsymbol{k}_{32} + \frac{1859}{4104}\boldsymbol{k}_{42} - \frac{11}{40}\boldsymbol{k}_{52}) + \mathbf{M}^{-1}\mathbf{f}(t_n + \frac{1}{2}\Delta t)\}\end{bmatrix}. \tag{B.14f}$$

Having the functions updated at $n+1$-th time-step, the updated solution at $n+1$-th step results in the local truncation error at time step $n+1$:

$$\tau_{n+1}(h) = |\frac{\widetilde{\boldsymbol{u}}_{n+1} - \boldsymbol{u}_{n+1}}{\Delta t}| = |\frac{1}{360}\boldsymbol{k}_1 - \frac{128}{4275}\boldsymbol{k}_3 - \frac{2197}{75240}\boldsymbol{k}_4 + \frac{1}{50}\boldsymbol{k}_5 + \frac{2}{55}\boldsymbol{k}_6|, \tag{B.15}$$

and the results based on the fourth-order scheme reads:

$$\boldsymbol{u}_{n+1} = \boldsymbol{u}_n + \Delta t(\frac{25}{216}\boldsymbol{k}_1 + \frac{1408}{2565}\boldsymbol{k}_3 + \frac{2197}{4104}\boldsymbol{k}_4 - \frac{1}{5}\boldsymbol{k}_5). \tag{B.16}$$

B.4.2 For three-dimensional problems

Comparing (2.102) with (2.95), we have:

$$\boldsymbol{y}(t) = \begin{bmatrix}\boldsymbol{d}_1\\ \boldsymbol{d}_2\\ \boldsymbol{d}_3\end{bmatrix}, \tag{B.17a}$$

$$\boldsymbol{f}(\boldsymbol{y}(t), t) = \begin{bmatrix}\mathbf{0} & \mathbf{I} & \mathbf{0}\\ \mathbf{0} & \mathbf{0} & \mathbf{I}\\ -\mathbf{M}^{-1}\mathbf{G} & -\mathbf{M}^{-1}\mathbf{K} & -\mathbf{M}^{-1}\mathbf{C}\end{bmatrix}\begin{bmatrix}\boldsymbol{d}_1\\ \boldsymbol{d}_2\\ \boldsymbol{d}_3\end{bmatrix} + \begin{bmatrix}\mathbf{0}\\ \mathbf{0}\\ \mathbf{M}^{-1}\mathbf{f}\end{bmatrix}. \tag{B.17b}$$

Hence, according to (2.118):

$$\boldsymbol{k}_1 = \begin{bmatrix} \boldsymbol{k}_{11} \\ \boldsymbol{k}_{12} \\ \boldsymbol{k}_{13} \end{bmatrix} = \begin{bmatrix} \mathbf{0} & \mathbf{I} & \mathbf{0} \\ \mathbf{0} & \mathbf{0} & \mathbf{I} \\ -\mathbf{M}^{-1}\mathbf{G} & -\mathbf{M}^{-1}\mathbf{K} & -\mathbf{M}^{-1}\mathbf{C} \end{bmatrix} \begin{bmatrix} \boldsymbol{d}_1(t_n) \\ \boldsymbol{d}_2(t_n) \\ \boldsymbol{d}_3(t_n) \end{bmatrix} + \begin{bmatrix} \mathbf{0} \\ \mathbf{0} \\ \mathbf{M}^{-1}\mathbf{f}(t_n) \end{bmatrix}$$
$$= \begin{bmatrix} \boldsymbol{d}_2(t_n) \\ \boldsymbol{d}_3(t_n) \\ -\mathbf{M}^{-1}\mathbf{G}\boldsymbol{d}_1(t_n) - \mathbf{M}^{-1}\mathbf{K}\boldsymbol{d}_2(t_n) - \mathbf{M}^{-1}\mathbf{C}\boldsymbol{d}_3(t_n) + \mathbf{M}^{-1}\mathbf{f}(t_n) \end{bmatrix}, \tag{B.18a}$$

$$\boldsymbol{k}_2 = \begin{bmatrix} \boldsymbol{k}_{21} \\ \boldsymbol{k}_{22} \\ \boldsymbol{k}_{23} \end{bmatrix} = \begin{bmatrix} \mathbf{0} & \mathbf{I} & \mathbf{0} \\ \mathbf{0} & \mathbf{0} & \mathbf{I} \\ -\mathbf{M}^{-1}\mathbf{G} & -\mathbf{M}^{-1}\mathbf{K} & -\mathbf{M}^{-1}\mathbf{C} \end{bmatrix} \begin{bmatrix} \boldsymbol{d}_1(t_n) + \frac{\Delta t}{4}\boldsymbol{k}_{11} \\ \boldsymbol{d}_2(t_n) + \frac{\Delta t}{4}\boldsymbol{k}_{12} \\ \boldsymbol{d}_3(t_n) + \frac{\Delta t}{4}\boldsymbol{k}_{13} \end{bmatrix} + \begin{bmatrix} \mathbf{0} \\ \mathbf{0} \\ \mathbf{M}^{-1}\mathbf{f}(t_n + \frac{1}{4}\Delta t) \end{bmatrix}$$
$$= \begin{bmatrix} \boldsymbol{d}_2(t_n) + \frac{\Delta t}{4}\boldsymbol{k}_{12} \\ \boldsymbol{d}_3(t_n) + \frac{\Delta t}{4}\boldsymbol{k}_{13} \\ \{-\mathbf{M}^{-1}\mathbf{G}(\boldsymbol{d}_1(t_n) + \frac{\Delta t}{4}\boldsymbol{k}_{11}) - \mathbf{M}^{-1}\mathbf{K}(\boldsymbol{d}_2(t_n) + \frac{\Delta t}{4}\boldsymbol{k}_{12}) - \mathbf{M}^{-1}\mathbf{C}(\boldsymbol{d}_3(t_n) + \frac{\Delta t}{4}\boldsymbol{k}_{13}) \\ +\mathbf{M}^{-1}\mathbf{f}(t_n + \frac{\Delta t}{4})\} \end{bmatrix}, \tag{B.18b}$$

$$\boldsymbol{k}_3 = \begin{bmatrix} \boldsymbol{k}_{31} \\ \boldsymbol{k}_{32} \\ \boldsymbol{k}_{33} \end{bmatrix} = \begin{bmatrix} \mathbf{0} & \mathbf{I} & \mathbf{0} \\ \mathbf{0} & \mathbf{0} & \mathbf{I} \\ -\mathbf{M}^{-1}\mathbf{G} & -\mathbf{M}^{-1}\mathbf{K} & -\mathbf{M}^{-1}\mathbf{C} \end{bmatrix} \begin{bmatrix} \boldsymbol{d}_1(t_n) + \frac{3\Delta t}{32}\boldsymbol{k}_{11} + \frac{9\Delta t}{32}\boldsymbol{k}_{21} \\ \boldsymbol{d}_2(t_n) + \frac{3\Delta t}{32}\boldsymbol{k}_{12} + \frac{9\Delta t}{32}\boldsymbol{k}_{22} \\ \boldsymbol{d}_3(t_n) + \frac{3\Delta t}{32}\boldsymbol{k}_{13} + \frac{9\Delta t}{32}\boldsymbol{k}_{23} \end{bmatrix}$$
$$+ \begin{bmatrix} \mathbf{0} \\ \mathbf{0} \\ \mathbf{M}^{-1}\mathbf{f}(t_n + \frac{3}{8}\Delta t) \end{bmatrix}$$
$$= \begin{bmatrix} \boldsymbol{d}_2(t_n) + \frac{3\Delta t}{32}\boldsymbol{k}_{12} + \frac{9\Delta t}{32}\boldsymbol{k}_{22} \\ \boldsymbol{d}_3(t_n) + \frac{3\Delta t}{32}\boldsymbol{k}_{13} + \frac{9\Delta t}{32}\boldsymbol{k}_{23} \\ \{-\mathbf{M}^{-1}\mathbf{G}(\boldsymbol{d}_1(t_n) + \frac{3\Delta t}{32}\boldsymbol{k}_{11} + \frac{9\Delta t}{32}\boldsymbol{k}_{21}) - \mathbf{M}^{-1}\mathbf{K}(\boldsymbol{d}_2(t_n) + \frac{3\Delta t}{32}\boldsymbol{k}_{12} + \frac{9\Delta t}{32}\boldsymbol{k}_{22}) \\ -\mathbf{M}^{-1}\mathbf{C}(\boldsymbol{d}_3(t_n) + \frac{3\Delta t}{32}\boldsymbol{k}_{13} + \frac{9\Delta t}{32}\boldsymbol{k}_{23}) + \mathbf{M}^{-1}\mathbf{f}(t_n + \frac{3}{8}\Delta t)\} \end{bmatrix}, \tag{B.18c}$$

$$\boldsymbol{k}_4 = \begin{bmatrix} \boldsymbol{k}_{41} \\ \boldsymbol{k}_{42} \\ \boldsymbol{k}_{43} \end{bmatrix} = \begin{bmatrix} \mathbf{0} & \mathbf{I} & \mathbf{0} \\ \mathbf{0} & \mathbf{0} & \mathbf{I} \\ -\mathbf{M}^{-1}\mathbf{G} & -\mathbf{M}^{-1}\mathbf{K} & -\mathbf{M}^{-1}\mathbf{C} \end{bmatrix} \begin{bmatrix} \boldsymbol{d}_1(t_n) + \frac{1932}{2197}\boldsymbol{k}_{11} - \frac{7200}{2197}\boldsymbol{k}_{21} + \frac{7296}{2197}\boldsymbol{k}_{31} \\ \boldsymbol{d}_2(t_n) + \frac{1932}{2197}\boldsymbol{k}_{12} - \frac{7200}{2197}\boldsymbol{k}_{22} + \frac{7296}{2197}\boldsymbol{k}_{32} \\ \boldsymbol{d}_3(t_n) + \frac{1932}{2197}\boldsymbol{k}_{13} - \frac{7200}{2197}\boldsymbol{k}_{23} + \frac{7296}{2197}\boldsymbol{k}_{33} \end{bmatrix}$$
$$+ \begin{bmatrix} \mathbf{0} \\ \mathbf{0} \\ \mathbf{M}^{-1}\mathbf{f}(t_n + \frac{12}{13}\Delta t) \end{bmatrix}$$
$$= \begin{bmatrix} \boldsymbol{d}_2(t_n) + \frac{1932}{2197}\boldsymbol{k}_{12} - \frac{7200}{2197}\boldsymbol{k}_{22} + \frac{7296}{2197}\boldsymbol{k}_{32} \\ \boldsymbol{d}_3(t_n) + \frac{1932}{2197}\boldsymbol{k}_{13} - \frac{7200}{2197}\boldsymbol{k}_{23} + \frac{7296}{2197}\boldsymbol{k}_{33} \\ \{-\mathbf{M}^{-1}\mathbf{G}(\boldsymbol{d}_1(t_n) + \frac{1932}{2197}\boldsymbol{k}_{11} - \frac{7200}{2197}\boldsymbol{k}_{21} + \frac{7296}{2197}\boldsymbol{k}_{31}) \\ -\mathbf{M}^{-1}\mathbf{K}(\boldsymbol{d}_2(t_n) + \frac{1932}{2197}\boldsymbol{k}_{12} - \frac{7200}{2197}\boldsymbol{k}_{22} + \frac{7296}{2197}\boldsymbol{k}_{32}) \\ -\mathbf{M}^{-1}\mathbf{C}(\boldsymbol{d}_3(t_n) + \frac{1932}{2197}\boldsymbol{k}_{13} - \frac{7200}{2197}\boldsymbol{k}_{23} + \frac{7296}{2197}\boldsymbol{k}_{33}) + \mathbf{M}^{-1}\mathbf{f}(t_n + \frac{12}{13}\Delta t)\} \end{bmatrix}, \tag{B.18d}$$

$$
\begin{aligned}
\boldsymbol{k}_5 = \begin{bmatrix}\boldsymbol{k}_{51}\\ \boldsymbol{k}_{52}\\ \boldsymbol{k}_{53}\end{bmatrix} &= \begin{bmatrix}\mathbf{0} & \mathbf{I} & \mathbf{0}\\ \mathbf{0} & \mathbf{0} & \mathbf{I}\\ -\mathbf{M}^{-1}\mathbf{G} & -\mathbf{M}^{-1}\mathbf{K} & -\mathbf{M}^{-1}\mathbf{C}\end{bmatrix}\begin{bmatrix}\boldsymbol{d}_1(t_n)+\frac{439}{216}\boldsymbol{k}_{11}-8\boldsymbol{k}_{21}+\frac{3680}{513}\boldsymbol{k}_{31}-\frac{845}{4104}\boldsymbol{k}_{41}\\ \boldsymbol{d}_2(t_n)+\frac{439}{216}\boldsymbol{k}_{12}-8\boldsymbol{k}_{22}+\frac{3680}{513}\boldsymbol{k}_{32}-\frac{845}{4104}\boldsymbol{k}_{42}\\ \boldsymbol{d}_3(t_n)+\frac{439}{216}\boldsymbol{k}_{13}-8\boldsymbol{k}_{23}+\frac{3680}{513}\boldsymbol{k}_{33}-\frac{845}{4104}\boldsymbol{k}_{43}\end{bmatrix}\\
&+\begin{bmatrix}\mathbf{0}\\ \mathbf{0}\\ \mathbf{M}^{-1}\mathbf{f}(t_n+\Delta t)\end{bmatrix}\\
&=\begin{bmatrix}\boldsymbol{d}_2(t_n)+\frac{439}{216}\boldsymbol{k}_{12}-8\boldsymbol{k}_{22}+\frac{3680}{513}\boldsymbol{k}_{32}-\frac{845}{4104}\boldsymbol{k}_{42}\\ \boldsymbol{d}_3(t_n)+\frac{439}{216}\boldsymbol{k}_{13}-8\boldsymbol{k}_{23}+\frac{3680}{513}\boldsymbol{k}_{33}-\frac{845}{4104}\boldsymbol{k}_{43}\\ \{-\mathbf{M}^{-1}\mathbf{G}(\boldsymbol{d}_1(t_n)+\frac{439}{216}\boldsymbol{k}_{11}-8\boldsymbol{k}_{21}+\frac{3680}{513}\boldsymbol{k}_{31}-\frac{845}{4104}\boldsymbol{k}_{41})\\ -\mathbf{M}^{-1}\mathbf{K}(\boldsymbol{d}_2(t_n)+\frac{439}{216}\boldsymbol{k}_{12}-8\boldsymbol{k}_{22}+\frac{3680}{513}\boldsymbol{k}_{32}-\frac{845}{4104}\boldsymbol{k}_{42})\\ -\mathbf{M}^{-1}\mathbf{C}(\boldsymbol{d}_3(t_n)+\frac{439}{216}\boldsymbol{k}_{13}-8\boldsymbol{k}_{23}+\frac{3680}{513}\boldsymbol{k}_{33}-\frac{845}{4104}\boldsymbol{k}_{43})+\mathbf{M}^{-1}\mathbf{f}(t_n+\Delta t)\}\end{bmatrix},
\end{aligned}
\tag{B.18e}
$$

$$
\begin{aligned}
\boldsymbol{k}_6 = \begin{bmatrix}\boldsymbol{k}_{61}\\ \boldsymbol{k}_{62}\\ \boldsymbol{k}_{63}\end{bmatrix} &= \begin{bmatrix}\mathbf{0} & \mathbf{I} & \mathbf{0}\\ \mathbf{0} & \mathbf{0} & \mathbf{I}\\ -\mathbf{M}^{-1}\mathbf{G} & -\mathbf{M}^{-1}\mathbf{K} & -\mathbf{M}^{-1}\mathbf{C}\end{bmatrix}\begin{bmatrix}\boldsymbol{d}_1-\frac{8}{27}\boldsymbol{k}_{11}+2\boldsymbol{k}_{21}-\frac{3544}{2565}\boldsymbol{k}_{31}+\frac{1859}{4104}\boldsymbol{k}_{41}-\frac{11}{40}\boldsymbol{k}_{51}\\ \boldsymbol{d}_2-\frac{8}{27}\boldsymbol{k}_{12}+2\boldsymbol{k}_{22}-\frac{3544}{2565}\boldsymbol{k}_{32}+\frac{1859}{4104}\boldsymbol{k}_{42}-\frac{11}{40}\boldsymbol{k}_{52}\\ \boldsymbol{d}_3-\frac{8}{27}\boldsymbol{k}_{13}+2\boldsymbol{k}_{23}-\frac{3544}{2565}\boldsymbol{k}_{33}+\frac{1859}{4104}\boldsymbol{k}_{43}-\frac{11}{40}\boldsymbol{k}_{53}\end{bmatrix}\\
&+\begin{bmatrix}\mathbf{0}\\ \mathbf{0}\\ \mathbf{M}^{-1}\mathbf{f}(t_n+\frac{1}{2}\Delta t)\end{bmatrix}\\
&=\begin{bmatrix}\boldsymbol{d}_2(t_n)-\frac{8}{27}\boldsymbol{k}_{12}+2\boldsymbol{k}_{22}-\frac{3544}{2565}\boldsymbol{k}_{32}+\frac{1859}{4104}\boldsymbol{k}_{42}-\frac{11}{40}\boldsymbol{k}_{52}\\ \boldsymbol{d}_3(t_n)-\frac{8}{27}\boldsymbol{k}_{13}+2\boldsymbol{k}_{23}-\frac{3544}{2565}\boldsymbol{k}_{33}+\frac{1859}{4104}\boldsymbol{k}_{43}-\frac{11}{40}\boldsymbol{k}_{53}\\ \{-\mathbf{M}^{-1}\mathbf{G}(\boldsymbol{d}_1(t_n)-\frac{8}{27}\boldsymbol{k}_{11}+2\boldsymbol{k}_{21}-\frac{3544}{2565}\boldsymbol{k}_{31}+\frac{1859}{4104}\boldsymbol{k}_{41}-\frac{11}{40}\boldsymbol{k}_{51})\\ -\mathbf{M}^{-1}\mathbf{K}(\boldsymbol{d}_2(t_n)-\frac{8}{27}\boldsymbol{k}_{12}+2\boldsymbol{k}_{22}-\frac{3544}{2565}\boldsymbol{k}_{32}+\frac{1859}{4104}\boldsymbol{k}_{42}-\frac{11}{40}\boldsymbol{k}_{52})\\ -\mathbf{M}^{-1}\mathbf{C}(\boldsymbol{d}_3(t_n)-\frac{8}{27}\boldsymbol{k}_{13}+2\boldsymbol{k}_{23}-\frac{3544}{2565}\boldsymbol{k}_{33}+\frac{1859}{4104}\boldsymbol{k}_{43}-\frac{11}{40}\boldsymbol{k}_{53})+\mathbf{M}^{-1}\mathbf{f}(t_n+\frac{1}{2}\Delta t)\}\end{bmatrix}.
\end{aligned}
\tag{B.18f}
$$

Having the functions updated at $n+1$-th time-step, the updated solution at $n+1$-th step results in the local truncation error at time step $n+1$:

$$
\tau_{n+1}(h) = |\frac{\widetilde{\boldsymbol{u}}_{n+1}-\boldsymbol{u}_{n+1}}{\Delta t}| = |\frac{1}{360}\boldsymbol{k}_1-\frac{128}{4275}\boldsymbol{k}_3-\frac{2197}{75240}\boldsymbol{k}_4+\frac{1}{50}\boldsymbol{k}_5+\frac{2}{55}\boldsymbol{k}_6|, \tag{B.19}
$$

and the results based on the fourth-order scheme reads:

$$
\boldsymbol{u}_{n+1} = \boldsymbol{u}_n + \Delta t(\frac{25}{216}\boldsymbol{k}_1+\frac{1408}{2565}\boldsymbol{k}_3+\frac{2197}{4104}\boldsymbol{k}_4-\frac{1}{5}\boldsymbol{k}_5). \tag{B.20}
$$

B.4.3 Algorithm

The explicit time integration algorithm based on the adaptive Runge-Kutta-Fehlberg method, described in Section 2.3.2.5, is presented in Algorithm 5.

Algorithm 5 Explicit time integration by adaptive Runge-Kutta-Fehlberg method

numerical solution of the initial-value problem:
$\dot{\boldsymbol{y}} = \boldsymbol{f}(t, \boldsymbol{y}), \quad 0 \leq t \leq T, \quad \boldsymbol{y}(0) = \boldsymbol{0}$ ▷ 2.98

inputs
$\boldsymbol{f}$: initial value problem
Δt_{max}: maximum allowable time-step
ε: error tolerance
q_{max}: maximum allowable rate for the time-step modifier
$step_{RKF}$: RK-4 repeats
T: total simulation time

output
approximation of y at i-th step

Steps

initialization
$t \longleftarrow \emptyset$
$\tau \longleftarrow \emptyset$ ▷ local truncation error
$step \longleftarrow \emptyset$ ▷ step number
$\Delta t \longleftarrow \Delta t_{max}$ ▷ set the initial time step
$\boldsymbol{u} \longleftarrow \emptyset$
while $t \leq T$ **do** ▷ loop over the time-steps
    $step \longleftarrow step + 1$
    if $step$ mod $step_{RKF} = 0$ **then** ▷ RKF
        $TimeStep\_Flag \leftarrow .False.$ ▷ to check the LTE
        while $TimeStep\_Flag = .False.$ **do** ▷ check LTE
            update the functions using RKF method
            $\boldsymbol{k}_1 \leftarrow$ update $\boldsymbol{k}_1$ ▷ 2D:B.14a-3D:B.18a
            $\boldsymbol{k}_2 \leftarrow$ update $\boldsymbol{k}_2$ ▷ 2D:B.14b-3D:B.18b
            $\boldsymbol{k}_3 \leftarrow$ update $\boldsymbol{k}_3$ ▷ 2D:B.14c-3D:B.18c
            $\boldsymbol{k}_4 \leftarrow$ update $\boldsymbol{k}_4$ ▷ 2D:B.14d-3D:B.18d
            $\boldsymbol{k}_5 \leftarrow$ update $\boldsymbol{k}_5$ ▷ 2D:B.14e-3D:B.18e
            $\boldsymbol{k}_6 \leftarrow$ update $\boldsymbol{k}_6$ ▷ 2D:B.14f-3D:B.18f

compute the LTE
$\tau = |\frac{1}{360}\boldsymbol{k}_1 - \frac{128}{4275}\boldsymbol{k}_3 - \frac{2197}{75240}\boldsymbol{k}_4 + \frac{1}{50}\boldsymbol{k}_5 + \frac{2}{55}\boldsymbol{k}_6|$; ▷ (B.19)
$q = 0.84(\frac{\varepsilon}{\tau})^{1/4}$ ▷ time-step modifier
if $q > q_{max}$ **then**
$q \leftarrow q_{max}$
end if
$\Delta t \leftarrow q\Delta t$
if $\Delta t > \Delta t_{max}$ **then**
$\Delta t \leftarrow \Delta t_{max}$
end if
if $\tau \leq \varepsilon$ **then**
$TimeStep\_Flag \leftarrow .True.$; ▷ to check the LTE
update results
$\boldsymbol{u} = \boldsymbol{u} + \Delta t(\frac{25}{216}\boldsymbol{k}_1 + \frac{1408}{2565}\boldsymbol{k}_2 + \frac{2197}{4104}\boldsymbol{k}_3 + \frac{1}{5}\boldsymbol{k}_4)$
print displacement, velocity, and acceleration
end if
end while
$t \longleftarrow t + \Delta t$; ▷ update time
else ▷ RK-4
update functions using RK-4 method
$\boldsymbol{k}_1 \leftarrow$ update $\boldsymbol{k}_1$ ▷ 2D:B.8a-3D:B.11a
$\boldsymbol{k}_2 \leftarrow$ update $\boldsymbol{k}_2$ ▷ 2D:B.8b-3D:B.11b
$\boldsymbol{k}_3 \leftarrow$ update $\boldsymbol{k}_3$ ▷ 2D:B.8c-3D:B.11c
$\boldsymbol{k}_4 \leftarrow$ update $\boldsymbol{k}_4$ ▷ 2D:B.8d-3D:B.11d
update results
$\boldsymbol{u} = \boldsymbol{u} + \dfrac{\Delta t}{6}(\boldsymbol{k}_1 + 2\boldsymbol{k}_2 + 2\boldsymbol{k}_3 + \boldsymbol{k}_4)$
print the results (displacement, velocity, and acceleration)
$t \longleftarrow t + \Delta t$; ▷ update time
end if
end while

Appendix C

Numerical toolchain

We developed a numerical toolchain according to the formulations that we discussed in Section 2. This toolchain has three main parts as illustrated in Figure C.1: preprocessor, parallel simulator, and post processor, which will be explained in the following sections.

C.1 Preprocessing

Once we establish the computational domain by placing appropriate conditions at the truncation surfaces, as shown in Figure C.2, the next step is domain discretization. To this end, we need a mesh generator, capable of generating highly unstructured, robust finite element mesh in large heterogeneous domains. Here, we favor ANSYS [8] in combination with an APDL script that reads the geometry, material properties, and discretization information.

ANSYS produces standard elements, e.g. an 8-noded serendipity element in 2D. An additional modification of the mesh is required if we want to use spectral elements. In this case, we need to add extra nodes to the elements, for instance, for a second-order two-dimensional element, we need to include the mid-node as shown in Figure C.3. The next step before we perform a large-scale simulation is

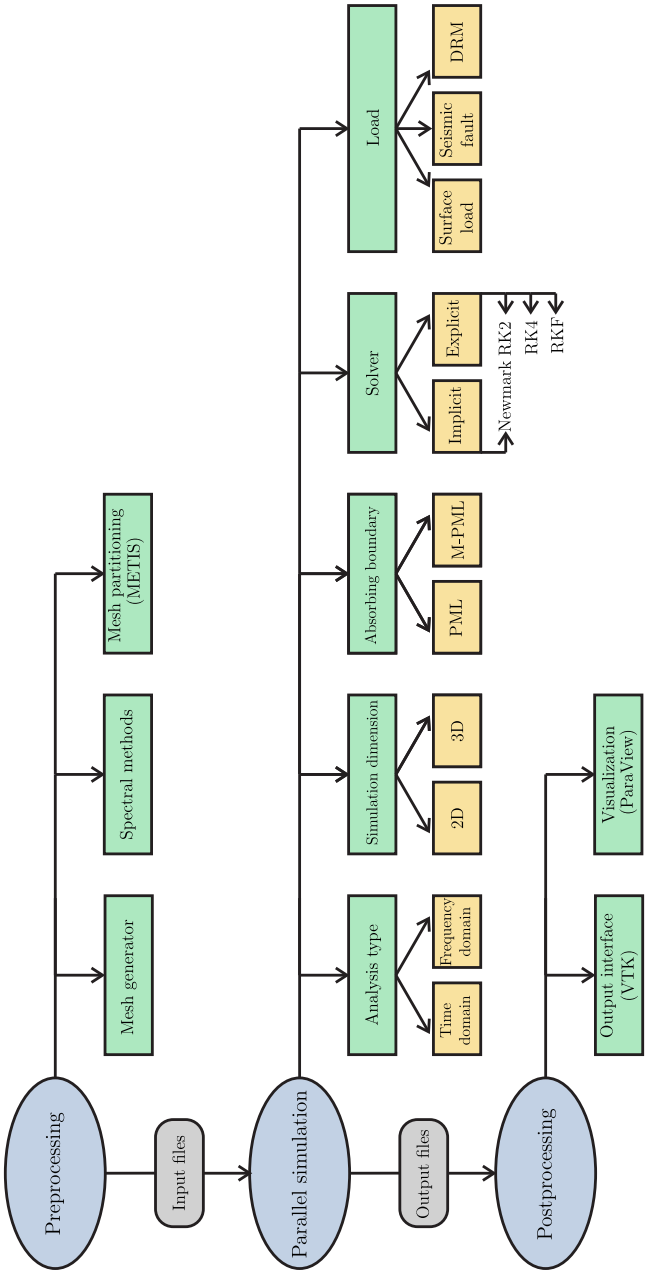

Figure C.1: The flowchart of the developed toolchain

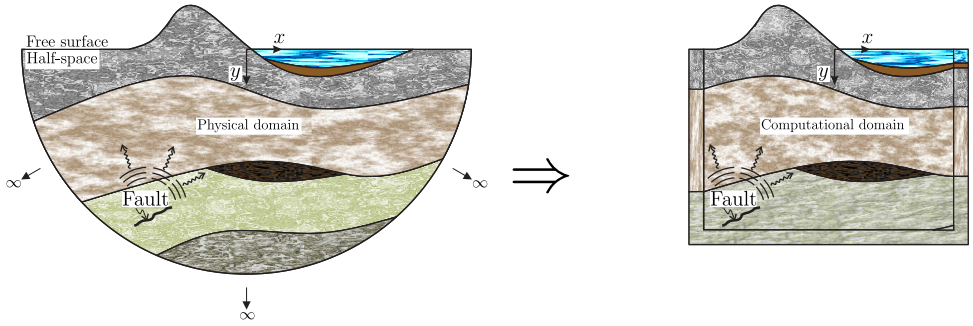

Figure C.2: Negotiating the extent of physical domain

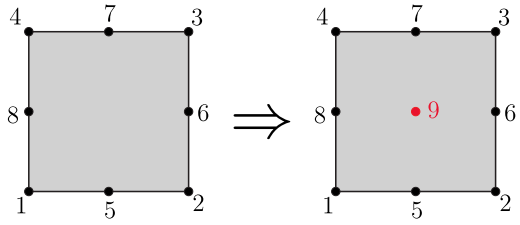

Figure C.3: Converting finite element to spectral element

data partitioning, aiming at evenly distributing data between processors. To this end, we developed PIC (Partitioner and Input Creator) that uses METIS (Karypis et al. (2013) [152, 153]). METIS ensures a balanced load by placement an almost equal number of elements on each processor with a minimal adjacency to reduce the communication between processors (see for example Figure C.4). Once METIS determines the elements for each processor, multiple node and element re-numberings are needed to create separate input files for each processor. Additionally, we create the geometry files for the visualization software during this step.

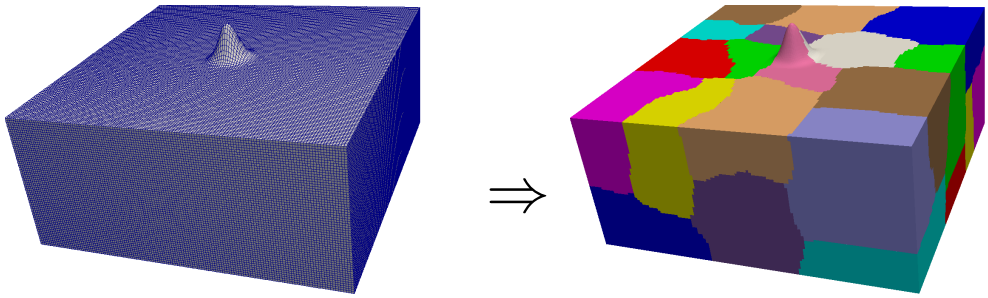

Figure C.4: Partitioning the discretized domain

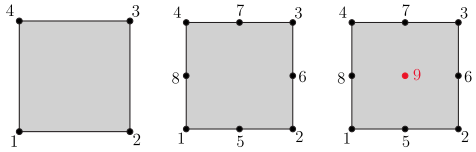

Figure C.5: Two-dimensional quadrilateral elements

C.2 Code input options

The simulation engine is a parallel Fortran code that is using the PETSc library (Portable, Extensible Toolkit for Scientific Computation) [18, 19, 20]. This software is capable of conducting two- and three-dimensional simulations in the time- and frequency-domains using structured and unstructured elements as depicted in Figures C.5, C.6, C.7. In terms of the loads, we can either apply nodal/surface pressure or impose seismic loads within the model. The possible choices for the time integrator are the implicit Newmark solver and explicit solvers (RK-2, RK-4, RKF).

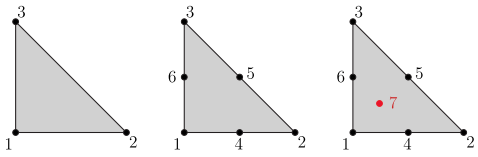

Figure C.6: Two-dimensional triangular elements

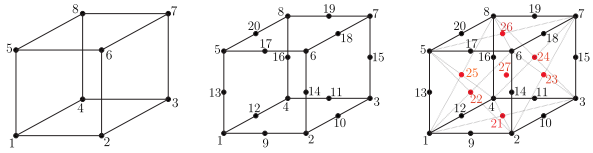

Figure C.7: Three-dimensional hexahedral elements

C.3 Postprocessing

To postprocess and visualize the results, we developed an interface to generate output files for *ParaView* visualization software [122]. ParaView is an open source, multi-platform parallel data analyzer and visualizer built on top of the Visualization Toolkit (VTK) (see Schroeder et al. (2000) [262]) and supports structured and unstructured grids, polygonal data, etc. The interface stores the output files from each processor in Hierarchical Data Format (HDF), which is a file format specifically developed to manage large data. Ultimately, a wrapper file integrates all the results for the visualizing software.

Appendix D

Remarks on adaptivity

We favor two time integration schemes in this study: the implicit Newmark method and the explicit Runge-Kutta technique with different orders. In this appendix, we briefly comment on the performance and the application of each algorithm.

The implicit Newmark method, described in Section 2.3.1, benefits from an unconditionally stable solution, i.e., there is no restriction on the time step. Nevertheless, the high cost of computations, especially in parallel computing, makes the method less attractive for large-scale simulations. Accordingly, we use the implicit algorithm only for verification purposes.

The explicit solvers are highly scalable in parallel computing, but, in contrast to the implicit solvers, are conditionally stable, which means the solution diverges if the time step exceeds an upper bound. Thus, the main challenge here is to determine the optimal time step which leads to a stable solution. Toward this end, most researchers use the Courant-Friedrichs-Lewy stability condition (CFL) to limit the time step, which states that the distance traveled by the solution in one time step, $c\Delta t$, must be less than the distance between two grid points. The following equations

can be obtained for a structured domain [278]:

$$\text{In 1D}: \qquad C = c_x \frac{\Delta t}{\Delta x}, \tag{D.1a}$$

$$\text{In 2D}: \qquad C = (c_x \frac{\Delta t}{\Delta x})^2 + (c_y \frac{\Delta t}{\Delta y})^2, \tag{D.1b}$$

$$\text{In 3D}: \qquad C = (c_x \frac{\Delta t}{\Delta x})^2 + (c_y \frac{\Delta t}{\Delta y})^2 + (c_z \frac{\Delta t}{\Delta z})^2, \tag{D.1c}$$

where c_i is the largest wave velocity, Δx, Δy, and Δz are the minimum grid spacing in the x, y, and z directions, respectively. C is the Courant number, which should remain less than the maximum Courant number, C_{max}. The maximum Courant number is based on empirical experiments and is subject to change depending on the problem. The convention for a structured discretization is to assume $C_{max} = 1$, but this number reduces for an unstructured discretization. Therefore, in the absence of any firm relation for the time step, a trial and error procedure is necessary to find the optimal time step.

We use a Runge-Kutta explicit solver in this research. Note that we exploit second-order elements to discretize the two- or three-dimensional domains, which lead to a second-order time integration scheme, for instance the second-order Runge-Kutta method. This scheme seems to be even more appealing owing to the lower computational cost in comparison to the fourth-order scheme. However, the region of convergence for this scheme is smaller than other higher order schemes, resulting in a smaller time step, yielding a less efficient technique. Hence, the fourth-order Runge-Kutta time scheme, even though it requires more computations in each time step, is more efficient (see [242] for more information).

The Runge-Kutta-Fehlberg adaptive time integration scheme eliminates the necessity of the trial and error process to find out the optimal time step. The adaptive algorithm monitors the LTE error and modifies the time step, if required, to maintain the error below a certain tolerance, which, as a result, guarantees that the solution never diverges. We demonstrate the efficiency of the explicit solvers in the following two-dimensional numerical experiments.

D.1 Example 1: Wave propagation in a homogeneous half-plane

Let us put the efficiency of the adaptive algorithm under scrutiny using the two-dimensional homogeneous model that we considered in Section 3.2.2 for verification purposes. The maximum allowable time step for this model with the element of size $\Delta x = 2.5$m and the pressure wave velocity $c_p = 350$m/s is $\Delta t_{max} = 0.0025$s, as stated in (D.1) for $C_{max} = 1$. For a time duration of $T = 4.5$s to cover the entire wave motion within the domain, the fourth-order Runge-Kutta with fixed time-step requires 1800 steps, which runs in 410 seconds on one CPU (average of ten simulations). However, running the same model, using the adaptive algorithm, requires only 1265 steps with a total runtime of 320s, i.e., 28% faster than the fixed time step. Indeed, the computational cost of each step of the adaptive algorithm is more than the fixed time step algorithm (see Section 2.3.2.5 for details), thus, the comparison of the total number of steps is not a firm measure of the efficiency of the adaptive algorithm, but the runtime.

We need to discuss the effects of the tunable parameters in the adaptive

algorithm; are include the error tolerance, the maximum allowable time step, the maximum allowable rate of change of time step, and the number of fixed time step iterations. According to our experiments, one can achieve the most efficient algorithm if the time step is limited to 1.45 times the Courant number (Δt_{max}), for a structured domain, in this example 0.0036s. The reason is if we do not have a cap for the time step, it increases considerably for the first few steps, results in a very large local truncation error that slows down the entire simulation. Additionally, the total error drives from the space and time discretizations, hence, reducing the error tolerance within the adaptive algorithm does not compensate the spacial discretization error, but, unnecessarily, increases the computational cost. To demonstrate this, we plot the local truncation error for four various error tolerances ε in Figure D.1(a). Even though the local truncation errors are vastly different, the displacement time history at the observation points for all levels of error are identical. For example, Figure D.2 shows the displacement time history at observation point 1 for the fixed time step algorithm and adaptive algorithm with $\varepsilon = 500$. Figure D.1(b) shows the time step for various error tolerances. For the smaller tolerance, the time step is smaller, which, in turn, increases the total cost computations. For example, the runtime for $\varepsilon = 50$ is 3140s. In conclusion, due to the spacial discretization error, we can choose a higher error tolerance for the time discretization.

In another experiment, we trial to simulate the same model using the fixed time step algorithm with a larger time step than the Courant number, because the adaptive simulation time step suggests that for this time duration a higher fixed time step may generate a convergent solution as well, for the limited time duration

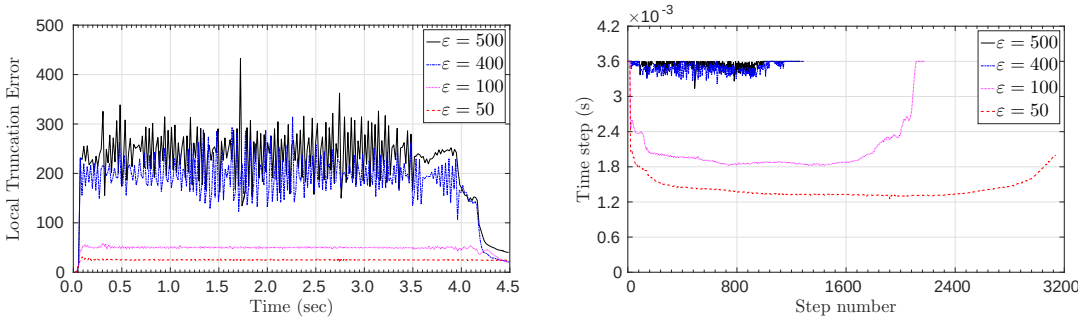

(a) (b)

Figure D.1: Adaptive time integration algorithm results: (a) Local Truncation Error, (b) time step versus step number, for four analyses with different error tolerances

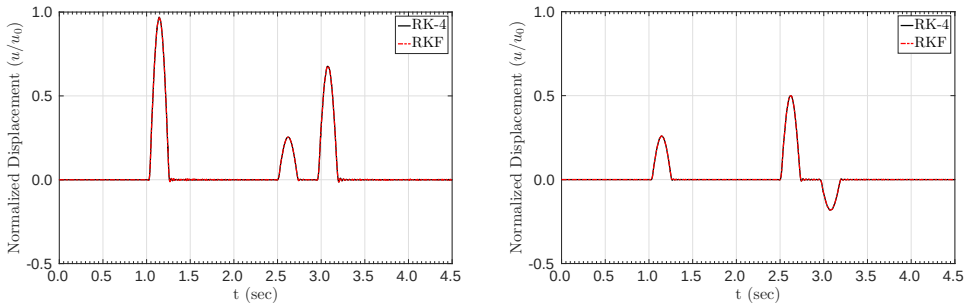

(a) (b)

Figure D.2: Comparison of the time histories of displacement computed from the fourth-order Runge-Kutta method and Runge-Kutta-Fehlberg with error tolerance $\varepsilon = 500$

of simulation. Using a trial and error process, it turns out that to have a converging solution, the maximum time step in the fourth-order Runge-Kutta method can go beyond the CFL number to 0.0034s, however, for second-order Runge-Kutta method is only $0.0003s$, which is even smaller than CFL number. The reason for lower time step in the second-order method is the smaller region of convergence of this Runge-Kutta method. It is important to mention that since we go beyond the CFL

condition, there is no guarantee that for longer simulations this time step yields a convergent solution.

In summary, we incorporated an adaptive algorithm that enhances the efficiency of the time integration scheme by computing the optimal time step using the local truncation error in each time step. This algorithm, in addition to being more efficient over the fixed time step algorithm, eliminates the concerns over choosing the right size of time step.

D.2 Example 2: Heterogeneous, sediment-filled valley

We use the heterogeneous, sediment-filled valley, explained in Section 5.1.2.1, to verify the adaptive algorithm for an unstructured discretization. The shape and discretization is depicted in Figure 5.13. Note that, in the absence of any criterion for choosing the time step in an unstructured domain (the CFL condition is given only for structured discretization), we have no estimation of the time step if we had to use a fixed time step algorithms; thus, a trial and error process was inevitable. To have a rough estimation, one idea is that we find the minimum grid space and use the one-dimensional CFL limit. Applying this method, it turns out that the time step should reduce to 59% of the one-dimensional CFL condition, i.e., from 0.00102s to 0.0006s, which requires multiple attempts as well. However, by using the adaptive algorithm, there is no need for any trial and error process. The displacement time histories at observation point 1 are depicted in Figure D.3 for the fixed and adaptive time step algorithms and show good agreement of the two methods.

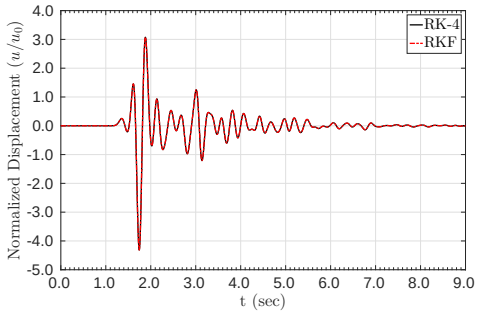

Figure D.3: Comparison of the time histories of displacement computed from the fourth-order Runge-Kutta method and Runge-Kutta-Fehlberg

Bibliography

[1] S. Abarbanel and D. Gottlieb. A Mathematical Analysis of the PML Method. *Journal of Computational Physics*, 134(2):357 – 363, 1997.

[2] J.D. Achenbach. *Wave propagation in elastic solids*. North-Holland series in applied mathematics and mechanics. North-Holland Pub. Co., 1973.

[3] K. Aki. Local site effects on weak and strong ground motion. *Tectonophysics*, 218(13):93–111, 1993.

[4] K. Aki and P.G. Richards. *Quantitative Seismology: Theory and Methods*. Geology (University Science Books).: Seismology. University Science Books, 2002.

[5] Z. Alterman and F. C. Karal. Propagation of elastic waves in layered media by finite difference methods. *Bulletin of the Seismological Society of America*, 58(1):367–398, 1968.

[6] S. Álvarez Rubio, J.J. Benito, F.J. Sánchez-Sesma, and E. Alarcón. The Use of Direct Boundary Element Method for Gaining Insight into Complex Seismic Site Response. *Comput. Struct.*, 83(10-11):821–835, April 2005.

[7] S. Álvarez Rubio, F.J. Sánchez-Sesma, J.J. Benito, and E. Alarcón. The direct boundary element method: 2D site effects assessment on laterally varying

layered media (methodology). *Soil Dynamics and Earthquake Engineering*, 24(2):167 – 180, 2004.

[8] ANSYS Academic Research Release 16.2. Ansys.

[9] S. Aoi and H. Fujiwara. 3D finite-difference method using discontinuous grids. *Bulletin of the Seismological Society of America*, 89(4):918–930, 1999.

[10] D. Appelö and G. Kreiss. A new absorbing layer for elastic waves. *Journal of Computational Physics*, 215:642–660, 2006.

[11] R.J. Archuleta and G.A. Frazier. Three-dimensional numerical simulations of dynamic faulting in a half-space. *Bulletin of the Seismological Society of America*, 68(3):541–572, 1978.

[12] S.A. Ashford and N. Sitar. Analysis of topographic amplification of inclined shear waves in a steep coastal bluff. *Bulletin of the Seismological Society of America*, 87(3):692–700, 1997.

[13] S.A. Ashford, N. Sitar, J. Lysmer, and N. Deng. Topographic effects on the seismic response of steep slopes. *Bulletin of the Seismological Society of America*, 87(3):701–709, 1997.

[14] D. Assimaki, G. Gazetas, and E. Kausel. Effects of local soil conditions on the topographic aggravation of seismic motion: parametric investigation and recorded field evidence from the 1999 Athens earthquake. *Bulletin of the Seismological Society of America*, 95(3):1059–1089, 2005.

[15] D. Assimaki, E. Kausel, and G. Gazetas. Soil-Dependent Topographic Effects: A Case Study from the 1999 Athens Earthquake. *Earthquake Spectra*, 21(4):929–966, 2005.

[16] D. Assimaki, E. Kausel, and G. Gazetas. Wave propagation and soil-structure interaction on a cliff crest during the 1999 Athens Earthquake. *Soil Dynamics and Earthquake Engineering*, 25(7-10):513 – 527, 2005. 11th International Conference on Soil Dynamics and Earthquake Engineering (ICSDEE): Part 1.

[17] D. Baffet, J. Bielak, D. Givoli, T. Hagstrom, and D. Rabinovich. Long-time stable high-order absorbing boundary conditions for elastodynamics. *Computer Methods in Applied Mechanics and Engineering*, 241244(0):20 – 37, 2012.

[18] S. Balay, J. Brown, K. Buschelman, V. Eijkhout, W.D. Gropp, D. Kaushik, M.G. Knepley, L. C. McInnes, B. F. Smith, and H. Zhang. PETSc users manual. Technical Report ANL-95/11 - Revision 3.4, Argonne National Laboratory, 2013.

[19] S. Balay, J. Brown, K. Buschelman, W. D. Gropp, D. Kaushik, M.G. Knepley, L.C. McInnes, B.F. Smith, and H. Zhang. PETSc Web page, 2013. http://www.mcs.anl.gov/petsc.

[20] S. Balay, W. D. Gropp, L. C. McInnes, and B. F. Smith. Efficient Management of Parallelism in Object Oriented Numerical Software Libraries. In E. Arge, A. M. Bruaset, and H. P. Langtangen, editors, *Modern Software Tools in Scientific Computing*, pages 163–202. Birkhäuser Press, 1997.

[21] H. Bao. *Finite element simulation of earthquake ground motion in realistic basins*. PhD thesis, Carnegie Mellon University, Pennsylvania, USA, March 1998.

[22] H. Bao, J. Bielak, O. Ghattas, L.F. Kallivokas, D.R. O'Hallaron, J.R. Shewchuk, and J. Xu. Large-scale simulation of elastic wave propagation in heterogeneous media on parallel computers. *Computer Methods in Applied Mechanics and Engineering*, 152(12):85 – 102, 1998. Containing papers presented at the Symposium on Advances in Computational Mechanics.

[23] P.-Y. Bard and M. Bouchon. The two-dimensional resonance of sediment-filled valleys. *Bulletin of the Seismological Society of America*, 75(2):519–541, 1985.

[24] P.Y. Bard. *Microtremor measurements: A tool for site effect estimation?*, pages 1251–1257. Seismological Society of America.

[25] P.Y. Bard. Diffracted waves and displacement field over two-dimensional elevated topographies. *Geophysical Journal of the Royal Astronomical Society*, 71(3):731–760, 1982.

[26] A. Barry, J. Bielak, and R.C. MacCamy. On absorbing boundary conditions for wave propagation. *Journal of Computational Physics*, 79:449–468, 1988.

[27] U. Basu. Explicit finite element perfectly matched layer for transient three-dimensional elastic waves. *International Journal for Numerical Methods in Engineering*, 77(2):151–176, 2009.

[28] U. Basu and A.K. Chopra. Perfectly matched layers for transient elastodynamics of unbounded domains. *International Journal for Numerical Methods in Engineering*, 59(8):1039–1074, 2004.

[29] E. Bécache, S. Fauqueux, and P. Joly. Stability of perfectly matched layers, group velocities and anisotropic waves. *Journal of Computational Physics*, 188:399–433, 2003.

[30] E. Bécache, P. Joly, and C. Tsogka. Fictitious domains, mixed finite elements and perfectly matched layers for 2D elastic wave propagation. *J. Comput. Acoust.*, 9(3):1175–1202, September 2001.

[31] M. Benzi, G.H. Golub, and J. Liesen. Numerical solution of saddle point problems. *Acta Numerica*, 14:1–137, 5 2005.

[32] J.P. Berenger. A perfectly matched layer for the absorption of electromagnetic waves. *Journal of Computational Physics*, 114(2):185 – 200, 1994.

[33] J. Bielak and P. Christiano. On the effective seismic input for non-linear soil-structure interaction systems. *Earthquake Engineering & Structural Dynamics*, 12(1):107–119, 1984.

[34] J. Bielak, O. Ghattas, and E.J. Kim. Parallel octree-based finite element method for large-scale earthquake ground motion simulaiton citation. *Computer Modeling in Engineering and Sciences*, 10(2):99–112, 2005.

[35] J. Bielak, R.W. Graves, K.B. Olsen, R. Taborda, L. Ramírez-Guzmán, S. M. Day, G.P. Ely, D. Roten, T. H. Jordan, P.J. Maechling, J. Urbanic, Y. Cui, and

G. Juve. The ShakeOut earthquake scenario: Verification of three simulation sets. *Geophysical Journal International*, 180(1):375–404, 2010.

[36] J. Bielak, L.F. Kallivokas, J. XU, and R. Monopoli. Finite Element Absorbing Boundary for the Wave Equation in a Half-plane with an Application to Engineering Seismology. In *Proceedings of the Third International Conference on Mathematical and Numberical Aspects of Wave Propagation*, pages 489–498, Mandeleiu-La Napoule, France, 1995. SIAM.

[37] J. Bielak, K. Loukakis, Y. Hisada, and C. Yoshimura. Domain Reduction Method for Three-Dimensional Earthquake Modeling in Localized Regions, Part I: Theory. *Bulletin of the Seismological Society of America*, 93(2):817–824, 2003.

[38] J. Bielak, J. Xu, and O. Ghattas. Earthquake Ground Motion and Structural Response in Alluvial Valleys. *Journal of Geotechnical and Geoenvironmental Engineering*, 125(5):413–423, 1999.

[39] D.M. Boore. A note on the effect of simple topography on seismic SH waves. *Bulletin of the Seismological Society of America*, 62(1):275–284, 1972.

[40] M. Bouchon. Discrete wave number representation of elastic wave fields in three-space dimensions. *Journal of Geophysical Research: Solid Earth*, 84(B7):3609–3614, 1979.

[41] M. Bouchon. A simple method to calculate Green's functions for elastic layered media. *Bulletin of the Seismological Society of America*, 71(4):959–971, 1981.

[42] M. Bouchon and K. Aki. Discrete wave-number representation of seismic-source wave fields. *Bulletin of the Seismological Society of America*, 67(2):259–277, 1977.

[43] M. Bouchon and J.S. Barker. Seismic response of a hill: The example of Tarzana, California. *Bulletin of the Seismological Society of America*, 86(1A):66–72, 1996.

[44] M. Bouchon, H. Karabulut, M. Bouin, J. Schmittbuhl, M. Vallée, R. Archuleta, S. Das, F. Renard, and D. Marsan. Faulting characteristics of supershear earthquakes. *Tectonophysics*, 493(3–4):244 – 253, 2010.

[45] G.D. Bouckovalas and A.G. Papadimitriou. Numerical evaluation of slope topography effects on seismic ground motion. *Soil Dynamics and Earthquake Engineering*, 25(7 – 10):547 – 558, 2005.

[46] W.E. Boyce and P.C. DiPrima. *Elementary Differential Equations and Boundary Value Problems*. John Wiley & Sons, 9 edition, 2008.

[47] F. Buech, T.R. Davies, and J.R. Pettinga. The Little Red Hill Seismic Experimental Study: Topographic Effects on Ground Motion at a Bedrock-Dominated Mountain Edifice. *Bulletin of the Seismological Society of America*, 100(5A):2219–2229, 2010.

[48] R. Burden and J. Faires. *Numerical Analysis*. Cengage Learning, 2010.

[49] R. Burridge and L. Knopoff. Body force equivalents for seismic dislocations. *Bulletin of the Seismological Society of America*, 54(6A):1875–1888, 1964.

[50] C. Burstedde, M. Burtscher, O. Ghattas, G. Stadler, T. Tu, and L. C. Wilcox. ALPS: A framework for parallel adaptive PDE solution. *Journal of Physics: Conference Series*, 180(1):012009, 2009.

[51] M. Campillo. Modeling of SH-wave propagation in an irregularly layered medium-application to seismic profiles near a dome. *Geophysical Prospecting*, 35(3):236–249, 1987.

[52] M. Campillo and M. Bouchon. Synthetic SH seismograms in a laterally varying medium by the discrete wavenumber method. *Geophysical Journal of the Royal Astronomical Society*, 83(1):307–317, 1985.

[53] L. Carrington, D. Komatitsch, M. Laurenzano, M.M. Tikir, D. Michéa, N. Le Goff, A. Snavely, and J. Tromp. High-frequency Simulations of Global Seismic Wave Propagation Using SPECFEM3D _ GLOBE on 62K Processors. In *Proceedings of the 2008 ACM/IEEE Conference on Supercomputing*, SC '08, pages 60:1–60:11, Piscataway, NJ, USA, 2008. IEEE Press.

[54] F. Casadei, E. Gabellini, G. Fotia, F. Maggio, and A. Quarteroni. A mortar spectral/finite element method for complex 2D and 3D elastodynamic problems. *Computer Methods in Applied Mechanics and Engineering*, 191(45):5119 – 5148, 2002.

[55] E. Casarotti, M. Stupazzini, Sh. Lee, D. Komatitsch, A. Piersanti, and J. Tromp. Cubit and seismic wave propagation based upon the spectral-element method: An advanced unstructured mesher for complex 3d geological media.

In M.L. Brewer and D. Marcum, editors, *Proceedings of the 16th International Meshing Roundtable*, pages 579–597. Springer Berlin Heidelberg, 2008.

[56] M. Çelebi. Topographical and geological amplifications determined from strong-motion and aftershock records of the 3 March 1985 Chile earthquake. *Bulletin of the Seismological Society of America*, 77(4):1147–1167, 1987.

[57] M. Çelebi. Topographical and geological amplification: case studies and engineering implications. *Structural Safety*, 10:199–217, 1991.

[58] E. Chaljub, Y. Capdeville, and J.-P. Vilotte. Solving elastodynamics in a fluid-solid heterogeneous sphere: a parallel spectral element approximation on non-conforming grids. *Journal of Computational Physics*, 187(2):457 – 491, 2003.

[59] E. Chaljub, P. Moczo, S. Tsuno, P.-Y. Bard, J. Kristek, M. Käser, M. Stupazzini, and M. Kristekova. Quantitative Comparison of Four Numerical Predictions of 3D Ground Motion in the Grenoble Valley, France. *Bulletin of the Seismological Society of America*, 100(4):1427–1455, 2010.

[60] W. C. Chew, J. M. Jin, and E. Michielssen. Complex coordinate system as a generalized absorbing boundary condition. In *Proc. 13th Annu. Rev. of Prog. Appl. Comp. Electromag.*, pages 909–914, Monterey,CA, 17-21 Mar. 1997. Vol. 2.

[61] W. C. Chew and Q. H. Liu. Perfectly matched layers for elastodynamics: a new

absorbing boundary condition. *Journal of Computational Acoustics*, 4(4):341–359, 1996.

[62] W. C. Chew and W. H. Weedon. A 3D perfectly matched medium from modified Maxwell's equations with stretched coordinates. *Micro. Opt. Tech. Lett.*, 7:599–604, 1994.

[63] R. Clayton and B. Engquist. Absorbing boundary conditions for acoustic and elastic wave equations. *Bulletin of the Seismological Society of America*, 67(6):1529–1540, 1977.

[64] G. Cohen. *Higher-Order Numerical Methods for Transient Wave Equations*. Lecture Notes in Economic and Mathematical Systems. Springer, 2002.

[65] G. Cohen and S. Fauqueux. Mixed spectral finite elements for the linear elasticity system in unbounded domains. *SIAM J. Sci. Comput.*, 26(3):864–884, 2005.

[66] G. Cohen, P. Joly, J.E. Roberts, and N. Tordjman. Higher Order Triangular Finite Elements with Mass Lumping for the Wave Equation. *SIAM Journal on Numerical Analysis*, 38(6):pp. 2047–2078, 2001.

[67] F. Collino. High order absorbing boundary conditions for wave propagation models: straight line boundary and corner cases. In R. Kleinman, editor, *Proceedings of the Second International Conference on Mathematical and Numerical Aspects of Wave Propagation*, pages 161–171. SIAM, 1993.

[68] F. Collino and C. Tsogka. Application of the perfectly matched absorbing layer model to the linear elastodynamic problem in anisotropic heterogeneous media. *Geophysics*, 66(1):294–307, February 2001.

[69] D. Correia and J.-M. Jin. Performance of regular PML, CFS-PML, and second-order PML for waveguide problems. *Microwave and Optical Technology Letters*, 48(10):2121–2126, October 2006.

[70] M.G. Cremonini, P. Christiano, and J. Bielak. Implementation of effective seismic input for soil-structure interaction systems. *Earthquake Engineering & Structural Dynamics*, 16(4):615–625, 1988.

[71] V. M. Cruz-Atienza and J. Virieux. Dynamic rupture simulation of non-planar faults with a finite-difference approach. *Geophysical Journal International*, 158(3):939–954, 2004.

[72] S.M. Day, R. Graves, J. Bielak, D. Dreger, S. Larsen, K.B. Olsen, A. Pitarka, and L. Ramirez-Guzman. Model for Basin Effects on Long-Period Response Spectra in Southern California. *Earthquake Engineering Research Institute*, 24(1):257–277, 2008.

[73] J. de la Puente, J.-P. Ampuero, and M. Käser. Dynamic rupture modeling on unstructured meshes using a discontinuous Galerkin method. *Journal of Geophysical Research: Solid Earth*, 114(B10), 2009.

[74] M.N. Dmitriev and V.V. Lisitsa. Application of M-PML reflectionless boundary conditions to the numerical simulation of wave propagation in anisotropic

media. part I: Reflectivity. *Numerical Analysis and Applications*, 4(4):271–280, 2011.

[75] M.N. Dmitriev and V.V. Lisitsa. Application of M-PML absorbing boundary conditions to the numerical simulation of wave propagation in anisotropic media. part II: Stability. *Numerical Analysis and Applications*, 5(1):36–44, 2012.

[76] F. H. Drossaert and A. Giannopoulos. A nonsplit complex frequency-shifted PML based on recursive integration for FDTD modeling of elastic waves. *Geophysics*, 72(2):T9–T17, March-April 2007.

[77] M. Dubiner. Spectral methods on triangles and other domains. *Journal of Scientific Computing*, 6:345–390, 1991.

[78] K. Duru and G. Kreiss. A well-posed and discretely stable perfectly matched layer for elastic wave equations in second order formulation. *Communications in Computational Physics*, 11(5):1643 – 1672, 2012.

[79] B. Engquist and A. Majda. Absorbing Boundary Conditions for the Numerical Simulation of Waves. *Mathematics of Computation*, 31(139):pp. 629–651, 1977.

[80] E. Esmaeilzadeh Seylabi, C. Jeong, and E. Taciroglu. On numerical computation of impedance functions for rigid soil-structure interfaces embedded in heterogeneous half-spaces. *Computers and Geotechnics*, 72:15–27, 2016.

[81] E. Esmaeilzadeh Seylabi, C. Jeong, and E. Taciroglu. Modal and nodal impedance functions for truncated semi-infinite soil domains. *Soil Dynamics and Earthquake Engineering*, 92:192–202, 2017.

[82] E. Esmaeilzadeh Seylabi, A. Kurtuluş, K. H. Stokoe, and E. Taciroglu. Interaction of a pile with layered-soil under vertical excitations: field experiments versus numerical simulations. *Bulletin of Earthquake Engineering*, pages 1–25, 2017.

[83] Esmaeilzadeh Seylabi, E. and Jahankhah, H. and Ghannad, M. A. Equivalent linearization of non-linear soil-structure systems. *Earthquake Engineering and Structural Dynamics*, 41:1775–1792, 2012.

[84] E. Faccioli, F. Maggio, R. Paolucci, and A. Quarteroni. 2D and 3D elastic wave propagation by a pseudo-spectral domain decomposition method. *Journal of Seismology*, 1(3):237–251, 1997.

[85] Q. Faqiang and L. Diankui. Antiplane response of isoceles triangular hill to incident SH waves. *Earthquake Engineering and Engineering Vibration*, 4(1):37–46, 2005.

[86] A. Fathi. *Full-waveform inversion in three-dimensional PML-truncated elastic media: theory, computations, and field experiments*. PhD thesis, University of Texas at Austin, Texas, USA, May 2015.

[87] A. Fathi, L.F. Kallivokas, and B. Poursartip. Full-waveform inversion in three-dimensional PML-truncated elastic media. *Computer Methods in Applied Mechanics and Engineering*, 296:39 – 72, 2015.

[88] A. Fathi, B. Poursartip, K. H. Stokoe II, and L. F. Kallivokas. Three-dimensional P- and S-wave velocity profiling of geotechnical sites using full-

waveform inversion driven by field data. *Soil Dynamics and Earthquake Engineering*, 87:63 – 81, 2016.

[89] A. Fathi, B. Poursartip, and L.F. Kallivokas. Time-domain hybrid formulations for wave simulations in three-dimensional PML-truncated heterogeneous media. *International Journal for Numerical Methods in Engineering*, 101(3):165–198, 2015.

[90] G. Festa, E. Delavaud, and J.-P. Vilotte. Interaction between surface waves and absorbing boundaries for wave propagation in geological basins: 2d numerical simulations. *Geophysical Research Letters*, 32(20), 2005.

[91] G. Festa and S. Nielsen. PML absorbing boundaries. *Bulletin of the Seismological Society of America*, 93(2):891–903, April 2003.

[92] G. Festa and J.-P. Vilotte. The Newmark scheme as velocity-stress time-staggering: an efficient PML implementation for spectral element simulations of elastodynamics. *Geophys. J. Int.*, 161:789–812, 2005.

[93] E. H. Field. Spectral amplification in a sediment-filled valley exhibiting clear basin-edge-induced waves. *Bulletin of the Seismological Society of America*, 86(4):991–1005, 1996.

[94] K.L. Fishman and S. Ahmad. Seismic response for alluvial valleys subjected to SH, P and SV waves. *Soil Dynamics and Earthquake Engineering*, 14(4):249 – 258, 1995.

[95] A. Frankel. Three-dimensional simulations of ground motions in the San Bernardino Valley, California, for hypothetical earthquakes on the San Andreas fault. *Bulletin of the Seismological Society of America*, 83(4):1020–1041, 1993.

[96] A. Frankel and W. Stephenson. Three-Dimensional Simulations of Ground Motions in the Seattle Region for Earthquakes in the Seattle Fault Zone. *Bulletin of the Seismological Society of America*, 90(5):1251–1267, 2000.

[97] A. Frankel and J. Vidale. A three-dimensional simulation of seismic waves in the Santa Clara Valley, California, from a Loma Prieta aftershock. *Bulletin of the Seismological Society of America*, 82(5):2045–2074, 1992.

[98] T. Furumura and K. Koketsu. Parallel 3-D Simulation of Ground Motion for the 1995 Kobe Earthquake: The Component Decomposition Approach. *pure and applied geophysics*, 157(11-12):2047–2062, 2000.

[99] A.A. Gabriel, J.P. Ampuero, L.A. Dalguer, and P.M. Mai. Source properties of dynamic rupture pulses with off-fault plasticity. *Journal of Geophysical Research: Solid Earth*, 118(8):4117–4126, 2013.

[100] P. Galvez, J.-P. Ampuero, L. A. Dalguer, S. N. Somala, and T. Nissen-Meyer. Dynamic earthquake rupture modelled with an unstructured 3-D spectral element method applied to the 2011 M9 Tohoku earthquake. *Geophysical Journal International*, 198(2):1222–1240, 2014.

[101] W. W. Garvin. Exact Transient Solution of the Buried Line Source Problem. *Proceedings of the Royal Society of London. Series A. Mathematical and Physical Sciences*, 234(1199):528–541, 1956.

[102] R. Gash, E. Esmaeilzadeh Seylabi, and E. Taciroglu. Implementation and stability analysis of discrete-time filters for approximating frequency-dependent impedance functions in the time domain. *Soil Dynamics and Earthquake Engineering*, 94:223 – 233, 2017.

[103] J. Gazdag. Modeling of the acoustic wave equation with transform methods. *GEOPHYSICS*, 46(6):854–859, 1981.

[104] S. D. Gedney. An anisotropic perfectly matched layer-absorbing medium for the truncation of FDTD lattices. *IEEE Transactions on Antennas and Propagation*, 44(12):1630–1639, December 1996.

[105] L. Geli, P.Y. Bard, and B. Jullien. The effect of topography on earthquake ground motion: A review and new results. *Bulletin of the Seismological Society of America*, 78(1):42–63, 1988.

[106] S.A Gil-Zepeda, J.C Montalvo-Arrieta, R Vai, and F.J Sánchez-Sesma. A hybrid indirect boundary element-discrete wave number method applied to simulate the seismic response of stratified alluvial valleys. *Soil Dynamics and Earthquake Engineering*, 23(1):77 – 86, 2003.

[107] D. Givoli and B. Neta. High-order non-reflecting boundary scheme for time-dependent waves. *Journal of Computational Physics*, 186(1):24–46, 2003.

[108] K.F. Graff. *Wave Motion in Elastic Solids*. Dover Books on Engineering Series. Dover Publications, 1975.

[109] V. Graizer. Low-velocity zone and topography as a source of site amplification effect on Tarzana hill, California. *Soil Dynamics and Earthquake Engineering*, 29(2):324 – 332, 2009.

[110] R.W. Graves. Modeling three-dimensional site response effects in the Marina District Basin, San Francisco, California. *Bulletin of the Seismological Society of America*, 83(4):1042–1063, 1993.

[111] R.W. Graves. Simulating seismic wave propagation in 3D elastic media using staggered-grid finite differences. *Bulletin of the Seismological Society of America*, 86(4):1091–1106, 1996.

[112] R.W. Graves. Three-dimensional finite-difference modeling of the San Andreas fault: Source parameterization and ground-motion levels. *Bulletin of the Seismological Society of America*, 88(4):881–897, 1998.

[113] M. Grote, A. Schneebeli, and D. Schötzau. Discontinuous Galerkin Finite Element Method for the Wave Equation. *SIAM Journal on Numerical Analysis*, 44(6):2408–2431, 2006.

[114] M. Guatteri, P.M. Mai, G.C. Beroza, and J. Boatwright. Strong Ground-Motion Prediction from Stochastic-Dynamic Source Models. *Bulletin of the Seismological Society of America*, 93(1):301–313, 2003.

[115] J.A. Gutierrez and A.K. Chopra. A substructure method for earthquake analysis of structures including structure-soil interaction. *Earthquake Engineering and Structural Dynamics*, 6(1):51–69, 1978.

[116] T. Hagstrom and T. Warburton. A new auxiliary variable formulation of high-order local radiation boundary conditions: corner compatibility conditions and extensions to first-order systems. *Wave Motion*, 39(4):327 – 338, 2004.

[117] I. Harari, M. Slavutin, and E. Turkel. Analytical and numerical studies of a finite element pml for the helmholtz equation. *Journal of Computational Acoustics*, 08(01):121–137, 2000.

[118] R.A. Harris and S.M. Day. Dynamic 3D simulations of earthquakes on En Echelon Faults. *Geophysical Research Letters*, 26(14):2089–2092, 1999.

[119] S. H. Hartzell, D. L. Carver, and K. W. King. Initial investigation of site and topographic effects at Robinwood Ridge, California. *Bulletin of the Seismological Society of America*, 84(5):1336–1349, 1994.

[120] F. D. Hastings, J. B. Schneider, and S. L. Broschat. Application of the perfectly matched layer (PML) absorbing boundary condition to elastic wave propagation. *J. Acoust. Soc. Am.*, 100(5):3061–3069, 1996.

[121] H.B. Havenith, D. Fäh, S. Alvarez-Rubio, and D. Roten. Response spectra for the deep sediment-filled Rhône Valley in the Swiss Alps. *Soil Dynamics and Earthquake Engineering*, 29(1):17 – 38, 2009.

[122] A. Henderson and J. Ahrens. *The Paraview guide : a parallel visualization application*. Kitware, Inc., New York, 2004.

[123] I. Herrera and J. Bielak. Soil-structure interaction as a diffraction problem. In *Proc. 6th World Conference on Earthquake Engineering*, volume 4, New Delhi, India, 1977.

[124] J. Hesthaven and C. Teng. Stable Spectral Methods on Tetrahedral Elements. *SIAM Journal on Scientific Computing*, 21(6):2352–2380, 2000.

[125] R. L. Higdon. Absorbing boundary conditions for acoustic and elastic waves in stratified media. *Journal of Computational Physics*, 101(2):386 – 418, 1992.

[126] R.L. Higdon. Absorbing boundary conditions for difference approximations to the multi-dimensional wave equation. *Math. Comput.*, 47(176):437–459, October 1986.

[127] R.L. Higdon. Radiation boundary conditions for elastic wave propagation. *SIAM J. Numer. Anal.*, 27(4):831–869, August 1990.

[128] Y. Hisada. An efficient method for computing Green's functions for a layered half-space with sources and receivers at close depths. *Bulletin of the Seismological Society of America*, 84(5):1456–1472, 1994.

[129] Y. Hisada. An efficient method for computing Green's functions for a layered half-space with sources and receivers at close depths (part 2). *Bulletin of the Seismological Society of America*, 85(4):1080–1093, 1995.

[130] Y. Hisada, J. Bielak, O. Ghattas, and D. R. O'Hallaron. Simulations of long-period ground motions during the 1995 Hyogoken-Nanbu (Kobe) earthquake using 3D finite element method. In *Proc. 2nd International Symposium on the Effect of Surface Geology on Seismic Motion*, pages 1353–1360, Yokohana, Japan, 1998.

[131] F. Q. Hu. On absorbing boundary conditions for linearized Euler equations by a perfectly matched layer. *Journal of Computational Physics*, 129:201–219, 1996.

[132] F.Q. Hu, M.Y. Hussaini, and P. Rasetarinera. An Analysis of the Discontinuous Galerkin Method for Wave Propagation Problems. *Journal of Computational Physics*, 151(2):921 – 946, 1999.

[133] Y. Huang, J.-P. Ampuero, and D.V. Helmberger. Earthquake ruptures modulated by waves in damaged fault zones. *Journal of Geophysical Research: Solid Earth*, 119(4):3133–3154, 2014.

[134] A. Iserles. *A First Course in the Numerical Analysis of Differential Equations*. A First Course in the Numerical Analysis of Differential Equations. Cambridge University Press, 2009.

[135] U. Iturrarán-Viveros, F. J. Sánchez-Sesma, and F. Janod. Scattering of elastic waves in heterogeneous media using the direct solution method. *Geophysical Journal International*, 156(2):222–236, 2004.

[136] C. Jeong, E. Esmaeilzadeh Seylabi, and E. Taciroglu. *A Time-Domain Substructuring Method for Dynamic Soil Structure Interaction Analysis of Arbitrarily Shaped Foundation Systems on Heterogeneous Media*, pages 346–353. ASCE, 2013.

[137] C. Jeong, L.F. Kallivokas, S. Kucukcoban, W. Deng, and A. Fathi. Maximization of wave motion within a hydrocarbon reservoir for wave-based enhanced oil recovery. *Journal of Petroleum Science and Engineering*, 129:205 – 220, 2015.

[138] P. Joly and C. Tsogka. *Numerical methods for treating unbounded media. "Effective computational methods for wave propagation"*, volume 5 of *Numer. Insights,*, pages 425–472. Chapman & Hall/CRC, 2008.

[139] P. Joly and C. Tsogka. High order absorbing boundary conditions for elastodynamics, lecture. 4th European Conference on Computational Mechanics, 2010.

[140] L. Jones, R. Bernknopf, D. Cox, J. Goltz, K. Hudnut, D. Mileti, S. Perry, D. Ponti, K. Porter, M. Reichle, H. Seligson, K. Shoaf, J. Treiman, and A. Wein. *The ShakeOut Scenario*. Technical Report, USGS R1150, CGS-P25, U.S. Geological Survey and California Geological Survey, 2008.

[141] L.F. Kallivokas, J. Bielak, and R. C. MacCamy. Symmetric Local Absorbing Boundaries in Time and Space. *Journal of Engineering Mechanics*, 117(9):2027–2048, 1991.

[142] L.F. Kallivokas, A. Fathi, S. Kucukcoban, K.H. Stokoe II, J. Bielak, and O. Ghattas. Site characterization using full waveform inversion. *Soil Dynamics and Earthquake Engineering*, 47(0):62 – 82, 2013.

[143] M. Kamalian, B. Gatmiri, A. Sohrabi-Bidar, and A. Khalaj. Amplification pattern of 2D semi-sine-shaped valleys subjected to vertically propagating incident waves. *Communications in Numerical Methods in Engineering*, 23(9):871–887, 2007.

[144] M. Kamalian, A. Sohrabi-Bidar, A. Razmkhah, A. Taghavi, and I. Rahmani. Considerations on seismic microzonation in areas with two-dimensional hills. *Journal of Earth System Science*, 117(2):783–796, 2008.

[145] Y. Kaneko, J.-P. Ampuero, and N. Lapusta. Spectral-element simulations of long-term fault slip: Effect of low-rigidity layers on earthquake-cycle dynamics. *Journal of Geophysical Research: Solid Earth*, 116(B10), 2011.

[146] G. Karniadakis and S.J. Sherwin. *Spectral/hp Element Methods for Computational Fluid Dynamics: Second Edition*. Numerical Mathematics and Scientific Computation. OUP Oxford, 2005.

[147] P. M. Karve. *Inverse source problems for focusing wave energy to targeted subsurface formations: theory and numerical experiments*. Doctoral dissertation, The University of Texas at Austin, 2016.

[148] P. M. Karve, A. Fathi, B. Poursartip, and L. F. Kallivokas. Source parameter inversion for wave energy focusing to a target inclusion embedded in a three-

dimensional heterogeneous halfspace. *International Journal for Numerical and Analytical Methods in Geomechanics*, 41(7):1016–1037, 2017. nag.2662.

[149] P. M. Karve and L. F. Kallivokas. Wave energy focusing to subsurface poroelastic formations to promote oil mobilization. *Geophysical Journal International*, 202(1):119–141, 2015.

[150] P. M. Karve, S. Kucukcoban, and L. F. Kallivokas. On an inverse source problem for enhanced oil recovery by wave motion maximization in reservoirs. *Computational Geosciences*, 19(1):233–256, 2015.

[151] P. M. Karve, L. Manuel, and L. F. Kallivokas. A framework for assessing the uncertainty in wave energy delivery to targeted subsurface formations. *Journal of applied geophysics*, 2015.

[152] G. Karypis. A Software Package for Partitioning Unstructured Graphs, Partitioning Meshes, and Computing Fill-Reducing Orderings of Sparse Matrices, Version 4.0, 2013.

[153] G. Karypis and K. Schloegel. ParMeTis: Parallel Graph Partitioning and Sparse Matrix Ordering Library, Version 4.0, 20011.

[154] M. Käser and M. Dumbser. An arbitrary high-order discontinuous Galerkin method for elastic waves on unstructured meshes I. The two-dimensional isotropic case with external source terms. *Geophysical Journal International*, 166(2):855–877, 2006.

[155] M. Käser and F. Gallovič. Effects of complicated 3-D rupture geometries on earthquake ground motion and their implications: a numerical study. *Geophysical Journal International*, 172(1):276–292, 2008.

[156] H. Kawase. Time-domain response of a semi-circular canyon for incident SV, P, and Rayleigh waves calculated by the discrete wavenumber boundary element method. *Bulletin of the Seismological Society of America*, 78(4):1415–1437, 1988.

[157] H. Kawase and K. Aki. Topography effect at the critical SV-wave incidence: Possible explanation of damage pattern by the Whittier Narrows, California, earthquake of 1 October 1987. *Bulletin of the Seismological Society of America*, 80(1):1–22, 1990.

[158] K. Kelly, R. Ward, S. Treitel, and R. Alford. Synthetic seismograms: a finite difference approach. *Geophysics*, 41(1):2–27, 1976.

[159] E. J. Kim, J. Bielak, and O. Ghattas. Large-scale Northridge earthquake simulation using octree-based multiresolution mesh method. In *Proceedings of the 16th ASCE Engineering Mechanics Conference*, Seattle, WA, 2003. University of Washington.

[160] J. Kim and A. Papageorgiou. Discrete Wave-Number Boundary-Element Method for 3-D Scattering Problems. *Journal of Engineering Mechanics*, 119(3):603–624, 1993.

[161] J. L. King and B. E. Tucker. Observed variations of earthquake motion across a sediment-filled valley. *Bulletin of the Seismological Society of America*, 74(1):137–151, 1984.

[162] D. Komatitsch, G. Erlebacher, D. G addeke, and D. Mich a. High-order finite-element seismic wave propagation modeling with MPI on a large GPU cluster. *Journal of Computational Physics*, 229(20):7692 – 7714, 2010.

[163] D. Komatitsch, Q. Liu, J. Tromp, P. Sss, C. Stidham, and J.H. Shaw. Simulations of Ground Motion in the Los Angeles Basin Based upon the Spectral-Element Method. *Bulletin of the Seismological Society of America*, 94(1):187–206, 2004.

[164] D. Komatitsch and R. Martin. An unsplit convolutional perfectly matched layer improved at grazing incidence for the seismic wave equation. *Geophysics*, 72(5):SM155–SM167, 2007.

[165] D. Komatitsch, R. Martin, J. Tromp, M.A. Taylor, and B.A. Wingate. Wave propagation in 2-D elastic media using a spectral element method with triangles and quadrangles. *Journal of Computational Acoustics*, 09(02):703–718, 2001.

[166] D. Komatitsch and J. Tromp. Introduction to the spectral element method for three-dimensional seismic wave propagation. *Geophysical Journal International*, 139(3):806–822, 1999.

[167] D. Komatitsch and J. Tromp. Spectral-element simulations of global seis-

mic wave propagation-II. Three-dimensional models, oceans, rotation and self-gravitation. *Geophysical Journal International*, 150(1):303–318, 2002.

[168] D. Komatitsch and J. Tromp. Spectral-element simulations of global seismic wave propagation -I. Validation. *Geophysical Journal International*, 149(2):390–412, 2002.

[169] D. Komatitsch and J. Tromp. A perfectly matched layer absorbing boundary condition for the second-order seismic wave equation. *Geophysical Journal International*, 154(1):146–153, 2003.

[170] D. Komatitsch, S. Tsuboi, and J.n Tromp. *The Spectral-Element Method in Seismology*, pages 205–227. American Geophysical Union, 2005.

[171] D. Komatitsch and J.-P. Vilotte. The spectral element method: An efficient tool to simulate the seismic response of 2D and 3D geological structures. *Bulletin of the Seismological Society of America*, 88(2):368–392, 1998.

[172] D. Komatitsch, J.-P. Vilotte, R. Vai, J. M. Castillo-covarrubias, and F.J. Sánchez-sesma. The Spectral Element method for elastic wave equations: application to 2D and 3D seismic problems. *International Journal for Numerical Methods in Engeneering*, 45:1139–1164, 1999.

[173] S. Kontoe, L. Zdravkovic, and D. Potts. The domain reduction method for dynamic coupled consolidation problems in geotechnical engineering. *International Journal for Numerical and Analytical Methods in Geomechanics*, 32(6):659–680, 2008.

[174] S. Koo. *Subsurface elastic wave energy focusing based on a time reversal concept*. Doctoral dissertation, The University of Texas at Austin, 2017.

[175] S. Koo, P. M. Karve, and L. F. Kallivokas. A comparison of time-reversal and inverse-source methods for the optimal delivery of wave energy to subsurface targets. *Wave Motion*, 67:121–140, 2016.

[176] D.A. Kopriva. *Implementing Spectral Methods for Partial Differential Equations: Algorithms for Scientists and Engineers*. Scientific Computation. Springer, 2009.

[177] D.D. Kosloff and E. Baysal. Forward modeling by a Fourier method. *Geophysics*, 47(10):1402–1412, 1982.

[178] S. Kucukcoban and L.F. Kallivokas. A mixed perfectly-matched-layer for transient wave simulations in axisymmetric elastic media. *CMES, Comput. Model. Eng. Sci.*, 64(2):109–145, 2010.

[179] S. Kucukcoban and L.F. Kallivokas. Mixed perfectly-matched-layers for direct transient analysis in 2D elastic heterogeneous media. *Computer Methods in Applied Mechanics and Engineering*, 200(1 4):57 – 76, 2011.

[180] S. Kucukcoban and L.F. Kallivokas. A symmetric hybrid formulation for transient wave simulations in PML-truncated heterogeneous media. *Wave Motion*, 50(1):57 – 79, 2013.

[181] H. Lamb. On the Propagation of Tremors over the Surface of an Elastic Solid. *Philosophical Transactions of the Royal Society of London. Series A, Containing Papers of a Mathematical or Physical Character*, 203(359-371):1–42, 1904.

[182] S.J. Lee, Y. C. Chan, D. Komatitsch, B. S. Huang, and J. Tromp. Effects of realistic surface topography on seismic ground motion in the Yangminshan region of Taiwan based on the spectral-element method and LiDAR DTM. *Bull. Seismol. Soc. Am.*, 99(2A):681–693, 2009.

[183] A.R. Levander. Fourth-order finite-difference P-SV seismograms. *Geophysics*, 53(11):1425–1436, 1988.

[184] E.L. Lindman. "Free-space" boundary conditions for the time dependent wave equation. *Journal of Computational Physics*, 18(1):66 – 78, 1975.

[185] Q. H. Liu. Perfectly matched layers for elastic waves in cylindrical and spherical coordinates. *J. Acoust. Soc. Am.*, 105(4):2075–2084, April 1999.

[186] K. Loukakis and J. Bielak. Seismic response of two-dimensional sediment-filled valleys to oblique incident SV-waves calculated by the finite element method. In *Proceedings of Fifth U.S. National Conference on Earthquake Engineering*, volume III, pages 25–34, Chicago, Illinois, 1994.

[187] J. E. Luco, H. L. Wong, and M. D. Trifunac. A note on the dynamic response of rigid embedded foundations. *Earthquake Engineering & Structural Dynamics*, 4(2):119–127, 1975.

[188] F. Luzón, L. Ramírez, F. J. Sánchez-Sesma, and A. Posadas. Propagation of SH elastic waves in deep sedimentary basins with an oblique velocity gradient. *Wave Motion*, 38(1):11 – 23, 2003.

[189] J. Lysmer and L.A. Drake. The propagation of Love waves across nonhorizontally layered structures. *Bulletin of the Seismological Society of America*, 61(5):1233–1251, 1971.

[190] J. Lysmer and L.A. Drake. *A finite element method for seismology*, volume 11. Academic Press, 1972.

[191] J. Lysmer and R. L. Kuhlemeyer. Finite dynamic model for the infinite media. *Journal of Engineering Mechanics Division*, 95:859–877, 1969.

[192] H. Magistrale, S. Day, R. W. Clayton, and R. Graves. The SCEC Southern California Reference Three-Dimensional Seismic Velocity Model Version 2. *Bulletin of the Seismological Society of America*, 90(6B):S65–S76, 2000.

[193] H. Magistrale, R. Graves, and R. W. Clayton. A standard three-dimensional seismic velocity model for southern California: Version 1. *EOS Trans. AGU*, 79(F605), 1998.

[194] P.M. Mai and G. C. Beroza. Source Scaling Properties from Finite-Fault-Rupture Models. *Bulletin of the Seismological Society of America*, 90(3):604–615, 2000.

[195] P.M. Mai and G.C. Beroza. A spatial random field model to characterize complexity in earthquake slip. *Journal of Geophysical Research: Solid Earth*, 107(B11):ESE 10–1–ESE 10–21, 2002.

[196] R. Martin, D. Komatitsch, and S. D. Gedney. A variational formulation of a stabilized unsplit convolutional perfectly matched layer for the isotropic or anisotropic seismic wave equation. *CMES*, 37(3):274–304, 2008.

[197] R. Martin, D. Komatitsch, S.D. Gedney, and E. Bruthiaux. A high-order time and space formulation of the unsplit perfectly matched layer for the seismic wave equation using Auxiliary Differential Equations (ADE-PML). *Computer Modelling in Engineering and Sciences - CMES*, 56(1):17–42, 2010.

[198] T. Maruyama. On the force equivalents of dynamical elastic dislocations with reference to the earthquake mechanism. *Bulletin of the Earthquake Research Institute*, 41(1):467–486, 1963.

[199] M. Massa, G. Ferretti, A. Cevasco, L. Isella, and C. Eva. Analysis of site amplification phenomena: An application in ripabottoni for the 2002 molise, italy, earthquake. *Earthquake Spectra*, 20(S1):S107–S118, 2004.

[200] M. Massa, S. Lovati, E. DAlema, G. Ferretti, and M. Bakavoli. An Experimental Approach for Estimating Seismic Amplification Effects at the Top of a Ridge, and the Implication for Ground-Motion Predictions: The Case of Narni, Central Italy. *Bulletin of the Seismological Society of America*, 100(6):3020–3034, 2010.

[201] P.J. Matuszyk and L.F. Demkowicz. Parametric finite elements, exact sequences and perfectly matched layers. *Computational Mechanics*, 51(1):35–45, 2013.

[202] I. Mazzieri, M. Stupazzini, R. Guidotti, and C. Smerzini. SPEED: SPectral Elements in Elastodynamics with Discontinuous Galerkin: a non-conforming approach for 3D multi-scale problems. *International Journal for Numerical Methods in Engineering*, 95(12):991–1010, 2013.

[203] K.L. McLaughlin and Steven M. Day. 3D elastic finite difference seismic wave simulations. *Computers in Physics*, 8(6):656–663, 1994.

[204] L. Meng, A. Inbal, and J.-P. Ampuero. A window into the complexity of the dynamic rupture of the 2011 Mw 9 Tohoku-Oki earthquake. *Geophysical Research Letters*, 38(7), 2011.

[205] E. D. Mercerat, J. P. Vilotte, and F. J. Sánchez-Sesma. Triangular Spectral Element simulation of two-dimensional elastic wave propagation using unstructured triangular grids. *Geophysical Journal International*, 166(2):679–698, 2006.

[206] K. C. Meza-Fajardo and A. S. Papageorgiou. A Nonconvolutional, Split-Field, Perfectly Matched Layer for Wave Propagation in Isotropic and Anisotropic Elastic Media: Stability Analysis. *Bulletin of the Seismological Society of America*, 98(4):1811–1836, 2008.

[207] K. C. Meza-Fajardo and A. S. Papageorgiou. Study of the accuracy of the multiaxial perfectly matched layer for the elastic-wave equation. *Bulletin of the Seismological Society of America*, 102(6):2458–2467, December 2012.

[208] K.C. Meza-Fajardo and A.S. Papageorgiou. On the stability of a non-convolutional perfectly matched layer for isotropic elastic media. *Soil Dynamics and Earthquake Engineering*, 30(3):68 – 81, 2010.

[209] P. Moczo, E. Bystrický, J. Kristek, J. M. Carcione, and M. Bouchon. Hybrid modeling of P-SV seismic motion at inhomogeneous viscoelastic topographic structures. *Bulletin of the Seismological Society of America*, 87(5):1305–1323, 1997.

[210] P. Moczo, J. Kristek, and E. Bystrický. Efficiency and Optimization of the 3-D Finite-Difference Modeling of Seismic Ground Motion. *Journal of Computational Acoustics*, 9(2):593, 2001.

[211] P. Moczo, M. Lucká, J. Kristek, and M. Kristeková. 3D Displacement finite differences and a combined memory optimization. *Bulletin of the Seismological Society of America*, 89(1):69–79, 1999.

[212] H. Nakano. Notes on the nature of the forces which give rise to the earthquake motions. *Seismological Bulletin of Central Metrological Observatory of Japan*, 1(1):92–120, 1923.

[213] K.V. Nguyen and B. Gatmiri. Evaluation of seismic ground motion induced by

topographic irregularity. *Soil Dynamics and Earthquake Engineering*, 27(2):183 – 188, 2007.

[214] A. Ohtsuki and K. Harumi. Effect of topography and subsurface inhomogeneities on seismic SV waves. *Earthquake Engineering & Structural Dynamics*, 11(4):441–462, 1983.

[215] A. Ohtsuki, H. Yamahara, and K. Harumi. Effect of topography and subsurface inhomogeneity on seismic rayleigh waves. *Earthquake Engineering & Structural Dynamics*, 12(1):37–58, 1984.

[216] K. B. Olsen and R.J. Archuleta. Three-dimensional simulation of earthquakes on the Los Angeles fault system. *Bulletin of the Seismological Society of America*, 86(3):575–596, 1996.

[217] K. B. Olsen, R.J. Archuleta, and J.R. Matarese. Three-Dimensional Simulation of a Magnitude 7.75 Earthquake on the San Andreas Fault. *Science*, 270(5242):1628–1632, 1995.

[218] K. B. Olsen, S. M. Day, J. B. Minster, Y. Cui, A. Chourasia, M. Faerman, R. Moore, P. Maechling, and T. Jordan. Strong shaking in Los Angeles expected from southern San Andreas earthquake. *Geophysical Research Letters*, 33(7), 2006.

[219] K. B. Olsen, S. M. Day, J. B. Minster, Y. Cui, A. Chourasia, D. Okaya, P. Maechling, and T. Jordan. TeraShake2: Spontaneous Rupture Simulations

of Mw 7.7 Earthquakes on the Southern San Andreas Fault. *Bulletin of the Seismological Society of America*, 98(3):1162–1185, 2008.

[220] K.B. Olsen, J.C. Pechmann, and G.T. Schuster. Simulation of 3D elastic wave propagation in the Salt Lake Basin. *Bulletin of the Seismological Society of America*, 85(6):1688–1710, 1995.

[221] I. Opršal and J. Zahradník. Elastic finite-difference method for irregular grids. *Geophysics*, 64(1):240–250, 1999.

[222] I. Opršal and J. Zahradník. Three-dimensional finite difference method and hybrid modeling of earthquake ground motion. *Journal of Geophysical Research: Solid Earth*, 107(B8):ESE 2–1–ESE 2–16, 2002.

[223] S.A. Orszag. Spectral methods for problems in complex geometries. *Journal of Computational Physics*, 37(1):70 – 92, 1980.

[224] R. Paolucci. Amplification of earthquake ground motion by steep topographic irregularities. *Earthquake Engineering & Structural Dynamics*, 31(10):1831–1853, 2002.

[225] R. Pasquetti and F. Rapetti. Spectral element methods on triangles and quadrilaterals: comparisons and applications. *Journal of Computational Physics*, 198(1):349 – 362, 2004.

[226] R. Pasquetti and F. Rapetti. Spectral Element Methods on Unstructured Meshes: Comparisons and Recent Advances. *Journal of Scientific Computing*, 27(1-3):377–387, 2006.

[227] R. Pasquetti and F. Rapetti. Spectral element methods on unstructured meshes: which interpolation points? *Numer. Algorithms*, 55(2-3):349–366, November 2010.

[228] A.T. Patera. A spectral element method for fluid dynamics: Laminar flow in a channel expansion. *Journal of Computational Physics*, 54(3):468 – 488, 1984.

[229] C. Pelties, J. de la Puente, J.-P. Ampuero, G. B. Brietzke, and M. Käser. Three-dimensional dynamic rupture simulation with a high-order discontinuous Galerkin method on unstructured tetrahedral meshes. *Journal of Geophysical Research: Solid Earth*, 117(B2), 2012.

[230] C. Pelties, A.-A. Gabriel, and J.-P. Ampuero. Verification of an ADER-DG method for complex dynamic rupture problems. *Geoscientific Model Development*, 7(3):847–866, 2014.

[231] D. Peter, D. Komatitsch, Y. Luo, R. Martin, N. Le Goff, E. Casarotti, P. Le Loher, F. Magnoni, Q. Liu, C. Blitz, T. Nissen-Meyer, P. Basini, and J. Tromp. Forward and adjoint simulations of seismic wave propagation on fully unstructured hexahedral meshes. *Geophysical Journal International*, 186(2):721–739, 2011.

[232] P. Ping, Y. Zhang, and Y. Xu. A multiaxial perfectly matched layer (M-PML) for the long-time simulation of elastic wave propagation in the second-order equations. *Journal of Applied Geophysics*, 101(0):124 – 135, 2014.

[233] A. Pitarka. 3D Elastic finite-difference modeling of seismic motion using staggered grids with nonuniform spacing. *Bulletin of the Seismological Society of America*, 89(1):54–68, 1999.

[234] A. Pitarka, K. Irikura, T. Iwata, and H. Sekiguchi. Three-dimensional simulation of the near-fault ground motion for the 1995 Hyogo-Ken Nanbu (Kobe), Japan, earthquake. *Bulletin of the Seismological Society of America*, 88(2):428–440, 1998.

[235] A. S. Pitarka, H. Takenaka, and D. Suetsugu. Modeling strong motion in the Ashigara Valley for the 1990 Odawara, Japan, earthquake. *Bulletin of the Seismological Society of America*, 84(5):1327–1335, 1994.

[236] B. Poursartip, A. Fathi, and L. F. Kallivokas. Seismic wave amplification by topographic features: A parametric study. *Soil Dynamics and Earthquake Engineering*, 92:503 – 527, 2017.

[237] B. Poursartip and L. F. Kallivokas. An Integrated Approach for the Large-Scale Simulation of Sedimentary Basins to Study Seismic Wave Amplification. In *AGU Fall Meeting Abstracts*, Decemeber 2015.

[238] B. Poursartip and V. Lotfi. Modal analysis of concrete arch dams in time domain including dam-reservoir interaction. In *The 14th world conference on Earthquake Engineering*, pages 12–17, October 2008.

[239] B. Poursartip and V. Lotfi. Modal analysis of concrete arch dams in time

domain including dam-reservoir interaction. *Journal of Algorithms and Computation*, 41(6):683–697, 2013.

[240] Babak Poursartip. Modal analysis of concrete arch dams in time domain including dam-reservoir interaction. Master's thesis, Amirkabir University of Technology, Tehran, Iran, 2005.

[241] G.A. Prieto, P.M. Shearer, F.L. Vernon, and D. Kilb. Earthquake source scaling and self-similarity estimation from stacking p and s spectra. *Journal of Geophysical Research.B.Solid Earth*, 109, 2004.

[242] A. Quarteroni, R. Sacco, and F. Saleri. *Numerical Mathematics*. Texts in Applied Mathematics. Springer, 2010.

[243] D. Rabinovich, D. Givoli, J. Bielak, and T. Hagstrom. A finite element scheme with a high order absorbing boundary condition for elastodynamics. *Computer Methods in Applied Mechanics and Engineering*, 200(2324):2048 – 2066, 2011.

[244] C. J. Randall. Absorbing boundary condition for the elastic wave equation: Velocity-stress formulation. *Geophysics*, 54:1141, September 1989.

[245] E. Reinoso, L.C. Wrobel, and H. Power. Three-dimensional scattering of seismic waves from topographical structures. *Soil Dynamics and Earthquake Engineering*, 16(1):41 – 61, 1997.

[246] D. Restrepo and J. Bielak. Virtual topography: A fictitious domain approach for analyzing free-surface irregularities in large-scale earthquake ground mo-

tion simulation. *International Journal for Numerical Methods in Engineering*, 100(7):504–533, 2014.

[247] J. A. Roden and S. D. Gedney. An efficient FDTD implementation of the PML with CFS in general media. *IEEE Antennas and Propagation Society International Symposium*, 3:1362–1265, July 2000.

[248] A. Rodríguez-Castellanos, F.J. Sánchez-Sesma, C. Ortiz-Alemán, and M. Orozco del Castillo. Least square approach to simulate wave propagation in irregular profiles using the indirect boundary element method. *Soil Dynamics and Earthquake Engineering*, 31(3):385 – 390, 2011.

[249] Ángel Rodríguez-Rozas and Julien Diaz. Non-conforming Curved Finite Element Schemes for Time-dependent Elastic-acoustic Coupled Problems. *J. Comput. Phys.*, 305(C):44–62, January 2016.

[250] K. Sagiyama, S. Govindjee, and P.-O. Persson. An efficient time-domain perfectly matched layers formulation for elastodynamics on spherical domains. *International Journal for Numerical Methods in Engineering*, 100(6):419–441, 2014.

[251] F. J. Sánchez-Sesma. Site effects on strong ground motion. *Soil Dynamics and Earthquake Engineering*, 6(2):124 – 132, 1987.

[252] F. J. Sánchez-Sesma. Elementary solutions for response of a wedge-shaped medium to incident SH and SV waves. *Bulletin of the Seismological Society of America*, 80(3):737–742, 1990.

[253] F. J. Sánchez-Sesma, M. Arellano-Guzmán, J. J. Pérez-Gavilán, M. Suarez, H. Marengo-Mogollón, S. Chaillat, J. D. Jaramillo, J. Gómez, U. Iturrarán-Viveros, and A. Rodríguez-Castellanos. Seismic response of three-dimensional rockfill dams using the Indirect Boundary Element Method. *IOP Conference Series: Materials Science and Engineering*, 10(1):012167, 2010.

[254] F. J. Sánchez-Sesma and M. Campillo. Diffraction of P, SV, and Rayleigh waves by topographic features: A boundary integral formulation. *Bulletin of the Seismological Society of America*, 81(6):2234–2253, 1991.

[255] F. J. Sánchez-Sesma and M. Campillo. Topographic effects for incident P, SV and Rayleigh waves. *Tectonophysics*, 218(13):113 – 125, 1993.

[256] F. J. Sánchez-Sesma, I. Herrera, and J. Avilés. A boundary method for elastic wave diffraction: Application to scattering of SH waves by surface irregularities. *Bulletin of the Seismological Society of America*, 72(2):473–490, 1982.

[257] F. J. Sánchez-Sesma and F. Luzón. Seismic response of three-dimensional alluvial valleys for incident P, S, and Rayleigh waves. *Bulletin of the Seismological Society of America*, 85(1):269–284, 1995.

[258] F. J. Sánchez-Sesma, R. Vai, and E. Dretta. The variational indirect boundary element method: A strategy toward the solution of very large problems of site response. *Journal of Computational Acoustics*, 09(02):531–541, 2001.

[259] F.J. Sánchez-Sesma. Diffraction of elastic waves by three-dimensional surface

irregularities. *Bulletin of the Seismological Society of America*, 73(6A):1621–1636, 1983.

[260] F.J. Sánchez-Sesma. Diffraction of elastic SH waves by wedges. *Bulletin of the Seismological Society of America*, 75(5):1435–1446, 1985.

[261] F.J. Sánchez-Sesma, M.A. Bravo, and I. Herrera. Surface motion of topographical irregularities for incident P, SV, and Rayleigh waves. *Bulletin of the Seismological Society of America*, 75(1):263–269, 1985.

[262] W. J. Schroeder, L.S. Avila, and W. Hoffman. Visualizing with VTK: A Tutorial. *IEEE Comput. Graph. Appl.*, 20(5):20–27, September 2000.

[263] C.W. Scrivner and D.V. Helmberger. Seismic waveform modeling in the Los Angeles Basin. *Bulletin of the Seismological Society of America*, 84(5):1310–1326, 1994.

[264] J.F. Semblat, M. Kham, E. Parara, P.Y. Bard, K. Pitilakis, K. Makra, and D. Raptakis. Seismic wave amplification: Basin geometry vs soil layering. *Soil Dynamics and Earthquake Engineering*, 25(710):529 – 538, 2005. 11th International Conference on Soil Dynamics and Earthquake Engineering (ICSDEE): Part 1.

[265] G. Seriani. A Parallel Spectral Element Method for Acoustic Wave Modeling. *Journal of Computational Acoustics*, 05(01):53–69, 1997.

[266] G. Seriani. 3-D large-scale wave propagation modeling by spectral element method on Cray T3E multiprocessor. *Computer Methods in Applied Mechanics and Engineering*, 164(1-2):235 – 247, 1998.

[267] S.J. Sherwin and G.E. Karniadakis. A triangular spectral element method; applications to the incompressible Navier-Stokes equations. *Computer Methods in Applied Mechanics and Engineering*, 123(1–4):189 – 229, 1995.

[268] S.J. Sherwin and G.E. Karniadakis. Tetrahedral hp Finite Elements: Algorithms and Flow Simulations. *Journal of Computational Physics*, 124(1):14 – 45, 1996.

[269] L.B. Sills. Scattering of horizontally-polarized shear waves by surface irregularities. *Geophysical Journal of the Royal Astronomical Society*, 54(2):319–348, 1978.

[270] C. Smerzini, J. Aviles, R. Paolucci, and F. J. Sánchez-Sesma. Effect of underground cavities on surface earthquake ground motion under SH wave propagation. *Earthquake Engineering and Structural Dynamics*, 38(12):1441–1460, 2009.

[271] C. M. Snelson, T. M. Brocher, K. C. Miller, T. L. Pratt, and A. M. Trhu. Seismic Amplification within the Seattle Basin, Washington State: Insights from SHIPS Seismic Tomography Experiments. *Bulletin of the Seismological Society of America*, 97(5):1432–1448, 2007.

[272] R. Snieder. The influence of topography on the propagation and scattering of surface waves. *Physics of the Earth and Planetary Interiors*, 44(3):226 – 241, 1986.

[273] A. Sohrabi-Bidar, M. Kamalian, and M. Jafari. Seismic response of 3-D Gaussian-shaped valleys to vertically propagating incident waves. *Geophysical Journal International*, 183(3):1429–1442, 2010.

[274] M.B. Sørensen, I. Oprsal, S. Bonnefoy-Claudet, K. Atakan, P. M. Mai, N. Pulido, and C. Yalciner. Local site effects in Ataköy, Istanbul, Turkey, due to a future large earthquake in the Marmara Sea. *Geophysical Journal International*, 167(3):1413–1424, 2006.

[275] R. Stacey. Improved transparent boundary formulations for the elastic-wave equation. *Bulletin of the Seismological Society of America*, 78(6):2089–2097, 1988.

[276] S. Stein and M. Wysession. *An Introduction to Seismology, Earthquakes, and Earth Structure*. Wiley, 1991.

[277] A.C. Stolte, B.R. Cox, and R.C. Lee. An Experimental Topographic Amplification Study at Los Alamos National Laboratory using Ambient Vibrations. *Bulletin of the Seismological Society of America*, 2017.

[278] G. Strang. *Computational Science and Engineering*. Wellesley-Cambridge Press, 2007.

[279] R. Taborda and J. Bielak. Ground Motion Simulation and Validation of the 2008 Chino Hills, California, Earthquake. *Bulletin of the Seismological Society of America*, 103(1):131–156, 2013.

[280] M. Taylor, B. Wingate, and R. Vincent. An Algorithm for Computing Fekete Points in the Triangle. *SIAM Journal on Numerical Analysis*, 38(5):1707–1720, 2000.

[281] M.A. Taylor and B.A. Wingate. A generalized diagonal mass matrix spectral element method for non-quadrilateral elements. *Applied Numerical Mathematics*, 33(1–4):259 – 265, 2000.

[282] F. L. Teixeira and W. C. Chew. Complex space approach to perfectly matched layers: a review and some new developments. *Int. J. Numer. Model.*, 13:441–455, 2000.

[283] S. A. Thau. Radiation and Scattering From a Rigid Inclusion in an Elastic Medium. *Journal of Applied Mechanics*, 34:909–911, 1967.

[284] T. Toshinawa and T. Ohmachi. Love-wave propagation in a three-dimensional sedimentary basin. *Bulletin of the Seismological Society of America*, 82(4):1661–1677, 1992.

[285] M. D. Trifunac. Scattering of plane SH waves by a semi-cylindrical canyon. *Earthquake Engineering & Structural Dynamics*, 1(3):267–281, 1972.

[286] R. Vai, J. M. Castillo-Covarrubias, F.J. Sánchez-Sesma, D. Komatitsch, and J.-P. Vilotte. Elastic wave propagation in an irregularly layered medium. *Soil Dynamics and Earthquake Engineering*, 18(1):11 – 18, 1999.

[287] J.E. Vidale and D.V. Helmberger. Elastic finite-difference modeling of the 1971 San Fernando, California earthquake. *Bulletin of the Seismological Society of America*, 78(1):122–141, 1988.

[288] D.J. Wald and R.W. Graves. The seismic response of the Los Angeles basin, California. *Bulletin of the Seismological Society of America*, 88(2):337–356, 1998.

[289] T. Wang and X. Tang. Finite-difference modeling of elastic wave propagation: A nonsplitting perfectly matched layer approach. *Geophysics*, 68(5):1749–1755, 2003.

[290] T. Warburton, S. Sherwin, and G. Karniadakis. Basis Functions for Triangular and Quadrilateral High-Order Elements. *SIAM Journal on Scientific Computing*, 20(5):1671–1695, 1999.

[291] L.C. Wilcox, G. Stadler, C. Burstedde, and O. Ghattas. A high-order discontinuous Galerkin method for wave propagation through coupled elasticacoustic media. *Journal of Computational Physics*, 229(24):9373 – 9396, 2010.

[292] H. L. Wong. Effect of surface topography on the diffraction of P, SV, and Rayleigh waves. *Bulletin of the Seismological Society of America*, 72(4):1167–1183, 1982.

[293] H. L. Wong and P. C. Jennings. Effects of canyon topography on strong ground motion. *Bulletin of the Seismological Society of America*, 65(5):1239–1257, 1975.

[294] C.M. Wood and B.R. Cox. Experimental Data Set of Mining-Induced Seismicity for Studies of Full-Scale Topographic Effects. *Earthquake Spectra*, 31(1):541–564, 2015.

[295] K. Yomogida and J.T. Etgen. 3-D wave propagation in the Los Angeles basin for the Whittier-Narrows earthquake. *Bulletin of the Seismological Society of America*, 83(5):1325–1344, 1993.

[296] C. Yoshimura, J. Bielak, Y. Hisada, and A. Fernández. Domain Reduction Method for Three-Dimensional Earthquake Modeling in Localized Regions, Part II: Verification and Applications. *Bulletin of the Seismological Society of America*, 93(2):825–841, 2003.

[297] J. Zahradník and P. Moczo. Hybrid seismic modeling based on discrete-wave number and finite-difference methods. *pure and applied geophysics*, 148(1-2):21–38, 1996.

[298] X. Zeng and J. Bielak. Stability assessment of a unified variational boundary integral method applicable to thin scatterers and scatterers with corners. *Computer Methods in Applied Mechanics and Engineering*, 111(3–4):305 – 321, 1994.

[299] Y. Q. Zeng, J. Q. He, and Q. H. Liu. The application of the perfectly matched layer in numerical modeling of wave propagation in poroelastic media. *Geophysics*, 66(4):1258–1266, 2001.

[300] B. Zhang, A. S. Papageorgiou, and J. L. Tassoulas. A hybrid numerical technique, combining the finite-element and boundary-element methods, for modeling the 3D response of 2D scatterers. *Bulletin of the Seismological Society of America*, 88(4):1036–1050, 1998.

[301] D.W. Zingg. Comparison of High-Accuracy Finite-Difference Methods for Linear Wave Propagation. *SIAM J. Sci. Comput.*, 22(2):476–502, February 2000.

Index

Vita

Babak Poursartip was born in Iran. He received his diploma from National Organization for Development of Exceptional Talents, subsequently, attended Shahid Chamran University of Ahvaz to obtain a Bachelor of Science in Civil Engineering. Afterwards, Babak received his Master's degree from Amirkabir University of Technology in Structural Engineering in 2005. Babak also worked in ScetIran consulting engineers company for four years, where he was designing concrete dams, buildings, and underground oil reservoirs. He also served in the Police force for two years. He joined the MUSE program in the University of Texas at Austin in Spring 2010 for his Ph.D. degree. Since then, he was graduate research assistant and also instructor for undergraduate differential equations. In June 2015, he was awarded for the runner up student poster in computational mechanics by the Engineering Mechanics Institute of ASCE under the auspices of the EMI 2015 conference held at Stanford University, California.

Email address: babakp@utexas.edu

This dissertation was typeset with LaTeX[†] by the author.

[†]LaTeX is a document preparation system developed by Leslie Lamport as a special version of Donald Knuth's TeX Program.